AD NUMBER

AD885000

NEW LIMITATION CHANGE

TO

Approved for public release, distribution unlimited

FROM

Distribution authorized to U.S. Gov't. agencies and their contractors; Critical Technology; MAR 1971. Other requests shall be referred to Air Force Materials Laboratory, Wright-Patterson AFB, OH 45433.

AUTHORITY

AFML ltr dtd 10 Apr 1973

AFML-TR-71-58

CORROSION CRACKING OF METALLIC MATERIALS

Mars G. Fontana

The Ohio State University
Department of Metallurgical Engineering

TECHNICAL REPORT AFML-71-58

March 1971

AIR FORCE MATERIALS LABORATORY
AIR FORCE SYSTEMS COMMAND
WRIGHT-PATTERSON AIR FORCE BASE, OHIO

NOTICE

When Government drawings, specifications, or other data are used for any purpose other than in connection with a definitely related Government procurement operation, the United States Government thereby incurs no responsibility nor any obligation whatsoever; and the fact that the Government may have formulated, furnished, or in any way supplied the said drawings, specifications, or other data, is not to be regarded by implication or otherwise as in any manner licensing the holder or any other person or corporation, or conveying any rights or permission to manufacture, use, or sell any patented invention that may in any way be related thereto.

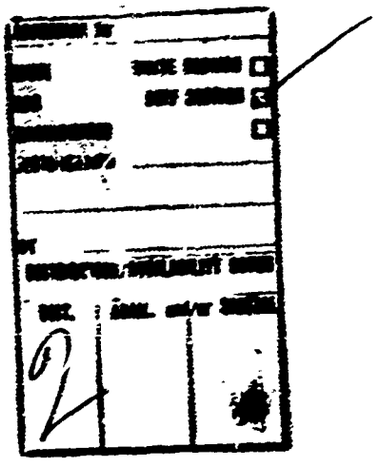

Copies of this report should not be returned unless return is required by security considerations, contractual obligations, or notice on a specific document.

Unclassified

Security Classification

DOCUMENT CONTROL DATA - R & D

(Security classification of title, body of abstract and indexing annotation must be entered when the overall report is classified)

1 ORIGINATING ACTIVITY (Corporate author)	2a. REPORT SECURITY CLASSIFICATION
The Ohio State University Research Foundation Columbus, Ohio 43212	Unclassified
	2b. GROUP N/C

3 REPORT TITLE

CORROSION CRACKING OF METALLIC MATERIALS

4 DESCRIPTIVE NOTES (Type of report and inclusive dates)

Technical - October, 1969 through October, 1970

5 AUTHOR(S) (First name, middle initial, last name)

Mars G. Fontana

6 REPORT DATE	7a. TOTAL NO. OF PAGES	7b. NO OF REFS
March 1971	203	56

8a. CONTRACT OR GRANT NO	9a. ORIGINATOR'S REPORT NUMBER(S)
F33615-69-C-1258 ✓	
8b. PROJECT NO 7312	
c. Task No. 731202	9b. OTHER REPORT NO(S) (Any other numbers that may be assigned this report) AFML-TR-71-58

10 DISTRIBUTION STATEMENT This document is subject to special export controls and each transmittal to foregin governments or foreign nationals may be made only with prior approval of the Metals and Ceramics Division Wright-Patterson Air Force Base, Ohio 45433

11 SUPPLEMENTARY NOTES	12 SPONSORING MILITARY ACTIVITY
	Air Force Materials Laboratory Wright-Patterson Air Force Base, Ohio 45433

13 ABSTRACT

Activation energies of 6-7 kcal for stress corrosion cracking were determined for unalloyed titanium and titanium alloys Ti-6-4 and Ti-8-1-1, and βIII in $CH_3OH + HCl + H_2O$ and $CH_3OH + Br_2$ solutions, suggesting that either chloride ion attack or titanium hydride formation describe the cracking mechanism. Chemical methods, to reduce the water content of methanol to low levels and to accurately determine these levels, have been developed to examine the effect of small water concentrations on the stress corrosion cracking behavior of titanium in methanol environments. Work on the fundamental aspects of stress corrosion cracking of high-strength steels includes studies of effects of structure on crack velocity, hydrogen interactions with the steel, acoustical emission, dissolution of iron carbides, and growth kinetics of passive films. Studies on hydrogen absorption show that the kinetics of hydrogen entry depended critically on the potential as it relates to the chemical identity of arsenic-containing species. Growth kinetics of passive films at pH 4 and 6 are reported and optical constants are found to exhibit wider variations at these pH's than at pH 8. The dissolution of the film was shown to increase with decreasing pH. Work on the delayed failure of high-strength steels shows that ductility is significantly affected by specimen size, hydrogen charging conditions, and extent of prior deformation.

DD FORM 1 NOV 68 1473

Unclassified

Security Classification

14 KEY WORDS	LINK A		LINK B		LINK C	
	ROLE	WT	ROLE	WT	ROLE	WT
Stress corrosion cracking						
Methanol						
Titanium						
Hydrogen absorption						
Passive films						

CORROSION CRACKING OF METALLIC MATERIALS

Mars G. Fontana

FOREWORD

This report was prepared by the Department of Metallurgical Engineering, The Ohio State University, Columbus, Ohio. The principal investigator for this project was Dr. Mars Fontana, under Contract F33(615)-69-C-1258. This contract was initiated under Project No. 7312, "Metal Surface Deterioration and Protection," Task No. 731202, "Metal Surface Deterioration," during the period October, 1969 through October, 1970. This work was administered by the Advanced Metallurgical Studies Branch of the Metals and Ceramics Division, Air Force Materials Laboratory, Wright-Patterson Air Force Base, Ohio, under the direction of Dr. C. T. Lynch and Dr. H. B. Kirkpatrick.

This manuscript was released by the author in January, 1971, for publication.

This technical report has been reviewed and is approved.

C. T. Lynch

C. T. LYNCH
Chief, Advanced Metallurgical Studies Branch
Metals and Ceramics Division
Air Force Materials Laboratory

ABSTRACT

Activation energies of 6-7 kcal for stress corrosion cracking were determined for unalloyed titanium and titanium alloys Ti-6-4 and Ti-8-1-1, and βIII in $CH_3OH + HCl + H_2O$ and $CH_3OH + Br_2$ solutions, suggesting that either chloride ion attack or titanium hydride formation describe the cracking mechanism. Chemical methods, to reduce the water content of methanol to low levels and tc accurately determine these levels, have been developed to examine the effect of small water concentrations on the stress corrosion cracking behavior of titanium in methanol environments. The effects of grain size and state of stress (including uniaxial tension, biaxial tension combined bending-torsion, and notched bars) on crack initiation, crack propagation, and crack mode are being evaluated for titanium alloys in methanol environments. Studies on the effect of grain size of Ti-6-4 on stress corrosion cracking in $CH_3OH + H_2O + NaCl$ solution show that increased resistance with decreasing grain size is due primarily to increased crack initiation time.

Work on the fundamental aspects of stress corrosion cracking of high-strength steels includes studies of effects of structure on crack velocity, hydrogen interactions with the steel, acoustical emission, dissolution of iron carbides, and growth kinetics of passive films. Crack velocity in a 250 maraging steel was changed substantially at the same strength level by altering the structure. Variations in crack velocity are related to microstructures determined by the electron microscope. Studies on hydrogen absorption show that the kinetics of hydrogen entry depended critically on the potential as it relates to the chemical identity of arsenic-containing species. Analysis of permeation transients for Fe-Cu alloys shows clear indications of variations in hydrogen trapping related to aging-related coherency strains. Growth kinetics of passive films at pH 4 and 6 are reported and optical constants are found to exhibit wider variations at these pH's than at pH 8. The dissolution of the film was shown to increase with decreasing pH.

Work on the delayed failure of high-strength steels shows that ductility is significantly affected by specimen size, hydrogen charging conditions, and extent of prior deformation. Failure times decrease with increase in charging times.

TABLE OF CONTENTS

TABLE OF CONTENTS - (Continued)

TABLE OF CONTENTS - (Continued)

ILLUSTRATIONS

ILLUSTRATIONS - (Continued)

ILLUSTRATIONS - (Continued)

ILLUSTRATIONS - (Continued)

ILLUSTRATIONS - (Continued)

ILLUSTRATIONS - (Continued)

ILLUSTRATIONS - (Continued)

ILLUSTRATIONS - (Continued)

ILLUSTRATIONS - (Continued)

TABLES

SECTION I

INTRODUCTION

This Technical Report covers the period October 1969 - October 1970. The program is aimed at developing fundamental information concerning the nature and control of stress corrosion cracking with primary emphasis on titanium alloys and high strength steels.

Pursuant to the coupling aspects of this program, five lectures and seminars were held at AFML by our staff. A post-doctoral fellow continued his research at AFML.

SECTION II

TITANIUM AND TITANIUM-BASE ALLOYS (F. H. Beck)

The objective of this program is to obtain a better understanding of the factors responsible for stress-corrosion cracking in titanium-base alloys. Investigations described below are designed to characterize various titanium-environment stress-cracking systems. The effects of microstructure and state of stress on crack initiation and propagation are important parts of these studies.

A. STRESS-CORROSION CRACKING OF UNALLOYED TITANIUM IN METHANOL SOLUTIONS (C. M. Chen)

1. Aims and Significance of Work

Stress-corrosion cracking studies of titanium alloys Ti-8-1-1 and Ti-6-4 in methanolic solutions have been presented in previous progress reports. This report is concerned with stress corrosion studies of unalloyed titanium (RMI-70) in CH_3OH + 0.17% HCl + X% H_2O solutions. Results show that when the water content of the solution is greater than 1.6% there is no stress corrosion susceptibility, and below this value intergranular failure occurs in about 1.5 hours (Fig. 1). The cracking mechanism is discussed in relation to the activation energy and the effect of grain size on susceptibility. An activation energy of about 5.7 kcal may be due to the diffusion of the chloride ion in the methanol solution. The linear relation between failure time and $D^{-\frac{1}{2}}$ (where D is the grain size) suggests that dislocation pile-ups, resulting from external loading, cause stress concentrations at the grain boundaries and thereby play an important role in the intergranular cracking susceptibility.

2. Experimental Procedure and Results

The legs of unnotched U-bend specimens (0.6 mm x 7 mm x 77 mm) were placed in short lengths of 25.4 mm glass tubing which served as stressing jigs. These assemblies were placed in the test solution and the temperature was controlled to within ±0.1°C with a thermoelectric temperature regulator. The specimens were oriented with the long axis perpendicular to the rolling direction. Grain size was adjusted by repeated straining (0.3% or 1%) and annealing for various times at 815°C in evacuated vycor capsules. Solutions of CH_3OH + HCl + H_2O were prepared from Baker absolute methanol, Applied Chemical reagent grade HCl, and double distilled water. The specimens were mechanically polished

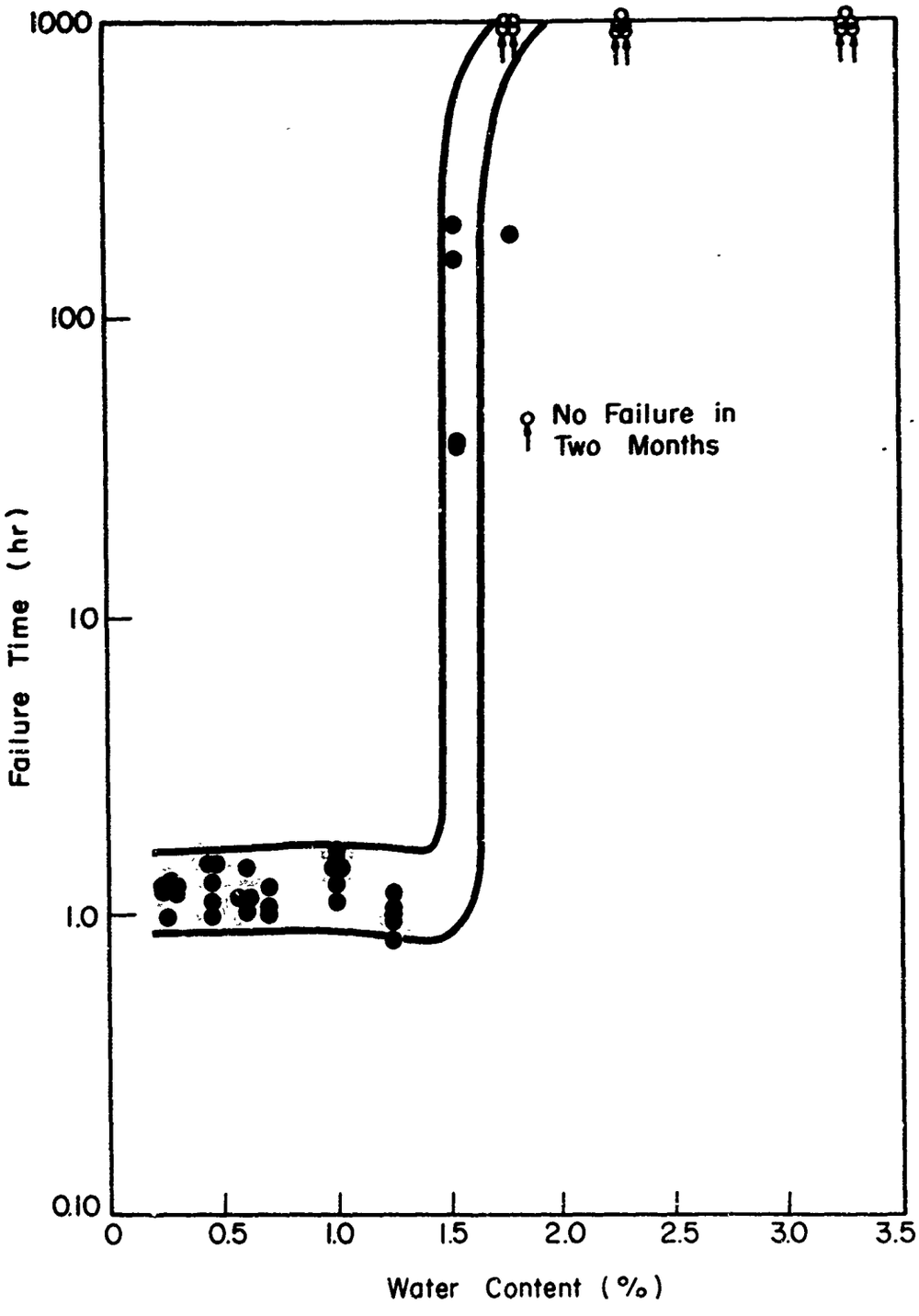

Fig. 1 - Effect of Water Content of CH_3OH + 0.17% HCl Solution on Failure Time of Unalloyed Titanium (tensile axis ⊥ to rolling direction; specimen stressed to yield).

through 600-grit emery and then rinsed in acetone and methanol prior to stress-corrosion testing. The composition of the unalloyed titanium is stated below.

Composition of Unalloyed Titanium

Element	% Element
C	0.02
N	0.011
Fe	0.31
O	0.30%
H	103 ppm

a. Effect of Water Content at Constant HCl Concentration of CH_3OH Solution on Stress Corrosion Susceptibility

Failure time vs. water content is shown in Fig. 1. When the water content is less than 1.3% the failure time is short--approximately 1.5 hours. When the water content is greater than 1.8%, the specimens did not fail in two months. The critical water content is about 1.6%. Cracking is intergranular as illustrated in Fig. 2.

b. Apparent Activation Energy of Stress Cracking

As is shown in Fig. 3, the activation energy was determined in the temperature range from 0° to 50°C. When the temperature was increased, the failure time was decreased and there was a linear relationship between the reciprocal temperature and the logarithmic failure time. The activation energy is about 5.7 kcal. This value is almost the same as those determined for Ti-6-4 and Ti-8-1-1 alloys shown in Fig. 4

c. Effect of Grain Size on Failure Time

Specimens were stress corrosion tested in CH_3OH + 0.28% H_2O + 0.17% HCl solution at 40°C. Figure 5 shows that as the grain size of the specimen was increased, the failure time was decreased. There is a linear relationship between the failure time and $D^{-\frac{1}{2}}$ where D is the grain diameter.

3. Discussion

The effect of water content in methanol solution on the stress-corrosion cracking of Ti-6-4 was discussed in detail in Technical

Fig. 2 - Intergranular Crack of Unalloyed Titanium in $CH_3OH + H_2O - HCl$ Solution

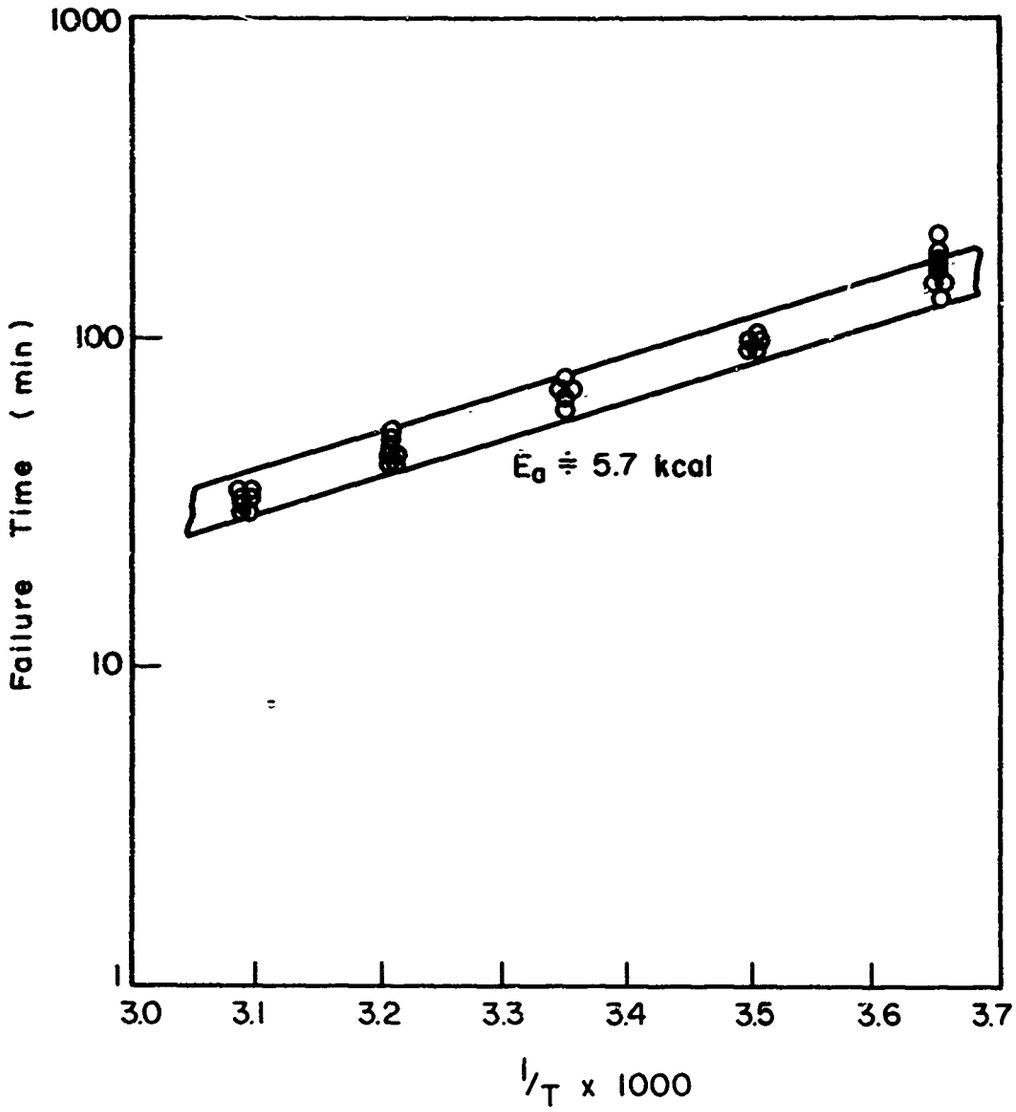

Fig. 3 - Failure Time vs. Reciprocal Temperature for Unalloyed Titanium (tensile axis ⊥ rolling direction; CH_3OH + HCl + H_2O test solution).

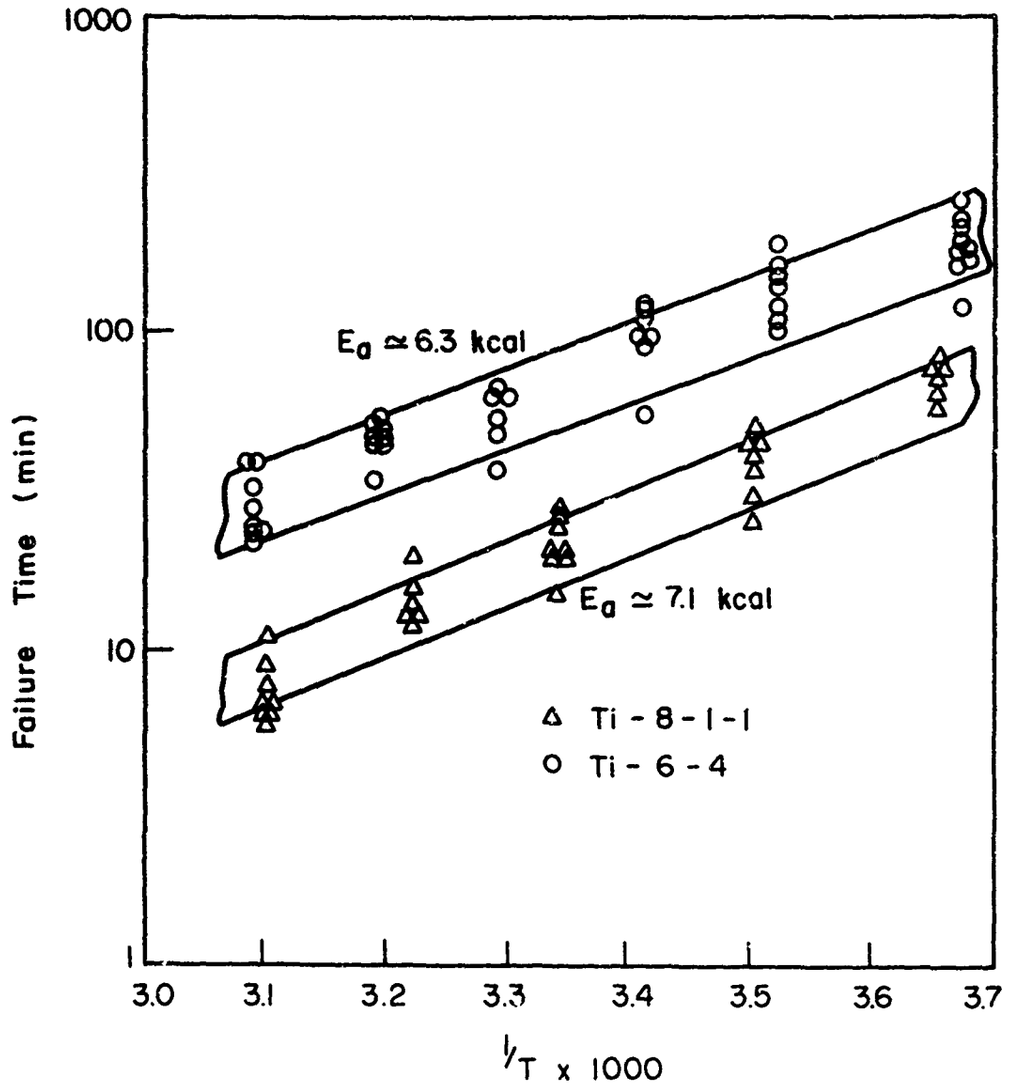

Fig. 4 - Failure Time vs. Reciprocal Temperature Ti-6-4 and Ti-8-1-1 (tensile axis ⊥ rolling direction; CH_3OH + HCl + H_2O test solution).

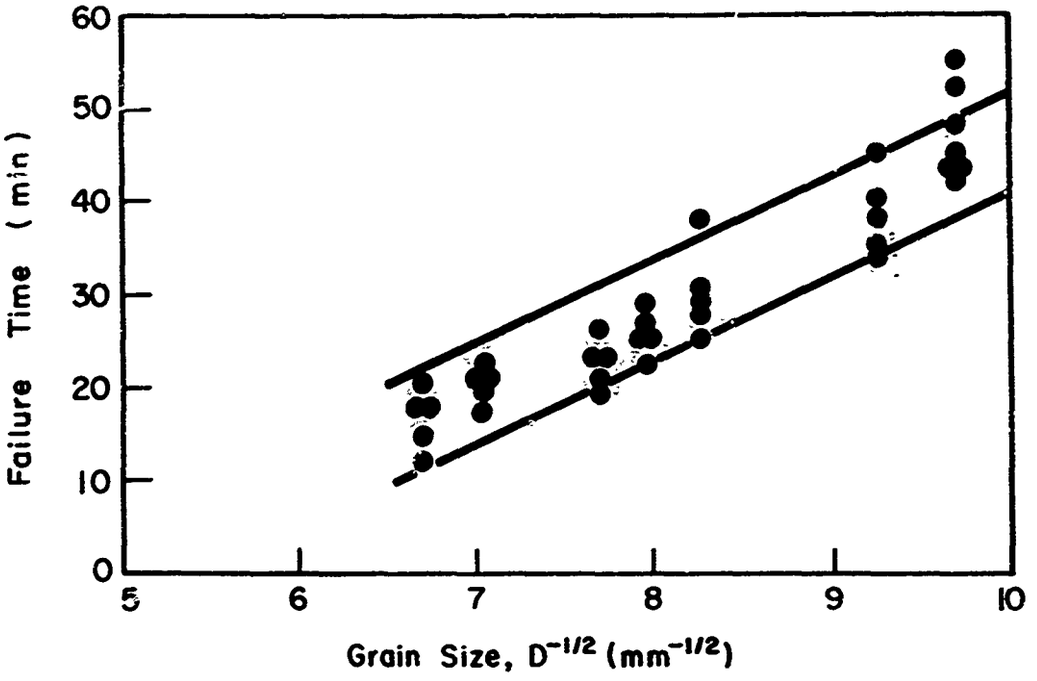

Fig. 5 - Failure Time vs. Grain Size for Unalloyed Titanium (tensile axis ⊥ to rolling direction; CH_3OH + 0.17% HCl + 0.28% H_2O solution).

Report AFML-70-2. When the water content is below 1.6%, the passivator, H_2O, is insufficient to passivate defects in the oxide film for specimens stressed in the solution. These defects are believed to be in the oxide and in the cracking paths located in the grain boundaries. The activation energy for stress-cracking is about 6 - 7 kcal for unalloyed titanium and titanium alloys Ti-6-4 or Ti-8-1-1. The stress corrosion mechanism is discussed as due to either titanium hydride formation or to chloride ion attack. Diffusion of hydrogen in β-titanium is much easier than in α-titanium, and the diffusion coefficients in these phases obey the following equations: *

$$D_\beta = 1.95 \cdot 10^{-3} \exp\left(-\frac{6,640 \pm 500}{RT}\right) cm^2/sec \qquad (1)$$

$$D_\alpha = 1.8 \cdot 10^{-2} \exp\left(-\frac{12,380 \pm 680}{RT}\right) cm^2/sec \qquad (2)$$

Although Ti-8-1-1 and Ti-6-4 alloys are α-alloys, it is possible to have α-phase plus intergranular β-phase by appropriate heat treatments. However, the unalloyed titanium shows only α-phase, and the measured activation energy is only one-half of that of the diffusion of hydrogen in the α-phase. On the other hand, the activation energy of diffusion for the chloride ion in aqueous solution is 4.2 kcal. Therefore, it is not unreasonable to assume that the activation energy for stress cracking is due to the diffusion of chloride ions to the crack apex in the methanol solution in the case of the unalloyed titanium.

In Petch's[1] relation, the fracture stress is proportional to $D^{-\frac{1}{2}}$. According to Eshelby, Frank, and Nabarro,[2] when the dislocation source is located at the center of the grain, the number of dislocations that can be accommodated in the grain is,

$$n = \frac{k\pi\tau_s D}{4Gb} \qquad (3)$$

where D is the grain diameter, and τ_s is the average resolved shear stress which is assumed to be equal to the applied stress τ_a minus the average internal stress τ_i to overcome the resistance to dislocation motion; i.e., $\tau_s = \tau_a - \tau_i$. The stress concentration due to n dislocation pile-ups is n times the average resolved shear stress; i.e.,

$$n\tau_s = \frac{k\pi\tau_s^2 D}{4Gb} \quad . \qquad (4)$$

*From R. J. Wasilewski and G. L. Kehl, "Diffusion of Hydrogen in Titanium," Metallurgia XI, 50, 301 (November, 1954).

Yielding is assumed to occur when a critical shear stress, τ_c, which is independent of the grain size, is produced at the head of the pile-up. If the shear stresses are converted to uniaxial tensile stresses such that $\tau_a = \sigma_a/2$, $\tau_i = \sigma_i/2$, and $\tau_c = \sigma_c/2$, then, the critical shear stress is given by

$$\frac{\pi k(\sigma_a-\sigma_i)^2 \cdot D}{8Gb} = \sigma_c \qquad (5)$$

Therefore,

$$\sigma_a = \sigma_i + \sqrt{\frac{8Gb\sigma_c}{\pi k} \cdot \frac{1}{D}} = \sigma_i + ky \cdot D^{-\frac{1}{2}} \qquad (6)$$

In addition to this shear stress, $n\tau_s$, there is a field of normal stress at the head of the dislocation pile-up according to Stroh's[3] analysis of the stress distribution. Stroh showed that the tensile stress normal to the line OP in Figure 6a is given by

$$\sigma = \frac{3}{4}\left(\frac{D}{\gamma}\right)^{\frac{1}{2}} \tau_s \sin\theta \cos\frac{\theta}{2} \qquad (7)$$

The maximum value of σ occurs at $\cos\theta = 1/3$ or $\theta = 70.5°$; i.e.,

$$\sigma_m = \frac{\tau_s}{\sqrt{3}}\left(\frac{D}{\gamma}\right)^{\frac{1}{2}} \qquad (8)$$

Therefore, when the grain size becomes larger, the normal stress concentration at the grain boundaries becomes larger and is proportional to $D^{\frac{1}{2}}$. Robertson and Tetelman[4] have shown that there are linear relations between failure time and $D^{-\frac{1}{2}}$ in the system of brass in mercury and brass in NH_3 environment. In the unalloyed titanium the failure is intergranular and the linear relation between the failure time and $D^{-\frac{1}{2}}$ suggests that the normal stress concentration caused by the dislocation pile-ups at the grain boundaries is related to the intergranular susceptibility as schematically shown in Fig. 6b.

B. STRESS CORROSION CRACKING OF α (UNALLOYED), α + β (Ti-6-4 and Ti-8-1-1) AND β-III (Ti-11.5Mo-6Zr-4.5Sn) ALLOYS IN METHANOL SOLUTIONS

1. Aims and Significance of Work

Stress corrosion cracking of unalloyed Ti, Ti-8-1-1, and

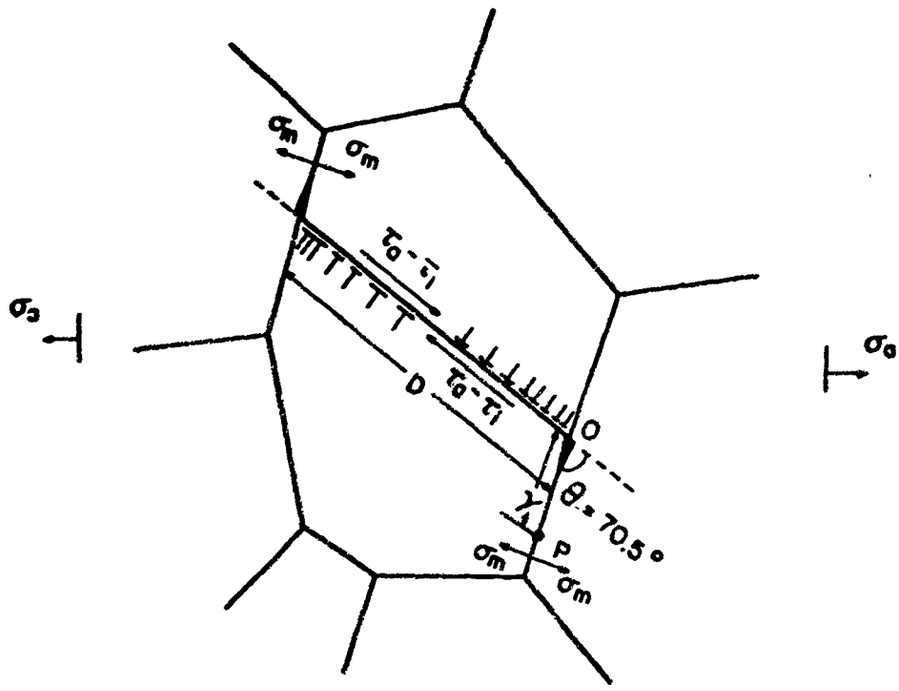

Fig. 6a - Schematic Diagram for Maximum Normal Stress σ_m at the Head of Dislocation Pile-up at the Grain Boundary[3]

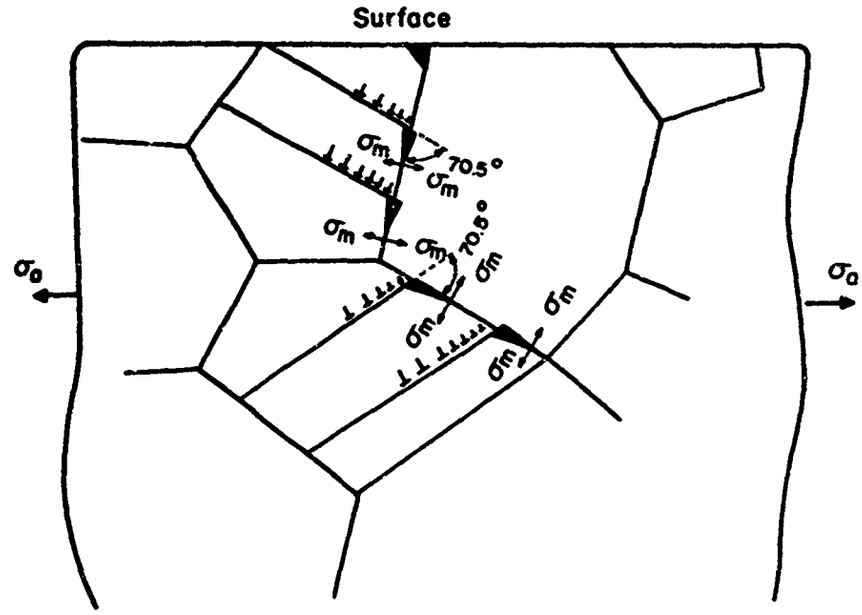

Fig. 6b - Schematic Diagram for Intergranular Cracking Due to the Normal Stress Concentration by Dislocation Pile-up at Grain Boundaries[4]

Ti-6-4 (i.e., α and α + β alloys) have been investigated in methanol + HCl + H_2O solutions. This report is concerned with stress corrosion studies of β-III (β-phase alloy) in methanol + HCl + H_2O solutions and unalloyed Ti, Ti-6-4, Ti-8-1-1, and β-III alloys in methanol + Br_2 solutions.

In methanol + 0.17% HCl + X H_2O solutions the water content necessary to prevent cracking of β-III was determined to be greater than 1.5% and the activation energy for cracking in the same environment was about 5.5 kcal; this activation energy is essentially the same as that obtained for unalloyed titanium and the α + β alloys. This suggests that the diffusion of chloride ion in the methanol solution plays an important role in the cracking process.

Tests on unalloyed Ti, Ti-6-4, Ti-8-1-1, and β-III alloys in methanol + Br_2 solutions show that very small amounts of bromine will cause stress corrosion cracking; e.g., with only 5×10^{-4}% Br_2, Ti-8-1-1 failed in 2-3 minutes, heat-treated β-III failed in 5-7 minutes, and Ti-6-4 failed in 20-50 minutes. When the Br_2 content was less than 5×10^{-5}, all the alloys failed except as-received Ti-8-1-1 ⊥ R.D. and the heat-treated β-III alloys.

Metallographic observations showed that when unstressed specimens of unalloyed Ti and β-III alloys are dipped in methanol + Br_2 solution, bromine attacks the grain boundaries, and after extended times these materials become somewhat porous and brittle. X-ray analysis for the unalloyed titanium after long exposure times showed a pattern for titanium only.

2. Experimental Procedure and Results

The legs of unnotched U-bend specimens (77 mm long x 7 mm wide) for unalloyed Ti (0.64 mm thickness), Ti-8-1-1 (0.25 mm), Ti-6-4 (0.25 mm) were placed in short lengths of 25.4-mm glass tubing which served as stressing jigs; similar type specimens of β-III alloy (0.13 mm x 6 mm x 40 mm) were stressed in short lengths of 17-mm glass tubing. All specimens were oriented with the long axis perpendicular to the rolling direction. β-III specimens were heated at 1700°F for two hours followed by a water quench to assure an all β microstructure.

All specimens were mechanically polished through 600-grit emery, rinsed in acetone, and dipped in methanol prior to stress-corrosion testing. Specimens for metallographic observation were rough polished with 6 μm diamond compound followed by 0.05 μm alumina, and etched with Kroll's solution.

Test solutions of CH_3OH + HCl + H_2O were prepared from Baker's absolute methanol, Allied Chemical reagent grade HCl and double distilled water. Solutions of CH_3OH + Br_2 were prepared from Baker's absolute methanol and purified bromine.

a. Effect of Water Content at Constant HCl Concentration of CH_3OH Solution on Stress Corrosion Susceptibility

Failure time vs. water content is shown in Fig. 7 for the as-received material of Ti-8-1-1 alloy. The critical water content is about 0.6% H_2O; specimens failed in 10-1000 minutes below this water content and in 1000-10,000 minutes or more when the water content was increased above 0.6%. Failure time vs. water content is shown in Fig. 8 for as-received material of β-III alloy. The failure time increased from about 20 minutes to about 100 minutes when the water content was increased from 0.28% to 1.3%; however, the failure time was greatly increased when the water content was greater than 1.5%.

b. Apparent Activation Energy of Stress Cracking of β-III Alloy

Figure 9 shows the activation energy for β-III alloy determined in the temperature range from 0° to 50°C. When the temperature was increased, the failure time decreased; the activation energy is about 5.5 kcal. This value is almost the same as those determined for unalloyed Ti (5.7 kcal), Ti-8-1-1 (7.1 kcal), and Ti-6-4 (6.3 kcal).

c. Stress Corrosion Cracking in CH_3OH + Br_2 Solutions

The effect of bromine concentration in CH_3OH on SCC is shown in Fig. 10a for Ti-8-1-1, in Fig. 10b for β-III, in Fig. 10c for Ti-6-4, and in Fig. 10d for unalloyed Ti. In all cases these are for as-received materials (either with or without mechanical polishing through 600-grit emery paper). Failure times are plotted against the logarithmic concentration of Br_2. In Ti-8-1-1 alloy the curve shows a minimum at about 0.5% Br_2. When the concentration of Br_2 was decreased the failure time increased and there appears to be a linear relationship between the failure time and logarithmic concentration of Br_2. The specimens without mechanical polishing are more susceptible than those with mechanical polishing; the β-III alloy shows the same tendency. Upon decreasing the Br_2 concentration, the failure time decreased at first and then increased linearly with the logarithmic concentration. When the concentration was reduced below 5×10^{-5}% Br_2, the specimen did not fail in 44 hours. Specimens without polishing are more susceptible than those with polishing. The failure time of Ti-6-4 was not greatly affected by Br_2 concentration above about 0.05%; reducing the concentration below 0.05% increased the failure time linearly with logarithmic concentration. When the concentration was below 5×10^{-5}% Br_2, the specimen did not fail in 44 hours. Unalloyed titanium specimens without polishing showed the same tendency as Ti-6-4. Specimens with polishing showed minima similar to the Ti-8-1-1 and β-III alloys. When the concentration was below 5.10^{-5}% Br_2, the specimens did not fail in 100 hours.

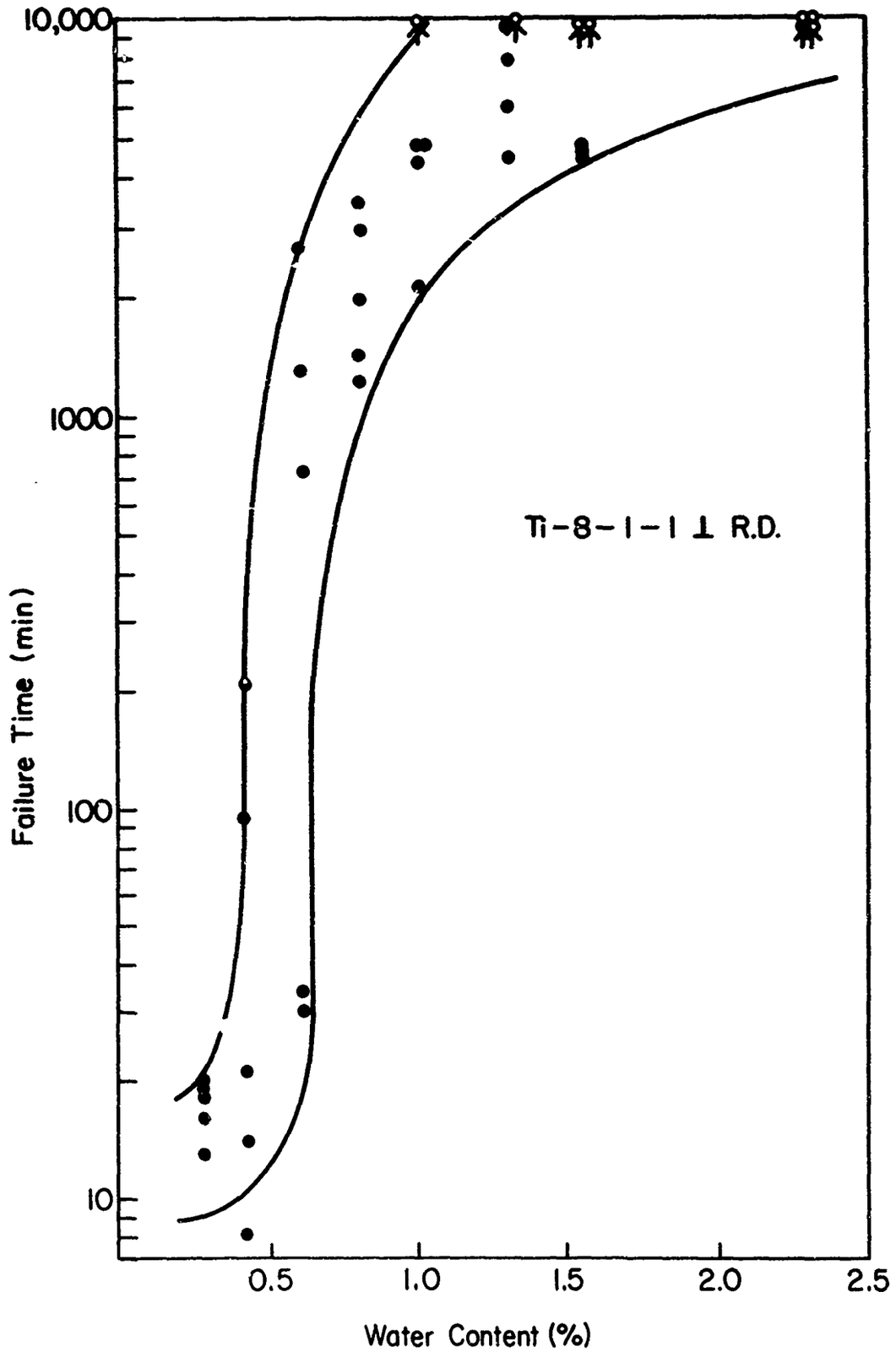

Fig. 7 - Failure Time of Ti-8-1-1 vs. Water Content (%) in CH_3OH + 17% HCl + X H_2O
(Tensile axis ⊥ to rolling direction, specimens stressed to yield)

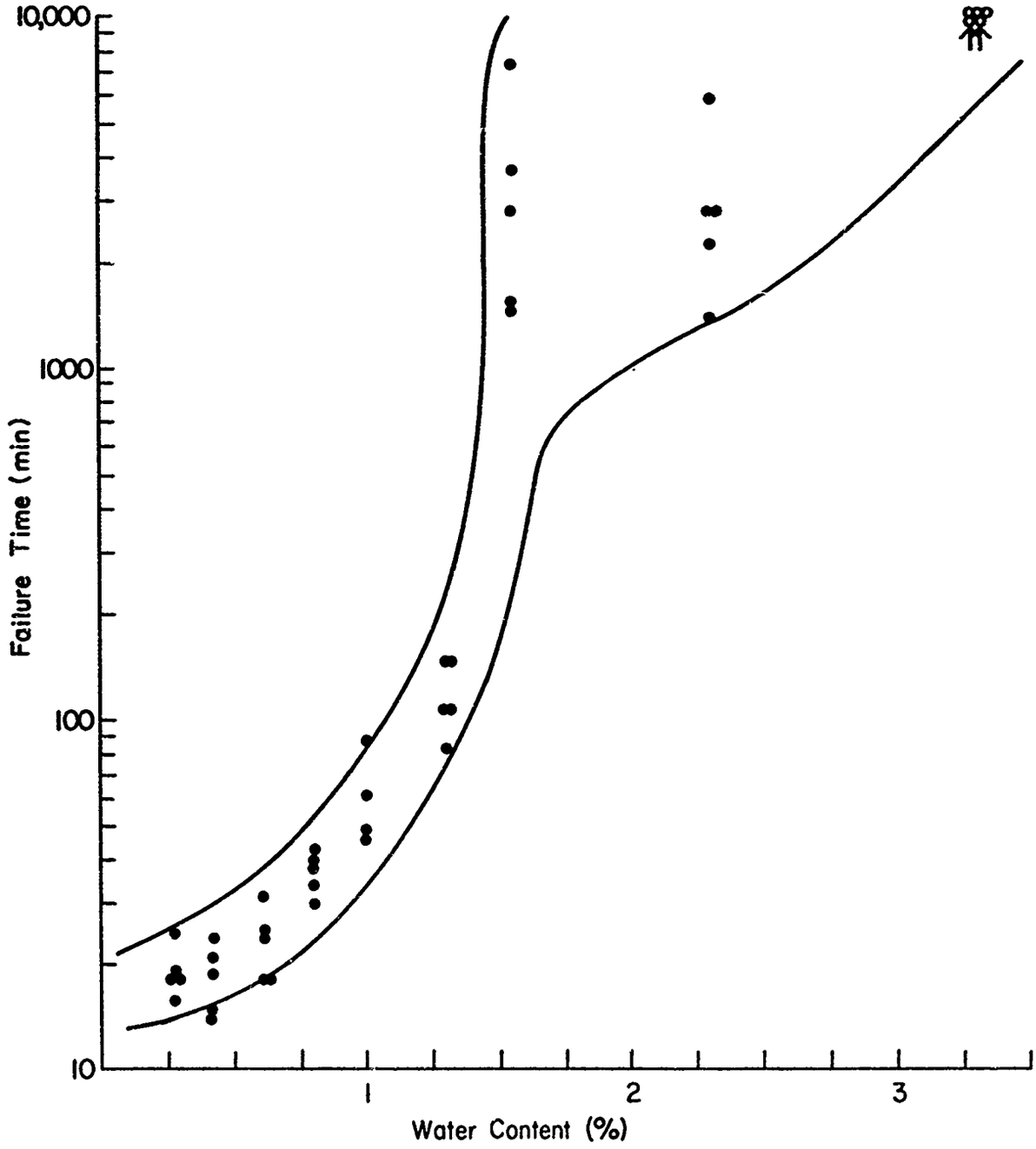

Fig. 8 - Failure Time of β-III Alloy vs. Water Content (%) in CH_3OH + 0.17% HCl + X H_2O (Tensile axis ⊥ to rolling direction, specimen stressed to yield).

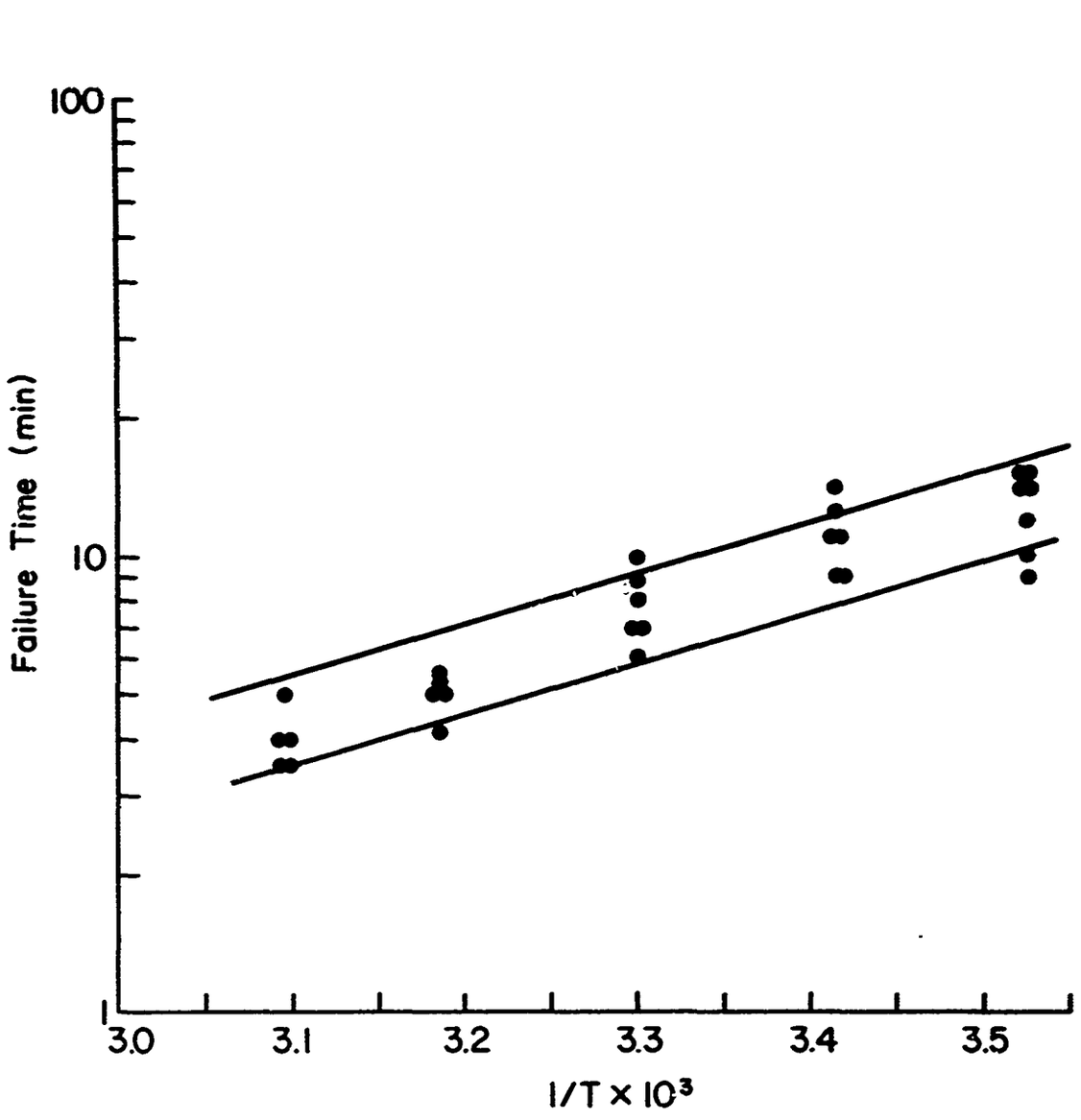

Fig. 9 - Failure Time of β-III Alloy vs. $1/T \times 10^3$ in CH_3OH + 0.17% HCl + 0.28% H_2O (Tensile axis ⊥ to rolling direction, specimen stressed to yield)

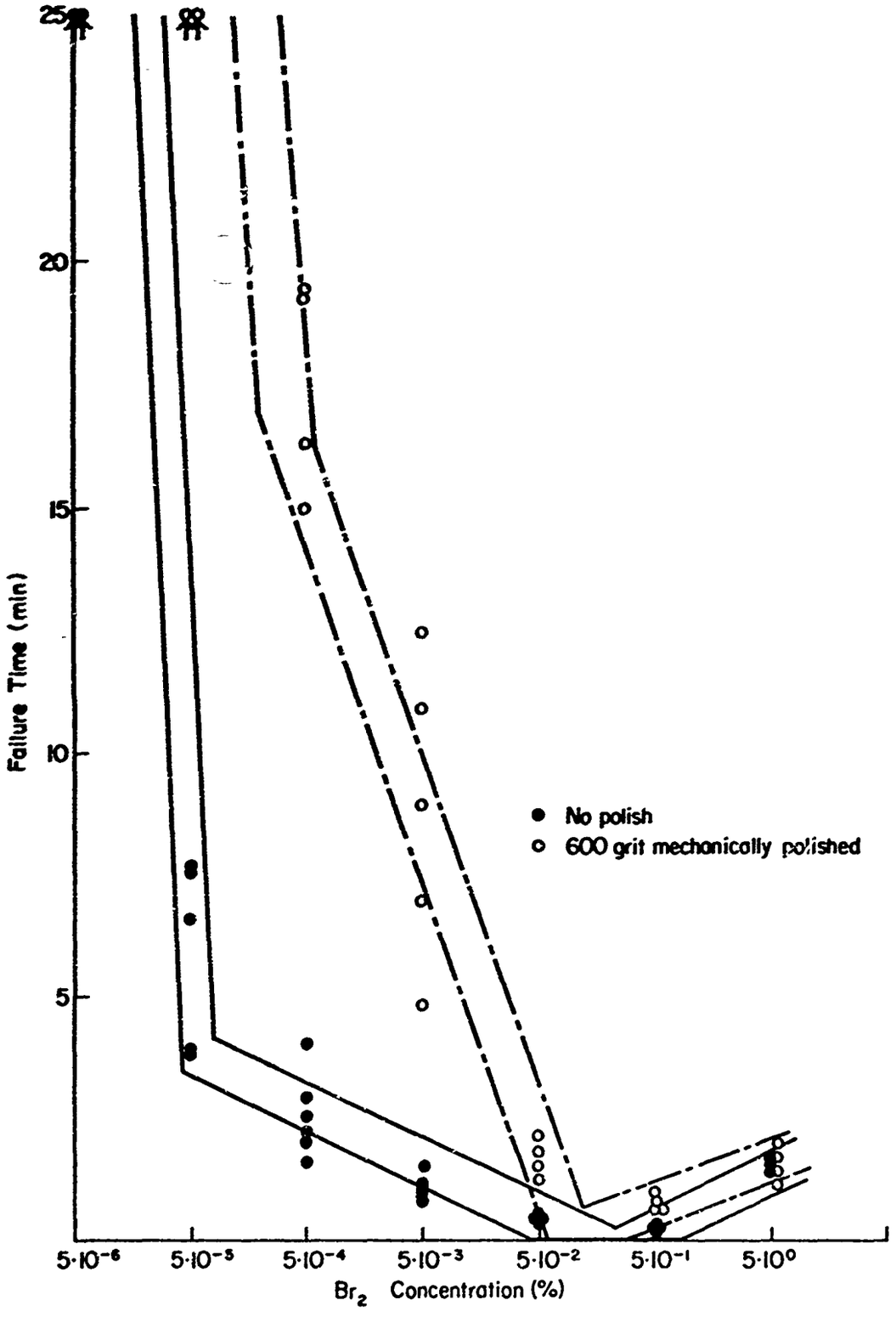

Fig. 10a - Failure Time of Ti-8-1-1 vs. Logarithmic Concentration of Br_2 in CH_3OH (Tensile axis ⊥ to rolling direction)

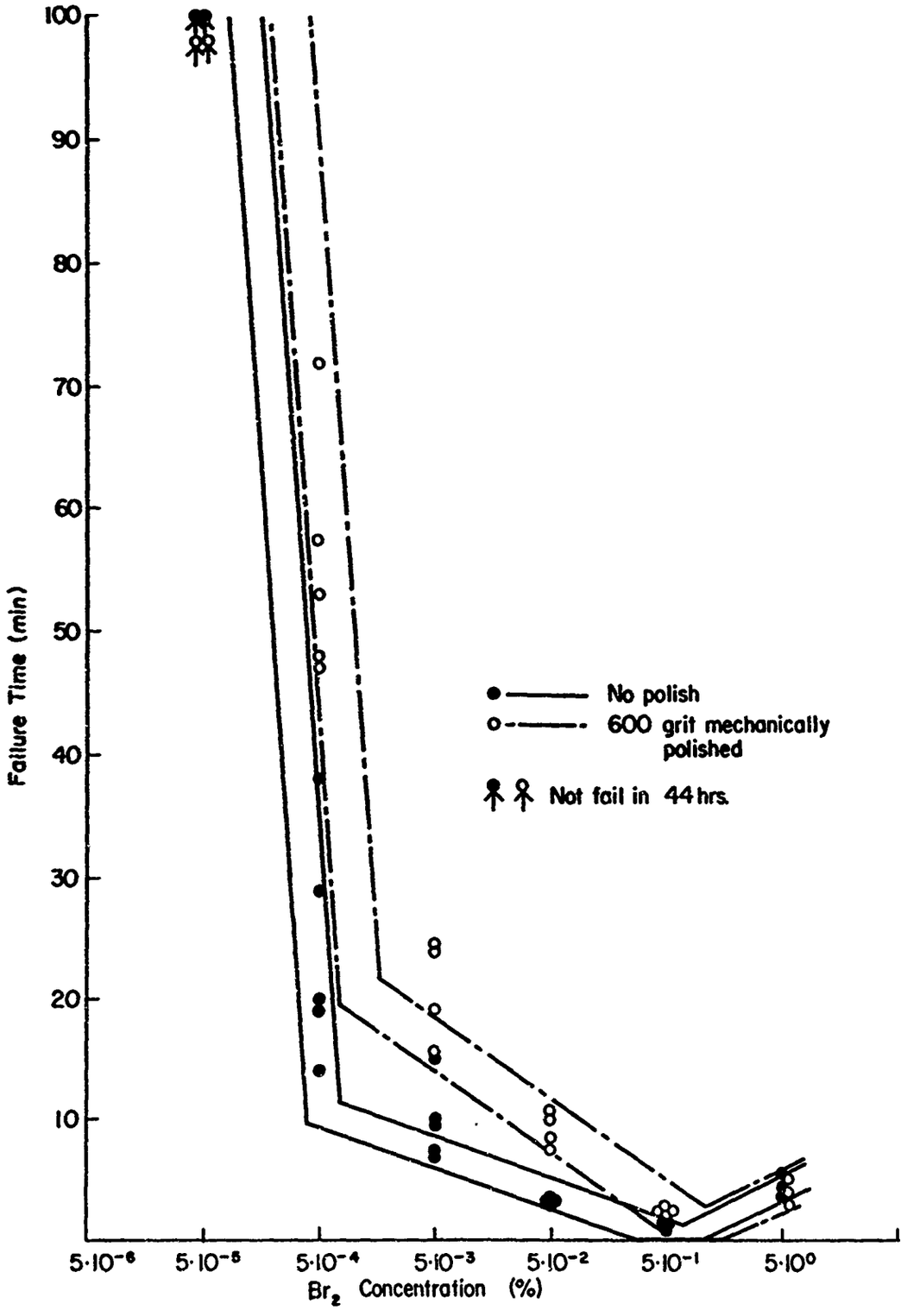

Fig. 10b - Failure Time of β-III Alloy vs. Logarithmic Concentration of Br_2 in CH_3OH (Tensile axis ⊥ to rolling direction).

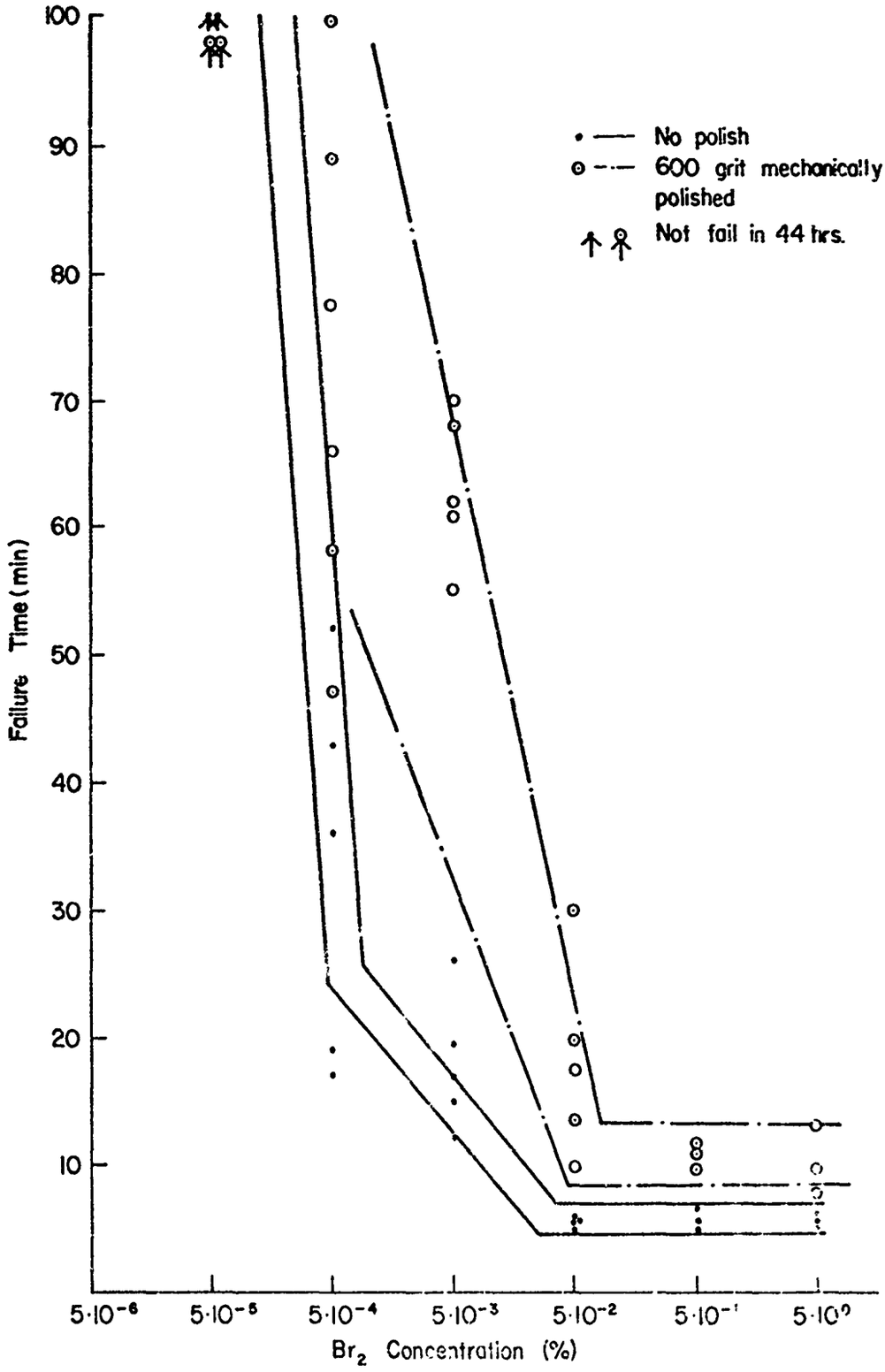

Fig. 10c - Failure Time of Ti-6-4 vs. Logarithmic Concentration of Br_2 in CH_3OH (Tensile axis ⊥ to rolling direction).

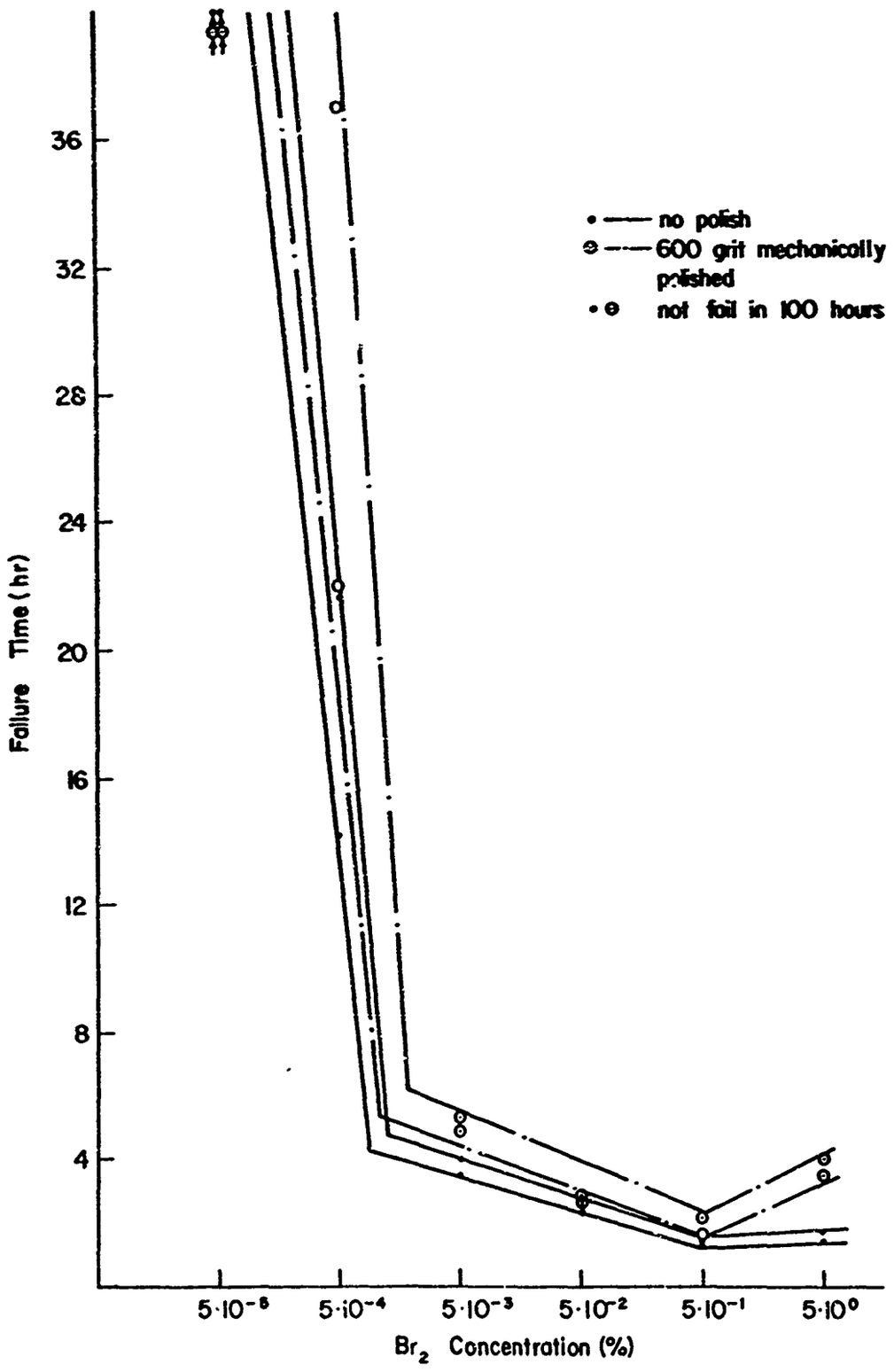

Fig. 10d - Failure Time of Unalloyed Titanium vs. Logarithmic Concentration of Br_2 in CH_3OH (Tensile axis ⊥ to rolling direction).

The curve for heat-treated β-III alloy is shown in Fig. 10e. This curve shows the same tendency as for the Ti-6-4 alloy. When the concentration was below 5×10^{-2}% Br_2, the specimen did not fail in 44 hours.

d. Metallographic Observations

1) When unstressed specimens of unalloyed titanium were dipped in a solution of methanol + 1% Br_2, bromine attacked the grain boundaries; with increased exposure time some of the grains were dissolved out and the material became porous and very brittle. Figure 11 shows the porous material after 68 hours exposure in the solution. This porous material was ground to powder for x-ray analysis to identify the corrosion products. However, it showed a pattern for titanium only.

2) When the unstressed specimens of heat-treated β-III alloy were exposed to a solution of methanol + 0.05% Br_2, bromine attacked the grain boundaries and the material became very brittle. Figure 12 shows the grain boundary corrosion of β-III exposed in the solution for 164 hours. When external stress was applied, transgramular and intergramular SCC occurred as shown in Fig. 13. When the external stress was very high the cracking was almost entirely transgramular and appeared to follow some characteristic crystal plane. The cracks crossed the slip lines (formed by plastic deformation) as shown in Fig. 14.

3) The heat-treated β-III specimen in methanol + 0.17% HCl + 0.28% H_2O failed by both transgramular and intergramular cracking. As shown in Fig. 15 the transgramular cracking follows some characteristic crystallographic direction.

4) The long axis of the Ti-8-1-1 specimen was cut parallel, at 45°, or perpendicular to the rolling direction, and the stress was applied parallel to the long axis of the specimen. As shown in Fig. 16 cracking follows, more or less, the rolling direction.

3. Discussion

In CH_3OH + 0.17% HCl + 0.28% H_2O solution, the activation enery of the cracking process for unalloyed Ti, Ti-6-4, Ti-8-1-1, and β-III alloys is about 6-7 kcal regardless of the phases present. If stress corrosion susceptibility of these alloys is due to titanium hydride formation by supersaturation of hydrogen in the material, the activation energy for the cracking process should be determined by the hydrogen diffusion process. Therefore, the activation energy should be different: 6.6 kcal in α-phase and 12.4 kcal in β-phase according to Eqs. (1) and (2) for the diffusion coefficients. This may suggest that the diffusion of the chloride ions in the solution plays the important role in the stress cracking process.

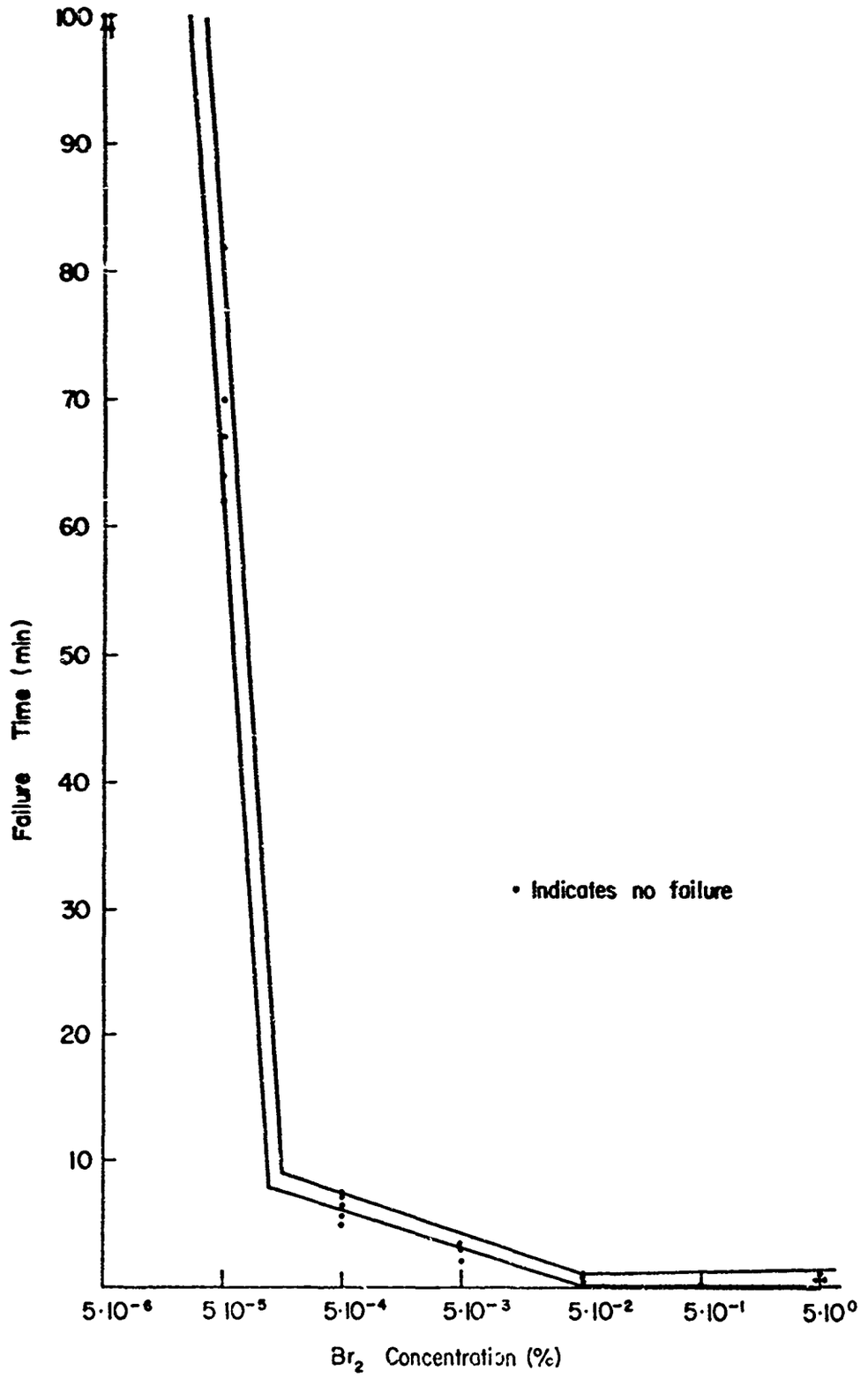

Fig. 10e - Failure Time of B-III Alloy vs. Logarithmic Concentration of Br_2 in CH OH (Specimen treated at 1700°F for 2 hrs and W. Q.)

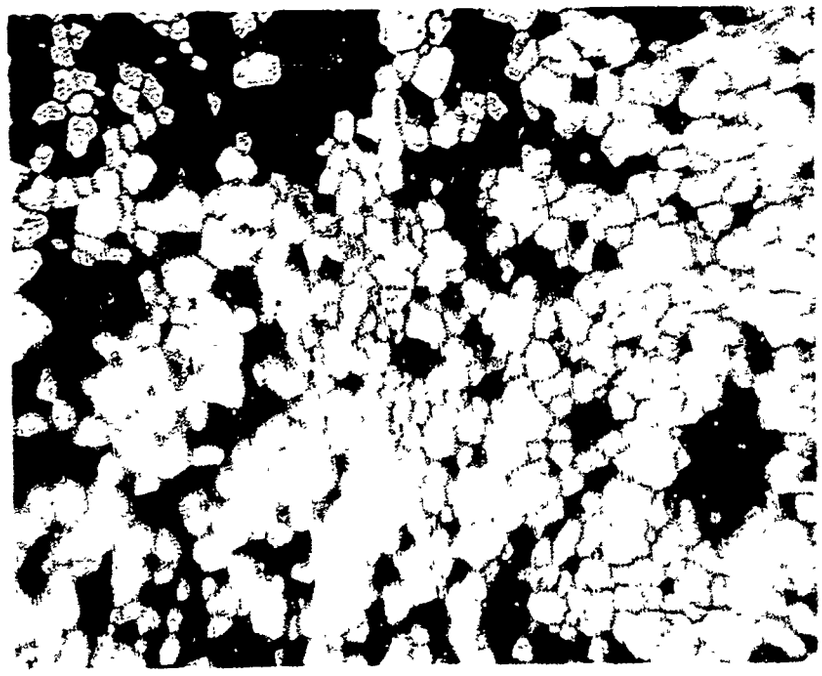

Fig. 11 - Porous Material of Unstressed Unalloyed Titanium Exposed in CH_3OH + 1% Br_2 for 68 Hours (X200)

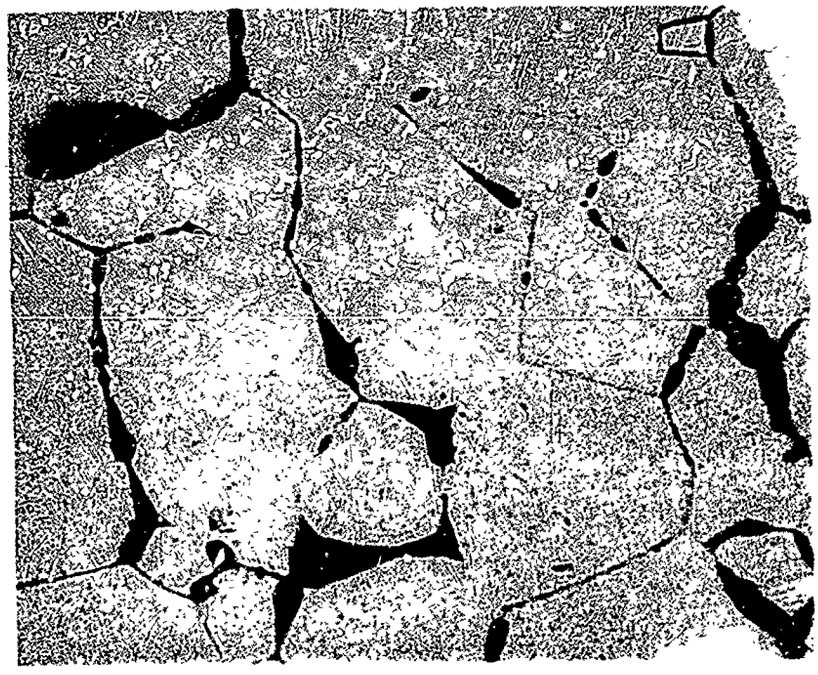

Fig. 12 - Grain Boundary Corrosion of Unstressed β-III Alloy Exposed in CH_3OH + 0.05% Br_2 Solution for 164 Hours (X210)

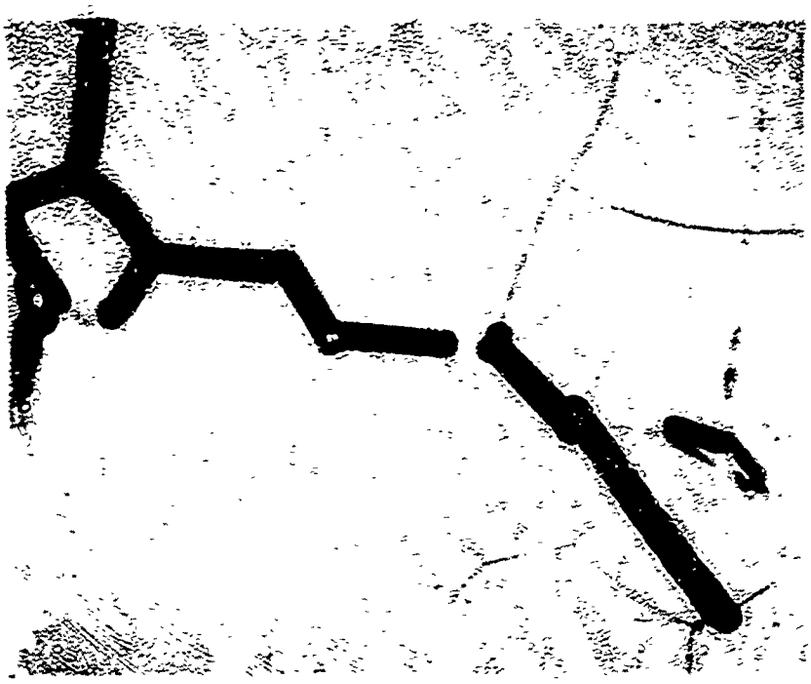

Fig. 13 - Stress Corrosion Cracking of β-III Alloy in CH_3OH + 0.05% Br_2 Solution. (X280)

Fig. 14 - Stress Corrosion Cracking of Highly Stressed β-III Alloy in CH_3OH + 0.5% Br_2 Solution; Transgranular Cracking Crosses Slip Lines Formed by Plastic Deformation (X800)

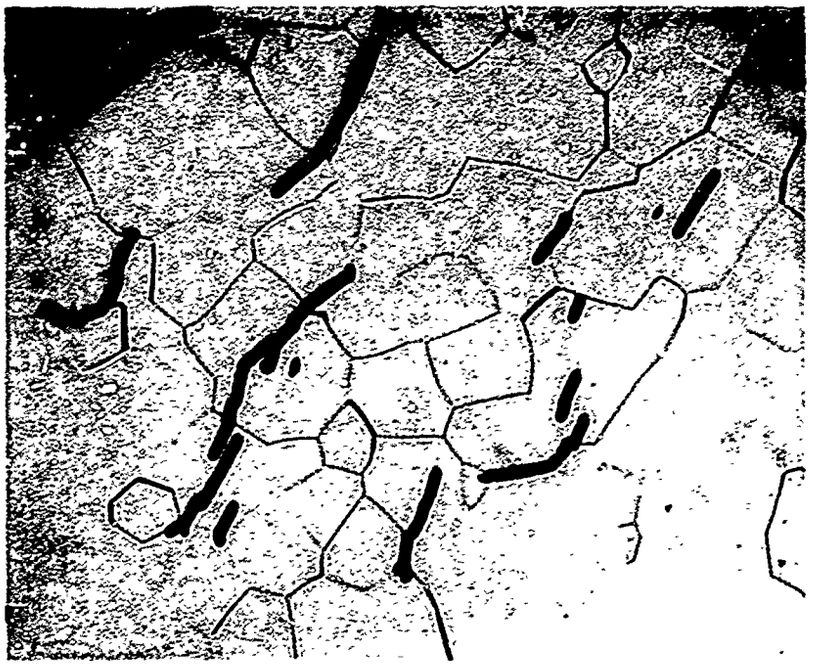

Fig. 15 - Stress Corrosion Cracking of β-III in CH_3OH + .17% HCl + 0.28% H_2O Solution (X100)

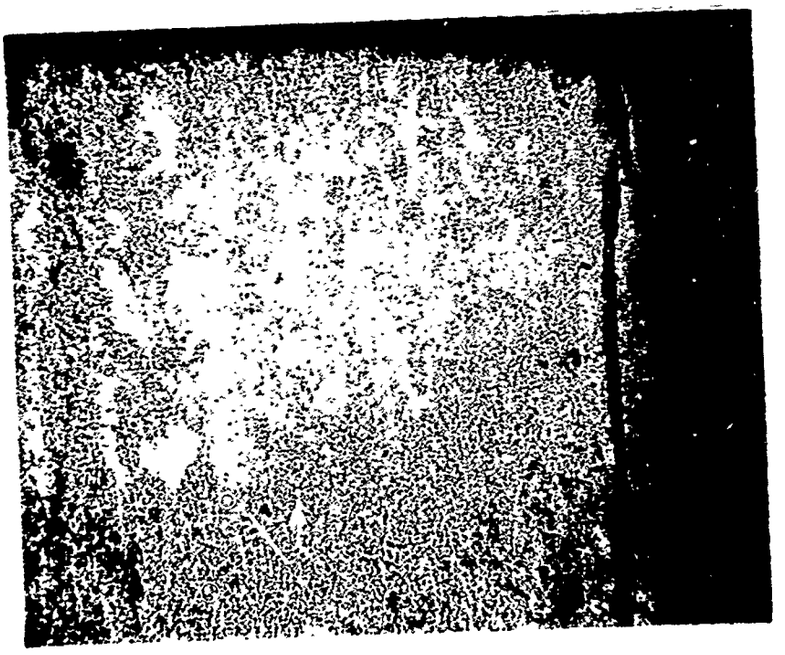

Fig. 16a - Stress Corrosion Cracking of Ti-8-1-1 in CH_3OH + 0.5% Br_2 (X50)

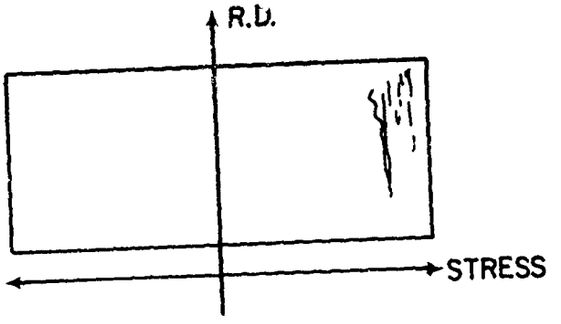

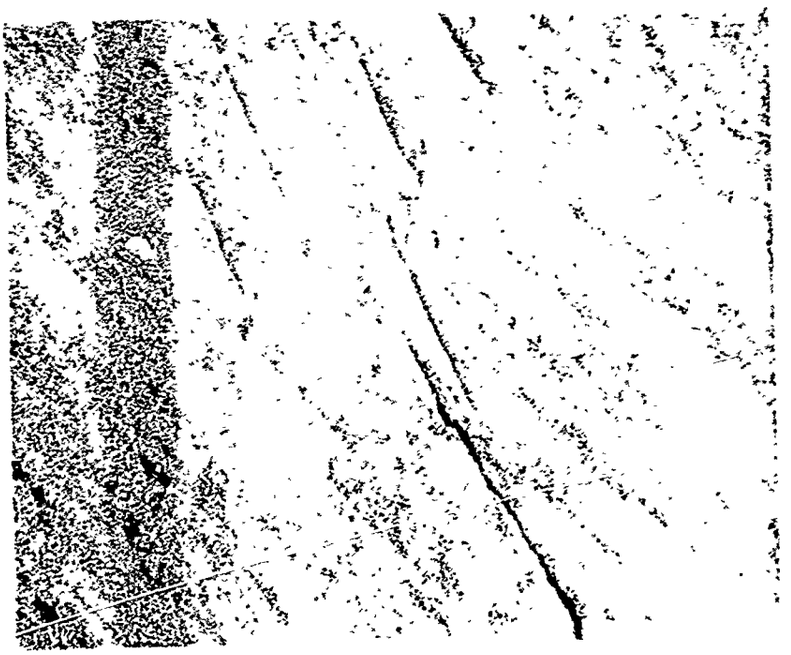

Fig. 16b - Stress Corrosion Cracking of Ti-8-1-1 in CH_3OH + 0.5% Br_2 (X50)

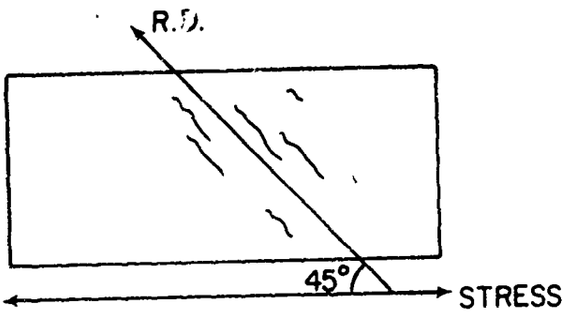

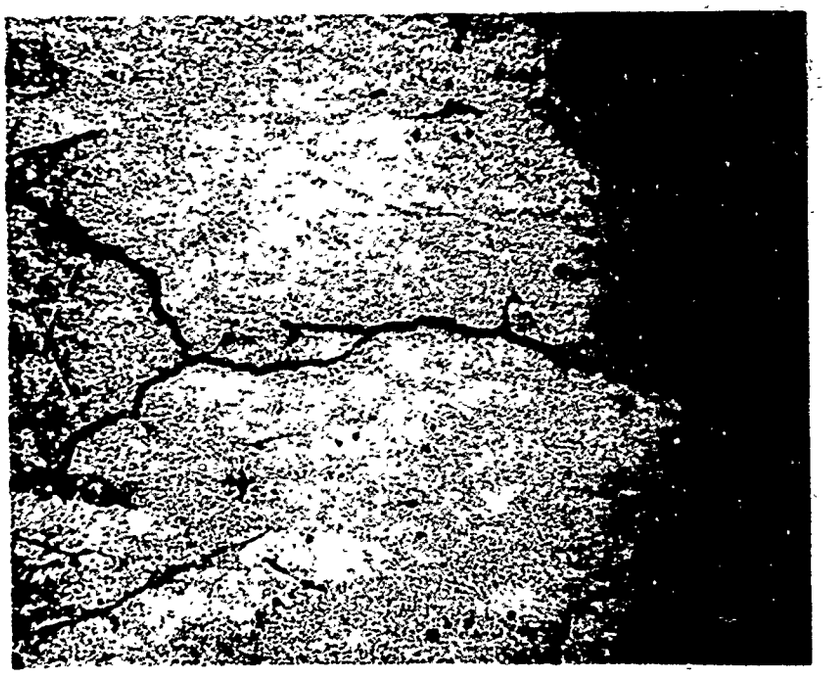

Fig. 16c - Stress Corrosion Cracking of Ti-8-1-1 in CH_3OH + 0.5% Br_2 (X50)

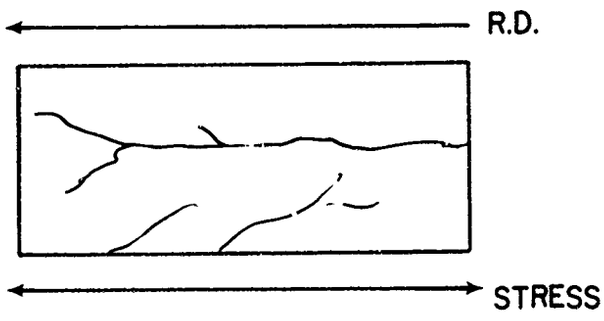

In methanol + Br_2 solution there is no doubt about the reaction of bromine with titanium and its alloys to form $TiBr_4$ which is very soluble in the methanol solution. Therefore, it is reasonable to assume that the process in the intergramular stress corrosion cracking is due to bromine attack as follows:

$$Ti + 2Br_2 \longrightarrow \underset{\text{dissolved in methanol}}{\downarrow TiBr_4} \qquad (9)$$

This reaction occurs at the grain boundary in the absence of an external stress. However, fast transgranular cracking of stressed specimens could result from bromine attack, titanium hydride formation, or stress sorption processes. This will be investigated in future studies.

4. Future Work

It is improbable that a universal model can be used to interpret all stress corrosion phenomena for titanium and its alloys. In aqueous and methanol solutions there are many controversies concerning titanium hydride formation and chloride ion attack. Furthermore, it is worth noting that stress corrosion susceptibility exists in pure carbon tetrachloride and mercury; in other words, without hydrogen or chloride ions. Therefore, the causes for the susceptibility may be different in the various environmental systems. Further research is designed to examine these variables, as follows:

a. Susceptibility due to titanium hydride formation will be intensified in α and $\alpha + \beta$ alloys by charging hydrogen, either by absorbing from hydrogen gas or by cathodic polarization. Titanium hydride is expected to be formed at the slip planes in α alloys and at α-β grain boundaries in $\alpha + \beta$ alloys.

b. Susceptibility due to chloride ion or anodic dissolution will be examined in β alloys; titanium hydride formation will be more difficult for specimens treated at the corrosion potential or at anodic polarization potentials. Also, the solubility of hydrogen in β-phase is very large.

c. Stress relaxation experiments direct observation of the cracking provess by microscopy, and investigations of susceptibility in a gaseous environment are planned.

C. EFFECT OF GRAIN SIZE ON STRESS CORROSION CRACKING OF Ti-6-4 ALLOY IN METHANOL-H_2O NaCl SOLUTION (I. J. Loomba)

1. Aim and Significance of the Work

Most of the work reported in the literature on stress corrosion cracking of titanium and its alloys has been devoted to examining the crack propagation path and the effect of different experimental variables on failure time. Section II-A reports the effect of grain size on failure time for unalloyed titanium in CH_3OH + 0.17% HCl + 0.28% H_2O solution.

The aim of this investigation was to determine the effect of grain size on crack initiation and crack propagation times, crack initiation and propagation paths, and the effect of stress on crack initiation and propagation times.

2. Experimental Procedure

a. Materials

The experimental work was carried out on 0.025-inch thick Ti-6-4 alloy sheet obtained from Reactive Metals, Inc. The composition of the alloy and physical properties of the as-received material are given in Table I. Strips were sheared from the alloy sheet with rolling direction parallel to the length of the strip. These strips were rolled to 10% reduction along their longitudinal direction. The rolled specimens were then annealed at 918 ± 10°C for different lengths of time to obtain different grain sizes. To determine the effect of stress on crack initiation and failure time, specimens were sheared similarly from the sheet and annealed at 600°C for six hours. The physical properties of these heat-treated specimens are given in Table II. The dimensions of the specimens in all cases were 0.020 inch thick x 0.25 inch wide x 1.468 inches long, with the long axis in rolling direction.

Heat treatment was done in a vacuum electric furnace at a pressure of 10^{-6} mmHg or better. Tensile testing was done on an Instron testing machine. Three specimens (0.022" x 0.25" x 1.5" gauge length) were tested for each heat treatment. Table II contains the average value of yield strength and Young's modulus.

After heat treatment all the specimens were polished on 600-grit silicon carbide paper. Specimens for metallographic work were final polished on 6-μm diamond polishing compound followed by 0.05 μm gamma alumina powder. Etching was done with the solution of following compositions: HF, 2%; HNO_3, 6%; H_2O, 92%.

Table I. Composition and Physical Properties of Ti-6Al-4V Alloy

Composition	
Element	**% Weight**
C	0.03
N	0.012
Fe	0.13
Al	6.4
V	4.3
O	0.108
H	58 ppm
Physical Properties	
Ultimate tensile strength	134.8/139.1 ksi
Yield stress (0.2% offset)(transverse)	127.0/132.9 ksi

Above composition and properties were provided by the supplier.

Table II. Physical Properties of 10% Rolled and Annealed at 918°C

Yield stress (0.2% offset) (transverse) (average)	127.5 ksi
Young's modulus (average)	6.335×10^6 psi

Physical Properties of Specimens Annealed at 600°C

Yield stress (0.2% offset) (transverse) (average)	130.0 ksi
Young's modulus (average)	8.0×10^6 psi

The test solution used throughout the investigation was methanol + 0.3% water saturated with NaCl. Sodium chloride and methanol were reagent grade (water content of methanol varied from 0.02% to 0.04%). Double distilled water, containing less than 1 ppm of impurities expressed in terms of NaCl, was used. Freshly prepared solution was used in each experiment.

b. Experimental Apparatus

Three-point loaded, unnotched bend specimens were used. A Ti-6Al-4V alloy wire was used to connect the specimen to an Anotrol potential controller. A Luggin probe placed near the sample surface was connected to the calomel reference electrode through KCl solution. A platinum electrode was used as the counter electrode. An optical microscope was used to observe crack initiation and propagation at 100X. The objective lens was coated with silicon to protect it from the methanol solution.

The deflection of the specimen is related to the stress by the following formula:

$$d = \frac{S\,L^2}{6Et} \quad ,$$

where

d = the maximum deflection in inches,

S = the maximum stress in psi,

L = the length between supports of specimen holder in inches,

E = the Young's modulus of the material in psi, and

t = the thickness of the specimen in inches.

The deflection was measured with a deflectometer to 0.0001-inch accuracy. After the specimen was stressed to the desired extent, the specimen and holder was placed in the test cell. The counter electrode was placed near the specimen and the glass dish was covered with a plexiglass sheet containing holes for receiving the microscope objective and Luggin probe (the cover was used to keep moisture pickup by methanol from the atmosphere to a minimum). The glass dish and Luggin probe were then filled with 600 ml of freshly prepared methanol + 0.3% water and NaCl (saturated) solution. A potential of 0 mV (SHE) was applied in all cases. The time was recorded from the time the potential was applied. Cracks were observed to initiate from pits. The initiation of the crack was recorded as that time when any of the pits transformed to a crack. Failure time was taken as that time when the material had failed completely.

3. Results

Examples of grain sizes obtained by strain annealing are shown in Figs. 17-23. Table III shows the grain size variation with change in annealing time.

a. Stress-Corrosion Cracking

In all stress corrosion test, when the potential was applied, corrosion started at once as localized corrosion in the form of pits elongated in a direction normal to the tensile axis (at 100X). Figure 24 shows some of these elongated pits. Cracks started inside the elongated pits in all the tests performed in this investigation. The crack appears as a dark black line against the dull black background of the pit. Almost every pit gave rise to a crack, as shown in Fig. 25. Almost every elongated pit shown in Fig. 24 contains a crack. In all cases the crack started from the middle of the specimen and not from the edges. These cracks were observed to propagate in a direction perpendicular to the applied stress. The cracks would then proceed to grow until encountering another crack, as shown in Fig. 26. Crack propagation rate was slow in the beginning but increased as the size of the crack increased. The crack size shown in Fig. 25 was obtained 18 minutes after initiation (Fig. 24). It took only eight minutes for the crack in Fig. 25 to grow across the width of the specimen.

b. Effect of Stress

Figures 27 and 28 show the relation of stress to initiation time, propagation time, failure time, and rate of crack propagation. As apparent from Fig. 27 the initiation time, propagation time, and failure time decreased with increasing stress level. As the stress level was increased from 50% of the yield stress (0.2% offset) to 110% of the yield stress the propagation time decreased from 139 minutes to 19 minutes. Table IV shows the applied stress, initiation time, propagation time, and failure time for these experiments.

c. Effect of Grain Size

Pit density and crack density increased with increasing grain size at a constant stress level. It was also observed that the pit had to grow larger in small grain size specimens to give rise to a crack as compared to larger grain size specimens.

Figure 29 shows that crack initiation (pitting) occurs at the α-β grain boundary. Cracks propagating from the pits are both transgranular and intergranular in nature. Figures 30-33 show the crack paths in different grain size specimens. The crack path is mixed (i.e., both intergranular and transgranular) in all the cases.

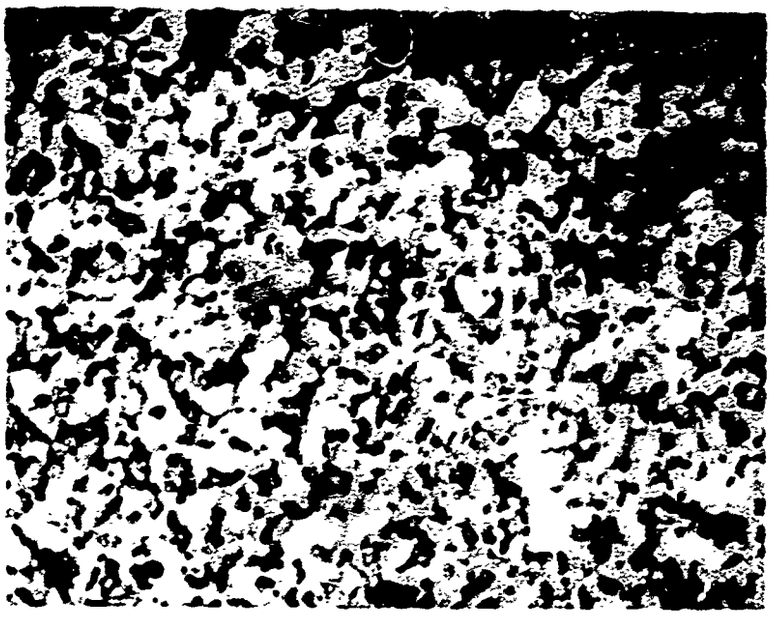

Fig. 17 - Grain Size of 10% Rolled and 1 Hour Annealed Specimen at 918°C; Average Grain Diameter 0.0044 Inch (1000X)

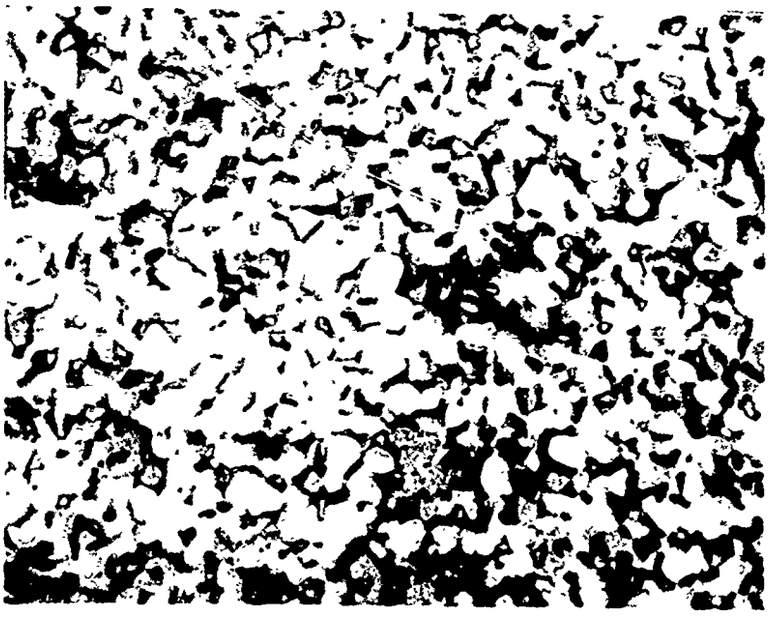

Fig. 18 - Grain Size of 10% Rolled and 2 Hour Annealed Specimen at 918°C; Average Grain Diameter 0.0057 Inch (1000X)

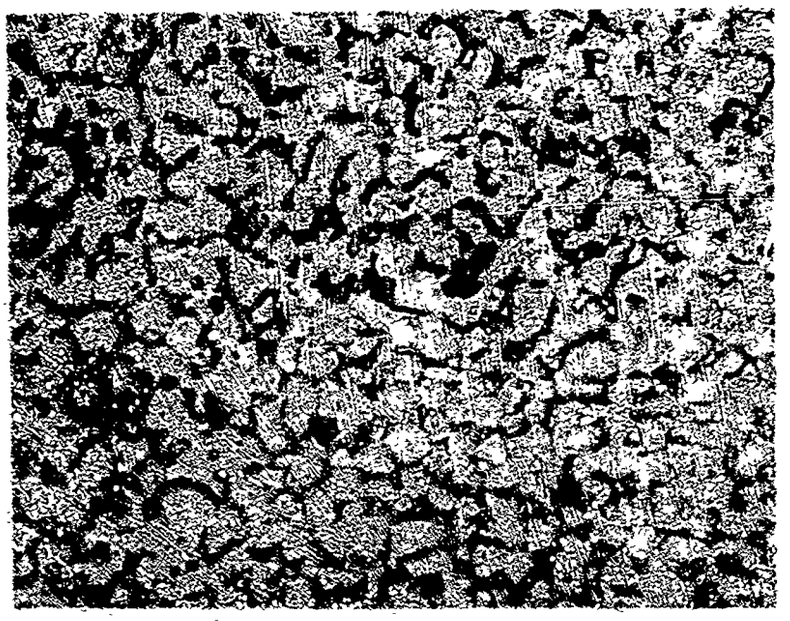

Fig. 19 - Grain Size of 10% Rolled and 4 Hour Annealed Specimen at 918°C; Average Grain Diameter 0.0064 Inch (1000X)

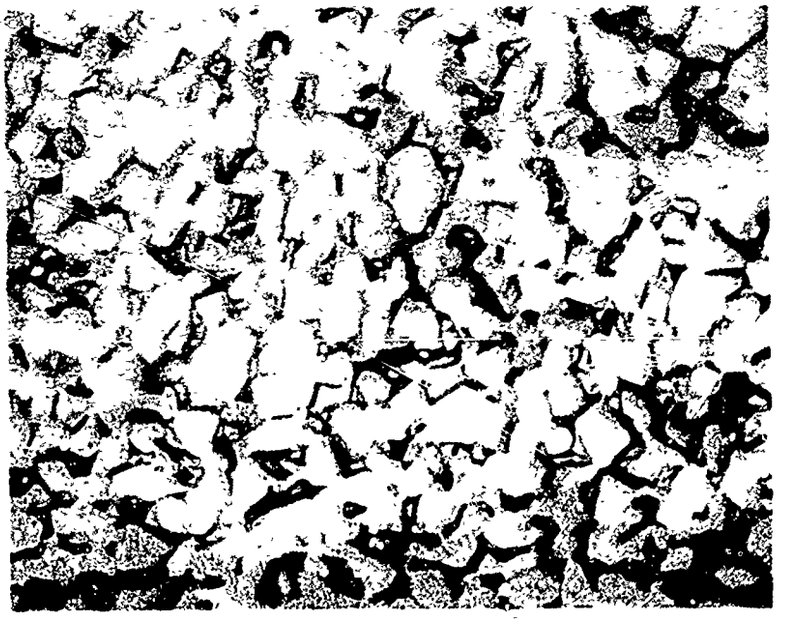

Fig. 20 - Grain Size of 10% Rolled and 8 Hour Annealed Specimen at 918°C; Average Grain Diameter 0.0072 Inch (1000X)

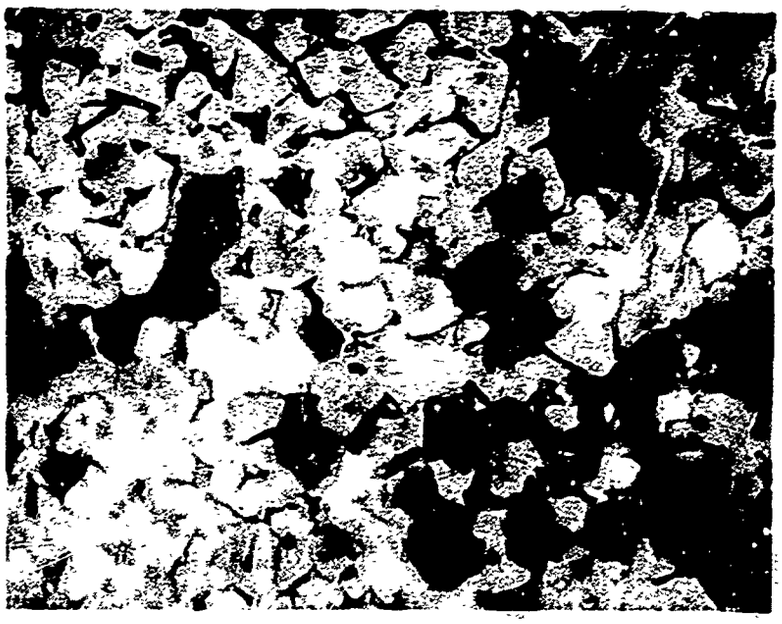

Fig. 21 - Grain Size of 10% Rolled and 16 Hour Annealed Specimen at 918°C; Average Grain Diameter 0.0095 Inch (1000X)

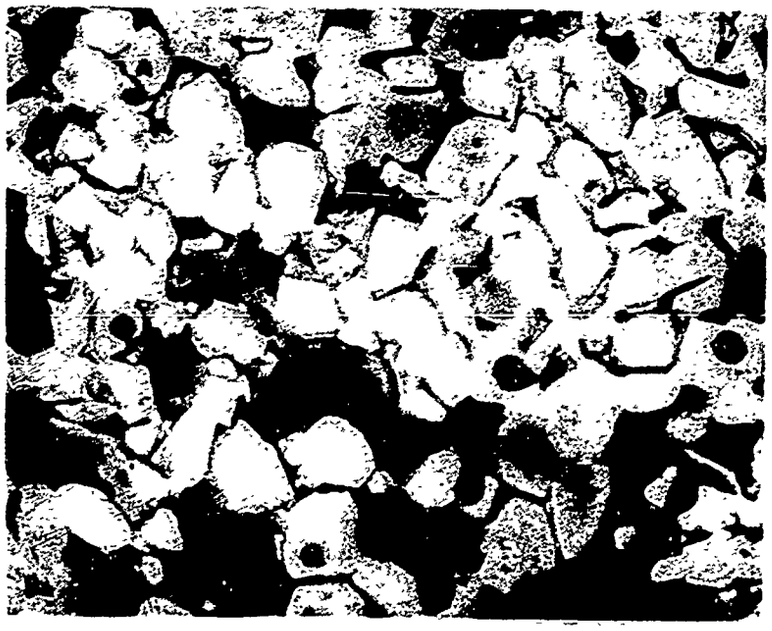

Fig. 22 - Grain Size of 10% Rolled and 32 Hour Annealed Specimen at 918°C; Average Grain Diameter 0.0110 Inch (1000X)

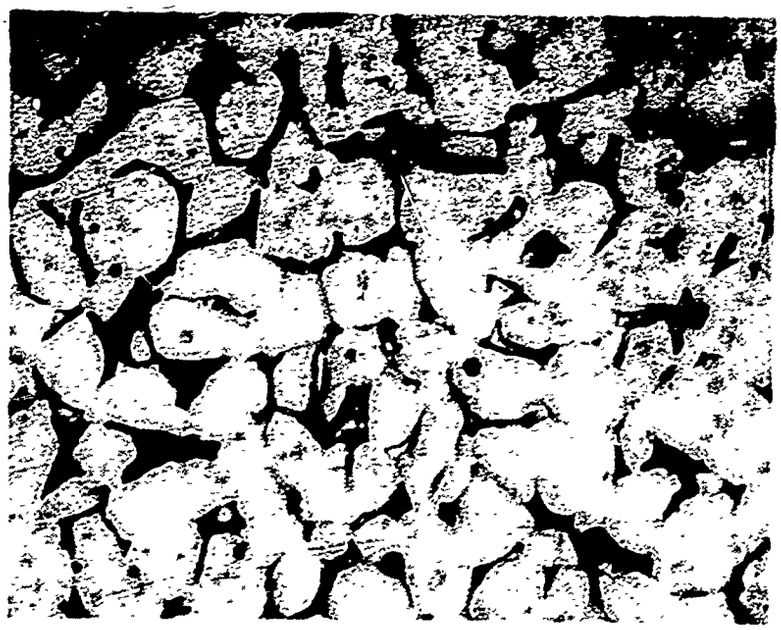

Fig. 23 - Grain Size of 10% Rolled and 64 Hour Annealed Specimen at 918°C; Average Grain Diameter 0.0130 Inch (1000X)

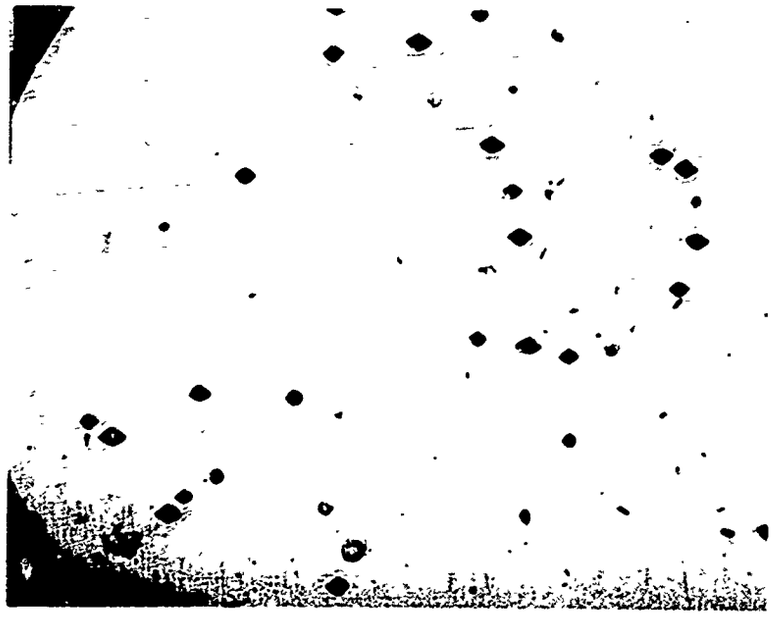

Fig. 24 - Pitting and Crack Initiation; Crack Initiation Occurred in 9 Minutes after Potential Was Applied. (100X)

Table III. Average Grain Diameter of Ti-6-4 Subsequent to 10% Cold Reduction (rolling) and Annealing for Various Times at 918°C

Annealing Time (hr)	Average Grain Diameter (inch)
1	0.0044
2	0.0057
4	0.0064
8	0.0072
16	0.0095
32	0.0110
64	0.0130

The grain diameter was calculated by counting the number of grains in a 4-inch^2 area of the photographs taken at 1000X.

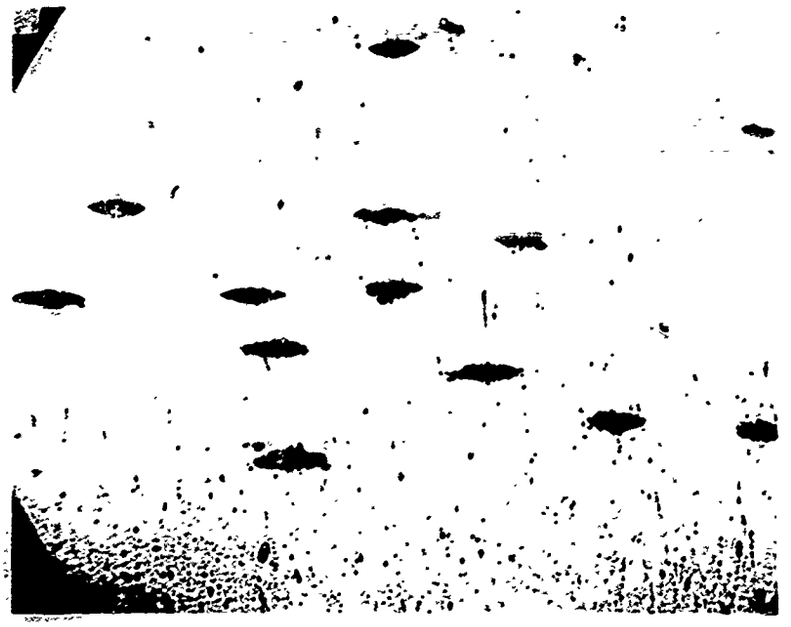

Fig. 25 - Crack Propagation from the Pit; Shape of the Crack 18 Minutes after the Initiation (100X)

Fig. 26 - Linking of Propagating Cracks; Shape of the Crack 18 Minutes after the Initiation (100X)

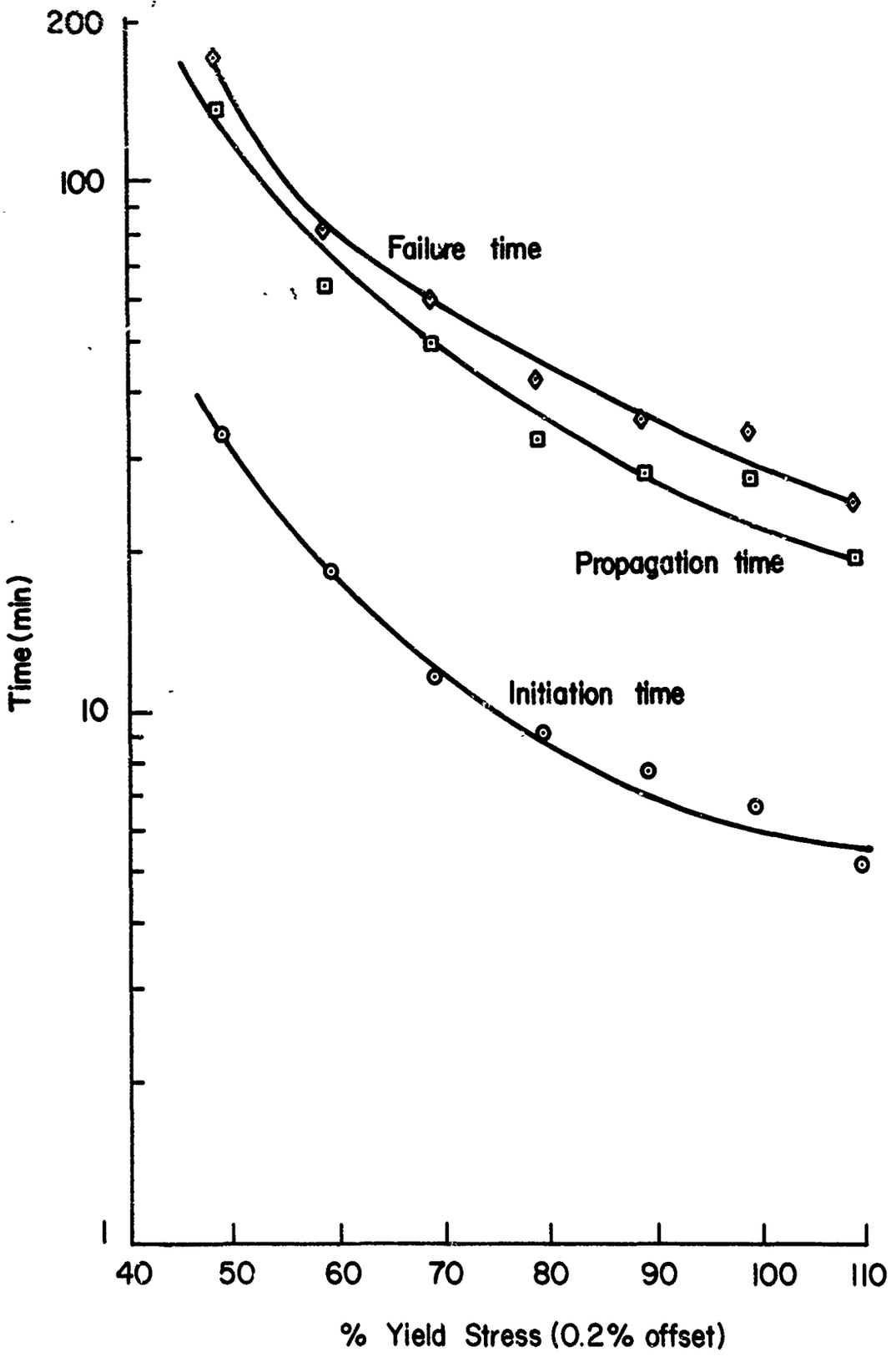

Fig. 27 - The Effect of Applied Stress on Crack Initiation, Crack Propagation and Failure Times

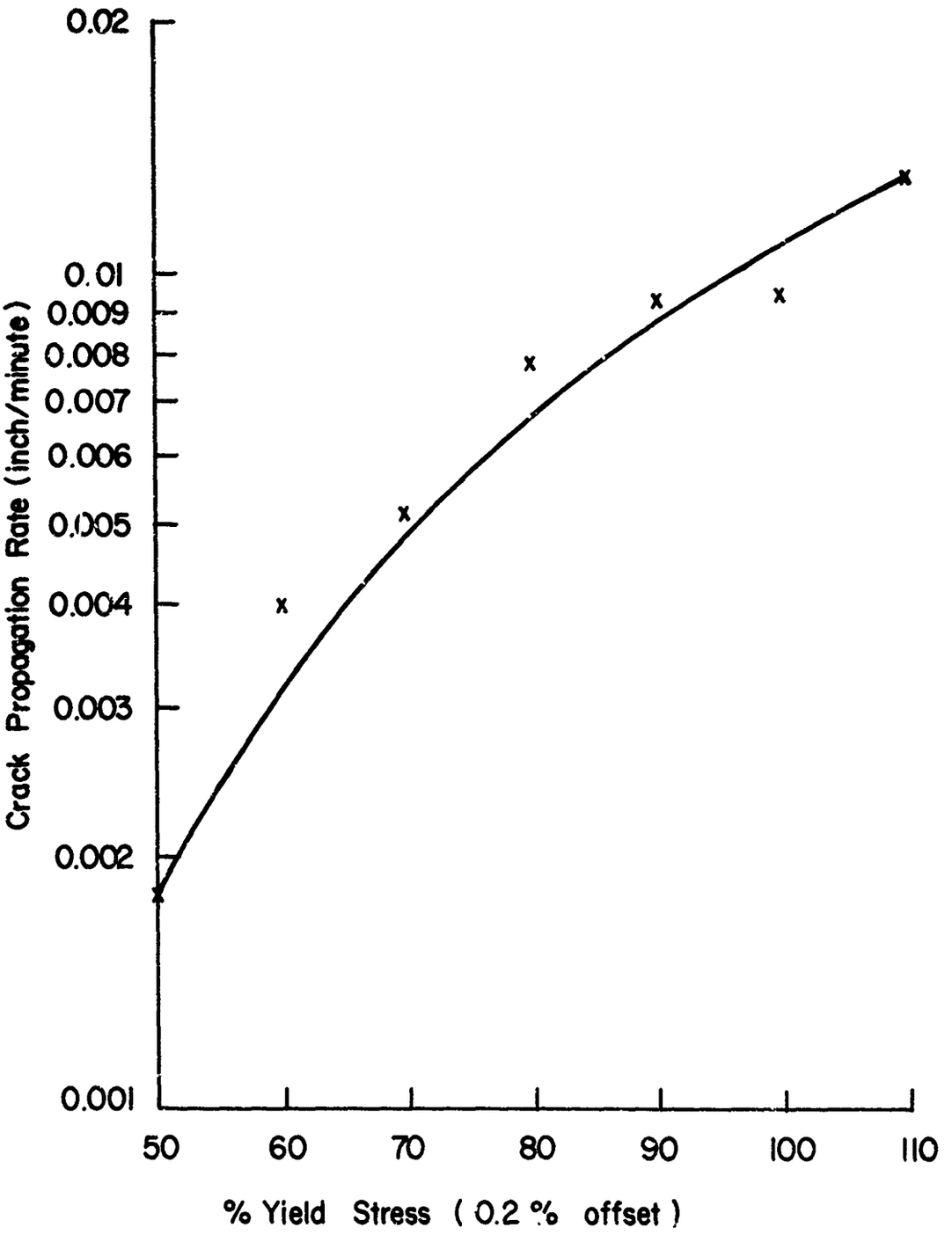

Fig. 28 - The Effect of Applied Stress on Crack Propagation Rate.

Table IV. Effect of Applied Stress on Crack Initiation, Crack Propagation, and Failure Times

% Yield Stress (0.2% offset)	Average Initiation Time (min)	Average Propagation Time (min)	Propagation Rate (inch/min)	Average Failure Time (min)
110	5	19	0.0132	24
100	6.5	27	0.0093	33
90	7.5	27.5	0.0092	35
80	9	32	0.0078	41
70	11.5	49	0.0051	60.5
60	18.5	63.5	0.0040	82
50	33.5	138.5	0.0018	172
40	No initiation even after 48 hours of exposure			

Average value was obtained from minimum of three tests. There was maximum variation of 3 minutes in initiation time and 5 minutes in failure time for specimens stressed to more than 60% of yield stress. The variation was about 15 minutes in failure time for specimens stressed to 50% of yield stress.

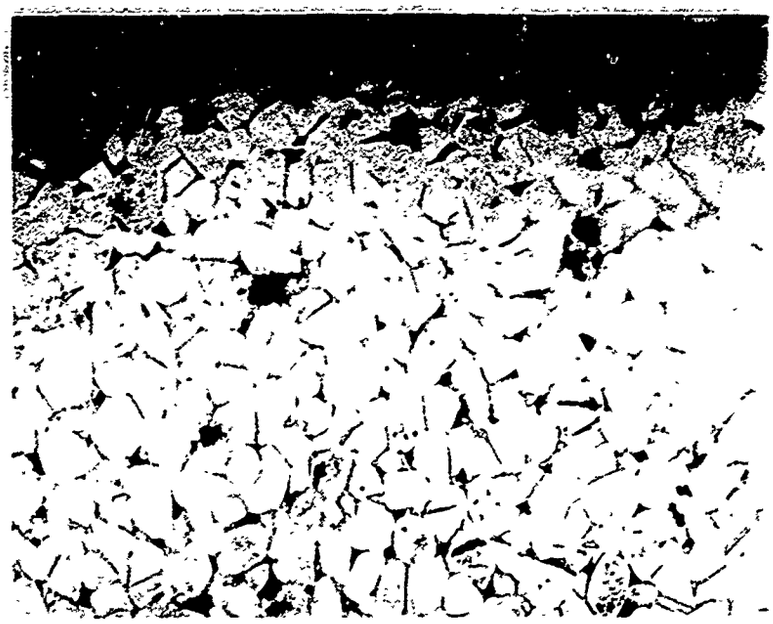

Fig. 29 - Pitting Occurs at the Grain Boundary (600X)

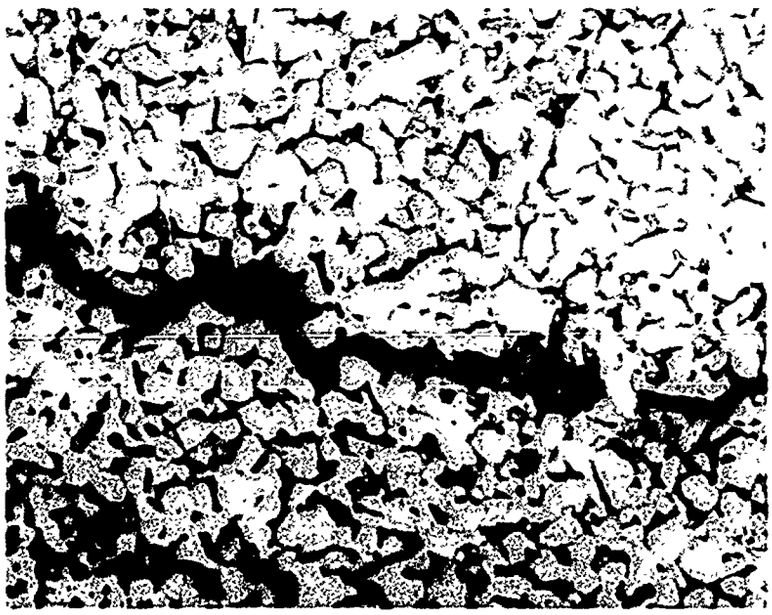

Fig. 30 - Mixed Mode of Failure in 10% Rolled and 2 Hour Annealed Specimen at 918°C (1000X)

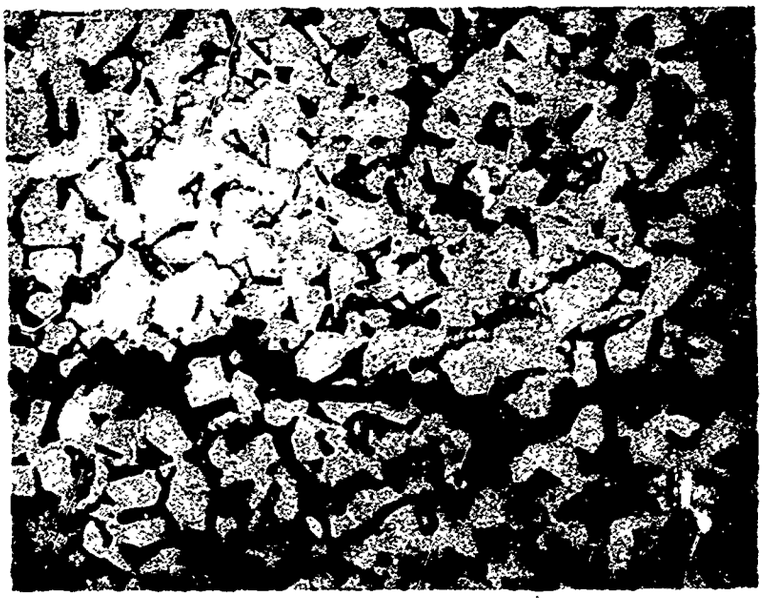

Fig. 31 - Mixed Mode of Failure in 10% Rolled and 8 Hour Annealed Specimen at 918°C (1000X)

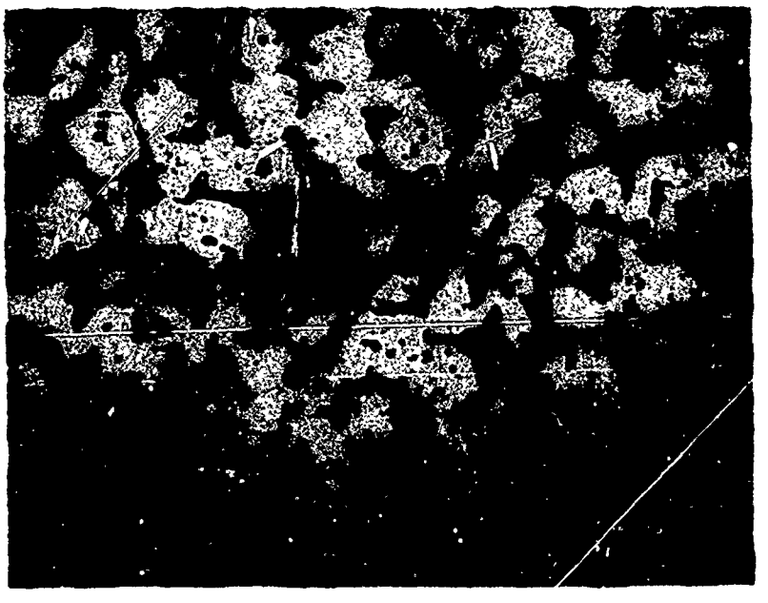

Fig. 32 - Mixed Mode of Failure in 10% Rolled and 32 Hour Annealed Specimen at 918°C (1000X)

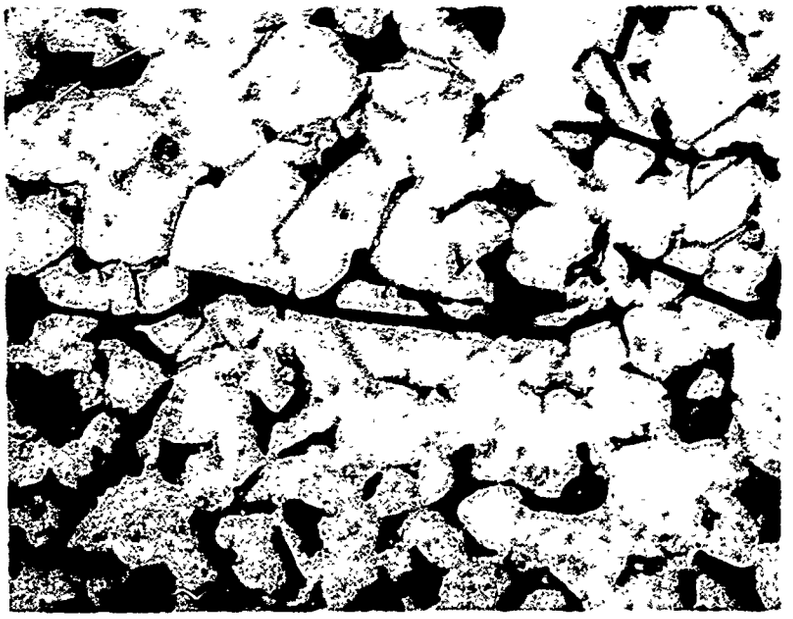

Fig. 33 - Mixed Mode of Failure in 10% Rolled and 64 Hour Annealed Specimen (1000X)

Figures 34-35 show the relation between $D^{-\frac{1}{2}}$ (D is grain diameter) to crack initiation time and failure time, respectively. The crack initiation time and failure time give straight lines when plotted against $D^{-\frac{1}{2}}$. The initiation time of the smallest grain size specimen is about 300% longer than that of the largest grain size specimen investigated. Also, the propagation time of the smallest grain size specimen (failure time less initiation time, Fig. 36) is about 21% longer than than of the largest grain. Thus, the decrease in failure time with increasing grain size is mainly attributed to the crack initiation time.

4. Discussion

Stress corrosion failure of Ti-6Al-4V in methanol + NaCl + water solution is made up of two parts; i.e., (a) initiation time and (b) propagation time.

a. Initiation Time

The resistance of titanium alloys to stress corrosion cracking is attributed to a stable passive film. Many investigators believe that crack initiation occurs when this passive oxide film is penetrated by the halide ions.[4-8] Film destruction may also be assisted by an applied stress. In this study, anodic dissolution occurred at local areas at α-β grain boundaries resulting in pits, as shown in Figs. 25 and 26. Localized attack at the grain boundary is reasonable since anodic dissolution is favorable at high-energy sites.

According to Petch[1] more dislocation pileups will occur at the surface in a large-grain size material than in a finer-grain size material at the same stress level. These dislocation pileups create high energy sites for incubation of stress corrosion cracks. This has been found to be true in the case of stress corrosion cracking of Ti-6-4 alloy. Figure 34 shows that as the grain size increases the incubation time decreases in accordance with the Petch equation. An increase in applied stress also decreases the initiation time, as shown in Fig. 27, by creating high energy sites. Barnwell, Myers and Saxer[9] also think that this dislocation pileup model accounts for lower crack initiation times in Type 302 steel.

Some authors[10,11] believe that crack initiation in α-Ti alloys in methanol + hydrochloric acid solutions occurs by some form of hydrogen embrittlement. The free corrosion potentials in methanol + iodine and methanol + bromine solutions are positive with respect to standard hydrogen electrode.[5,12,13] Thus, in methanol + bromine solutions the reduction of bromine to bromide is a more likely cathodic reaction[12] than the evolution of hydrogen. Similar arguments may apply in the case of methanol + iodine sclutions.[13] In the case of Ti-5 wt% Al-2.5 wt% Sn alloy in methanol + 0.6 wt% HCl + 1.0 wt% water, the free corrosion potential is -10 mV(SHE) and the application of small cathodic currents

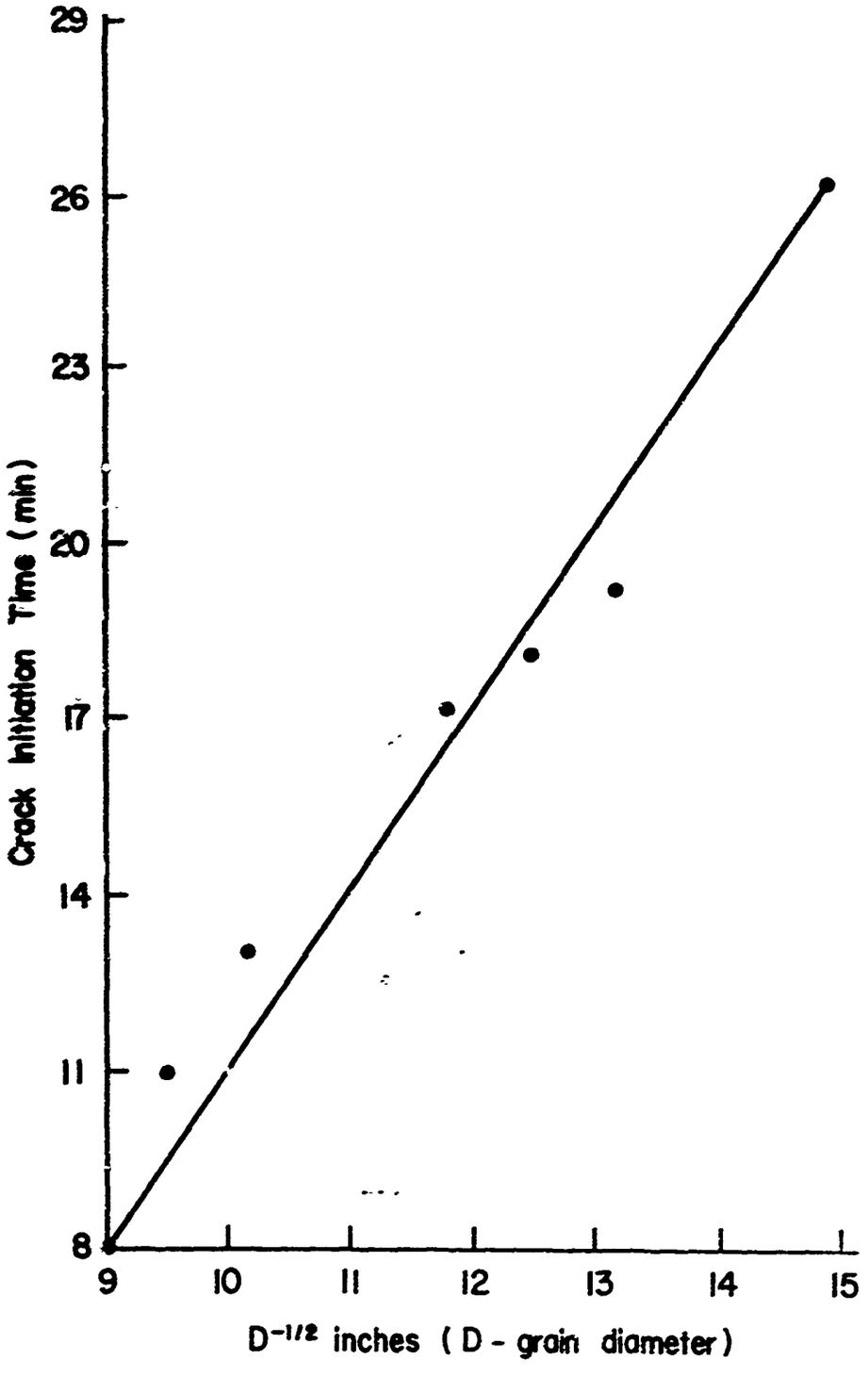

Fig. 34 - Effect of Grain Size upon Crack Initiation Time

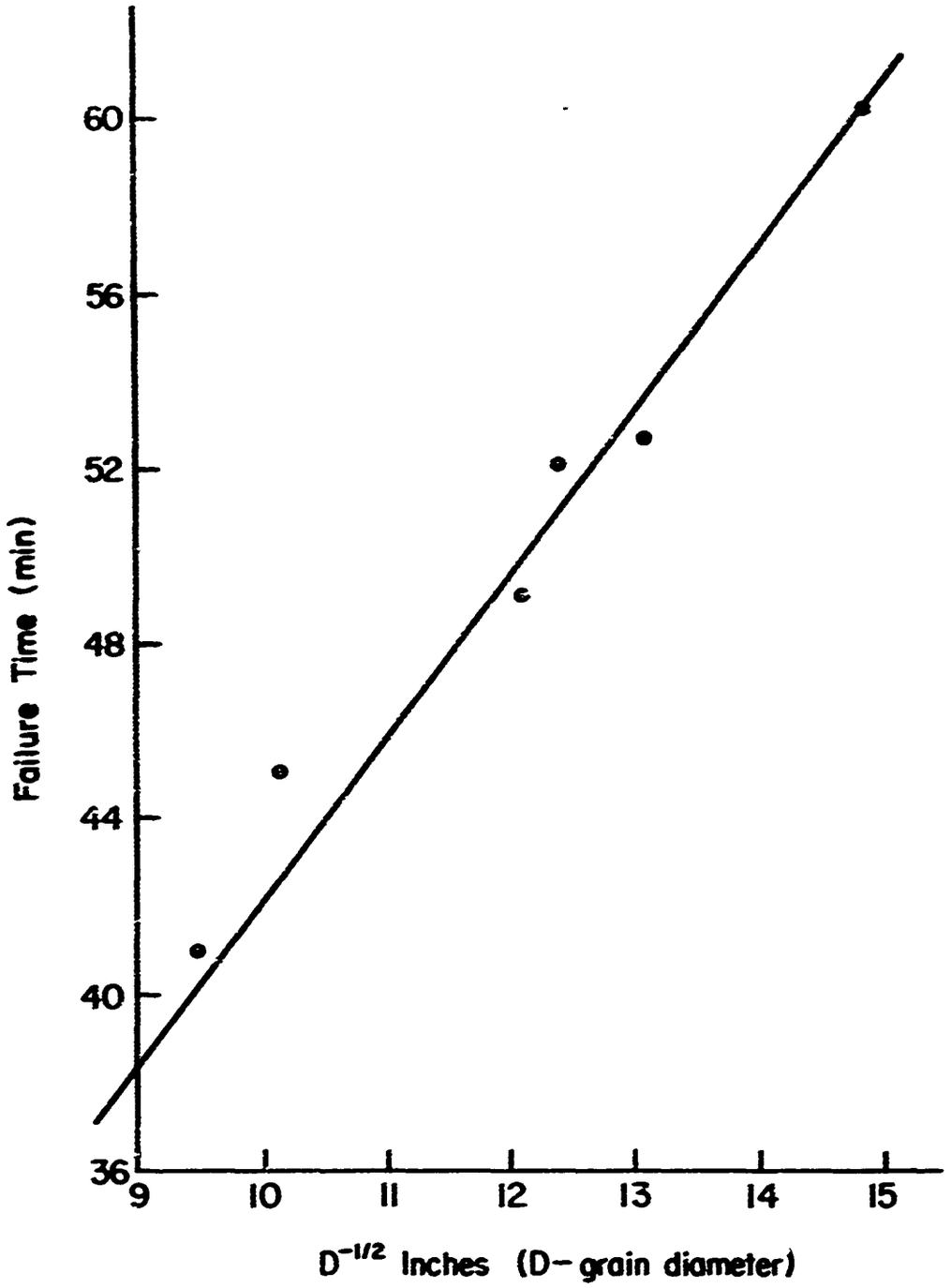

Fig. 35 - Effect of Varying Grain Size upon Failure Time

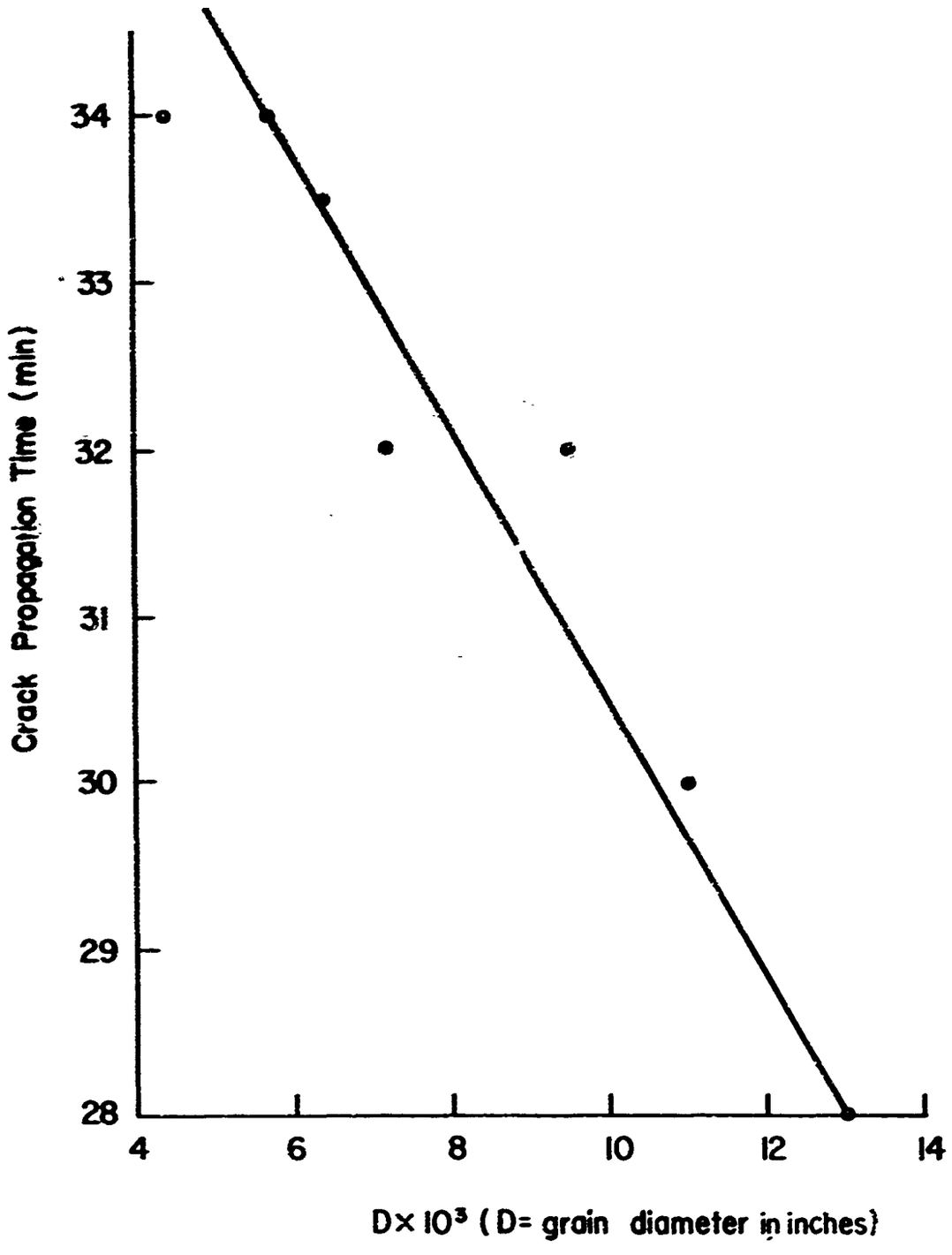

Fig. 36 - Effect of Grain Size upon Crack Propagation Time

should favor the evolution of hydrogen and result in a decrease in initiation time if hydrogen embrittlement is responsible for the crack initiation. On the other hand, if anodic dissolution is responsible for crack initiation, the application of small anodic currents would be expected to reduce times-to-failure. Such behavior which is similar to that observed in methanol + iodine solutions[13] indicates that the crack initiation involves anodic dissolution. This evidence supports the theory that crack initiation in Ti-6Al-4V in methanol + NaCl + water solution is most probably due to anodic dissolution.

The pits formed by the anodic dissolution of Ti-6Al-4V alloy, shown in Fig. 24, act as notches, which serve as stress raisers. Also, increased stress results from dislocation pileups at the head of the notch. A stress raiser has been shown to be necessary for transgranular stress corrosion cracking.[14,15] The presence of a notch, attendant dislocation pileups, and chloride ions all seem to have a part in the crack initiation process.

The decrease in stress corrosion failure time of Ti-6Al-4V in methanol + NaCl + water solution is mainly due to a decrease in initiation time with increasing grain size. The greater proportion of the failure time is accounted for by the initiation time as the grain size of the alloy decreases. Similar results were obtained by Green and Myers[16] for Type 302 austenitic stainless steel exposed to boiling 42 wt% magnesium chloride solution.

b. Crack Propagation

The crack propagation of Ti-6Al-4V in methanol + NaCl + water solution is of a mixed mode (i.e., intergranular and transgranular), as shown in Figs 30-33. Other investigators[17] have also found that Ti-6Al-4V fails in both intergranular and transgranular manners. The intergranular part of the crack is believed to result from the anodic dissolution. This is supported by the observation of intergranular cracking along with cleavage failure of Ti-5Al-2.5Sn in methanol + HCl + water solution.[8] Powell and Scully[8] also observed that increasing the potential in the anodic direction increases intergranular stress corrosion cracking of the alloy and at very high positive potentials the alloy fails entirely by the intergranular mode.

The transgranular part of the crack observed in Ti-6Al-4V in this investigation is due to cleavage. This is supported by many investigators.[8,14,18,19] Transgranular failure occurs in alloys which show reduced propensity for cross slip.[7,14,18,20] The function of aluminum is important in this respect since it inhibits cross slip in the titanium lattice.[21] Sedriks, Green, and Slattery[7] showed that the path of cracking was influenced by the aluminum content. The stress corrosion cracking path in pure titanium and Ti-2.09 wt% Al alloy was intergranular. Ti-5.1 wt% Al alloy gave a mixed type of fracture (i.e., both intergranular and transgranular) and entirely transgranular fracture

was obtained in the Ti-7.76 wt% Al alloy. Beck et al.[22] observed that increasing the aluminum content of titanium changes the dislocation structure from the tangled networks of the metal to the co-planar arrays, the formation of which results in reduced propensity for cross slip. The slip steps gradually become broader and the alloys become increasingly more difficult to passivate and, therefore, to repassivate.[19] This type of mechanism is suggested to be operating in stress corrosion cracking of Ti-6Al-4V in methanol + NaCl + water solution.

After the crack has initiated, a current of chloride ions flows into the tip zone, according to Beck.[23] These chloride ions are responsible for stress corrosion cracking of Ti-6Al-4V either through chemical or surface processes. According to the electrochemical mass transport kinetic model of Beck[23] only a mass-transport limited current of halide ions goes to the crack tip. The magnitude of this current is approximately equal to the current required for the formation of a monolayer of chloride ions or the formation of titanium halide at the crack tip zone. According to Pourbaix, titanium of valence 2 is thermodynamically stable at the suspected negative potential of the crack tip. The activation energy of 3.5 kcal obtained by Beck[23] is consistent with mass-transport limited current of halide ions.

Chloride ions at the crack tip zone probably reduce the surface energy of Ti-6Al-4V alloy and transgranular stress corrosion cracking (cleavage failure) occurs at lower stresses than the yield strength of the alloy. Coleman, Weinstein and Rostoker[6] experimentally found that mild steel with adsorbed hydrogen has about 500 erg/cm^2 of surface energy while the accepted value for iron with respect to its vapor is about 1600 ergs/cm^2. The interfacial energy of solid iron with respect to liquid lithium is about 730 ergs/cm^2. Solid 70/30 brass has an interfacial energy with respect to mercury of 280 ergs/cm^2 and the accepted value of surface energy of 70/30 brass with respect to its own vapor is about 1500 ergs/cm^2. Thus, it is not unreasonable to assume that the surface energy of Ti-6Al-4V decreases in the presence of chloride ions.

Increasing the stress level decreases the propagation time as shown in Fig. 27. This is in accordance with the literature.[7,22,24]

Figure 36 demonstrates that crack propagation time increases linearly with decreasing grain size; however, this effect of grain size on crack propagation is small over the range of grain size studied. This suggests that the improved resistance of fine-grained Ti-6-4 alloy to stress corrosion cracking is due primarily to the increased crack initiation time.

5. Conclusions

a. An increase in stress decreases the crack initiation and crack propagation times.

b. Crack initiation time decreases as the grain size increases for tests conducted at the same stress level according to the Petch equation.

c. Although the crack propagation time decreases with increasing grain size, this difference is not very significant when compared to crack initiation time.

d. Crack initiation starts at the grain boundary and occurs by an anodic dissolution process.

e. Cracks propagate by both intergranular and transgramular manners. Chloride ions are a significant factor in the initiation and propagation of stress corrosion cracks.

D. AN INVESTIGATION OF THE FACTORS AFFECTING THE STRESS CORROSION CRACKING OF TITANIUM AND TITANIUM ALLOYS IN METHANOL ENVIRONMENTS (J. F. Gloz)

1. Aims and Significance

The principal aim of this investigation is to characterize the factors affecting the stress corrosion cracking of titanium in methanol environments and to develop this characterization into a mechanism. The development of a mechanism, in turn, would facilitate the prediction of conditions necessary for failure as well as suggesting means of preventing it.

To pursue the aim of characterizing the factors affecting susceptibility, it is necessary to have a better understanding of the role of the various chemical factors involved. The role of halide ions, particularly chloride, is still a subject of great interest. Cracking has been shown to occur in methanol-chloride environments but it has not been firmly established whether the presence of halid ions is a necessary condition for failure or only a sufficient one. If cracking can be shown to occur in the absence of halide ions, then a mechanism based on the interaction between titanium and methanol alone must be considered.

2. Moisture Contamination Problems

As previously reported, a serious problem in obtaining meaningful stress corrosion data in methanol solutions is contamination by moisture. The passivating properties of water are well known and even the presence of very small amounts can markedly affect cracking behavior. This problem is aggravated by the fact that methanol is very hygroscopic and readily absorbs moisture from the atmosphere. The seriousness of this problem is illustrated in Fig. 37 where the water content of a methanol solution is plotted as a function of atmospheric exposure time. It can be seen that the water content of the solution increased by two orders of magnitude in about five hours. This indicates the absolute necessity of isolating methanol test solutions from the atmosphere. The erratic results reported by some investigators[25] have been attributed to a large change in the water content of their test solutions. To avoid the problems associated with moisture contamination, techniques were developed to dry the methanol and analyze its water content.

a. Water Determination Technique

An electrometric direct titration "dead stop" method[26] based on a Karl Fischer titration was used in the water determination. The sensitivity of this method is approximately ±0.001 wt% water.

b. Methanol Drying Technique

Several methods were considered for reducing the moisture content of the methanol to a reproducibly low level. Water removal by passing the methanol over molecular sieves (Linde 3Å) was tried but found to be unsatisfactory. The apparent water content could not be reduced below 0.05% and the resultant solution appeared to contain a significant amount of ionic contaminatns. Since these contaminants could interfere with the water determination, conductivity measurements will be made to determine the extent of the problem. A method initially proposed by Lund and Bjerrum[27] for the dehydration of ethanol was found to give better results. This method involves the refluxing of boiling methanol over magnesium chips. The magnesium reacts with the methanol to form magnesium methylate according to the reaction,

$$Mg + 2CH_3OH \rightarrow Mg(CH_3O)_2 + H_2 \quad . \qquad (10)$$

The magnesium methylate then reacts with any water present to form magnesium hydroxide as follows:

$$Mg(CH_3O)_2 + 2H_2O \rightarrow Mg(OH)_2 + 2CH_3OH \quad . \qquad (11)$$

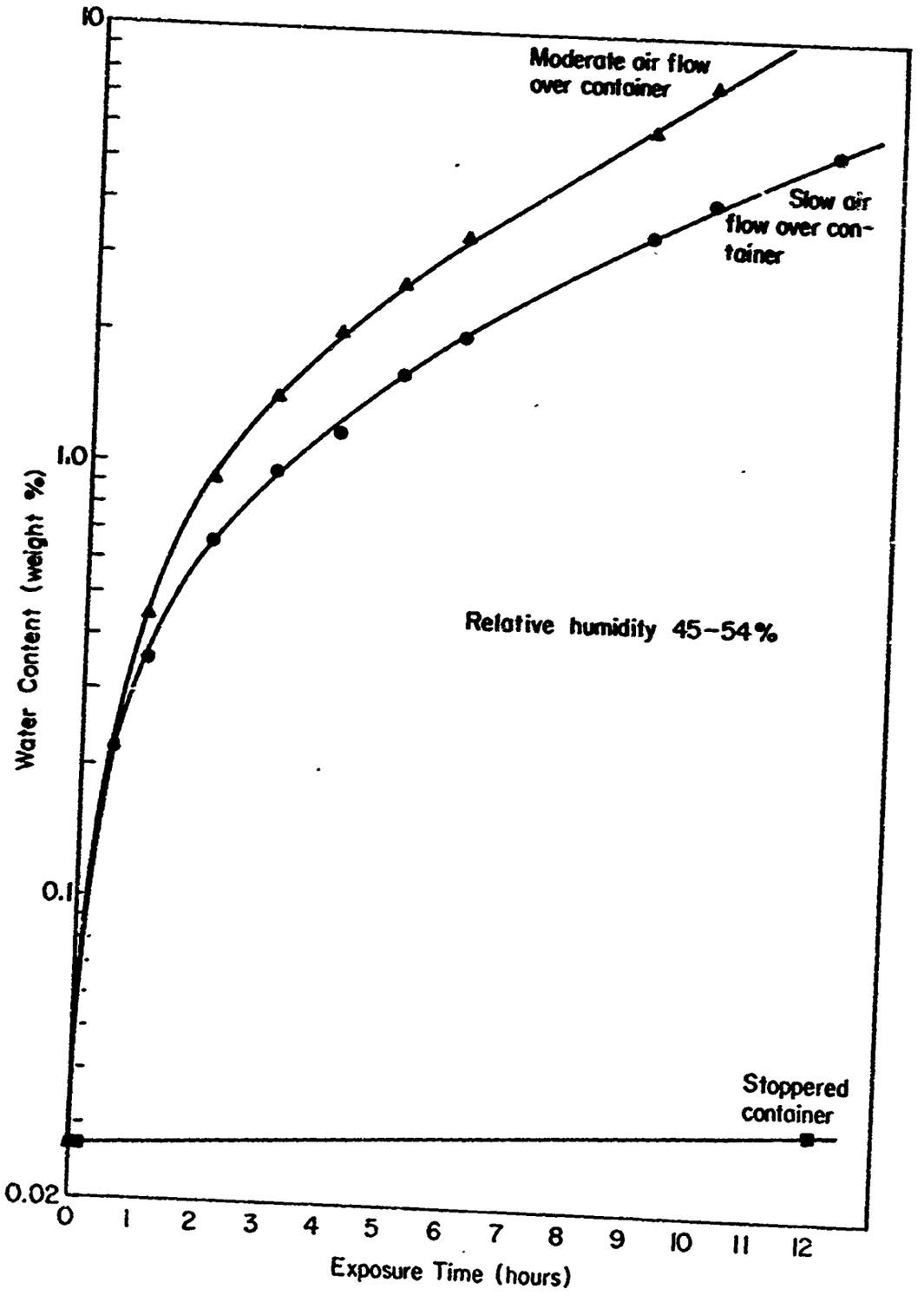

Fig. 37 - Moisture pickup by Methanol vs. Atmospheric Exposure Time

Magnesium hydroxide is very insoluble and precipitates out of solution. The resultant solution is distilled to give pure dry methanol. The water content of the distillate has been found to be 0.007%. To maintain this level of purity a completely enclosed system for storing and transferring the methanol was deemed necessary. A schematic diagram of the drying apparatus and test cell is shown in Fig. 38. Pure, dry nitrogen is used to pump the solution through the sytem.

3. Future Work

In conjunction with the tests of unalloyed titanium in pure methanol, an attempt will be made to study the reaction of an oxide-free titanium surface with methanol. Titanium forms an oxide so readily that the maintenance of a clean surface long enough to study the reaction is a major problem. However, recent work by Leith, Hightower, and Harkins[28] on the vapor-phase interaction between titanium and methanol indicates that such experiments are feasible and can greatly increase the understanding of the dissolution processes involved in stress corrosion cracking.

The effect of the chloride ion concentration will also be considered. Specifically, it would be desirable to know the relationship between cracking behavior and the chloride ion concentration in the region of the crack tip. Several methods for studying this factor are being considered, including an analytical technique to determine the very low concentrations that may be present in nominally halide free solutions.

E. EFFECT OF STATE OF STRESS ON THE SUSCEPTIBILITY OF TITANIUM BASE ALLOYS TO STRESS CORROSION CRACKING (S. Mahmoud)

1. Aims and Significance of Work

The mechanisms by which mechanical and metallurgical variables influence the stress-corrosion cracking behavior of titanium-base alloys are not clearly understood at the present time. This lack of understanding is due, in part, to an incomplete appreciation of the state of stress, deformation behavior of the alloy, surface characteristics, stress gradient, and the composite role of such variables upon susceptibility to stress-corrosion cracking. This work is designed to review some of the principal known facts governing mechanical and metallurgical behavior in the absence of stress corrosion environments, and then to determine the manner in which such behavior may be influenced by stress-corrosion cracking environments.

The specific influence of the state of stress on susceptibility to stress-corrosion cracking, especially the initial stage, has not

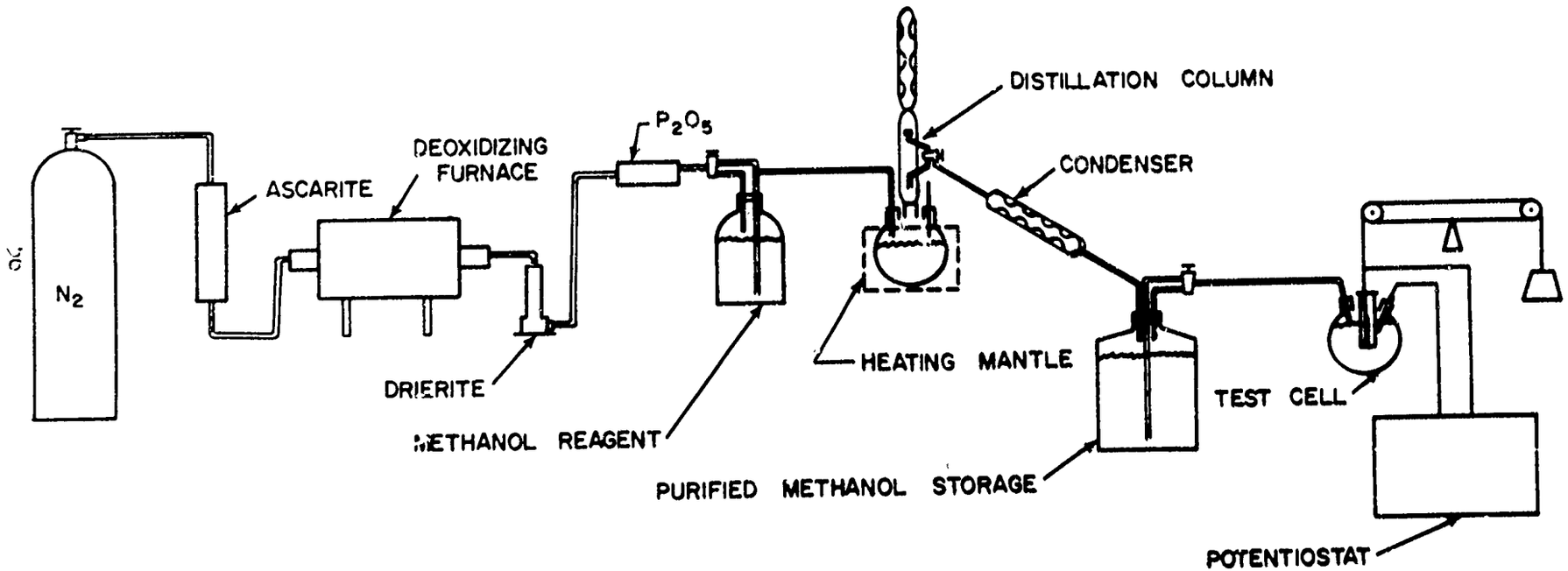

Fig. 38 - Schematic Diagram of Methanol Drying Apparatus and Test Cell

been well defined. Laboratory work is being undertaken to study chemical cracking as a function of the state of stress. The several states of stress being studied are,

(a) uniaxial tension,
(b) biaxial tension,
(c) combined bending and torsion, and
(d) notched bar specimens.

The results of biaxial tension tests were reported earlier[29] and the combined bending-torsion test method has been determined.[30]

Experiments to define the state of stress in the vicinity of a notch (notch bend specimens) are in progress. Alloy composition and specimen dimensions were also reported.[30]

The present report is concerned with the following studies.

a. Definition of the crack initiation process in terms of point of origin and path of propagation.

b. Separation of the total fracture energy into crack initiation and crack propagation components.

c. Evaluation of a maximum strain criterion for crack initiation.

d. Investigation of the sequence of events in the plastic zone at the crack-tip.

2. Preliminary Results

a. Stress Analysis

The theoretical stress analysis is given in Ref. 22 of the previous report.[30] Experimental stress analysis consisted of determining the elastic stress concentration factor, K_e, which was found to be 2.06. Using a scaled-up bakelite model, the distribution of the bending stress is shown in Fig. 39. The strain field or the fringe pattern is shown in Fig. 40.

b. Load-Deflection Curves

Generation of a load-deflection diagram during a notched bar test provides one way for determining crack initiation and crack propagation energies. Such a curve further enables the two components of toughness, i.e., strength and ductility, to be assessed. Measurements of the diagram were made in air and in the methanol + 0.37% HCl + 0.63% H_2O test environment. Figure 41 shows the experimental set-up

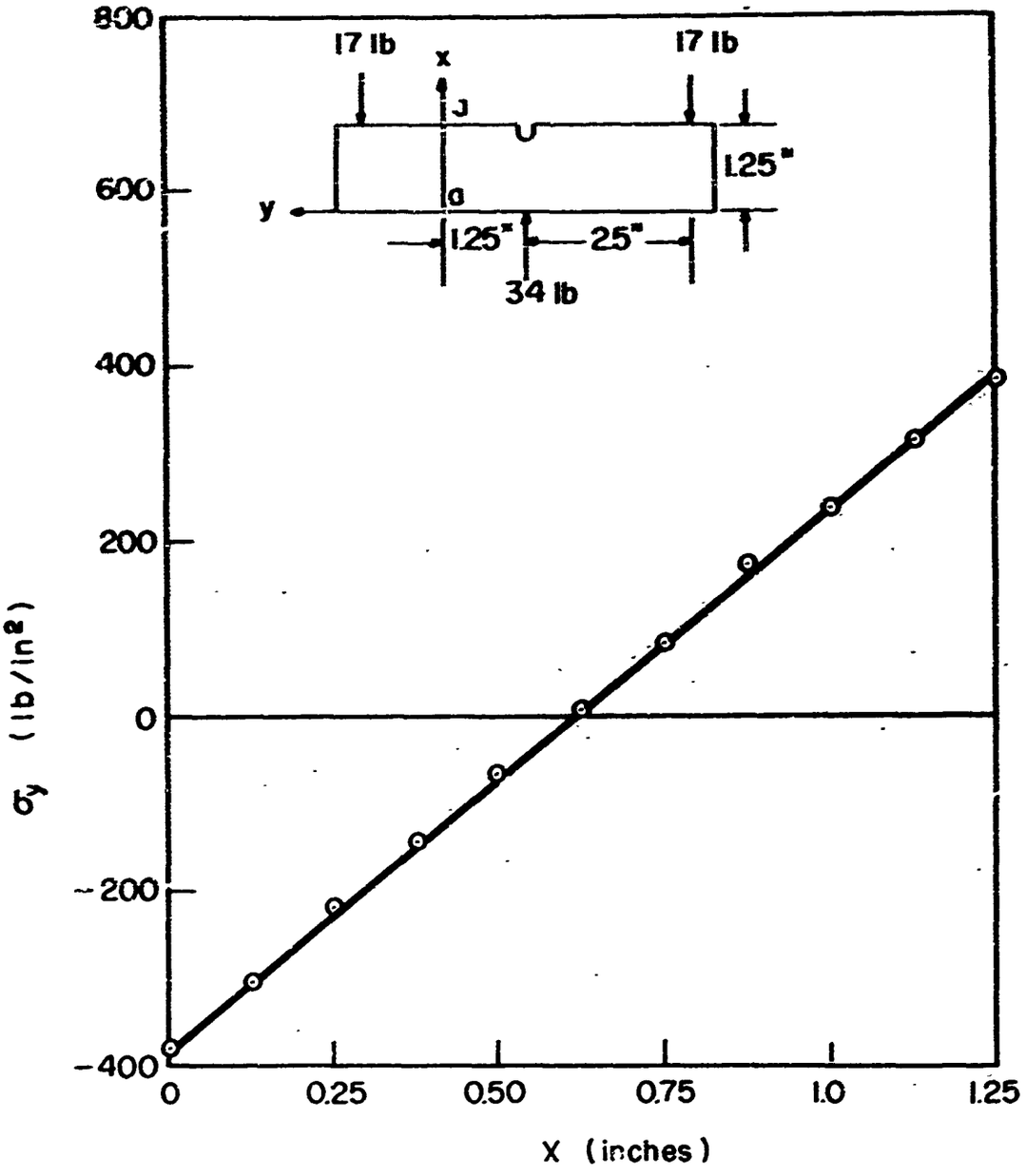

Fig. 39 - Normal Stress Distribution across Section a-a
(Photoelastic Material, PSM-5)

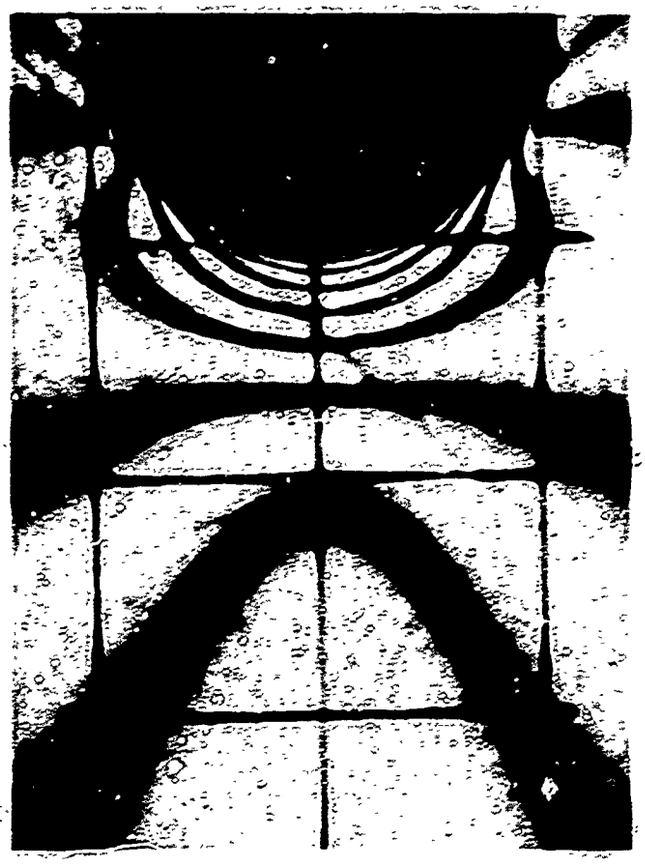

Fig. 40 - Fringe Pattern under Notch (7 fringes are showing)

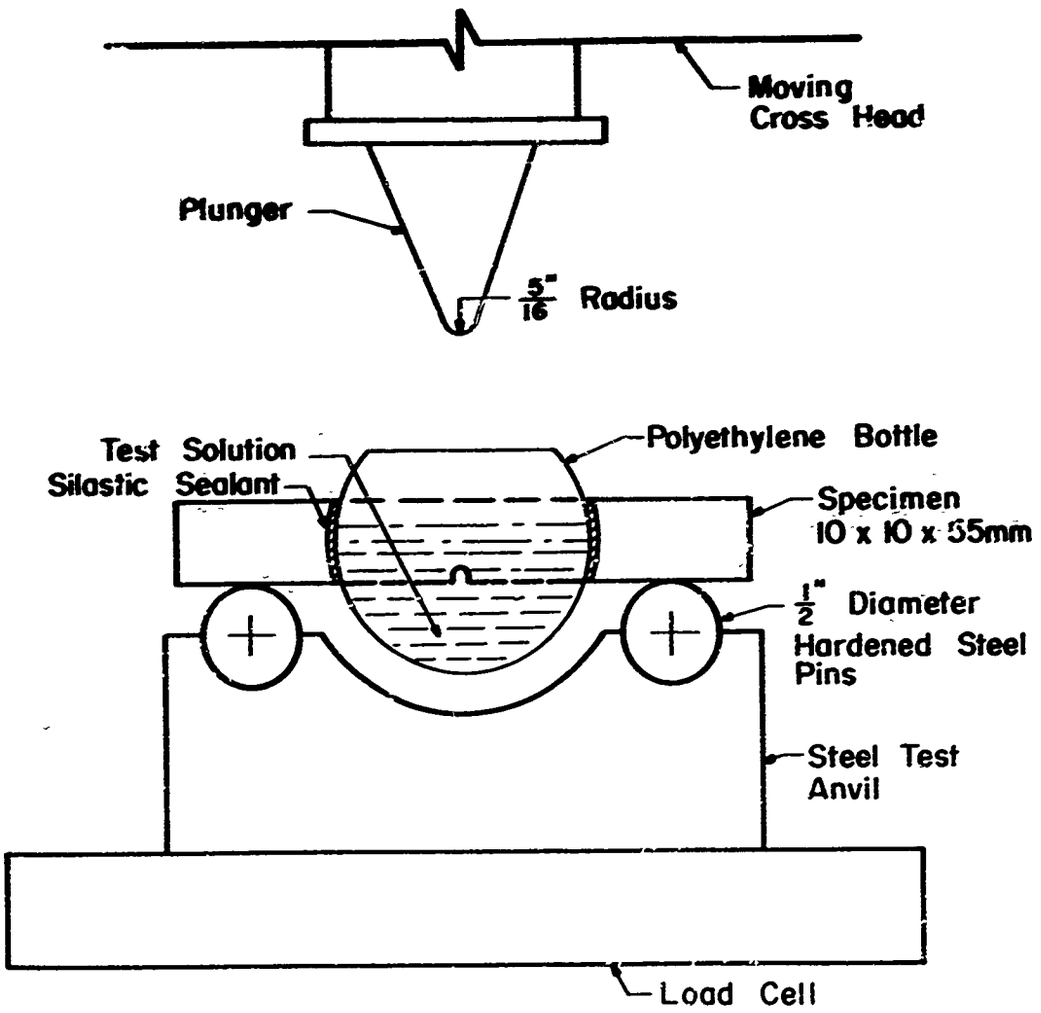

Fig. 41 - Schematic Diagram of Test Apparatus

while representative curves are shown in Fig. 42. Somewhere between the start of loading and the maximum load, a crack forms at the notch root close to the mid-longitudinal section of the bar. The exact location, on the load-deflection diagram, of the point of initiation has proved difficult to determine with precision. The area under the curve to this point represents the crack initiation energy. The total area minus that for crack initiation represents the crack propagation energy.

The most common method of discerning between elastic and plastic deformation has been by etch pitting techniques. This etch serves to reveal areas which have been deformed beyond the yield. Several trials, none of which proved entirely successful, were attempted to discern plastically deformed regions. Figure 43 shows a photograph of these plastic zones. Further work is in progress to reveal the size of the plastic zone using microhardness techniques. This technique is used for several purposes:

(1) To compare the size of the plastic zone measured experimentally to that predicted theoretically.

(2) To obtain a qualitative description of the development of the plastic zone.

(3) To determine the volume of the deformed metal in the fractured bars. This quantity will be obtained for both halves of the fractured bars on their surface and mid-thickness sections.

c. Critical Strain Measurements

It was found that the plastic zone at the tip of the notch or a crack expands on loading until a critical strain at the notch root is attained. At this strain, the material undergoes a rheological transformation into fluid-like flow, in which it is susceptible to localization of flow along "characteristics" (slip lines in slip line fields), which are directions of critical maximum shear stress and also directions of pure shear. Plastic instabilities may be mounted along these directions. Weak instabilities lead to stable slow crack propagation; strong instabilities lead to unstable fast propagation (brittle fracture)." * Measurements were made for some of the specimens to estimate the strain at the root of the notch. These measurements consisted of measuring the contraction in the transverse directions before and after loading. The following are typical values:

No. of Specimens	Thickness before Testing	Thickness after Testing
8 (in methanol + HCl + H_2O solution)	0.394"	0.377" - 0.388"
2 (in air)	0.394"	0.383" - 0.387"

More specimens will be tested to define this quantity precisely.

*J. W. Spretnak and C. A. Griffis, "Research on Notch Plasticity May Contribute to the Understanding of Stress Corrosion Cracking," Corrosion, 25:5, 193 (May, 1969).

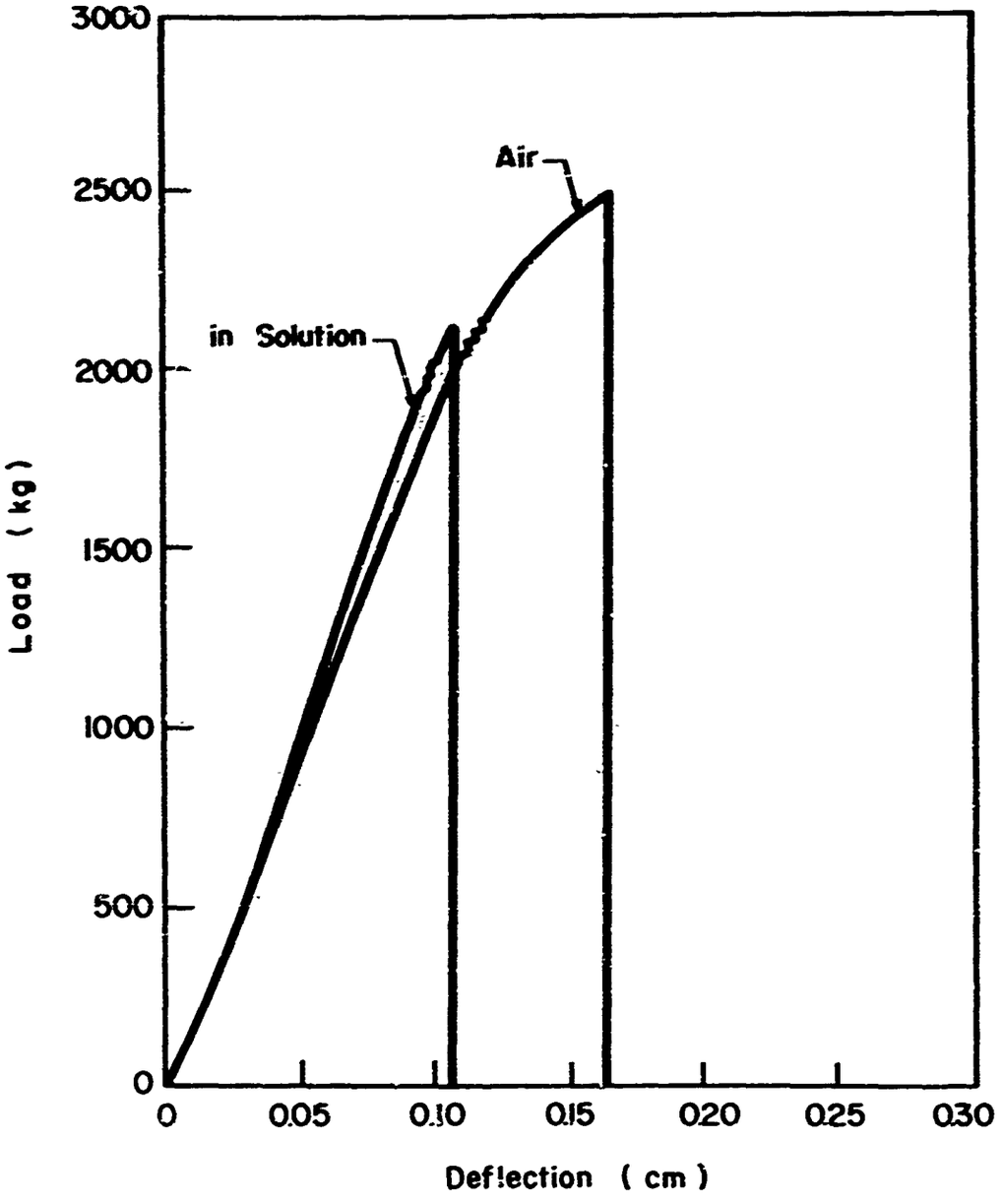

Fig. 42 - Load-Deflection Diagram for Ti-6-4 in Air and in CH_3OH + HCl + H_2O Solution (Cross-head speed = 0.05 cm/min)

Fig. 43 - Tested Specimens Showing Plastic Zone under Notch

d. Angle of Bend

Bend angle measurements are in progress. A correlation between the bend angle and the conventional strain will be made by the following methods:

(1) Determinations from the load-deflection curves

(2) Photographically by measuring the radius of curvature

(3) Measurements from scaled-up model.

e. Fractographic Studies

Limited fractographic analysis was performed. Scanning electron fractographs were made from specimens tested in air and in the CH_3OH-HCl-H_2O environments. No evidence was found for "hard particle"-induced dimple formation.

SECTION III

STRESS CORROSION CRACKING OF STEELS (R. W. Staehle)

A. OBJECTIVES AND SCOPE

The aim of this program is to identify and quantify processes which are fundamental to the initiation and propagation of stress corrosion cracks. The individual efforts described herein are considered to be key factors from which an effective quantitative basis for stress corrosion cracking can be developed.

The ultimate aim of the work is to provide a quantitative basis for designing high strength alloys and heat treatments which are resistant to catastrophic stress corrosion cracking.

B. EFFECTS OF METALLURGICAL STRUCTURE (M. T. Wang)

1. Aims and Significance

The objective of this study is to investigate the effects of metallurgical structure on the stress corrosion cracking of high-strength steels. The point of view here is that SCC crack propagation is a structure-sensitive as well as an environment-sensitive process.

The general approach here is to keep the continuum variable constant (strength level) and vary the microstructure (through heat treatment), alloy chemistry, state of stress, and environment. The two alloys to be used here are AISI 4340 steel and 18% Ni 250 maraging steel. These provide two basically different structures and alloy chemistries.

2. Background

The propagation of stress corrosion cracks is usually considered macroscopically to be a result of a slow growth of subcritical cracks by the combined action of stress and environments. Environmentally, hydrogen absorption plays an important role in the SCC of high-strength steels in aqueous environments. This concept is strongly supported by evidence of the local acidification at crack tip by hydrolysis. Brown and his co-workers[31,32] successfully developed experimental techniques for measuring acidification at crack tip and found that during SCC of AISI 4340 high-strength steel the pH at the crack tip is low regardless of the external environment. In the present investigation, 3.5% NaCl aqueous solution is being used as a controlled environment with a basic assumption that hydrogen absorption controls the SCC of high-strength steel.

3. Fracture Mechanics Consideration

In these experiments, holding constant the state of stress and stress intensity at the crack tip (K_I) or its equivalent crack extension force ($\mathcal{G}_I$) reduces the uncertainties. The SCC experiments were conducted by using tapered double-cantilever specimens which permit a constant stress intensity for constant load. The justification for this approach lies in the fracture mechanics analysis which is reviewed below.

From an energy consideration, it was first proposed by Irwin[33] that energy balance of the fracture process in a system can be expressed as

$$p\frac{d\ell}{da} + \frac{dE}{da} = \frac{dW}{da} + \frac{dK}{da} \quad , \tag{12}$$

where

a = crack length
p = applied load
E = strain energy
K = kinetic energy
W = work done by fracture and plastic flow, and
ℓ = length between grips.

Two assumptions have been made in this analysis. First, the rate of kinetic energy change as a function of crack length is assumed to be zero. The slow growth of cracks in the SCC experiment satisfies this requirement because of the trivial kinetic energy produced from the slow crack velocity and the negligible mass removed from the crack tip. Second, the plastic flow capacity of the steel investigated is required to be small, such that the length between grip (ℓ) can remain constant and that the plastic zone size at the crack tip is small enough to meet the boundary condition in fracture mechanics analysis. To meet this requirement, the strength levels of the steels investigated were heat treated to a minimum of 200 ksi to produce a limited flow capacity. Evidences of limited flow capacity of the steels investigated are shown in the load extension curve of the 18% Ni maraging steel of Fig. 44, where the steels were heat treated to a minimum strength of 200 ksi through different aging treatments. Table V summarizes the mechanical properties of the 18% Ni maraging steel.

From linear elasticity, the strain energy release rate (dE/da), known as crack extension force ($\mathcal{G}_I$) can be expressed as

$$\frac{dE}{da} = \mathcal{G}_I = \frac{1}{2} p^2 \frac{\partial\left(\frac{1}{M}\right)}{\partial a} \tag{13}$$

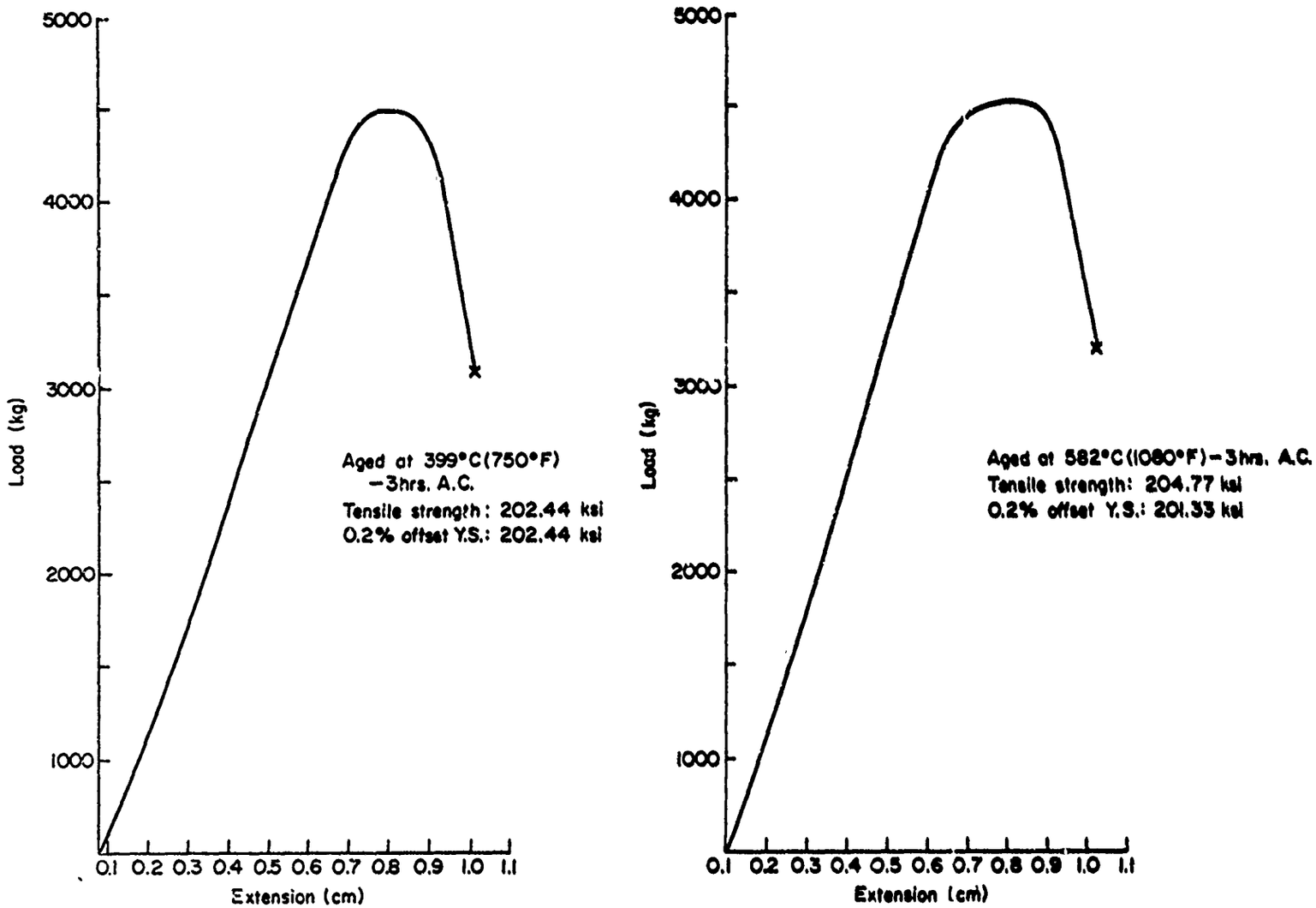

Fig. 44 - Load Extension Curve of Two Different Heat-Treatments of 18% Ni Maraging (RMS 250) Steel with Standard Round 0.250-Inch Diameter and 1.0-Inch Gage Length Specimen

Table V. Mechanical Properties* of 18% Ni Maraging Steel

Aging Treatment** 3 Hours Air-Cooled Temp. (°C)	Temp. (°F)	Tensile Strength (ksi)	Yield Strength 0.2% Offset (ksi)	Elongation (%)	Reduction Area (%)	Rockwell Hardness (Rc)
399	750	202.44	202.44	13.06	25.47	47.5
		198.59	198.59	15.73	28.43	47.0
		191.47	191.47	13.1	33.5	47.7
438	820	216.88	216.88			
		207.59	207.59	9.5	31.5	49.5
510	950	235.80	233.16	10.1	29.5	52.2
554	1030	210.13	205.70	11.1	30.2	49.6
582	1080	204.71	201.83	16.2	30.7	47.4
		195.88	192.55	16.4	28.9	47.3
593	1100	196.92	193.49	12.8	32.5	46.1

* Determined from standard, round 0.250-inch diameter tensile specimens with cross-head speed at 0.5 cm/min and rolling direction parallel to tensile axis.

** Prior to aging treatment, specimens were double austenitized at 899°C (1650°F) 1 hour air-cooled + reaustenitized at 816°C (1550°F) 1 hour air-cooled.

where

p = applied load per unit thickness,
M = spring constant per unit thickness, and
a = crack length.

The tapered double-cantilever specimen configuration, as shown in Fig. 45, is so designed[34] to provide a constancy of the term $\partial(1/M)/\partial a$ such that a constant crack extension force ($\mathcal{G}_I$) can be achieved under a given load over a certain crack length. The crack extension force also depends on the material properties under a given specimen geometrical condition. The crack extension force ($\mathcal{G}_I$) can be related to the stress intensity factor at the crack tip (K_I) as

$$K_I^2 = E\mathcal{G}_I \quad , \quad \text{for plane stress condition} \tag{14}$$

and

$$K_I^2 = \frac{E\mathcal{G}_I}{1 - \nu^2} \quad , \text{ for plane strain condition} \tag{15}$$

where

E = Young's modulus for the material, and
ν = Poisson's ratio.

The stress intensity factor at crack tip can be approximately related to the material property to account for the local plastic yielding as

$$K_I = \sigma_{y.s.}(2\pi r_y)^{1/2} \quad , \tag{16}$$

where

r_y = plastic zone size,
K_I = stress intensity factor at crack tip, and
$\sigma_{y.s.}$ = 0.2% offset yield strength.

From Eqs. (14), (15), and (16) it can be seen that the crack extension force ($\mathcal{G}_I$) is also a function of yield strength of the material. Thus, the study of the metallurgical structural effects on the SCC of high-strength steels becomes significant only if the steels investigated have identical strengths. Table V lists the strength and mechanical properties of 18% Ni (250) maraging steel used in this investigation.

The crack velocity (da/dt) can be obtained by differentiating Eq. (13) with respect to time (t). Under the conditions of constant load (P) and crack extension force ($\mathcal{G}_I$), the crack propagation rate can be obtained as follows:

$$\frac{da}{dt} = \frac{C}{P}\frac{d\delta}{dt} \quad , \tag{17}$$

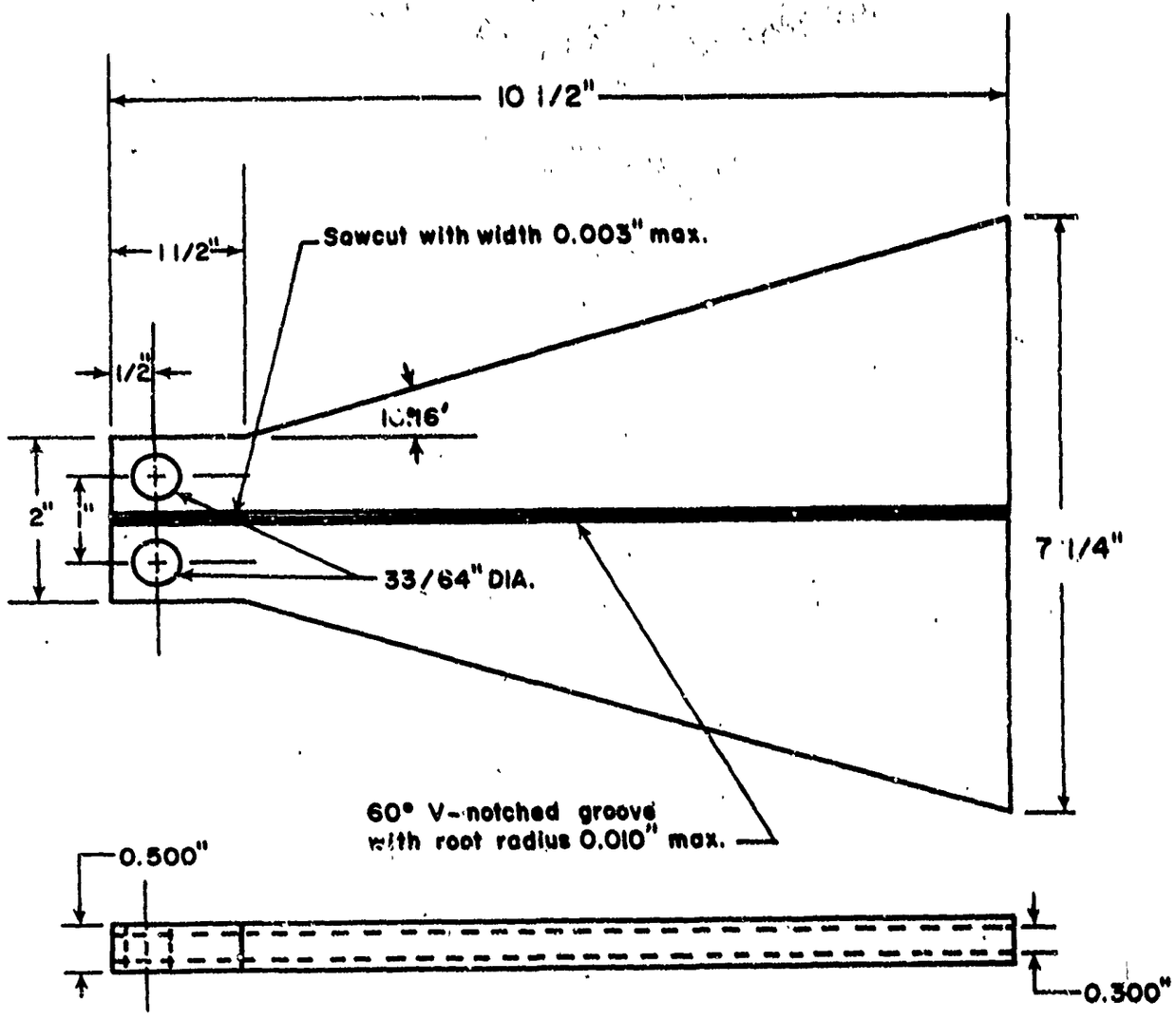

Fig. 45 - Tapered Double Cantilever Beam Specimen

where

$$C = \frac{1}{\frac{\partial(1/M)}{\partial a}} = \text{constant for a specific material},$$

t = time,
δ = deflection at crack tip.

To the first approximation, the deflection at the load points of the specimen is considered to be proportional to the displacement at crack tip. This provides a good experimental technique to solve the dilemma in measuring the actual crack tip displacement. The utilization of Eq. (17) to obtain the crack propagation rate have been successfully carried out by Van Der Sluys[35] and others.

4. Crack Propagation Measurements

Crack propagation rates were measured from the tapered double-cantilever beam specimen at different heat treating conditions of the two steels by using Eq. (17) in term of deflection rate of the specimen under a constant load. The specimens were precracked chemically with concentrated hydrochloric acid, and then baked at 176°C for one hour to prevent any hydrogen uptake during the chemical cracking process. Constant loads were applied through a modified SATEC Mode D creep tester, and deflections of the specimen at the load points were measured from a Daytronic Model DS 100 linear variable differential transducer (LVDT). The 3.5% NaCl aqueous solution was adjusted to pH 6 and deaerated by bubbling prepurified nitrogen gas in a reservoir for 24 hours. An overall view of the experimental arrangement is shown in Fig. 46 and a close-up view of experimental cell and the location of LVDT is shown in Fig. 47. The deflections of the LVDT were calibrated by a mechanical displacement from a Starrett micrometer with an accuracy of 0.0001 inch. The calibration curve for the LVDT deflection with respect to mechanical displacement is shown in Fig. 48. The error in linearity of the LVDT deflection is about 0.25% within the range of calibration. Deflections were recorded by an Esterline Angus strip chart recorder at speeds from 0.5 inch/hr up to 1 inch/min at different load conditions. The deflection measured at each data point is in the range 0.002-0.005 inch which requires from 30 minutes to 24 hours for each determination. The crack propagation rates in terms of deflection rates at the load points were obtained from the recorded chart using least square analysis.

To the present time, crack propagation rates as a function of applied load have been measured on 18% Ni maraging steel with three aging treatments as shown in Fig. 49. The measurements of crack propagation rates as a function of applied load for AISI 4340 steel with tempered martensite and tempered bainite structures are being undertaken and calculation of data will be carried out in the near future.

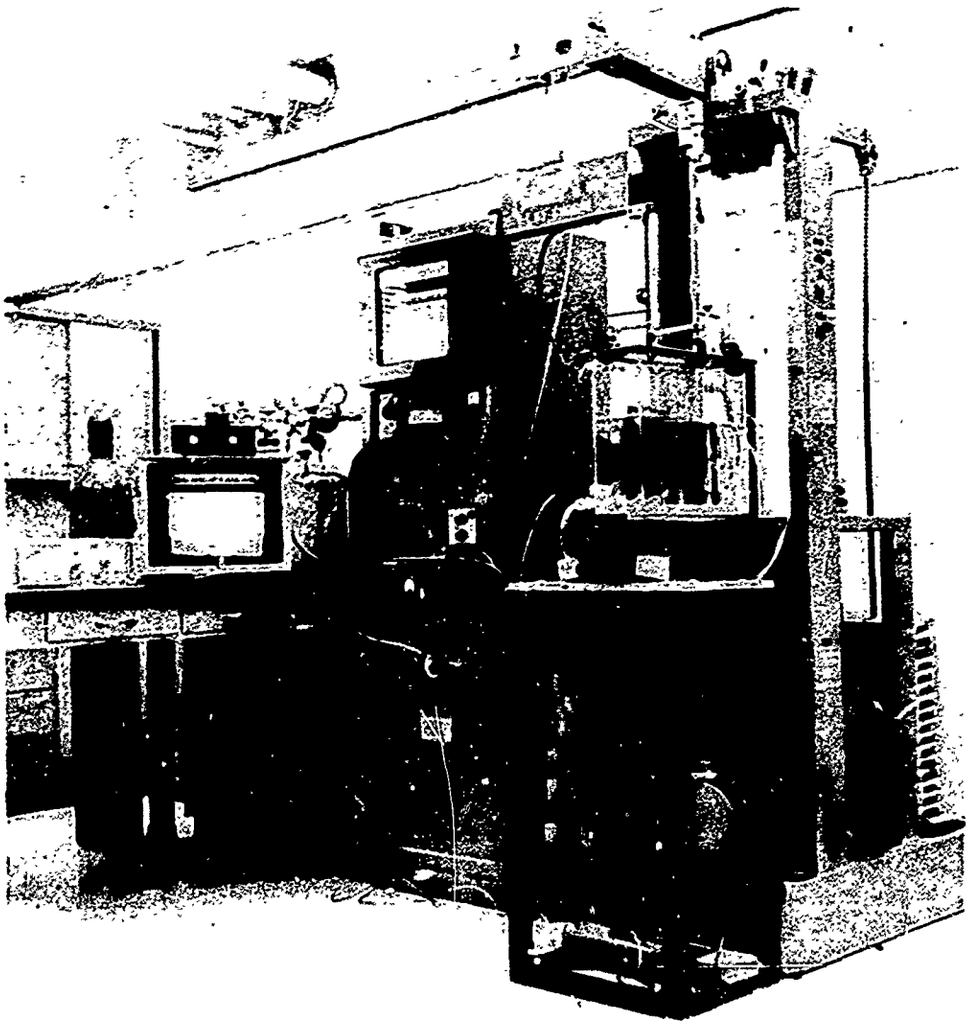

Fig. 46 - Apparatus for the Crack Propagation Test

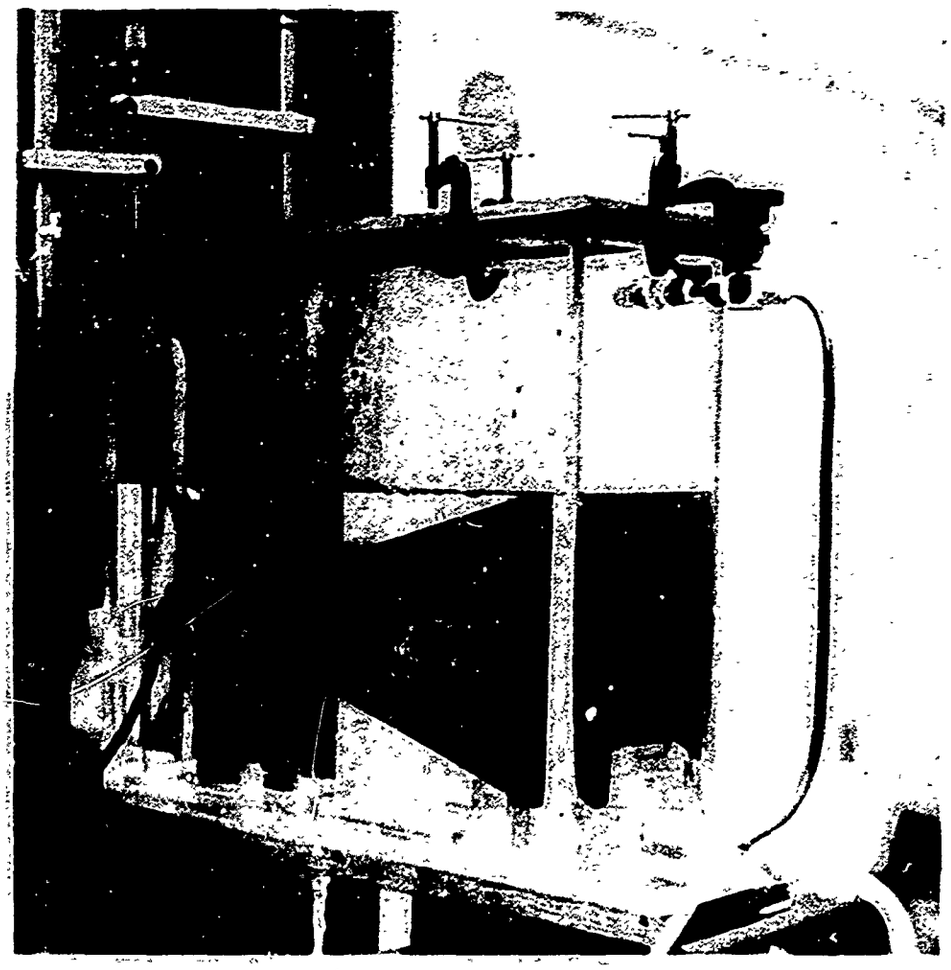

Fig. 47 - A Close-Up View of Environmental Cell and Location of LVDT

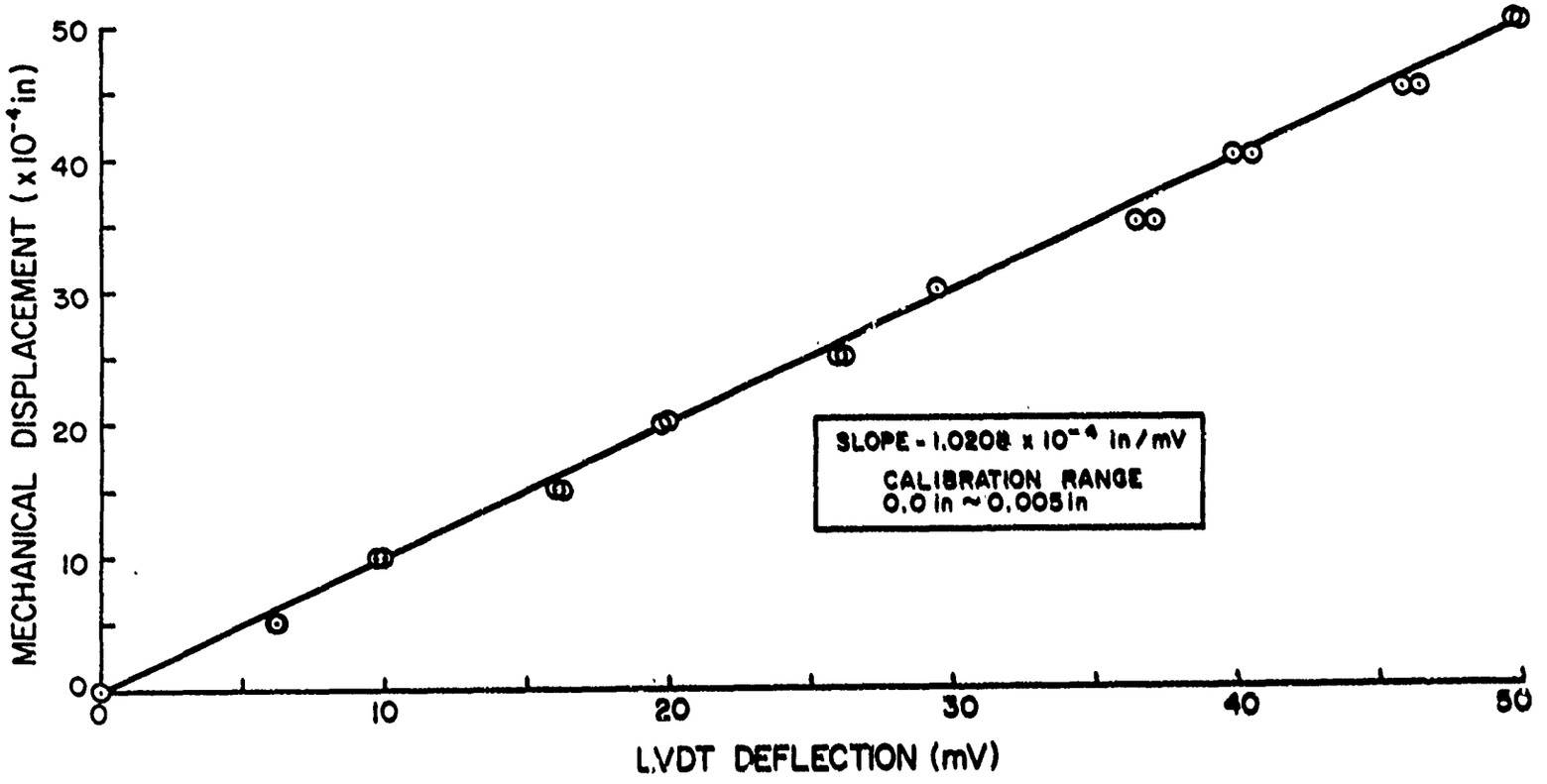

Fig. 48 - Calibration Curve for Linear Variable Differential Transducer

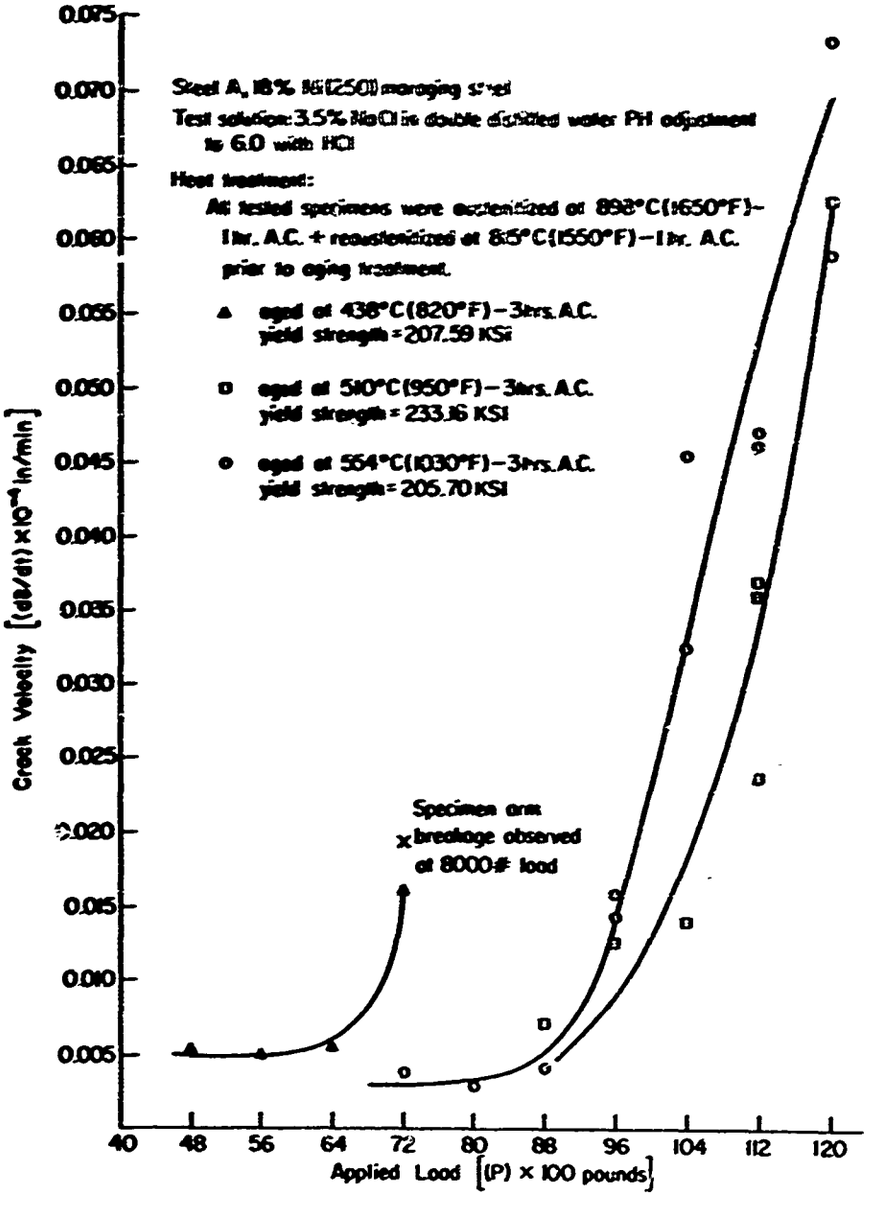

Fig. 49 - Subcritical Crack Growth of 18% Ni (250) Maraging Steel

The resultant data of crack propagation rate as a function of applied loads on the 18% Ni maraging steel, shown in Fig. 49, clearly demonstrates that the metallurgical structure alters the crack propagation rates. It is noteworthy, from Table V, that the ductility parameters for the two similar strength conditions do not differ significantly. The comparison of crack propagation rates on the aged specimens at 438°C (820°F) and 554°C (1030°F) are fruitful because of their identical strength. The crack propagation rates for aged specimens at 510°C (1950°F) are not comparable to the other two specimens because of the difference in strength levels. However, it is of practical importance to document the crack propagation rates of this aging condition for reference because aging at 510°C (950°F) for three hours is a standard commercial heat treatment for 18% Ni (250) maraging steel. Correlation of crack propagation rates to the metallurgical structures will be made when the analysis of metallurgical structures is completed.

Because of the high fracture toughness of 18% Ni maraging steel and the limited 120,000 lb loading capacity of the SATEC Model D creep tester, no crack propagation rates can be obtained at high stress intensity levels for the specimen of 554°C (1030°F) aged condition. To overcome this experimental difficulty, a reduced-size, tapered, double-cantilever specimen is designed for future investigation (see Fig. 50).

5. Metallurgical Structure Consideration

The high-strength steels used in this investigation exhibit two basically different structures and alloy chemistries. Two commercial heats of consumable electrode vacuum melt 18% Ni (RMS 250) maraging steel and AISI 4340 steel were purchased from Republic Steel Corporation in the form of hot-rolled 0.5-inch thick plates with a final mill-annealed condition. The certified chemical analysis of the two steels is tabulated in Table VI.

Maraging steel derives its high fracture toughness and strength by martensite transformation through slow cooling, and precipitation hardening through aging; whereas, the typical low alloy AISI 4340 steel yields an optimum combination of toughness and strength through quench-temper or austempering with tempered martensite and bainite structures, respectively. The susceptibility of SCC for these two steels in terms of time-to-failure has been observed by Steigerwald and Benjamin[36] to have two orders of magnitude difference at the same strength level of 236 ksi. From a microstructural viewpoint, the only structure of the two steels in common is grain size. Indeed, SCC has been, from time to time, reported to have intergranular fracture and grain size dependent in nature. The objective of this investigation is to determine the characteristic responses to SCC of the two high-strength steels, each with different structures. Various heat treatments are used in the steels to obtain identical strength and grain size with significant difference in microstructures.

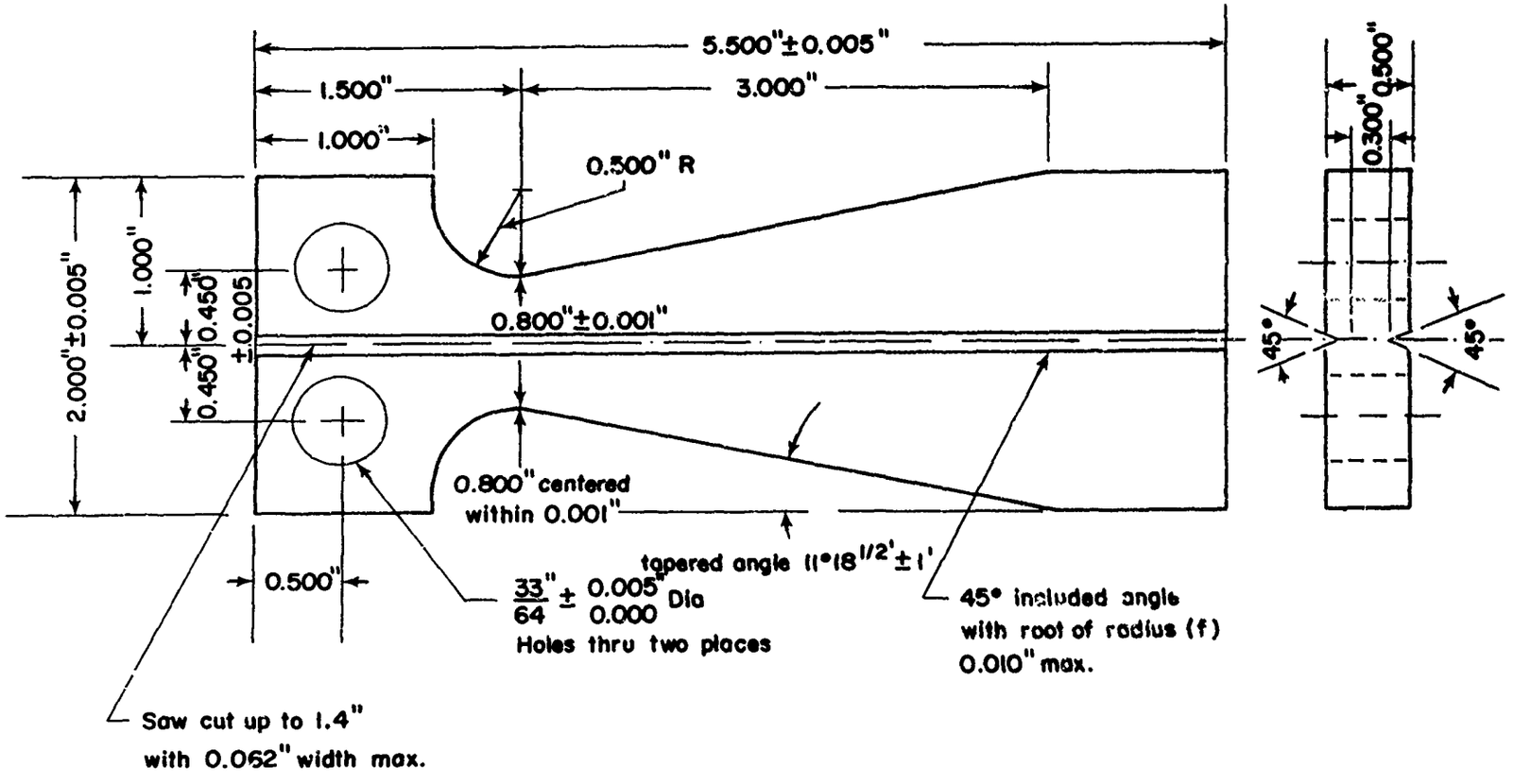

Fig. 50 - Tapered Double-Cantilever Beam Specimen

Table VI. Chemical Composition of High-Strength Steels*

Steel No.	Steel	C	Mn	P	S	Si	Ni	Co	Mo	Ti	Al	Zr	B	Ca	Cr
A	AISI 4340 Steel Heat No. 3952755	0.41	0.73	0.005	0.005	0.23	1.81		0.25						
B	18% Ni (RMS 250) Maraging Steel Heat No. 3951440	0.029	0.09	0.006	0.007	0.09	17.68	7.18	4.86	1.38	0.05	0.02	0.003	0.06	0.83

*Republic Steel Corp. certified analysis; chemical composition in weight percent

The heat treatments for 18% Ni maraging steel are austenitized at 899°C for one hour and air-cooled, plus reaustenitized at 816°C for one hour and air-cooled prior to aging at different temperatures for three hours. The hardness and strengths of aging response on 18% Ni maraging steel are shown in Fig. 51 and Table V. The use of double austenitized temperatures at 898°C (1650°F) and 815°C (1550°F) aims at minimizing the anisotropic mechanical properties and eliminating the significant difference in grain size during the subsequent aging treatment at different temperatures. Moreover, the choice of temperatures in the double austenitizing treatment is intentional to avoid the grain boundary segregation to response for thermal embrittlement in maraging steel.

Recent publication on SCC of 18% Ni (300) maraging steel by Stavros and Paxton[57] show intergranular fractures for the steel with six different heat treatments and identical strengths. It appears that those heat treatments used in their investigations may have produced thermal embrittlement which enhanced SCC. Thermal embrittlements in maraging steel has been reported to produce intergranular fracture.

For practical purposes the grain sizes, which are duplex fine grains from all different aging treatments, are approximately in the range of ASTM No. 9 to 11. The microstructural constituents in this steel with various aging treatments are mainly cubic martensite, precipitation phases, and reversion austenite. Reversion austenite in maraging steel is a typical structure resulting from the hysteresis of the transformation in the iron-nickel system and from the partitioning of alloying elemnts upon precipitation. The enhancement of ductility and toughness by reversion austenite in 18% Ni maraging steel may give rise to beneficial effects on the resistance to crack propagations of SCC.

Two major structures have been produced in AISI 4340 steel through the following heat-treatment schedules:

A. Tempered martensite structure with quench-temper treatment

Normalized at 899°C (1650°F), 40 min A.C. + austenitized at 843°C (1550°F), 30 min, then oil quenched + tempered at 426°C (800°F) 1 hour A.C.

B. Temper bainite structure with austempering treatment

Normalized at 899°C (1650°F), 40 min A.C. + austenitized at 843°C (1550°F), 30 min + rapid quenched at 315°C (600 ± 10°F), 2 hours A.C. + tempered at 400°C (750°F), 1 hour A.C.

These treatments give the same strength of the steel for tempered martensite and bainite with Rockwell hardness between 44-46 R_C; these treatments produce the same grain size and carbide distribution and morphology in the structures being studied. It is worthwhile to

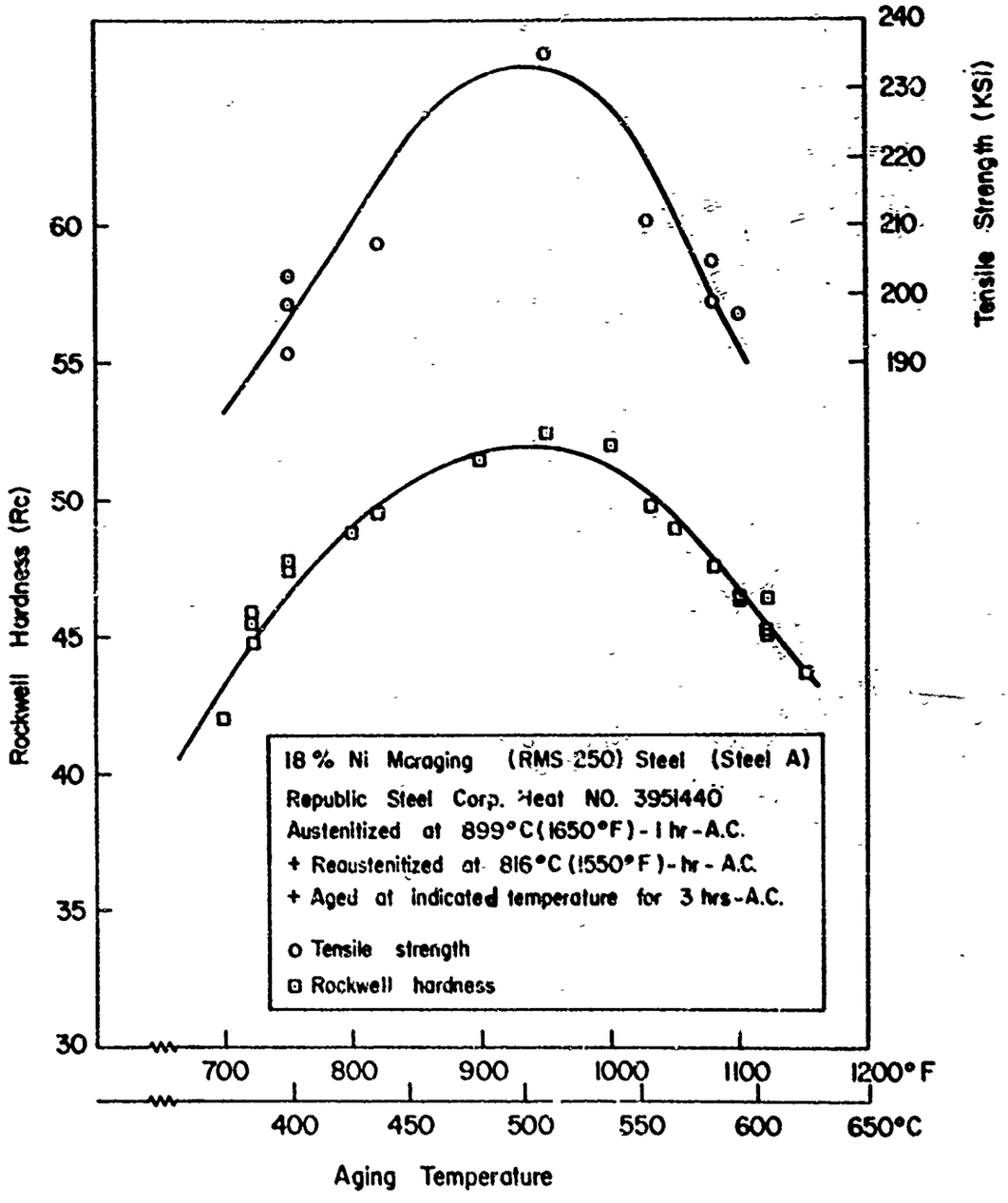

Fig. 51 - Hardness and Tensile Strength as a Function of Aging Temperature of 18% Ni Maraging (RMS 250) Steel

mention that tempering at 400°C in AISI 4340 steel is in the third stage of tempering in which retained austenites are completely decomposed and epsilon carbides are completely transformed to cementite in an early stage of spheroidization.

6. Electron Metallographic Examination

Microstructures of the steel specimens were examined by electron transmission using thin foils.

a. Examination of Maraging Steel

Upon air cooling from the austenitizing temperature, a low-carbon cubic martensite matrix with high dislocation densities is anticipated in the 18% Ni maraging steels. The high dislocation density in the cubic martensite matrix is attributed to the metastable austenite-alpha prime (γ-α') transformations. Aging at 438°C (820°F) for three hours produces annihilation and intersection of dislocations to form dislocation cell structures. Figure 52 shows the dislocation cell structures in the cubic martensite matrix. Whether the dislocation cell structure is equivalent or related to the martensite laths remains to be verified. It is important to mention that precipitations of second phases (intermetallic compounds) have already formed at 438°C (820°F) aging; however, the tiny coherent precipitates are too small to be observed at this magnification with thin-foil techniques as shown in Fig. 52. As the aging temperature increases to 510°C (950°F) for three hours, the dislocation density drastically decreases and a small amount of reversion austenite formed at the sub-boundaries can be observed, as shown in Fig. 53. Extensive examination of thin foils at higher magnification suggests that reversion austenites in 18% Ni maraging steel form by nucleation and growth at the sub-boundaries. The terminology of martensite laths used here is to distinguish the incoherent un-twinned cubic martensite from the twin plates of medium carbon martensite in AISI 4340 steel. The low-carbon cubic martensite in maraging steel is believed to be incoherent at the lath interfaces. The amount of reversion austenite increases as aging temperature increases. Figure 54 shows the increasing amount of reversion austenite aged at 554°C (1030°F). Positive identification of reversion austenite in maraging steel will be carried out in the next period of work.

b. Examination of AISI 4340 Steel

The purpose of this investigation is to compare the crack propagation characteristic of martensite and bainite structures. Figures 55 and 56 reveal the morphologies of tempered martensite and bainite, respectively. The third-stage tempering process is intentionally used here not only to avoid the tempered martensite embrittlement [i.e., 204°C (400°F), 371°C (700°F) tempering] and the reversible temper embrittlement (i.e., 482°C-593°C tempering), but also to attempt to obtain a similar

Fig. 52 - Microstructure of 18% Ni Maraging Steel
Heat treatment: 899°C (1650°F)-1 hr. A.C. +
815°C (1550°F)-1 hr. A.C. +
438°C (820°F)-3 hr. A.C.
Tensile strength: 235.80 ksi
Yield strength: 233.16 ksi
Rockwell hardness, R_c: 52.2

Fig. 53 - Microstructures of 18% Ni Maraging Steel
Heat treatment: 899°C (1650°F)-1 hr. A.C. +
816°C (1550°F)-1 hr. A.C. +
510°C (950°F)-3 hr. A.C.
Tensile strength: 235.80 ksi
Yield strength: 233.16 ksi
Rockwell hardness, R_c: 52.2

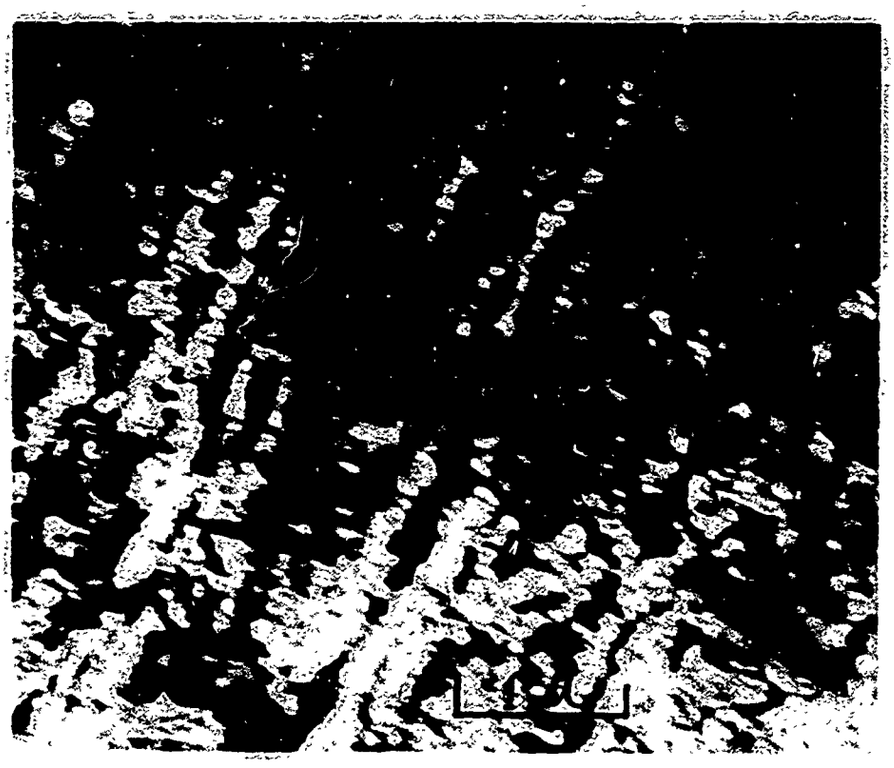

Fig. 54 - Microstructures of 18% Ni Maraging Steel
Heat treatment: 899°C (1650°F)-1 hr. A.C. +
815°C (1550°F)-1 hr. A.C. +
554°C (1030°F)-3 hr. A.C.
Tensile strength: 210.13 ksi
Yield strength: 205.70 ksi
Rockwell hardness, R_c: 44.6

Fig. 55 - Morphology of Tempered Martensite in AISI 4340 Steel
Heat treatment: Oil quenched + tempering at 425°C (800°F) for one hour A.C.

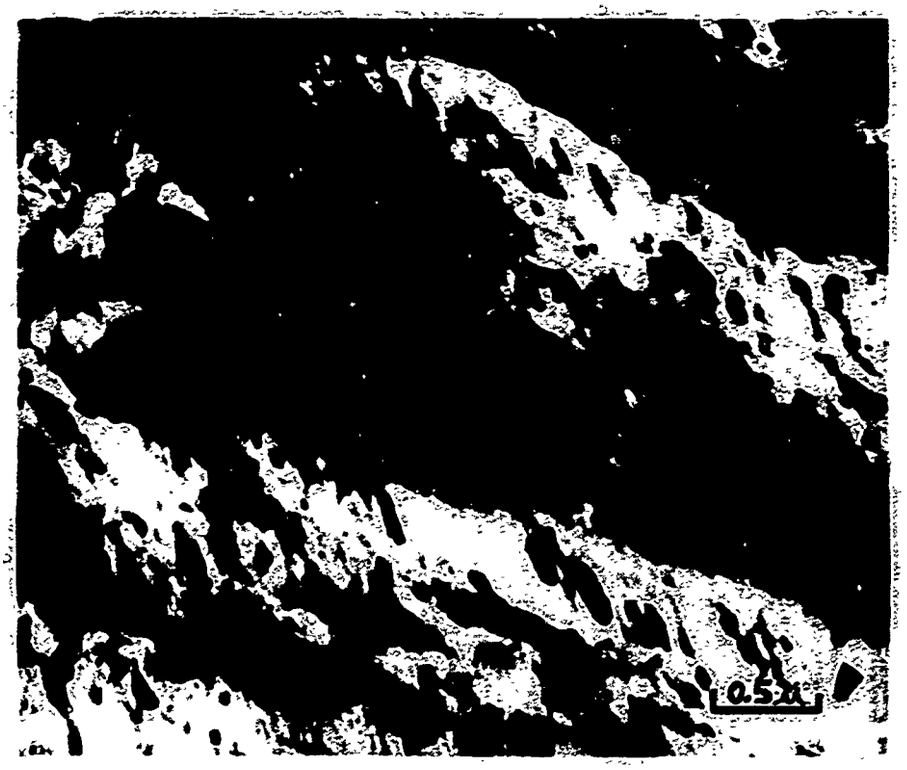

Fig. 56 - Morphology of Tempered Bainite in AISI 4340 Steel
Heat treatment: Austempering at 315°C (600 ± 10°F)
for two hours A.C. + tempering at
400°C (750°F) for one hour A.C.

morphology and distribution of carbides in both tempered martensite and bainite. No retained austenites were observed in either structure; this is in agreement with a review of literature showing that retained austenite is completely decomposed in the third stage of tempering. The carbides in both structures exhibit a similar morphology of the early stage of spheroidization. The amount of carbides appears to be more dense in tempered bainite than in tempered martensite. No further adjustments of the tempering temperatures have been made because of the identical strength requirement from a fracture mechanics consideration. The morphology and distribution of carbides are shown in Fig. 57. Intergranular fracture has been hypothesized to be related to the grain boundary precipitation of second phases; i.e., carbides. An extensive search of grain boundaries in the thin foils of both structures shows very clean grain boundaries without any carbide precipitation, as shown in Fig. 58.

To reveal the significant difference between tempered martensite and tempered bainite, selected area diffraction analyses have been performed at the interfaces of the martensite plates and bainite laths. Figure 59 shows a selected area diffraction micrograph from the interface of a pair of tempered martensite plates. Preliminary analysis indicates that the tempered martensite plates are essentially coherent microtwins. To confirm this analysis, selected area diffraction in association with dark field techniques have been used to delineate the slight misorientation between the microtwins, as shown in Fig. 60. Similar examination techniques are undertaken to examine the interface between bainite cells to see the significant differences between these two types of substructures.

7. Results and Discussion

Results of crack propagation in the 18% Ni maraging steel of identical strength with 438°C (820°F) and 554°C (1030°F) aging condition shows a close but as yet not rational relationship to microstructures. The presence of reversion austenite at the cell or martensite laths interface may block the propagation of cracks, and hence, reduce crack velocity. The appearance of reversion austenite in the 510°C (950°F) aged specimen can be rationalized in such a manner that slow crack propagation velocity in this aged condition is attributed partly to the higher strength level and comparing the 510°C (950°F) with the 554°C (1030°F) aged condition, it appears that a small amount of reversion austenite at the interfaces of boundaries shows significant retardation of the crack propagation; however, increasing the amount of reversion austenite does not cause further reduction in crack propagation velocity.

Preliminary selected area diffraction analysis on tempered martensite indicates that the martensite plates appears to be composed of a group of microtwins. This sugeests that tempered martensite in AISI 4340 steel may have a higher crack propagation rate as a result of hydrogen trapping at the coherent microtwin interfaces.

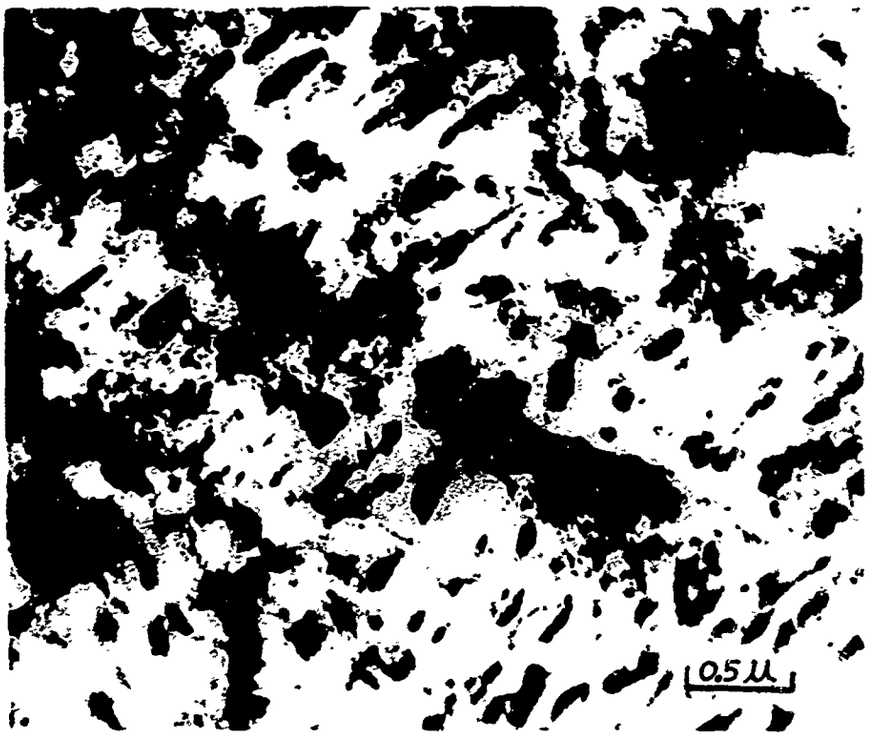

Fig. 57 - Morphology of Spheroidized Carbide in Tempered Bainite of AISI 4340 Steel
Heat treatment: Austempering at 315°C (600 ± 10°F) for 2 hours A.C. + tempering at 400°C (750°F) for 1 hour A.C.

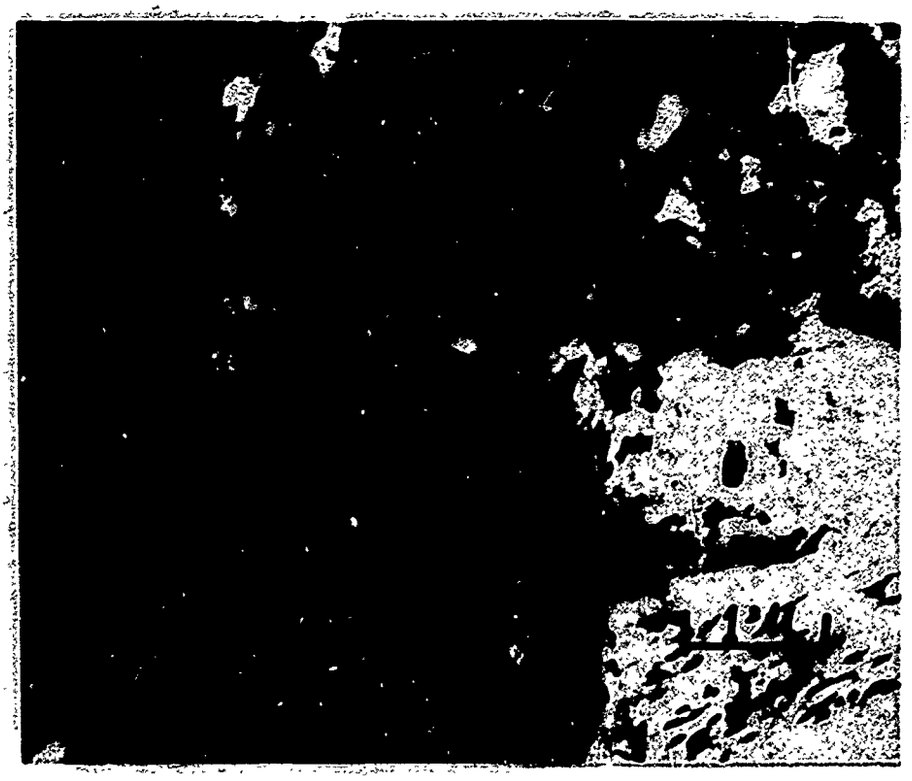

Fig. 58 - Grain Boundaries in AISI 4340 Steel of Tempered Bainite Structures Showing No Grain Boundary Precipitation of Carbides

Fig. 58 - Grain Boundaries in AISI 4340 Steel of Tempered Bainite Structures Showing No Grain Boundary Precipitation of Carbides

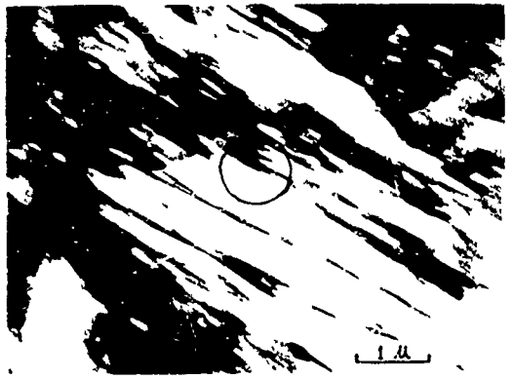

a. Bright field of tempered martensite plates. Circle indicates selected area

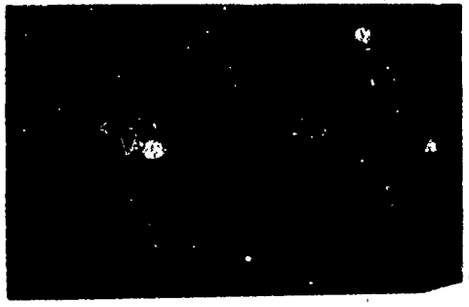

b. Selected area diffraction of encircled area

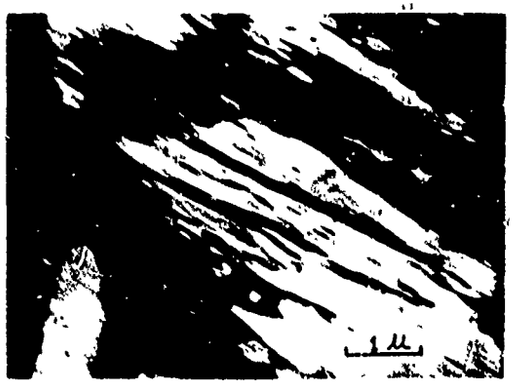

c. Dark field of spot A, the common diffraction of both twin and matrix at $[\bar{1}\ \bar{1}\ 0]$ direction

d. Dark field of spot B, $(0\ \bar{1}\ 1)_M$ direction of matrix

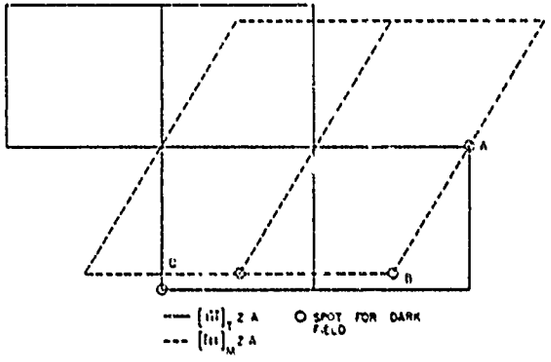

e. Trace of diffraction pattern from b

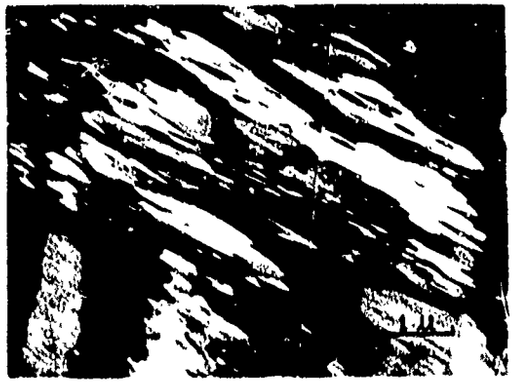

f. Dark field of spot C, $(0\ \bar{1}\ 1)_T$ direct of twin

Fig. 60 - Slight Misorientation of Tempered Martensite Plates in AISI 4340 Steel with Selected Area Diffraction and Dark Field Techniques (Index of diffraction patterns, see Fig. 59)

8. Future Work

Continuation of crack propagation and advanced microstructural examination and analysis on the 18% Ni maraging and AISI 4340 steels with different heat-treated conditions will be carried out. Extensive selected area diffraction analysis between tempered martensite and bainite interfaces will be performed to determine the significant differences in coherency on these interfaces.

C. INTERACTION OF HYDROGEN WITH STEELS
(R. B. McCright)

1. Objectives and Background

The purpose of this work is to investigate the hydrogen interaction with the metal, i.e., the entry kinetics of the hydrogen, its subsequent movement in the metal, and its evolution from the metal. Previous work has considered the effect of adding cathodic promoters on the entry kinetics, the effect of palladizing the exit side of the membrane, and calculation of the apparent diffusivity from analysis of the hydrogen permeation transients. All of these experiments were done on a mild steel (AISI-1010).

The work reported herein considers some additional experiments with the cathodic promoters on AISI-1010 steel, and permeation through pure iron and Fe, 1% Cu foils in which the size, and presumably, the coherency, of the second phase particles can be controlled by appropriate heat treatments.

2. Experimental Results and Discussion - Promoter Effects

a. Galvanostatic and Potentiostatic Control

The establishment of defined boundary conditions for the iron or steel foil is of paramount importance for the mathematical models needed to solve the diffusion equation. Most of the work reported in the literature has described a galvanostatically controlled system where the control of the input hydrogen is by a constant current; this control can also be had by applying a constant potential to the entry side.

b. Effect of Arsenite as a Cathodic Promoter

Sodium arsenite greatly increases the hydrogen permeability. At potentials at which hydrogen is deposited, arsenite is reduced, according to Fig. 61, which is the equilibrium pH-potential diagram. The specific equilibria for the concentrations of arsenite and pH's of solutions used in this investigation are shown. The rest potentials

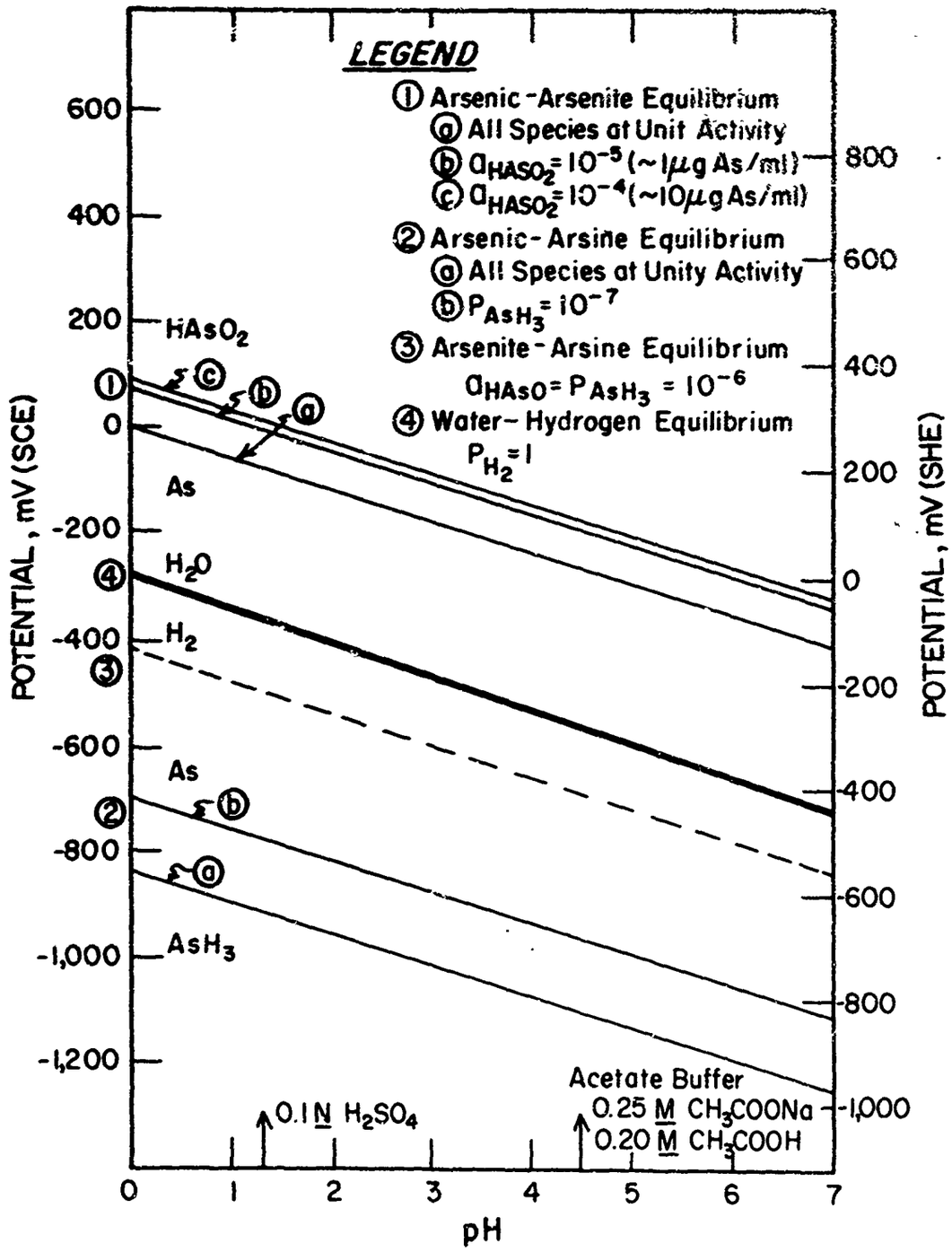

Fig. 61 - Equilibrium Potential-pH Diagram for the System Arsenic-Water at 25°C

for sulfuric acid and acetate solutions containing arsenite additions (expressed as μg As/mℓ) are shown in Fig. 62. The concentration dependence of these varies approximately according to the Nernst equation for the arsenite/arsenic equilibrium.

Permeation transients of 1010 steel galvanostatically charged with hydrogen from the acetate buffer containing arsenite are shown in Fig.63 . The transients for the different charging currents show an increase of permeation current with the increase in charging current density and also illustrate the different behaviors, reflecting hydrogen interaction with the metal structure. The initial transient often shows a long time to come to steady state, while subsequent ones at relatively low current densities show the "normal" behavior, a sharp rise to a constant permeation current. Upon increasing the charging current density there can be a slight decline of the permeation current after the system appeared to reach steady state. Finally, at high charging current densities, the permeation current reaches a maximum and declines rather sharply, the "sharpness" usually increasing with the charging current densities.

In the next set of experiments described, the hydrogen was charged into the steel potentiostatically or galvanostatically and the steady state permeation current measured. These results are plotted in Figs. 64-67. The graphs show points where the anomalous behavior described in Fig. 63 occurred. One notes from these that in sulfuric acid (Figs. 64 and 65):

1. Arsenite additions are more effective in increasing the permeation current as the potential becomes more active or the charging current becomes larger.

2. The onset of the anomalous behavior--sharp maximum in the permeation current transient--occurs at more active potentials or higher charging currents when arsenite is present.

These same conclusions hold for the specimens charged with hydrogen from the acetate buffer (Figs. 66 and 67). In addition, some of the specimens were pre-deposited with a thin coating of arsenic (about 50 μCb). These curves have the same general shape as those in which the charging solution contained arsenite, but the magnitude of the permeation is not as great. Generally, the pre-deposit arsenic specimen behave similar to specimens charged from more concentrated arsenite-containing solutions (> 30 μg As/mℓ).

In galvanostatic charging the expected relationship between i_p and i_c is $i_p \alpha i_c^{n}$ if the recombination step is the rate controlling one. The exponent of proportionality is 0.6 - 0.9 for these experiments. Similarly, there is an exponential relationship between the permeation current and the cathodic potential, which seems to hold at the less active potentials.

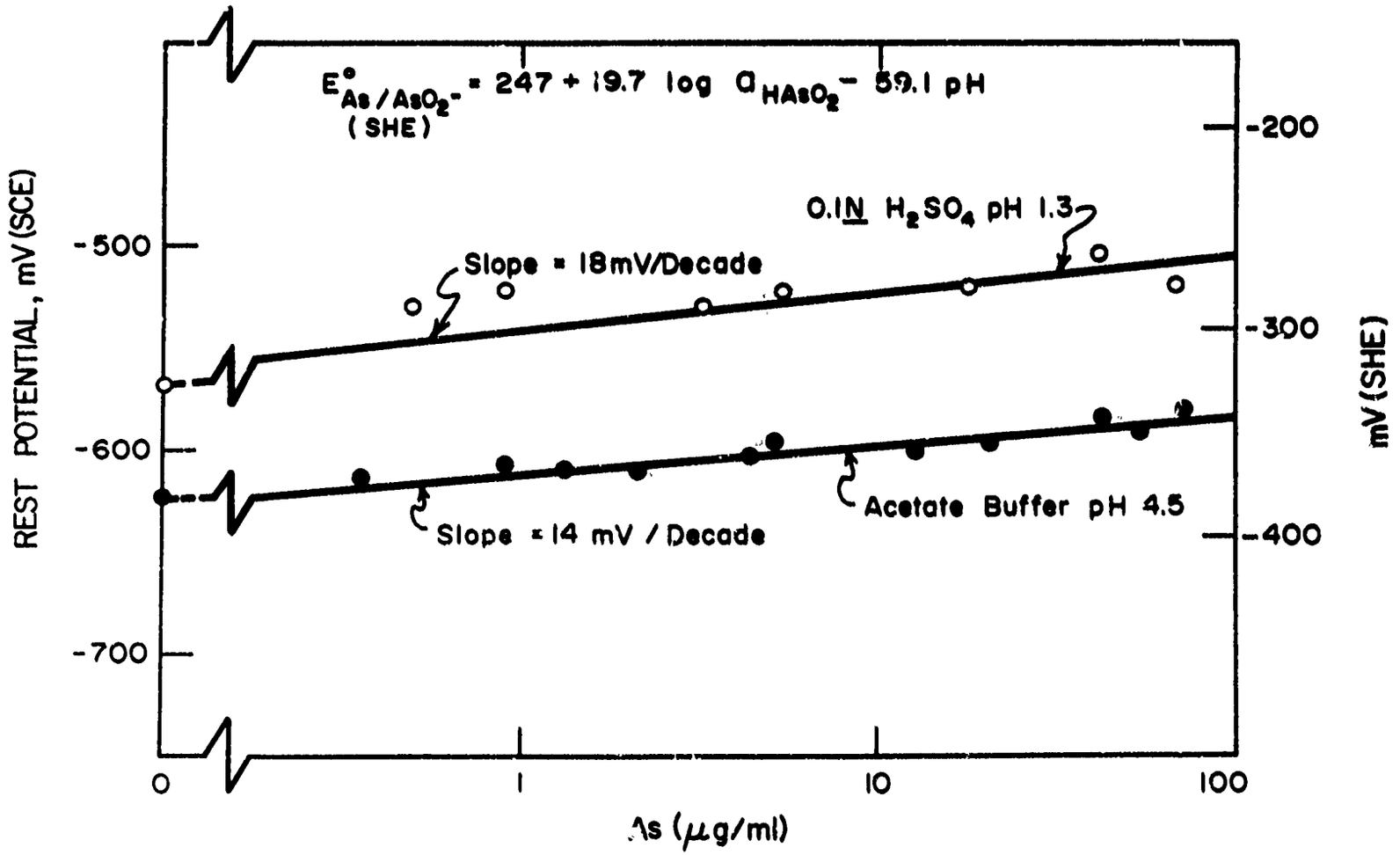

Fig. 62 - Rest Potential of Steel Electrodes as a Function of the Arsenite Concentration

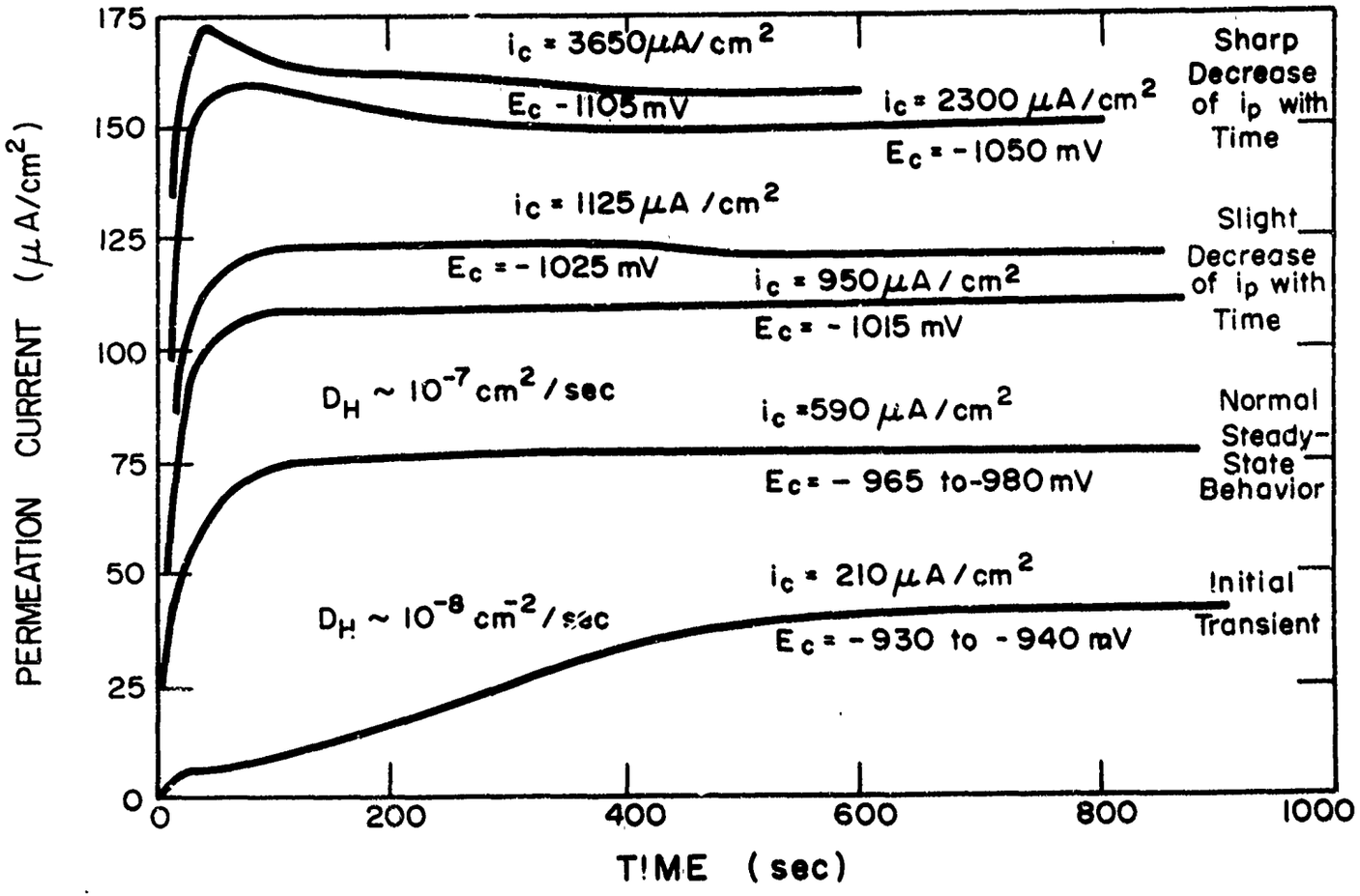

Fig. 63 - Examples of Hydrogen Permeation Rise Transients. Conditions: Charging Solution, Acetate Buffer pH 4.5 with Arsenite Additions (0.9μg AS/ml); Membrane, 2-mil Thick 1010 Steel, Vacuum Annealed at 650°C for 2 hrs., Palladized on Exit Surface; Exit Solution, 0.1N NaOH

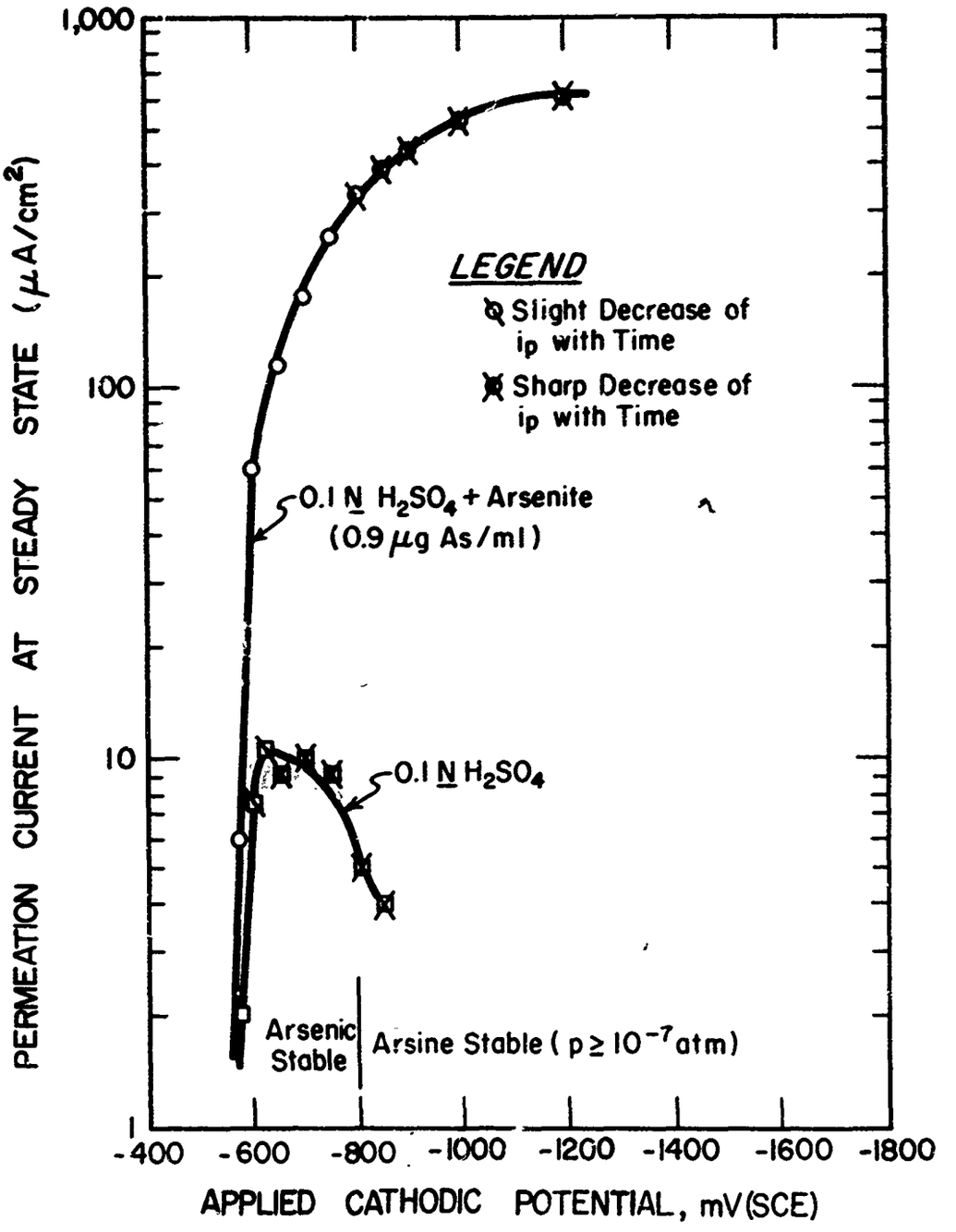

Fig. 64 - Steady State Hydrogen Permeation of 1010 Steel as a Function of the Cathodic Potential (Sulfuric Acid Solutions)

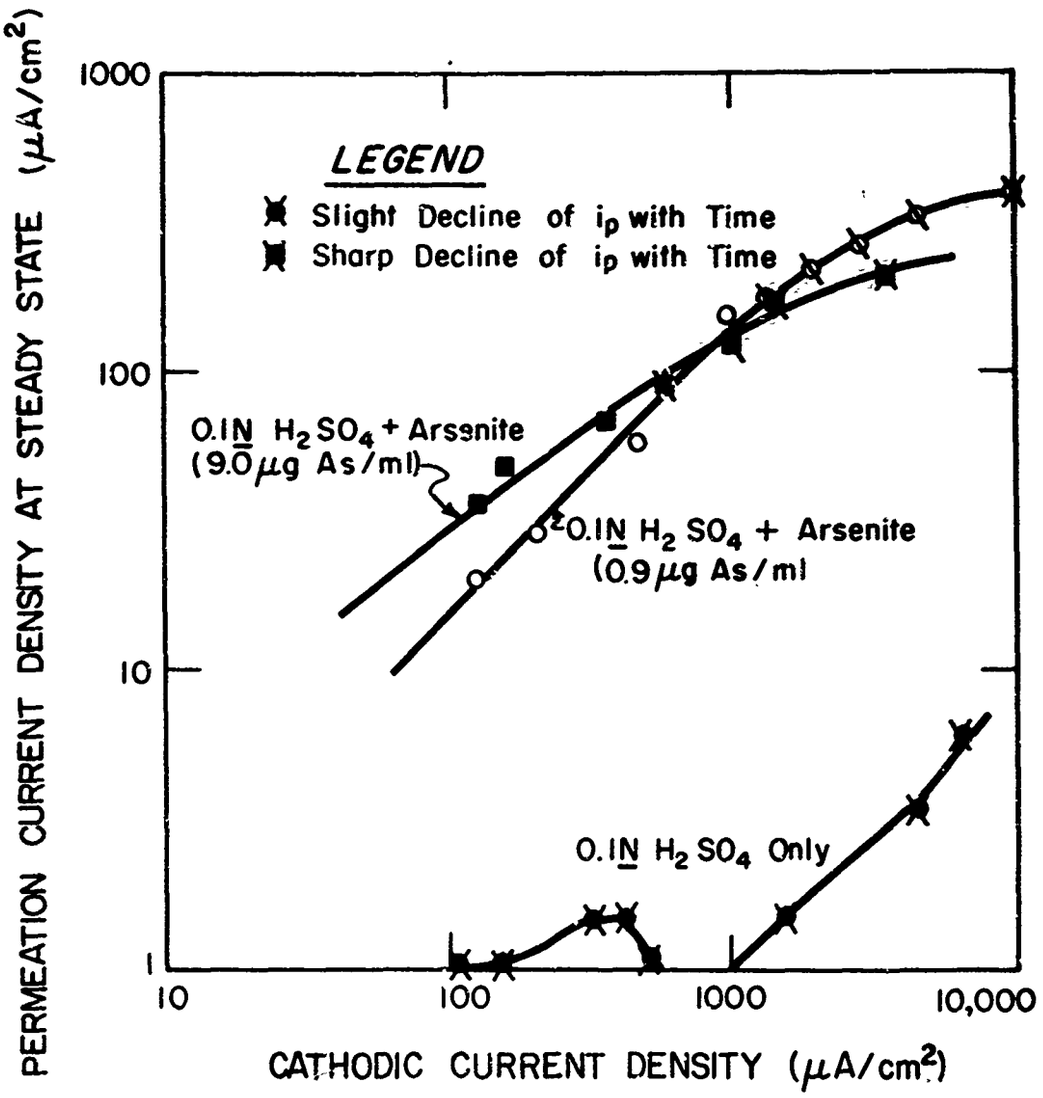

Fig. 65 - Steady State Hydrogen Permeation of 1010 Steel as a Function of the Cathodic Current Density

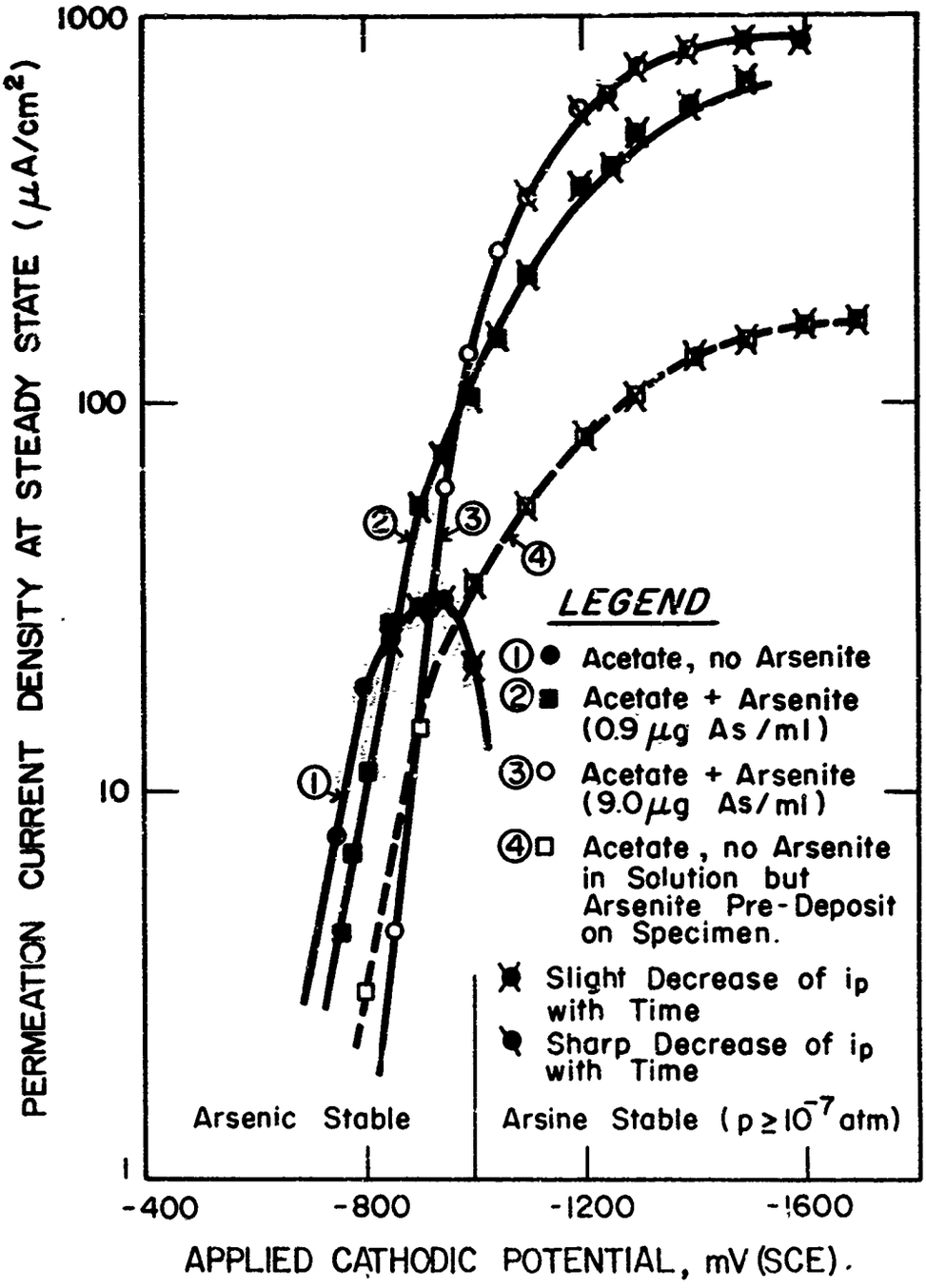

Fig. 66 - Steady State Hydrogen Permeation of 1010 Steel as a Function of the Cathodic Potential (Acetate Solutions)

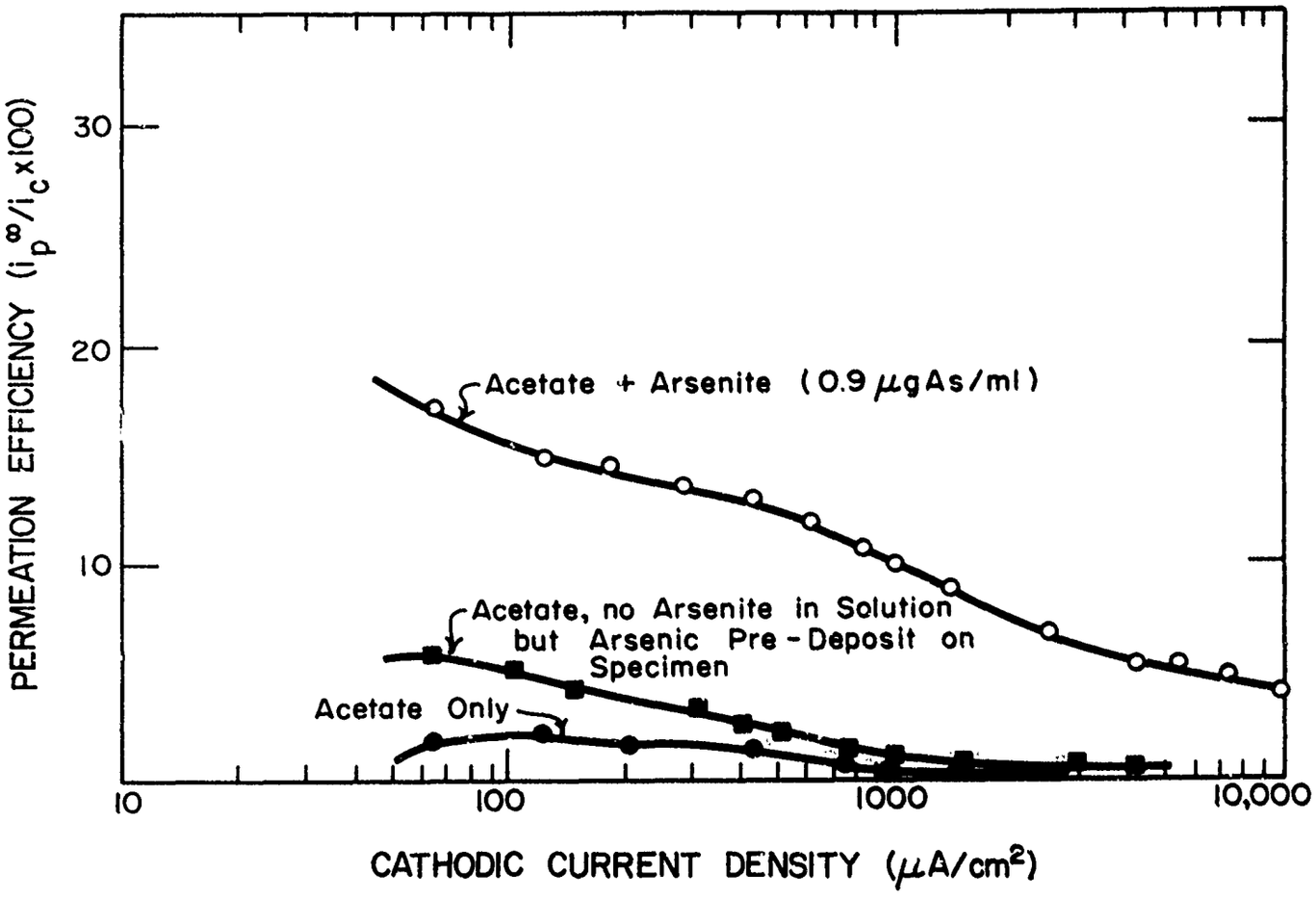

Fig. 67 - Permeation Efficiency of 1010 Steel Membranes as a Function of the Cathodic Current Density (Acetate Solutions)

Another way of plotting these data is to show the relationship between the permeation efficiency and either the applied potential or charging current density. The permeation efficiency is the ratio of the permeation current density (at steady state, or at the maximum if anomalous behavior obtains) to the charging current density. This gives the percent of hydrogen entering the metal and diffusing through it, assuming that all of the cathodic current is utilized for hydrogen ion reduction.

Figures 68 and 69 illustrate the relationship between permeation efficiency and the applied potential. At potentials slightly cathodic with respect to the rest potential, say, less than -600 mV (SCE) in the absolute sense for the 0.1N H_2SO_4 and less than -750 mV (SCE) for the acetate buffer, the permeation efficiency of the pure acid is either higher or about the same value as the acid containing arsenite. However, the permeation efficiency of the former decreases rather drastically above these values while that of the latter increases. The case where arsenic was pre-deposited shows behavior like that of the pure acid case except that the permeation efficiency is higher for the arsenic predeposit at all potentials. In some of the early work[38] in which the arsenite additions to the acid enhanced the permeation, but not until some critical potential was exceeded, it was concluded that the formation of the promoter hydride (here, arsine, AsH_3) was a necessary condition for the increase in permeation current. The critical potentials in this cited work corresponded to an arsine fugacity (partial pressure)of about 10^{-7} atmospheres. In the present work the equilibrium potential for the arsenic (arsine, $P_{AsH_3} = 10^{-7}$ is shown. This potential is more active than the permeation efficiency maxima which would correspond to much lower arsine fugacity ($de/d \log P_{AsH_3} = -19$ mV/decade). Of course, this vanishingly small amount of arsine may be significant, although it appears that the species enhancing the permeability is arsenic.

Permeation efficiency vs. cathodic charging current density is plotted in Fig. 70 for the galvanostatic controlled case with charging from acetate solution. There does not appear to be a maximum but the smallest charging current attainable with the experimental apparatus was 60 $\mu A/cm^2$ which corresponds to a potential more active than the potential at which the maximum occurred for the corresponding potentiostatic charging and the value of i_c when i_p reached steady state is the one used for the calculation of permeation efficiency. In Fig. 71, the potentiostatic control gives higher efficiencies than galvanostatic control.

c. Discussion of Arsenic Effects

The metals with the greatest tendency to form solid solutions with hydrogen are those with the largest number of "d" electrons. While these metals have a rather large exothermic heat of hydrogen adsorption (25-40 kcal/mole), the solubility of hydrogen increases with the decrease in bond energy of the metal-hydrogen bond for the transition

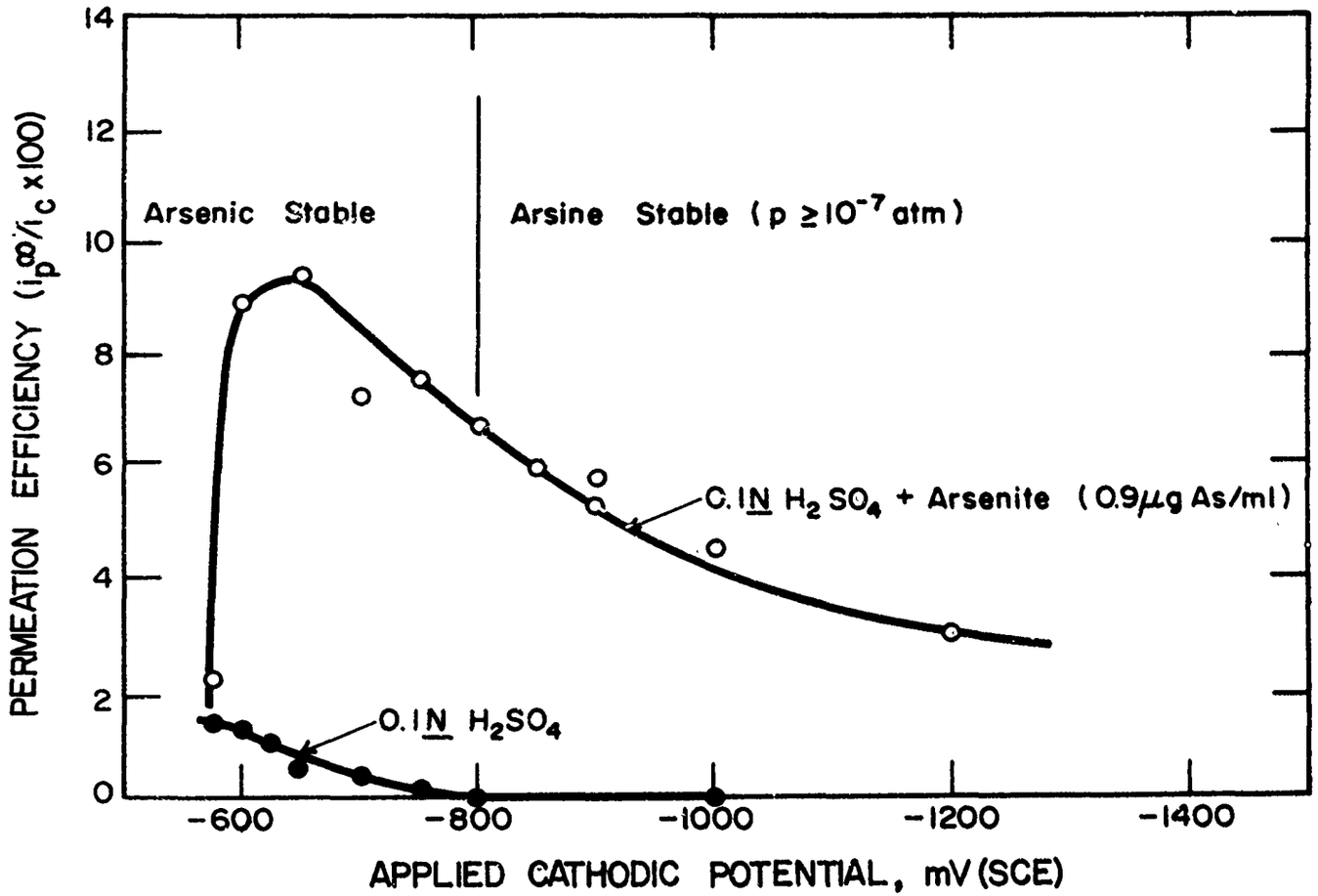

Fig. 68 - Permeation Efficiencies of 1010 Steel Membranes as a Function of the Cathodic Potential (Sulfuric Acid Solutions)

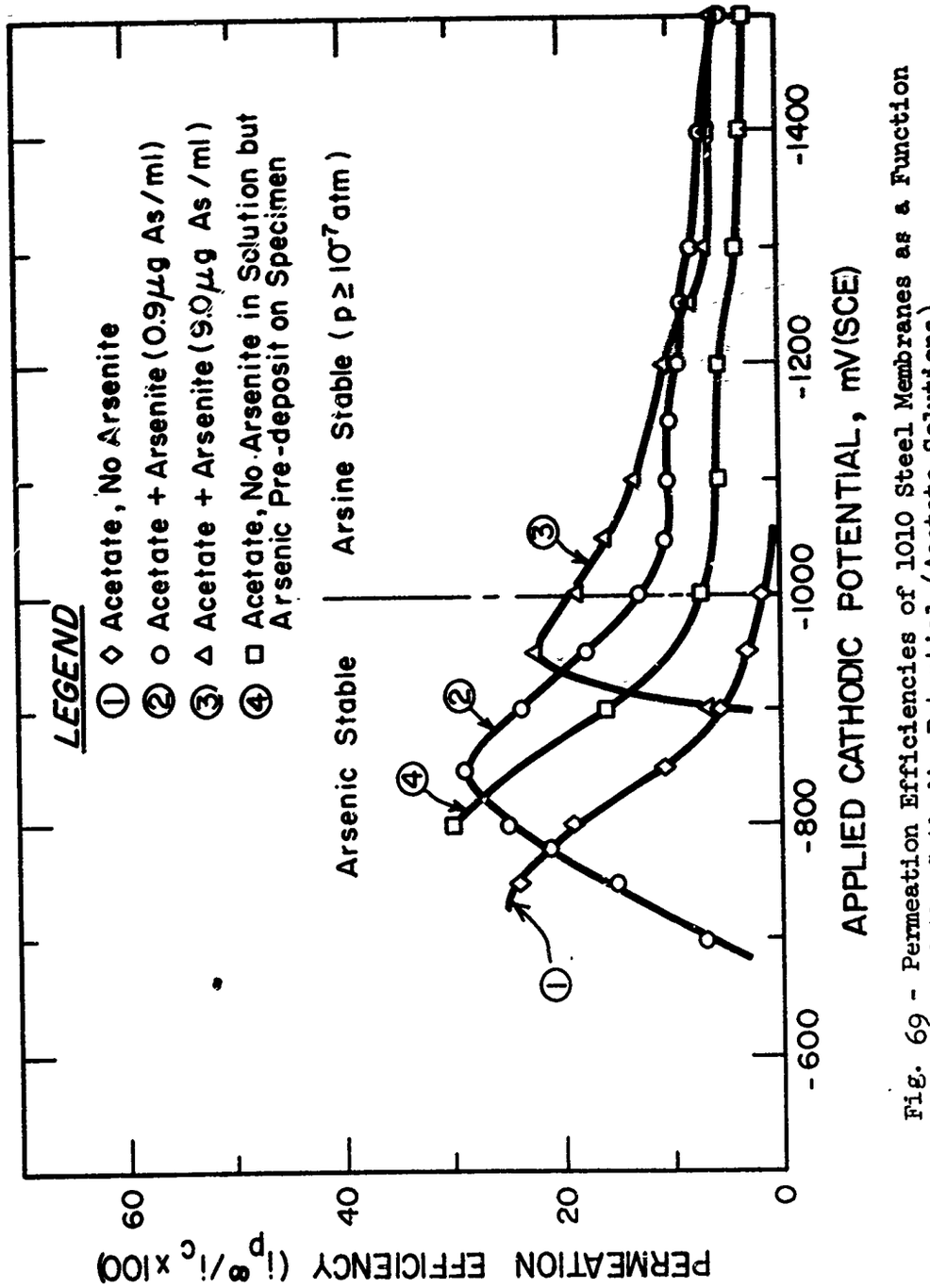

Fig. 69 - Permeation Efficiencies of 1010 Steel Membranes as a Function of the Cathodic Potential (Acetate Solutions)

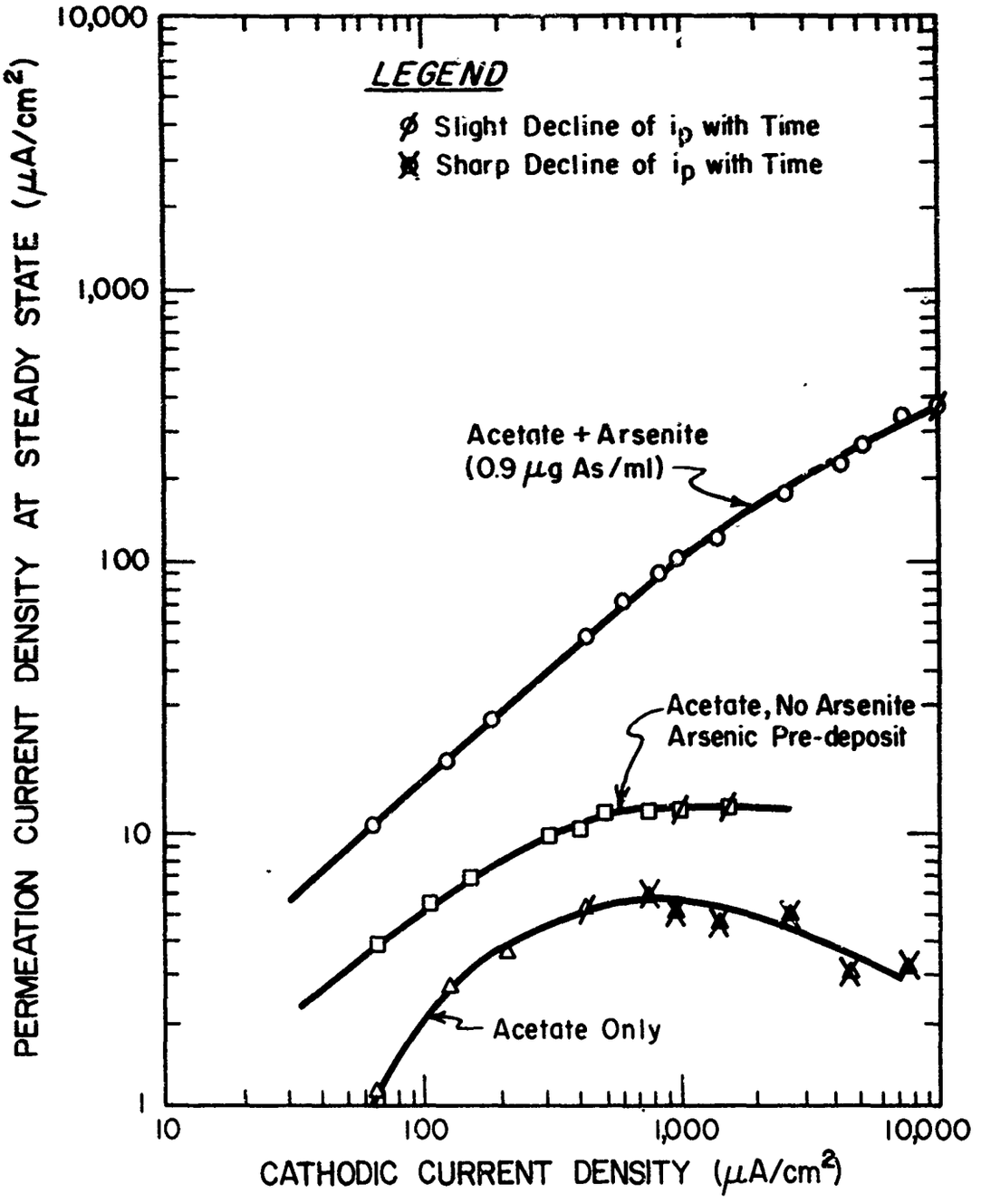

Fig. 70 - Permeation Efficiencies of 1010 Steel Membranes as a Function of the Cathodic Charging Current (Acetate Solutions)

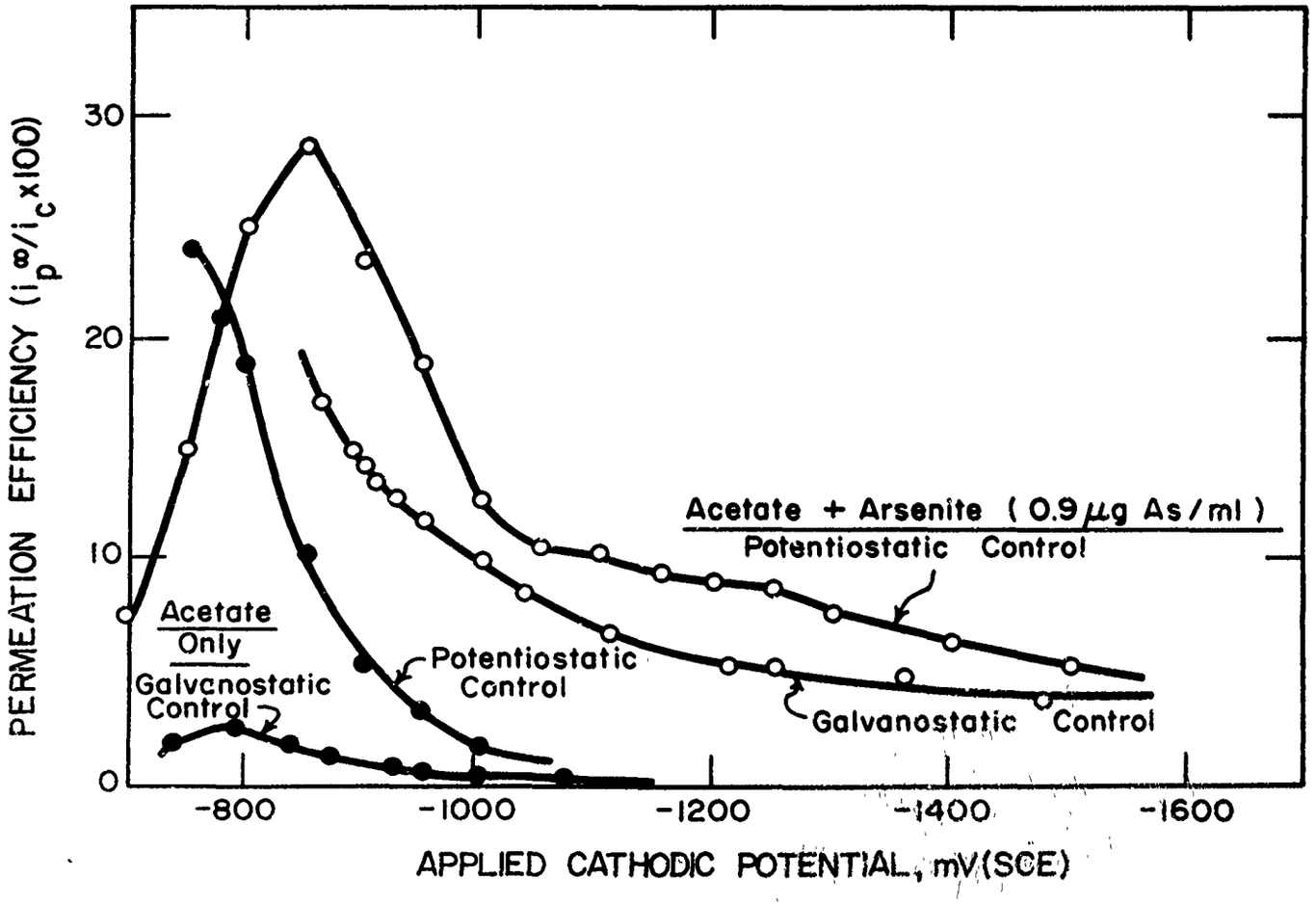

Fig. 71 - Permeation Efficiences on 1010 Steel Membranes as a Function of the Cathodic Potential for Galvanostatically and Potentiostatically Controlled Charging from Acetate Solutions

metals. This probably indicates the need for a more unsaturated bonding arrangement to promote hydrogen entry. An adatom-like elemental arsenic deposited on the surface along with adsorbed hydrogen can promote the entry of the latter in either or both of two ways; i.e., by supplying additional electrons to the metal or by decreasing the heat of hydrogen adsorption by lateral interaction between co-deposited arsenic and hydrogen. At the same time these interactions of the hydrogen with the metal and the arsenic slow down the kinetics of hydrogen atom recombination.

Cathodic promoters have electrons that can be given to or shared with the substrate, thus raising the "d" electron density of the metal. Examples of promoters are S^{2-}, P^{3-}, CN^-, Cl^-, Se^0, As^0, and As^{3-}, to list a few. Some of these are adsorbed on the surface (Cl^-, CN^-, H_2S), some are deposited electrochemically (Se from H_2SeO_2, As from $HAsO_2$). Elemental arsenic has five valence electrons which could be shared with the substrate if it is plated. Arsenic in the form of arsine would have a pair of unshared electrons that would be shared with the substrate if it were strongly adsorbed. The electron density of the iron atoms is thereby increased by the presence of these compounds or elements and, thus, the iron should form a more unsaturated bond with the hydrogen. Because of the open BCC structure of the iron, it requires little energy for movement of a strongly adsorbed hydrogen into the metal lattice. Therefore, a high concentration of hydrogen adatoms is tantamount to a high permeation rate.

Therefore, the maxima in the permeation efficiency vs. potential plots (Figs. 69, 70, and 71) occur in the arsenic stable region because arsenic is a better supplier of electrons to the "d" shell of the iron than is arsine. As the potential becomes more active, arsine is formed from the arsenic (although there is experimental evidence that this reaction is not efficient)[37] and permeation efficiency falls. Another contributing factor, and perhaps a more important one, is that the permeation reaction depends on the concentration (surface coverage) of hydrogen adatoms, θ, while the competing recombination reaction of the hydrogen adatoms depends on θ^2. Increasing the cathodic current or moving the cathodic potential in the active direction will increase θ, so that at these more severe charging conditions, the permeation efficiency would be expected to fall off even if arsenic were stable over this entire potential range.

d. Polarization Work

Some additional polarization curves were run on the 1010 steel in the environments selected for the permeation studies. Figure 72 shows the results for 0.1N H_2SO_4 and Fig. 73 for the acetate buffer with various amounts of sodium arsenite added (always expressed as μg As/mℓ). At all potentials in the sulfuric acid solution and at potentials less active than about -1050 mV(SCE) in the acetate, the presence of the arsenite is to reduce the overall cathodic kinetics. The curves for the arsenite containing solutions have a shape that is characteristic

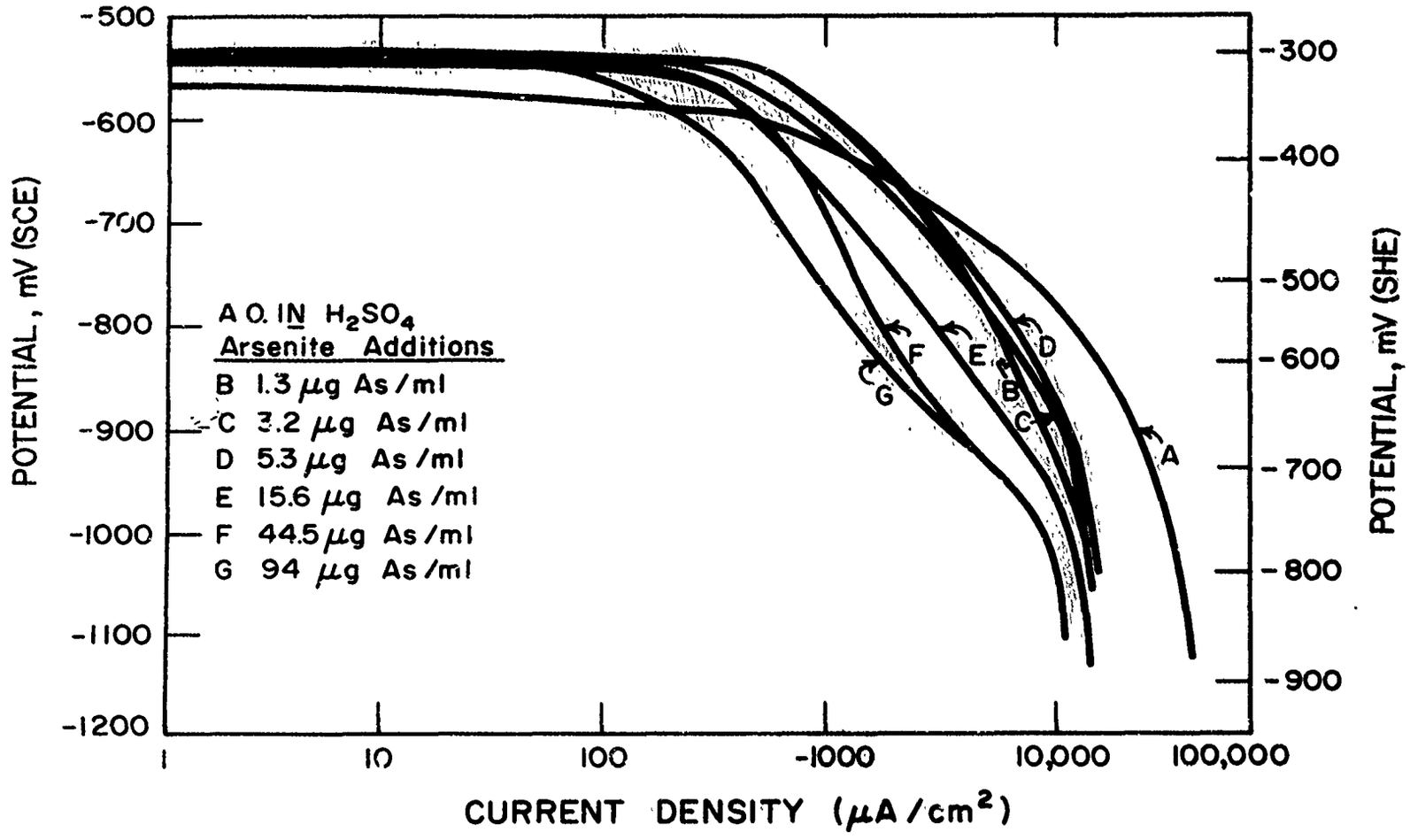

Fig. 72 - Potentiokinetic Polarization Curves for 1010 Steel in 0.1N H_2SO_4 with Arsenite Additions. Scan Rate: 15,000 mV/hr

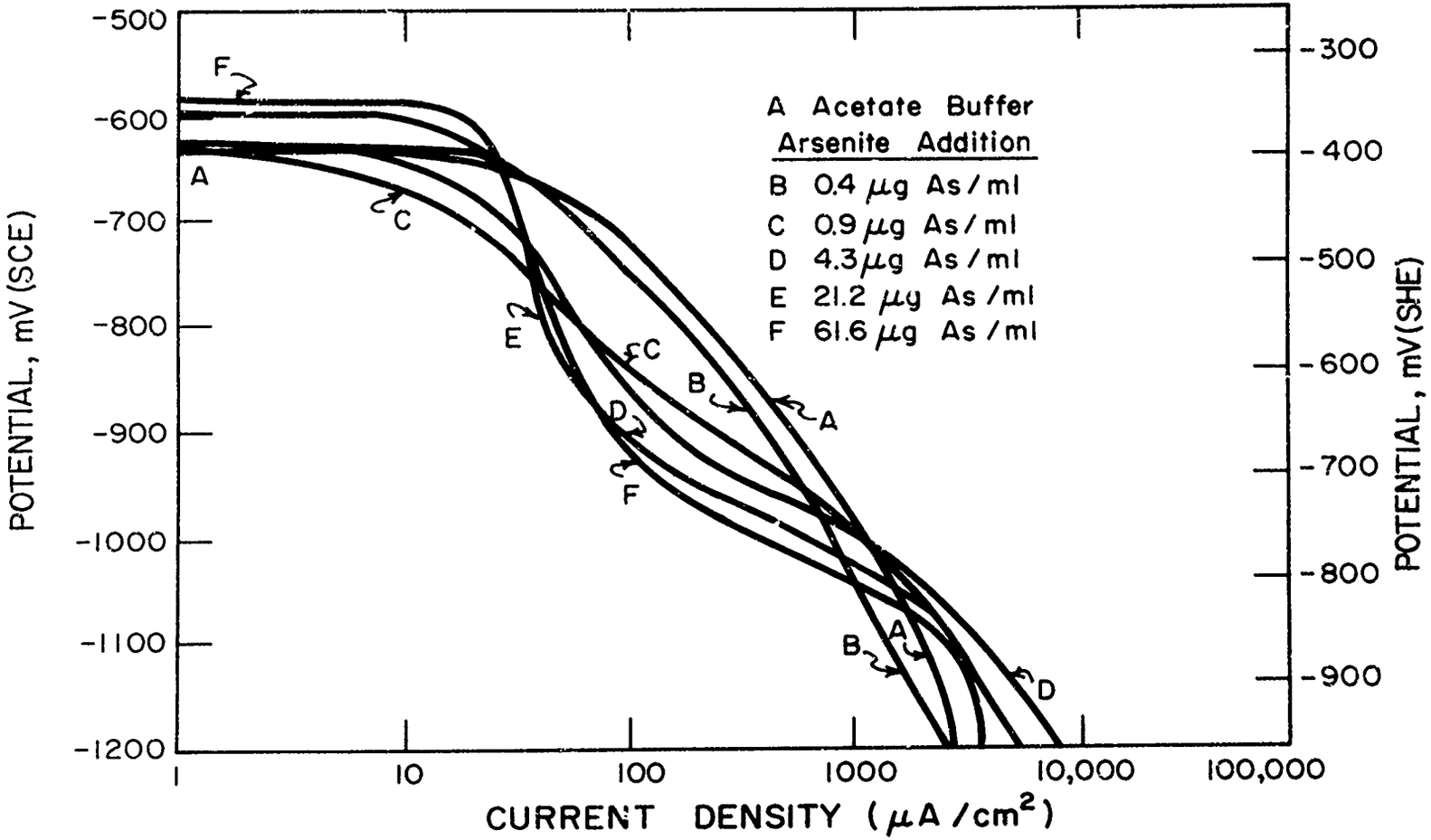

Fig. 73 - Potentiokinetic Polarization Curves for 1010 Steel in Acetate Buffer Solutions (pH 4.5) with Arsenite Additions

of two reduction reactions, each predominating in a different potential region. In other words, these curves are like those used for polarographic analysis. The first wave (the one at the less active potential) corresponds to arsenite reduction to elemental arsenic, and the second wave to hydrogen ion reduction on the arsenated steel surface. A possible and probable additional reaction to the second wave is the further reduction of arsenic to arsine or another hydride, this occurring at the most active potentials.

The relationship between the arsenite concentration and the apparent limiting current density that obtains in the potential region where arsenite-to-arsenic reduction predominates is not the one observed for concentration polarization; that is, the limiting current density is proportional to the concentration (activity) of the species in question. In this investigation the higher the arsenite concentration, the lower the apparent limiting current density and the more sharply defined it is.

Arsenic, as it is initially deposited, has an amorphous, vitreous structure with a high resistivity that partially insulates the metal underneath; the resistivity of this deposit was estimated at 10^8 Ω-cm. By continued electrolysis this arsenic deposit takes on a crystalline charcter. Electron diffraction patterns (extraction replicas) confirmed the presence of amorphous and crystalline As.

The hydrogen evolution reaction on the now arsenated surface is suppressed and the slope (de/d log i) is lower than that for hydrogen evolution in acid alone. Comparison with Figs. 68 and 69 show that the permection efficiency maximum occurs at more active potentials as the arsenite concentration increases. The hydrogen reaction is suppressed until the arsenite-to-arsenic reaction occurs, which is the case of the acetate solution (Fig. 69) containing 9 μg As/mℓ in the region -700 to -900 mV (SCE). Once the potential is achieved at which hydrogen-ion reduction predominates, the kinetics of the hydrogen reaction are changed by comparison with the acid-only case. The smaller slope (Fig. 73) in the Tafel region of hydrogen ion reduction in arsenite-containing solutions is characteristic of a system where the recombination is the overall rate controlling step. At room temperature and assuming a symmetry coefficient of 0.5, the slope of the hydrogen ion reduction polarization curve is 30 mV/decade if the recombination step controls and 120 mV/decade if the discharge step controls. These slopes are for activation kinetics only. In this investigation it was not possible to eliminate concentration and resistance polarization effects because a static electrode with solution agitation was used and the pH of the acetate solutions was high (4.5). The suppression of the hydrogen reaction to more active potentials is explained by noting that the exchange current density for the reaction on an iron surface is of the order 10^{-7} A/cm^2 while on an arsenic surface it is of the order 10^{-12} A/cm^2 in very acid solutions.[39]

A further example of the suppression of the over-all kinetics in arsenite-acetate solutions is shown in Fig. 74. The steel sample was held at -900 mV (SCE) in acetate solution and the current density decreased with time. When sodium arsenite was added at t = 100 sec., there was a sharp increase in the current followed by an even sharper decrease in the current. The current maximum is the super positioning of the arsenic reaction on the hydrogen reaction. However, the very limited amount of arsenite in the solution causes the onset of concentration polarization, and the arsenic deposits themselves on the surface impede the hydrogen reaction; thus there is the sharp decrease in the current. The result shown in Fig. 74 is the same as going from Curve A to Curve F in Fig. 73 at -900 mV (SCE).

The oxygen content of the solutions was determined by the Winkler method (thiosulfate titration, determination of end point with iodine). This was found to be 0.43 ppm O_2.

e. Significance of Polarization and Permeation Work

The significance of this argument is that potentiostatic and galvanostatic control of the hydrogen reaction can lead to quite different conclusions. Many investigators[38, 40, 41, 42] have charged their specimens galvanostatically and have measured either the hydrogen permeability by the permeation current technique, determined the hydrogen content analytically, or have measured some physical property while charging, as the expansion of the sample due to hydrogen absorption. All of these methods have shown the hydrogen uptake in the metal increasing with arsenite concentration in the charging solution until some critical concentration is reached, beyond which the hydrogen uptake is constant despite an increasing arsenite concentration. This critical concentration is of the order 1-5 μg As/mℓ.

By potentiostatic control of the charging reaction the permeation can be increased or discreased by arsenite additions. Referring again to Fig. 66 at -700 mV (SCE) the permeation is decreased by adding arsenite (compare curve 1 with curves 2 and 3). At -800 mV (SCE) the permeation can be decreased by adding arsenite at a concentration of 9 μg As/mℓ. At -850 mV (SCE) the permeation is increased by adding arsenite at a concentration of 0.9 μg As/mℓ, but is decreased by adding the arsenite at a concentration of 9 μg As/mℓ etc. The plot of permeation efficiency vs. potential, shown in Fig. 69 illustrates this point even more effectively.

f. Trapping Effects

Hydrogen moving through interstitial sites in the lattice has a high diffusivity even at room temperature because the activation energy for this movement is about 2 kcal/mole. Defects in the lattice decrease the hydrogen diffusivity, whereas these defects are usually regarded as high diffusivity paths for substitutional species. These defects are called "traps." Comparison of high- and low-temperature

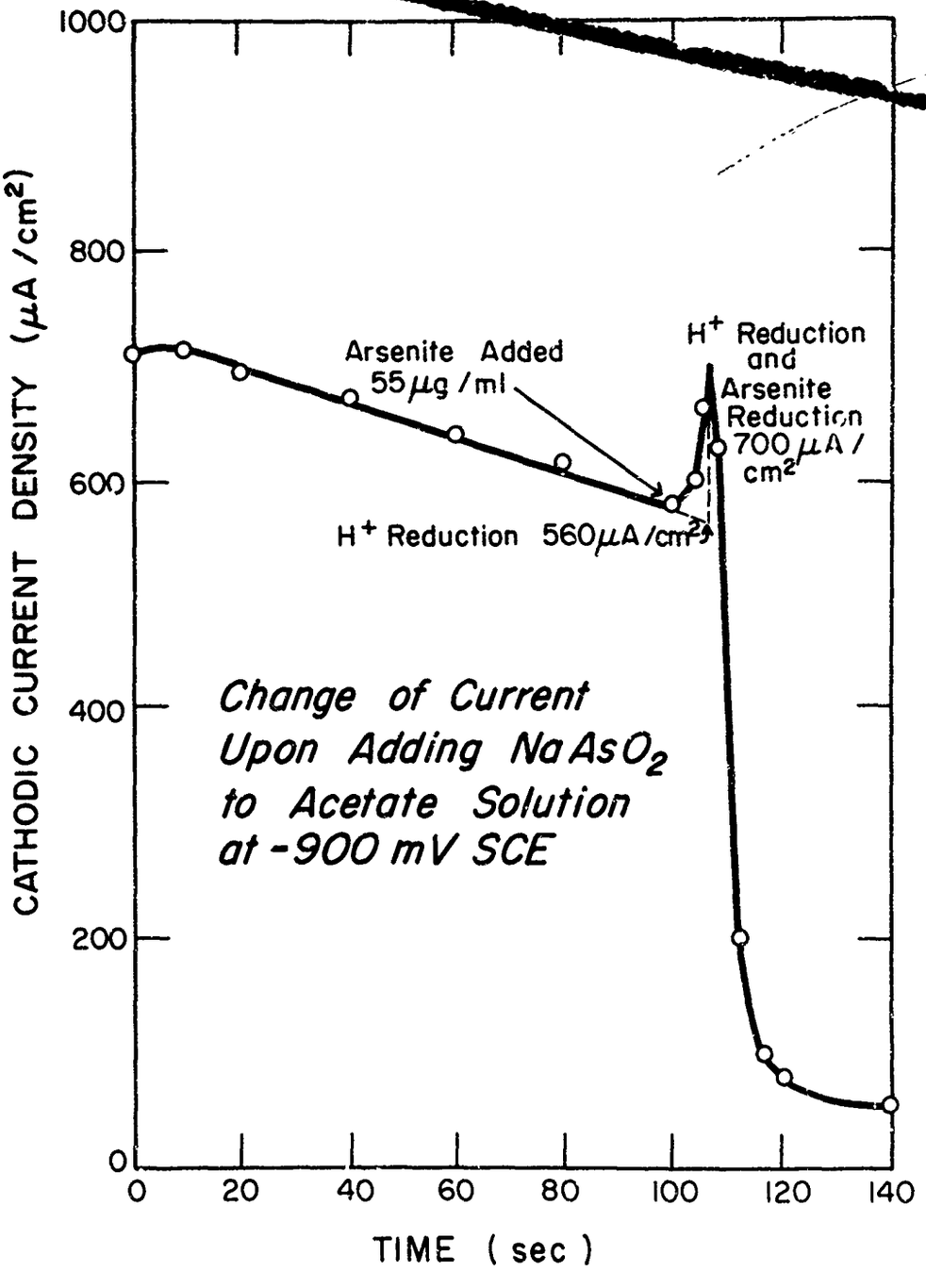

Fig. 74 - Change of Current upon Adding Arsenite to Acetate Solution at Constant Potential

diffusion data show that the mode of transport is through the lattice at high temperatures (above about 200°C) but that the hydrogen tends to associate itself with defects at lower temperatures. The activation energy for the movement through the defects is 6-9 kcal/mole. Because of the high fugacity of electrolytically discharged atomic hydrogen, all accommodating lattice sites are filled and excess hydrogen lodges in the vicinity of defects (vacancies, stacking faults, dislocations, interfaces). The extrapolated lattice diffusion coefficient for α-Fe at room temperature is of the magnitude 10^{-5} cm^2/s; this value has been corroborated by room temperature internal friction measurements and by electrolytic-charging permeation methods under certain circumstances. The diffusivity which is often calculated from room temperature permeation studies is, therefore, an "apparent diffusivity" when there is trapping in a defected region. The "apparent diffusivity" is always less than the "true diffusivity" associated only with movement through the perfect lattice.

There are at least two kinds of trap.[43] The first kind does not retain the hydrogen permanently but slows down its passage. The second kind causes molecularization of the atomic hydrogen and this hydrogen is extremely slow at room temperatures. The activation energy of the first kind of trapped hydrogen is perhaps approximately 16 kcal/mole.[44]

In Fig. 63 the initial transient shows a lower apparent diffusivity than subsequent ones. (The time to reach steady state is inversely proportional to the diffusivity.) This is an example of the first kind of trapping effects. At several charging conditions in which the permeation current reaches a maximum and then drops off sharply with time is regarded as the second, or permanent, type of trapping.[45]

3. Experiments with Iron and Iron-Copper Alloys

A recent paper[44] has shown that interfaces are the most important sites for trapping hydrogen. This trapped hydrogen need not be held permanently in the metal; it is more likely that the hydrogen atom is slowed down in its passage through the defects. The apparent diffusivity calculated from permeation transients is of the order 10^{-6} cm^2/s for single pass zone-refined iron (80 ppm total impurities) and 10^{-8} cm^2/s for 1010 steel. Both materials had the same grain size (annealed at 650°C for two hours before the permeation test) so that the only major difference was the carbide precipitation (pearlite colonies) in the steel. This second phase is, therefore, responsible for the lower diffusivity. The iron-copper system was selected for study[42,46] because the system is precipitation hardenable and the particles can be grown by aging. At room temperature the terminal solubilities of copper in iron and iron in copper are very small. The iron and copper atoms are of comparable size but the metals are of different crystal structures. Because of this mismatch the precipitates tend to be incoherent with the matrix.

For this investigation the Fe-1% Cu alloy was solution treated at 840°C for 93 hours for homogenization. This temperature is above the solvus line but below the $\alpha \rightarrow \gamma$ transformation temperature. The alloy samples encapsulated in argon-filled quartz cylinders to minimize oxidation were quenched in water, then aged at 500 and 700°C to precipitate the copper phase. Hardness measurements for these conditions were made and are shown in Fig. 75. Sample thickness was 10 mils.

The specimens were hydrogen charged from acetate buffer solutions (pH 4.5) containing arsenite (0.9 μg As/mℓ). The permeation transients of some of the specimens charged at -900 mV(SCE) and -1000 mV, (SCE) are shown in Figs. 76 and 77, respectively. These results are summarized in Table VII, along with some others.

These data show that the tendency for trapping occurs as the aging time increases and as the charging conditions become more severe (more active charging potential). In addition, the type of trapping [illegible] temporary to permanent (tendency toward anomalous behavior) as the aging time [illegible] given charging potential. The apparent diffusivity decreases generally with the aging [illegible] shown in Table VII. In all cases, some degree of trapping is presumed because single pass zone refined iron charged under the conditions of -800 mV(SCE) yielded an apparent diffusivity of 3×10^{-6} cm^2/s, well below the 10^{-5} cm^2/s value for lattice diffusion. Permeation measurements alone are not sufficient evidence that hydrogen entry is responsible for susceptibility to embrittlement. Either solubility or diffusivity must be determined in addition to the permeability. Although the susceptibility to hydrogen cracking in a Ni-Cr-Mo high-strength steel increases with the yield strength, the steady-state hydrogen permeability is nearly the same regardless of the heat treatment. The time required to come to steady state increases as the yield strength increases. Since the diffusivity is inversely proportional to the lag time, it decreases with increasing yield strength. Since the deviation of the apparent diffusivity from the true lattice diffusivity is a measure of the extent of trapping, it is the degree of trapping that is the critical diagnosis.

The most significant change occurs upon initial aging of the solution treated metal. For moderate charging conditions (-800 and -900 mV) the solution-treated metal has high permeability and diffusivity. The diffusivity decreases generally with aging time. At more severe charging conditions the permeation response generally shows a sharp maximum followed by a decrease. The diffusivity cannot be determined for this type of behavior since there is no steady state region. The rise and fall is believed to be caused by recombination of trapped hydrogen atoms on internal surfaces. These specimens showed blistered and plastically deformed areas.

Although there is scatter of the diffusivity and solubility data, the solubility of hydrogen in the metal in the aged condition is larger than in the solution-treated condition. It would appear that the interface around the copper precipitates and the precipitates themselves

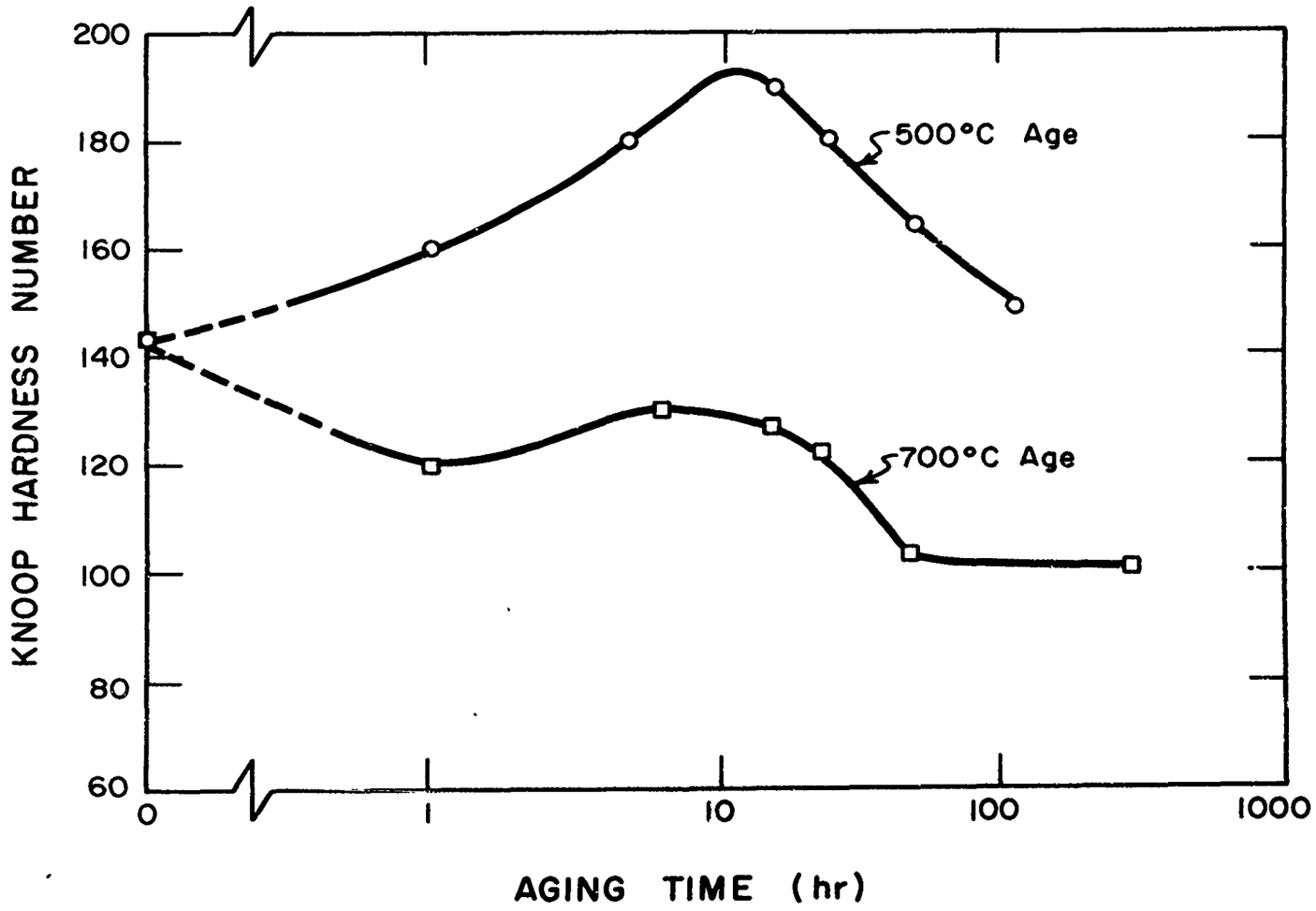

Fig. 75 - Microhardness of Aged Iron-1% Copper Alloy Specimens

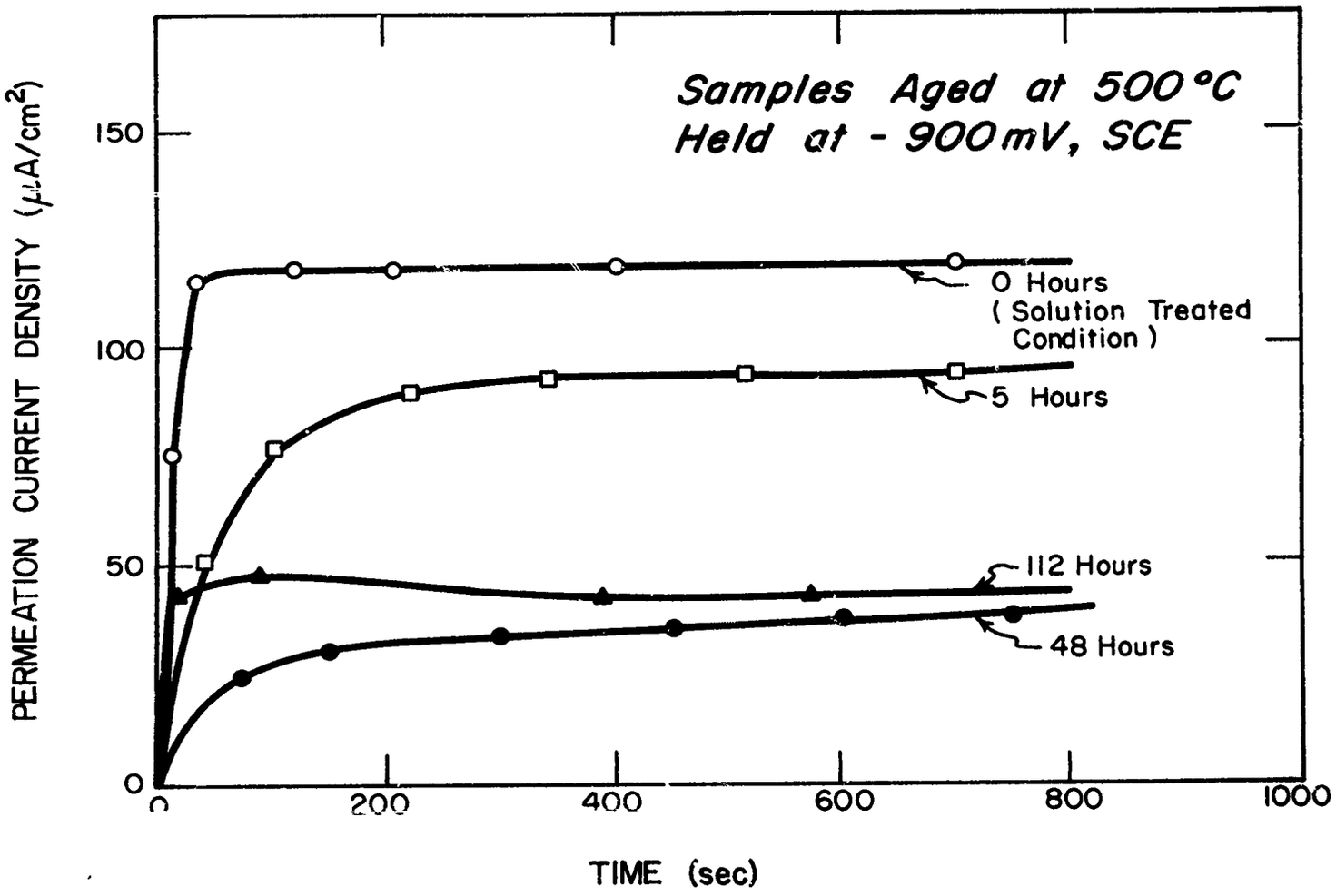

Fig. 76 - Hydrogen Permeation Rise Transients for Fe-1% Cu Alloy Specimens Aged at 500°C for Various Times. Conditions: Charging Potential, -900 mV SCE; Charging Solution, Acetate Buffer plus Arsenite (0.9 μg As/ml); Specimen Thickness, 10 mils, Palladized at Exit Surface; Exit Solution, 0.1N NaOH

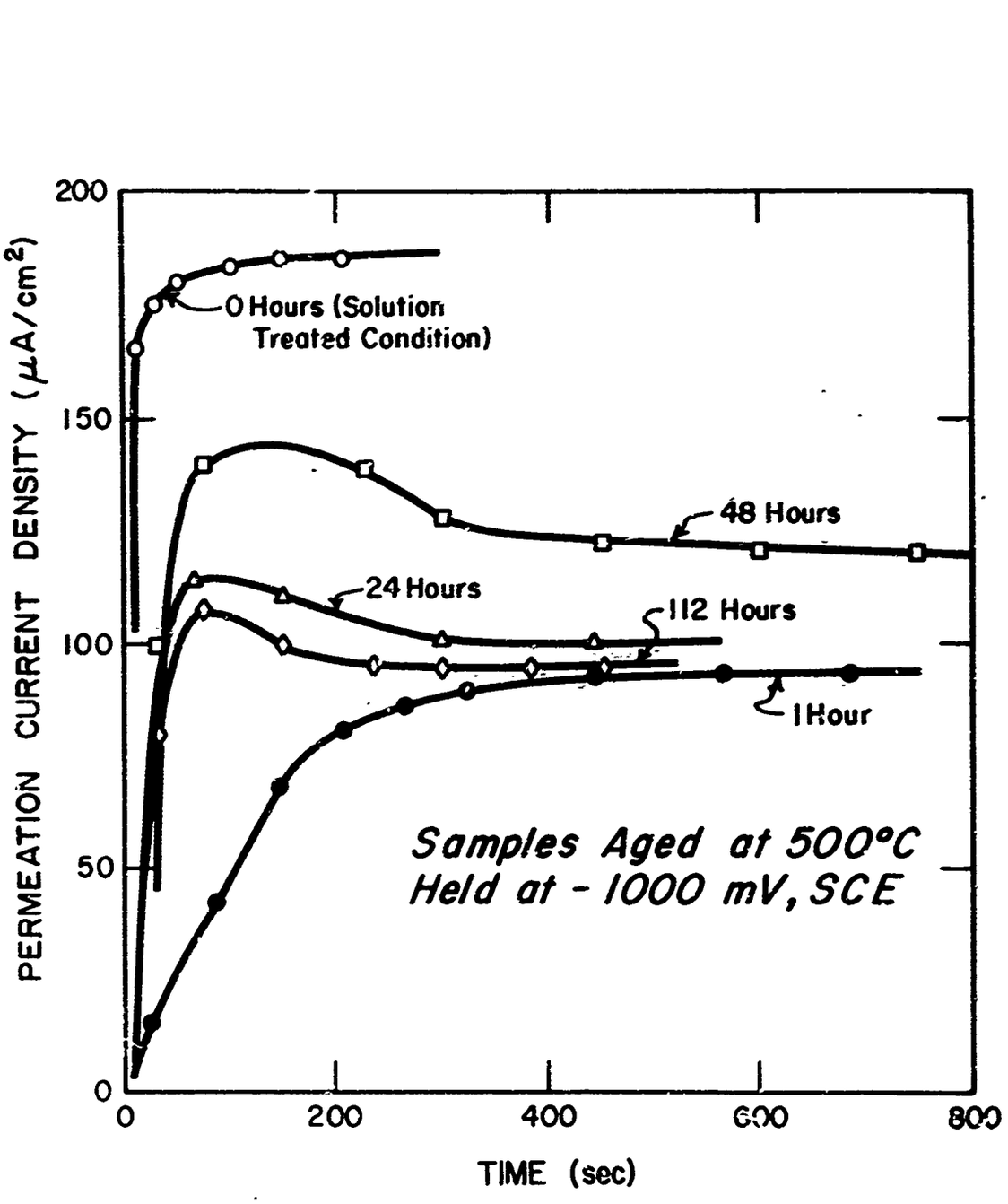

Fig. 77 - Hydrogen Permeation Rise Transients for Fe-1% Cu Alloy Specimens Aged at 500°C for Various Times. Conditions: Charging Potential, -1000 mV SCE; Charging Solution, Acetate Buffer plus Arsenite (0.9 μg As/ml); Specimen Thickness, 10 mils, Palladized at Exit Surface; Exit Solution, 0.1N NaOH

Table VII - Calculation of Hydrogen Diffusivities and Saturation Solubilities for Fe-Cu Alloy Aged for Different Times

Aging Condition (°C)	Time (hr)	Charging Condition mV(SCE)	Steady State Permeation Current Density ($\mu A/cm^2$)	Calculated Diffusivity ($cm^2/s \times 10^{-7}$)	Saturation of Hydrogen ($mole/cm^3 \times 10^{-6}$)	Charging Condition mV(SCE)	Steady State Permeation Current Density ($\mu A/cm^2$)	Calculated Diffusivity ($cm^2/s \times 10^{-7}$)	Saturation of Hydrogen ($mole/cm^3 \times 10^{-6}$)
Solution treated		-800	34	8.75	9.9	-900	138	19.4	176
500	1	-800	7	6.7	26				
500	3	-800	10.5	9.48	49	-900	98	5.65	43
500	16	-800	2.5	3.0	12.7				
500	24	-800	9	4.87	33.6				
500	48	-800	4.5	3.9	29.4	-900	36	2.98	114
500	112	-800	9.9	5.0	15.8	-900	47	1.46	820
700	1	-800	16.5	25	16.7				
700	3	-800	8	9.3	98.2				
700	16	-800	1	5.84	4.0	-900	23	1.84	118
700	24	-800	2	5.47	9.1	-900	93	1.75	1370
700	50	-800	6	9.0	32.	-900	41	4.86	475
700	100	-800	12	3.14	97.	-900	72	3.0	420
700	280	-800	16	3.5	119.	-900	86	1.17	1870

dissolve considerable hydrogen. Metallographic examination (transmission electron microscopy) showed that copper precipitates were visible after one hour aging at 500°C and that there was some growth and clustering of these precipitates at longer times and higher temperatures. As with the permeation data, the most noticeable change occurred between the solution-treated condition and the first aged condition.

D. ANALYSIS OF ACOUSTIC EMISSION
(K. Graff and B. Dettloff)*

1. Aims and Significance of Work

Cracks which propagate in high strength steels emit elastic waves which can be detected by acoustical techniques. The energy emitted is related to the release of elastic energy when the crack advances in each increment. Work by various investigators to date has measured only the frequency of these emissions. The results therefrom have been most illuminating but these measurements are not definitive with respect to the processes which produce the emissions. Since the further analysis of these acoustical emissions appears to offer substantial promise of further illuminating the complexities of crack advance, this present effort has been organized to define the nature of the acoustical emission process. Both the theory and methods of emission are being considered.

Various investigators have established the relationship between acoustic phenomena generated in these specimens and the deformation of the specimen for a number of materials. These acoustic emissions can be generally divided into low energy and high energy emissions. Low energy emissions are generally connected with plastic strains and their signal levels at the point of generation have been estimated at about 1000 eV. High energy emissions seem to emanate from cracks during their formation in the bulk of the specimen or in coatings on various surfaces of the specimen, and their signal level has been estimated at about 1 erg. These estimates seem rather vague since they do not take into consideration the various modes of acoustic energy transmission. Moreover, when comparisons were made to signal levels produced by a transmitting acoustic transducer it was probably neglected that the transducer acted like a piston and emitted in a concentrated beam while the actual acoustic source approaches a point source and radiates in all directions.

More recent work in this field is concerned with relating these acoustic emissions with the various actual occurrences. One such attempt is made in trying to follow the progress of a crack in high

*The Ohio State University Department of Engineering Mechanics. This work is a joint effort of the Departments of Metallurgical Engineering and Engineering Mechanics.

strength steel during corrosion cracking. It is desired to extract from the acoustic signal such information as the incremental step size of the advancing crack and the surface energy of the new surface.

It appears that all workers in this field so far have been concerned with showing a certain relationship between the advancing crack and a count generated by the acoustic signal regardless of reflections of the acoustic signal in the test specimen or other reverberations. Thus, it seems that any quantitative data obtained for this type of experiment may be grossly inaccurate.

Some investigators working with low energy acoustic emissions have worked with signal levels close to the absolute signal-noise threshold where it was necessary to resort to such techniques as using resonant transducers. Unfortunately, other researchers working with the high energy emissions seem to have accepted the same techniques. This is not necessary in view of signal levels several orders of magnitude stronger. To obtain a one-to-one correspondence between events in the test specimen and counts electronically sensed it is imperative that multipath signals or reverberations are eliminated, either mechanically, through proper placement of the receiving transducer and dampening, or electronically, such as through the use of correlation techniques. It may also be possible to determine the frequency spectrum or the actual wave shape of the original signal with proper choice of transducers and the application of wide band techniques.

The following section describes initial work to gain insight into the physics of relatively weak acoustic signals, in particular, to find the transducer best suited for the signal considered, to determine the effects of test specimen geometry on the transmission of the signal so that placing of the transducer can be optimized, and to build devices capable of simulating the actual acoustic source in size and emitted signal for calibration.

2. Experiments and Results

a. Signal Source Simulation

All work to date has been concerned with the evaluation of transducer response to highly transient signals. Therefore a reasonably reliable source of acoustic pulses of relatively low energy was needed. Periodicity of this source seemed highly desirable to facilitate the display on the oscilloscope of the transducer output. Efforts were directed toward building devices capable of generating shorter and shorter pulses of low magnitude in a predictable manner. To gain a perspective in terms of more tenable quantities it should be visualized that 1 erg is approximately the kinetic energy in a 10 mg mass dropped through 1 mm. But since only 15% of the kinetic energy in a steel ball

during elastic impact on a steel surface is converted to acoustic energy, the above steel ball would deliver 0.15 erg. On the other hand, a 1/16-inch steel ball (16.4 mg) impacting elastically a steel surface delivers a pulse about 4 μs long and of approximately Gaussian shape. Smaller balls generate shorter pulses.

Initially these tapping devices were built on a solenoid principle, see Fig. 78, but residual magnetism and the steel test specimen made operation impossible when balls were made smaller. Therefore, a different tapper was built with the output of a loud speaker funneled through a pipette driving the miniature balls by the oscillation of the air, see Fig. 79. Both types were powered by the output from an audio-amplifier driven by an oscillator. The smallest and shortest signal generated in this manner employed a steel ball approximately 15 mil in diameter. This ball weighed about 1/4 mg and generated a pulse duration of about 1 μs.

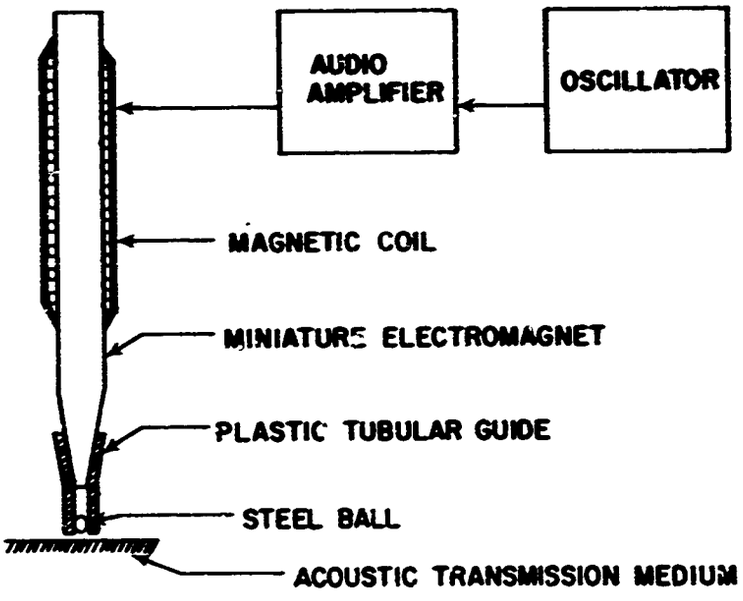

Fig. 78 - Schematic of Miniature Electromagnetic Tapper

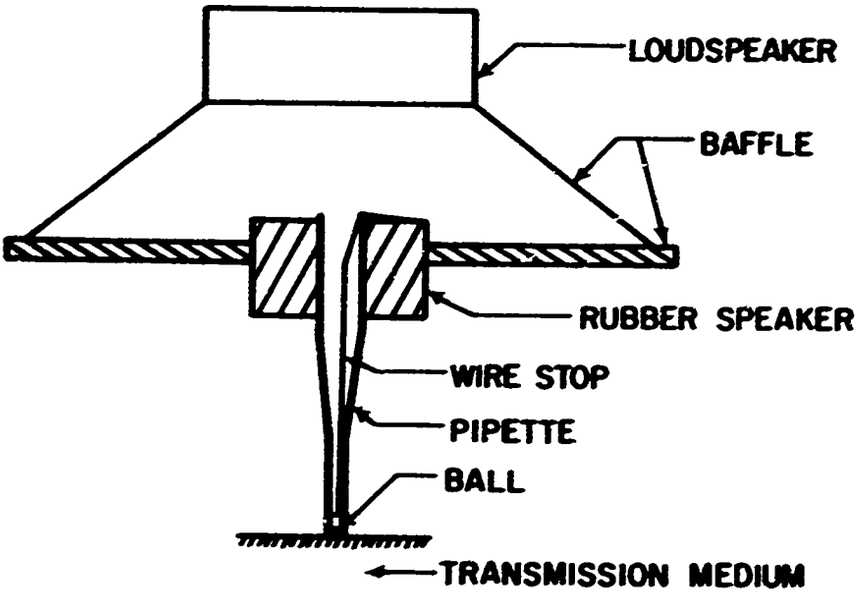

Fig. 79 - Miniature Tapper Using the Vibrations of a Loudspeaker

b. Transducers

During the whole investigation signals of undetermined origins appeared on the screen of the oscilloscope. To eliminate the possibility of transducer-generated additions to the output an attempt was made to use transducers of higher resonance frequency and lower Q.

Initial tests were run with a B & K 4331 accelerometer. Its nominal resonance frequency is 43 kHz. The signal spectrum received was generally well above this frequency so that the output must have been considerably distorted.

Disk-type piezoelectric transducers were obtained, 47 mil and 10.5 mil thick, with corresponding thickness resonance of 1.8 MHz and 8 MHz, respectively. The material is probably barium titanate with silver electrodes on both faces. Initially, these disk-shaped transducers were used in their original configuration, but attachment of leads became a problem, overhang because of size and/or for lead attachment could have caused flexural excitation of the disks, and dampening to lower their Q seemed desirable. Therefore, two transducers were constructed, one of each thickness. The ground was brought to the back face by plating the ceramic disk around its edge and the whole back potted in silicone rubber for dampening, see Fig. 80. The final nominal dimensions of the active transducer are 1/2" x 0.047" and 1/4" x 0.010".

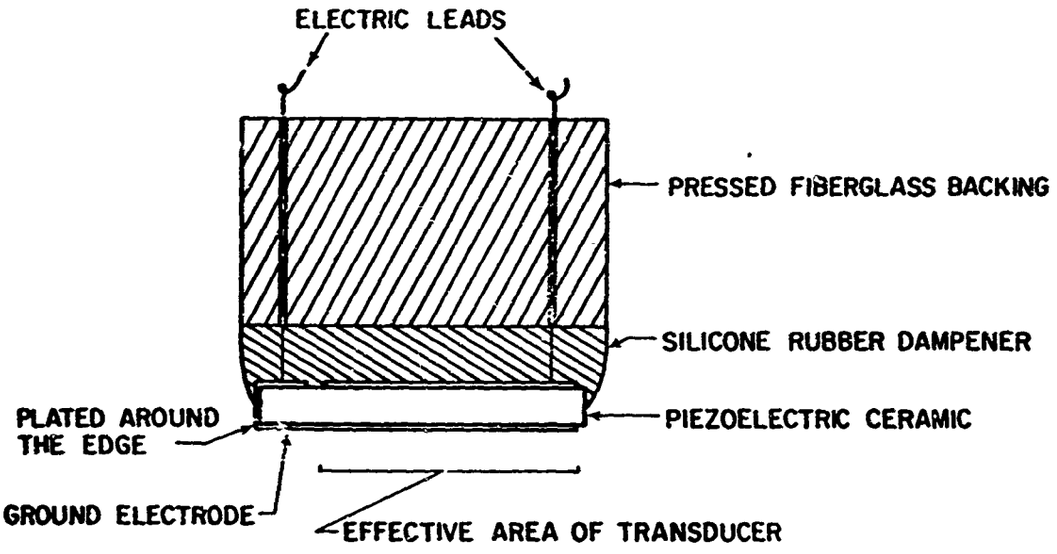

Fig. 80 - Construction Details of Transducers

Initial tests were run on a steel bar 1" diameter x 72". Figure 81 shows the dispersion of the signal after one length of the bar. This signal originated on the far end of the bar by impact of a 1/16" diameter steel ball falling from a height of 1 mm. The transducer was a B & K 4331 accelerometer whose output is amplified by a B & K charge amplifier, then a Keithley 103 amplifier, before display on the scope. This is actually a time exposure of some 140 traces. Figure 82 shows the same signal as received by a 10-mil piezoelectric disk. Most of the signal could be made visible only through a photographic time integration, otherwise it would disappear in the noise. As part of this experiment it was determined that the signal spectrum is affected by the duration of the input pulse--a longer duration pulse produces a lower frequency output spectrum.

A second series of tests were conducted on a steel block 3 3/4" x 5" x 8", the signal being introduced at the center of one 5" x 8" face and sent through the 3-3/4" depth to a 47-mil thick transducer. This experiment was meant to give the actual wave shape of the signal introduced since the dilatational wave is nondispersive and the next fastest path should have delayed the signal enought to separate the first and the second arrival by about 8 μs. But a continuous train of signals was obtained and the reason for this discrepancy has not been determined as yet.

The response of the 47-mil transducer was isolated next by introducing an electronically generated pulse using the 10-mil transducer. It seems fairly certain that the signal represents the ringing of the 47-mil transducer at its own resonance frequency of 1.8 MHz the oscillation dying out rapidly since the transducer is dampened, see Fig. 83. The impact pulse can practically be considered a step wave.

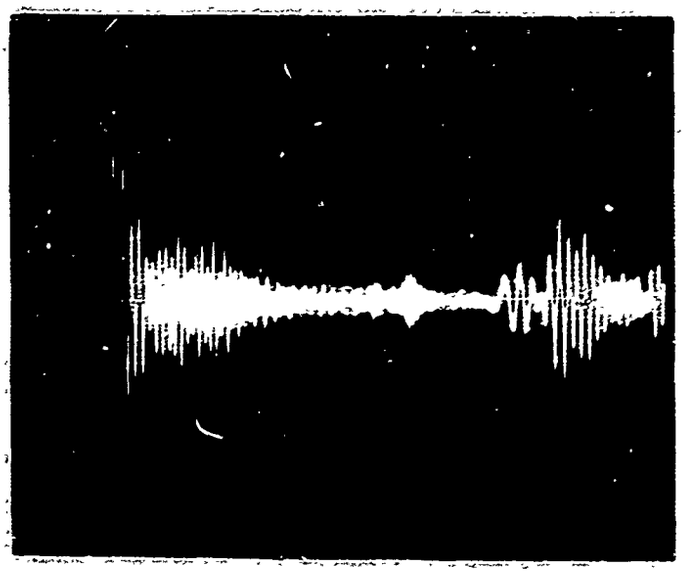

Fig. 81 - Signal Dispersions in a Long Rod Detected by an Accelerometer. Sweep - 0.1 ms/cm; Vertical Sensitivity - 2 V/cm. Note: 6.6 cm from start of trace is first echo

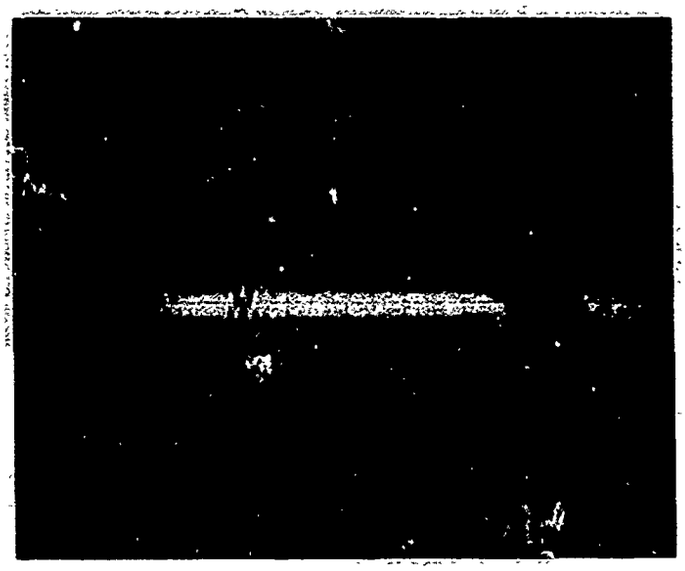

Fig. 82 - Signal Dispersion in a Long Rod Detected by a Thin Disk Type Transducer. Sweep: 0.1 ms/cm, Vertical Sensitivity: 0.05 V/cm

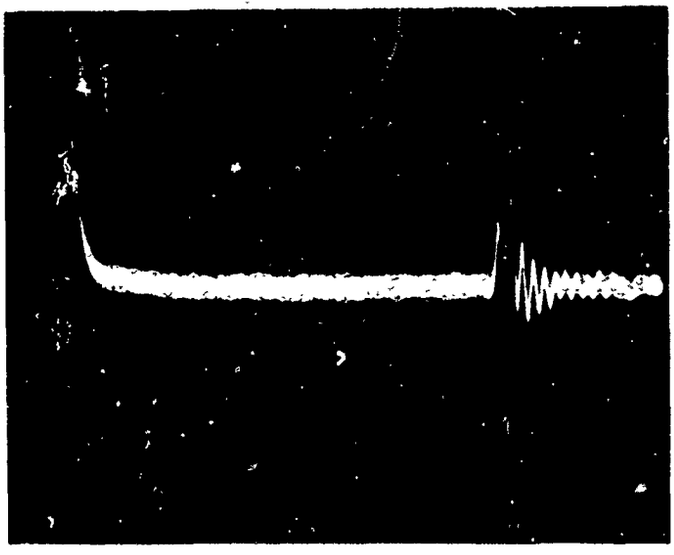

Fig. 83 - Oscillations in a Dampened 47-mil Thick Receiver Caused by a Step Wave. Sweep: 2.8 μs/cm; Vertical Sensitivity: 0.1 mV/cm

The 47-mil and the 10-mil transducers were placed face to face with a 3-mil steel sheet between them for electrical shielding. Two frequencies were excited on the receiver on pulse and step excitation regardless of which transducer was the transmitter. One of the frequencies was an expected 1.67 MHz while the other at 15.5 MHz has not been explained. There exists the possibility that the oscilloscope may have gone into parasitic oscillations.

3. Discussions

No final answers have been discovered to the questions raised at the beginning of the investigation. The main reason is probably that the propagation of the acoustic signal has not been analyzed correctly.

Separating the initial undisturbed signal from the following train of multipath signals has presented unexpected difficulties. It appears also that some electronically generated oscillation may have occurred originating possibly in the oscilloscope.

As a result the question of placement of the transducer has not been resolved. The idea of placing the transducer as close as possible to the source is being favored. This will reduce spectral dispersions of the signal and will permit reception of the strongest possible signal relative to multipath signals.

The choice of piezoelectric transducer depends largely on the signal to be received. No decision has been reached on which signal mode will be best suited for reception or if the best choice of transducer is one with very high resonance frequency, i.e., approaching a film type transducer, or if a very thick transducer will give better results.

However, one intermediate result is encouraging; it has been experienced that acoustic signal levels of 1 erg are fairly easy to handle. Nevertheless, every experimental setup seems to have its own peculiar problem since operations are generally conducted at the limits of performance for some component in the system.

E. DISSOLUTION OF IRON CARBIDE AND SOME OTHER TRANSITION METAL CARBIDES

(J. Payer)

1. Aims and Significance

Iron carbide and alloy carbides are important constituents of high-strength steels. The corrosion behavior of an alloy can be greatly affected by the dissolution behavior of the carbides present. The purpose of this investigation is to define the reaction kinetics of carbide dissolution. An understanding of these dissolution processes will be

used to determine in what way and to what extent carbides take part in the stress-corrosion cracking of high-strength steels.

Iron carbide alloys containing various amounts of cementite (Fe_3C) are exposed at constant potential to aqueous environments. The products of carbide dissolution are quantitatively determined using gas chromatography. The polarization behavior of some other transition-metal carbides is also determined.

2. Experimental

a. Characterization of Materials

(1) Iron-Carbon Alloys

Three Fe-C alloys have been cast; i.e., a 0.8 wt% C (eutectoid) alloy, a 2.0 wt% C alloy, and a 4.3 wt% C (eutectic) alloy. The as-cast 0.8 wt% C and 2.0 wt% C alloys were solution-treated at 815°C for 25 minutes and then held at 650°C for 50 hours. The 4.3 wt% C alloy was solution-treated at 815° for 20 minutes and then held at 650° for 20 hours. A molten salt bath was used during heat treating in order to avoid oxidation of the specimens. Figures 84(a) and (b) are metallographs of the 0.8 wt% C alloy after heat treatment. In the structure the carbides are evenly distributed and roughly spherical in shape. Figures 85(a) and (b) are metallographs of the 2.0 wt% C alloy after heat treatment. The carbides in this structure are elongated as spherodization of the cementite lamellae is not complete. Figures 86(a) and (b) are metallographs of the 4.3 wt% C alloy after heat treatment. Cementite is the continuous phase in this alloy.

X-ray diffractometer scans of all the heat-treated alloys showed strong lines for both α-Fe and Fe_3C. No peaks for γ-Fe, Fe_2C, or graphite were observed.

(2) $Cr_{23}C_6$, VC, and TiC

The chromium carbide ($Cr_{23}C_6$) sample was prepared by induction melting, using conventional practices.* X-ray diffraction analyses indicate it is stoichiometric and no other carbides, nor elemental Cr, are present.

Single crystal samples of TiC and VC were prepared from sintered powder rods of 80-90% density by the floating zone technique.** The samples were subsequently annealed at 1800°C for 5 hours

*$Cr_{23}C_6$ provided by Dr. C. S. Tedmon of the General Electric Company Research & Development Center; Schenectady, N. Y.

**TiC and VC supplied by Dr. G. E. Hollox of Brown, Boveri and Company; Baden, Switzerland.

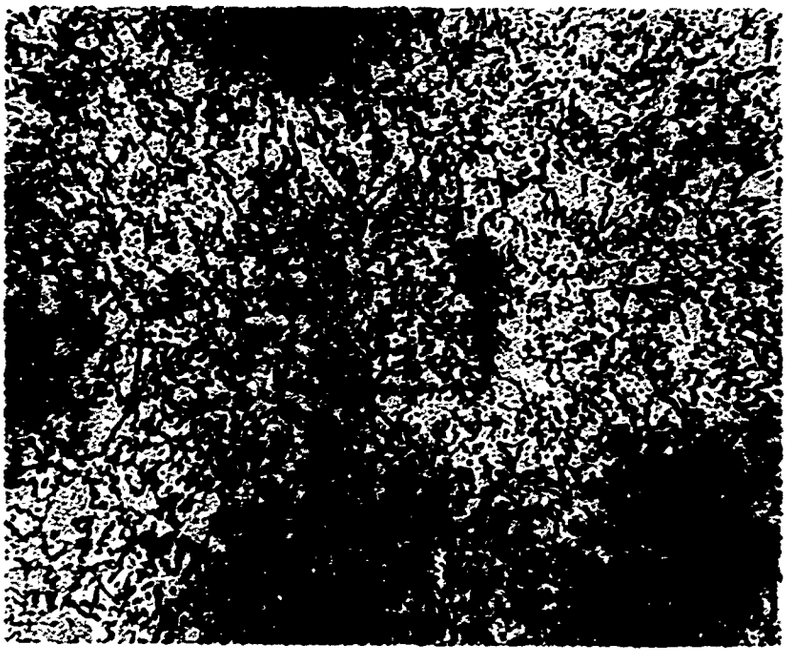

(a) 150X

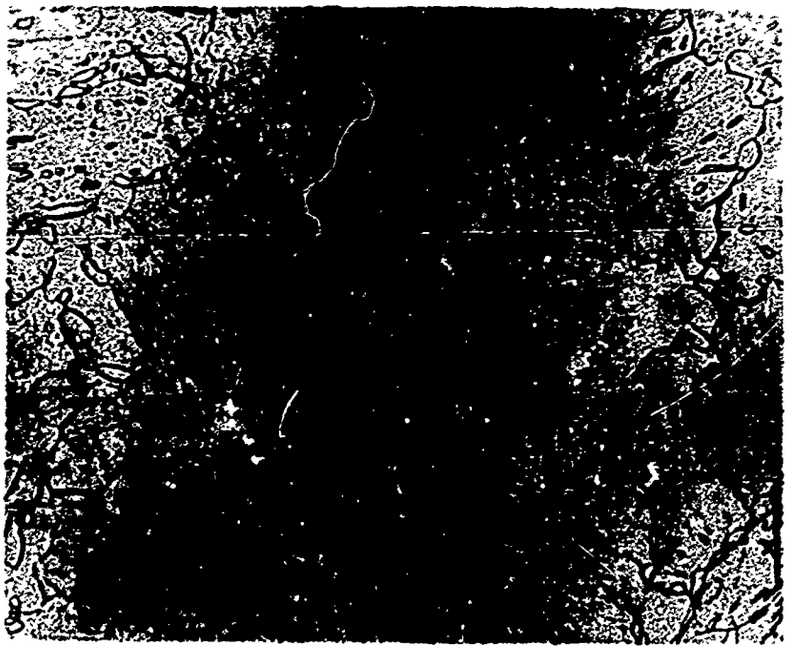

(b) 1000X

Fig. 84 - Carbide Morphology and Distribution in 0.8 C w/o Iron-Carbon Alloy (Heat Treatment - 815°C, 25 min and 650°C, 50 hr) 3% Nital Etch

150X (a)

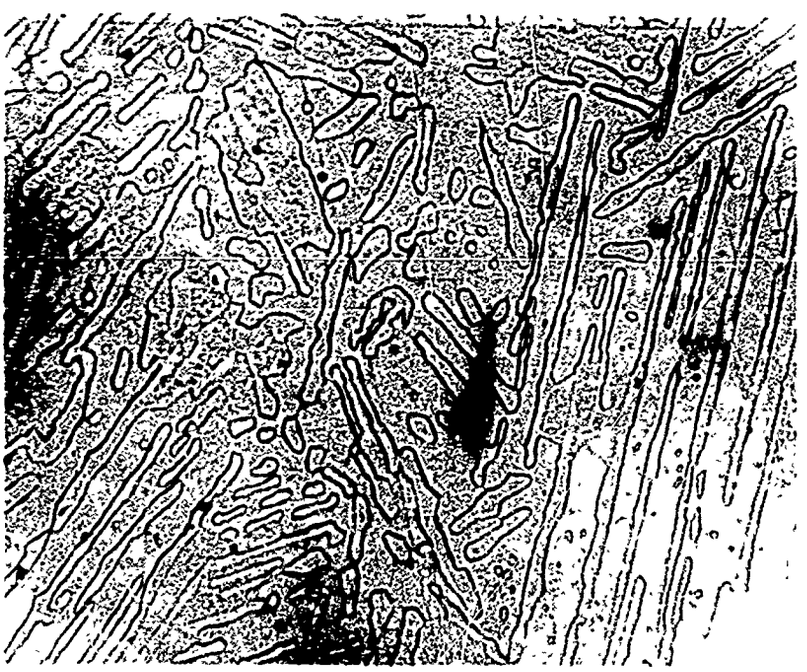

1000X (b)

Fig. 85 - Carbide Morphology and Distribution in 2.0 w/o C Iron-Carbon Alloy (Heat Treatment - 815°C, 25 min and 650°C, 50 hr) 3% Nital Etch

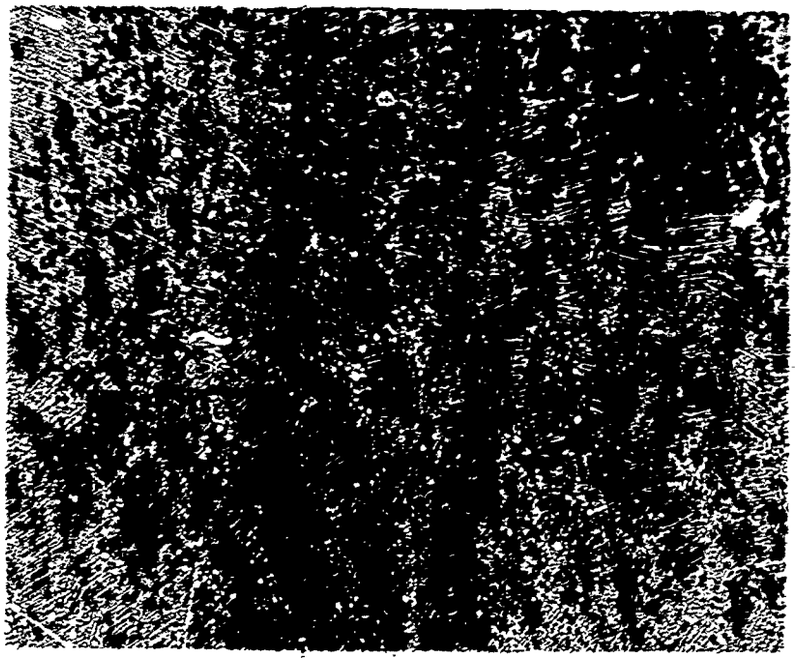

(a) 150X

(b) 1000X

Fig. 86 - Carbide Morphology and Distribution in 4.3 w/o C Iron-Carbon Alloy (Heat Treatment - 815°C, 20 min and 650°C, 20 hr) 3% Nital Etch

and furnace cooled. Chemical analyses indicates that the crystals contained approximately 0.01 w/o each of oxygen and nitrogen, and traces (< 0.1%) of metallic impurities such as Cr and Fe. The stoichiometry of the vanadium carbide is $VC_{0.85}$. The approximate size of each sample is 6 mm x 2 mm x 2 mm.

b. Description of Gas Chromatographic Technique to Analyze Gaseous Products of Carbide Dissolution

(1) Theory of Operation

Figure 87 is a schematic diagram of a gas chromatograph. A gas sample to be analyzed is inserted into the carrier gas stream. Separation of the sample into its constituents occurs as they progress at different rates along the column. If the temperature, carrier gas flow rate, and column substrate are correctly selected, each constituent occupies a space containing only carrier gas. Therefore the effluent from the column consists of a sequence of vapor pockets, each pocket consisting of a different constituent. The effluent passes through the sensing filaments of the dector, while the reference gas passes through the reference filaments

Detectors may be of several types; i.e., thermal conductivity, flame ionization, or electron capture. The operation of a thermal conductivity detector will be discussed here. The detector bridge circuits control the signal to the recorder. This signal is proportional to the difference in thermal conductivity of the gases in the sensing and reference chambers. The output is adjusted to give zero output when pure carrier gas is present in both compartments. The sensing and reference filaments form the four legs of the detector bridge. The presence of vapor, other than the carrier gas, in the sensing chamber alters the sensing filament electrical resistance, thus unbalancing the bridge and producing a difference in potential at the output terminals. For any concentration of vapor, the unbalance voltage is constant. The resulting chromatogram is interpreted quantitatively by comparing it with chromatograms of known samples. The constituents are identified by their characteristic retention times, while the amount present is determined by comparing the given area under a peak on the unkrown to the area for a known quantity. A typical chromatogram is shown in Fig. 88, where the potential difference between the sensing and reference filaments of the detector is plotted versus time after sample injection.

(2) Analysis of Carbon-Containing Species

This investigation requires analysis of the following constituents which may be products of carbide dissolution: H_2, O_2, CO, CO_2, CH_4, plus several higher hydrocarbons. The gases from nydrogen through methane are analyzed by using two columns in series.

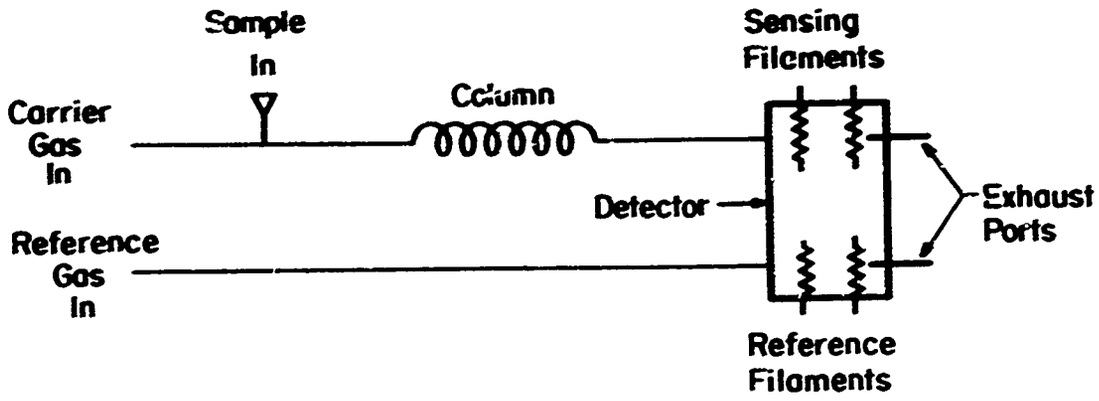

Fig. 87 - Schematic of Gas Chromatograph

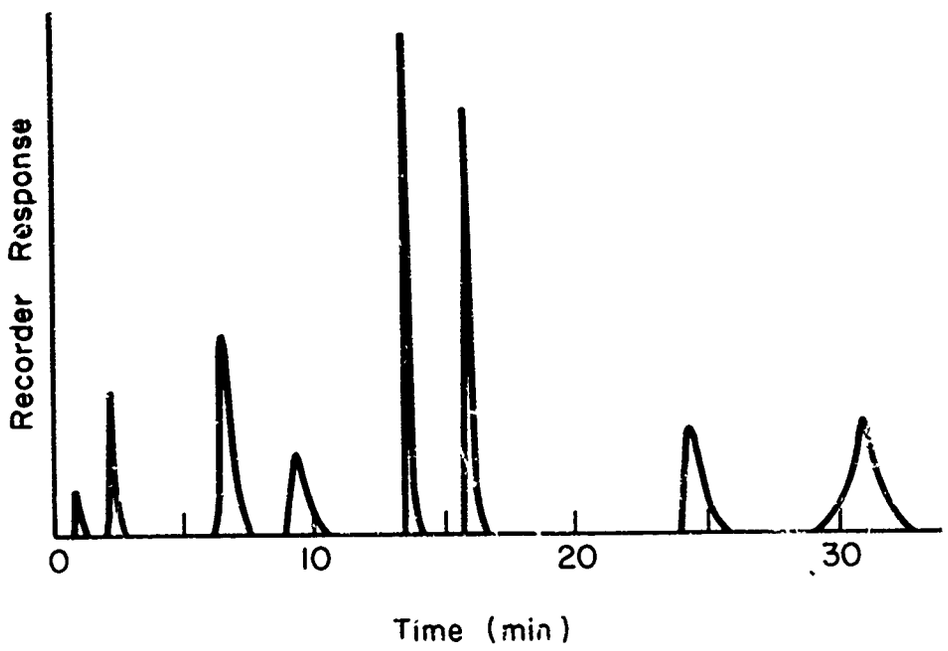

Fig. 88 - Typical Gas Chromatograph

A Por-A-Pak Q column is attached to the sensing side of the dectector and a 5 A Molecular Sieve column is attached between the sensing and reference sides of the detector. After sample injection all the gases except carbon dioxide are eluted through the Por-A-Pak and show up as a single composite peak on the recorder. The CO_2 is held up and appears as the next peak. Meanwhile, the other gases, such as O_2, CO, CH_4, are being separated in the Molecular Sieve column. As they are eluted into the detector they are sensed by the reference filaments and subsequently exhausted. The column lengths and operating parameters are chosen so that no peaks overlap. The carrier gas flows through the injector, into the Por-A-Pak column, then into the sensing side of the detector, through the molecular sieve, into the reference side of the detector, and finally, into the atmosphere. Figure 89 is a schematic of this column arrangement and a typical chromatogram from it.

The hydrocarbons higher than methane are analyzed using a 3% Squalane-97% Burell medium-activity silica gel column. This column will separate the following constituents: ethane, ethylene, n-propane, actelylene, n-butane, propylene, isopentane, n-pentane, and butene-1.

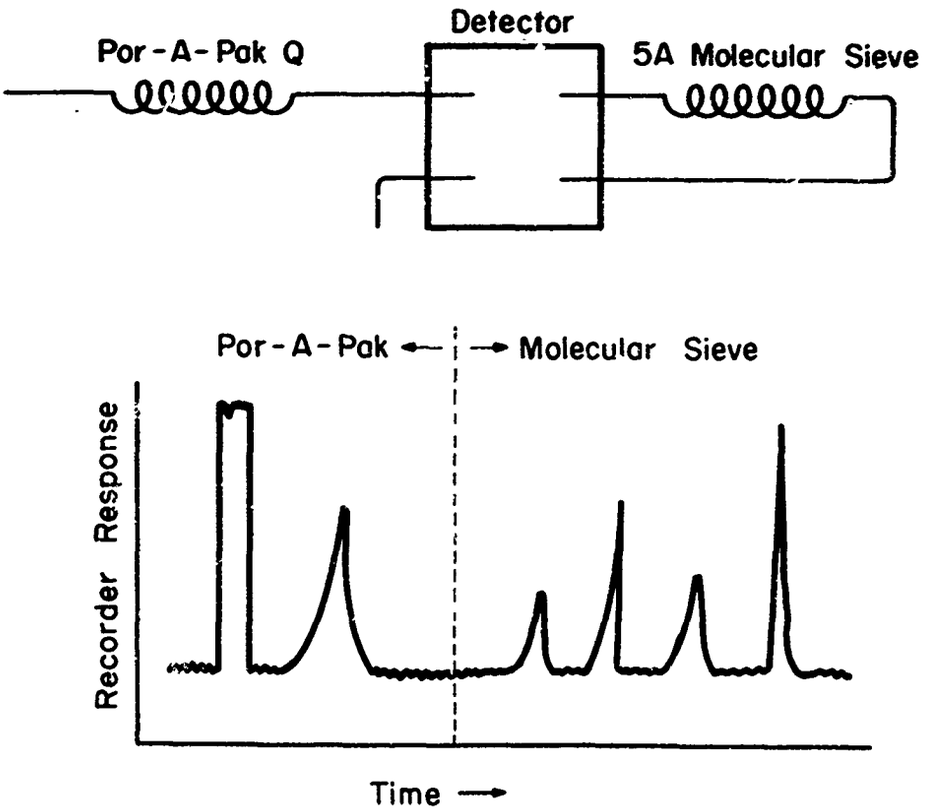

Fig. 89 - Two-Column Arrangement

c. Electrochemical Procedure

In order to better understand the general behavior of the sample materials, polarization curves are obtained by standard potentiodynamic techniques. Samples are exposed over a range of pH (pH 2—pH 6) and to environments containing either chloride or sulfate. All tests are run at 25°C. The solutions are deaerated before the test and stirred throughout the test.

Samples are exposed at constant potentials for various times. Subsequent to exposure the gas over the aqueous solution is analyzed for carbon products using gas chromatography.

3. Discussion

It has been reported earlier (AFML-TR-70-2), that the dissolution behavior of iron-iron carbide structures is a function of potential, pH, and anion. Figure 90 shows the modes of attack observed when thin foils of Fe-0.45 w/o C were exposed to various environments at constant potential. It is of interest to note that in many environments the carbide is quite reactive. While this is not unexpected, in lieu of thermodynamic predictions which show cementite to be unstable in aqueous environments at all values of potential and pH, it does contradict the prevalent notion that cementite is inert and will therefore act as a cathode in materials exposed to aqueous solutions. This work is aimed at better understanding the parameters which control carbide dissolution.

F. KINETICS OF GROWTH OF PASSIVE FILMS(K. N. Goswami)

1. Objective and Background

The objective of this study is to determine the growth kinetics of passive films on iron-base alloy surfaces. This work is directly relevant to the state of affairs immediately following the formation of fresh surfaces at a crack tip. The rate of formation of passive films affects the quantity of ions going into solution and also provides a barrier to the subsequent entry of hydrogen into the metal.

2. Experimental

The theory of ellipsometric measurement of kinetics of growth of passive films and the detailed experimental arrangement is reported in Technical Report AFML-69-16 and AFML-70-2. For the results described herein, a deaerated solution of 0.5M H_2SO_4 + 0.5N Na_2SO_4 + NaOH of pH 4 and 6 were used for the anodic passivation. The solution was kept under a stream of purified helium.

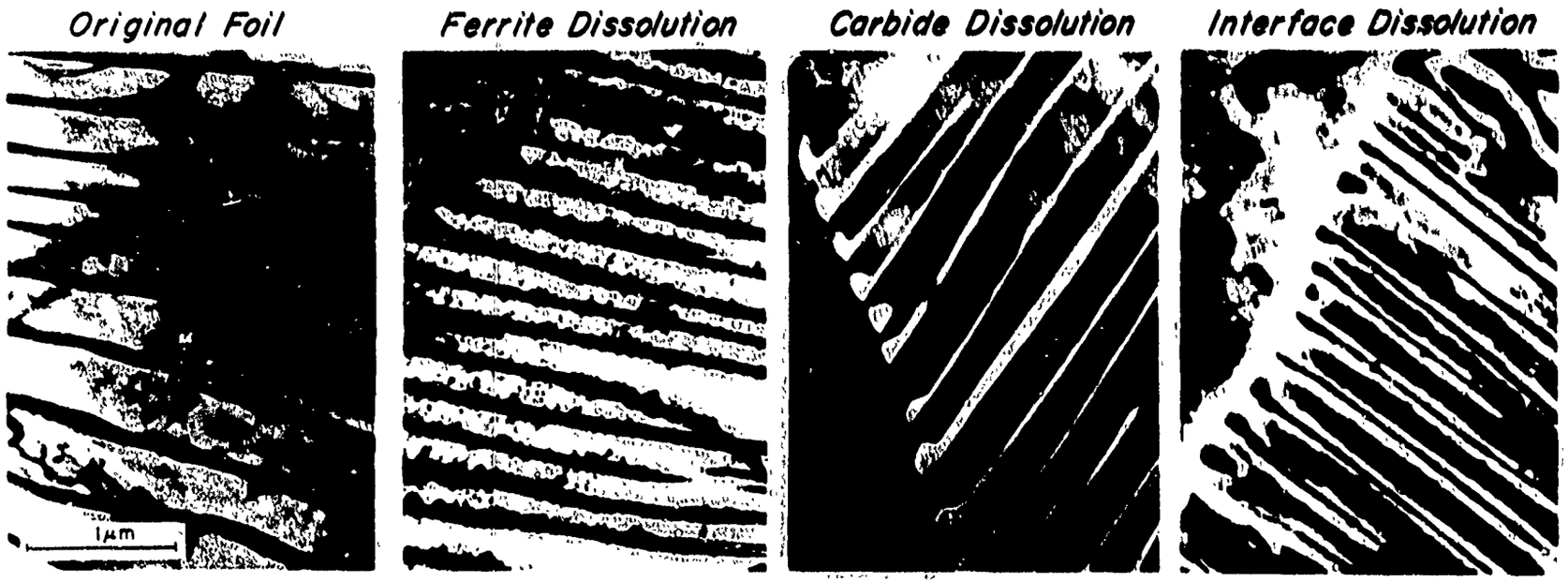

Fig. 90 - Transmission Electron Micrographs Showing the Modes of Attack Observed after Thin Foils of an Fe-0.45 w/o C Alloy Were Exposed to Various Environments at Constant Potential

The specimens of Fe-10Ni, Fe-10Cr, and Fe-10Ni-10Cr were mechanically polished with diamond abrasives (final polishing with 1 μm diamond abrasive), washed in spectrographic grade methanol, dried quickly by absorbing the methanol with lens paper, and placed in the cell. Prior to insertion of the specimen in the cell, the cell was flushed with purified helium gas. The oxide films formed on the specimen surfaces by existing air were reduced potentiostatically at a constant potential of -900 mV (SCE) in the solution of pH 10. When the surface was so reduced, optical readings were made and then the solution was completely replaced by a fresh solution of the required pH. After cathodic reduction and replacing the solution, the specimen was quickly polarized at a constant potential at which film starts to form. The film formation was carried out in the potential region of -200 to +1200 mV (SCE). Before anodic polarization at a different potential, the specimen was freshly polished and cathodically reduced. Throughout the experiment purified helium was bubbled in the cell.

3. Results and Discussion

The optical constants and thickness of passive films formed on Fe-10Ni, Fe-10Cr, and Fe-10Cr-10Ni surfaces were calculated by trial and error methods, using the McCrackin program for analysis of ellipsometric measurements from an electronic computer. Optical constants of the passive films formed on surfaces of these alloys are given in Tables VIII and IX for pH 4 and 6, respectively. These are different for passive films on Fe-10Ni, Fe-10Cr, and Fe-10Cr-10Ni surfaces, indicating that the composition of passive films is different. Since the optical constants vary with passivation potential, the composition of films is also potential-dependent. The composition of films near Flade potential and oxygen evolution potential are different than the films formed at passive potentials.

The growth kinetics of these films are similar to the films formed at pH 8.4.[47] The data fit equally well either the logarithmic or inverse logarithmic rate laws. The plots of growth rates are shown in Figs. 91-102 for pH 4 and 6. It has been found that the direct logarithmic rate is independent of potential (approximately parallel lines for different potentials), but the intercept varies with potential. This type of growth rate has been interpreted in terms of the "place-exchange" mechanism.[48] According to this mechanism film grows by the simultaneous exchange of positions between oxygen and metal ions for all layers of these two species forming the film.

The inverse logarithmic growth rate can be interpreted by Cabrera-Mott[49] theory. According to this theory the growth of film is controlled by the escape of metal ions from metal lattice over an activation barrier, W. The equation for the ion current, neglecting the backward field is

$$i = 2a^{*}n\nu qe \exp - \left[\frac{W - qea^{*}\eta/x}{RT}\right] \qquad (18)$$

Table VIII. The Optical Constants, n(1-ik), of Passive Films Formed on Fe-10Ni, Fe-10Cr, and Fe-10Cr-10Ni Alloys in a Solution of pH 4

Potential, mV	Fe-10Ni		Fe-10Cr		Fe-10Cr-10Ni	
	n	k	n	k	n	k
100	--	--	2.00	0.14	--	--
200	--	--	--	--	2.20	0.12
400	2.10	0.12	2.00	0.14	2.20	0.12
600	2.10	0.12	2.00	0.14	2.20	0.12
800	2.10	0.12	2.00	0.14	2.30	0.14
1000	2.20	0.14	2.00	0.14	2.30	0.14
1200	2.20	0.14	2.00	0.14	--	--

Table IX - The Optical Constants, n(1-ik), of Passive Films Formed on Fe-10Ni, Fe-10Cr, and Fe-10Cr-10Ni Alloys in a Solution of pH 6

Potential, mV	Fe-10Ni		Fe-10Cr		Fe-10Cr-10Ni	
	n	k	n	k	n	k
0	--	--	2.30	0.08	2.20	0.10
200	--	--	2.30	0.08	2.20	0.10
250	2.40	0.12	--	--	--	--
400	2.40	0.12	2.30	0.08	2.20	0.10
600	2.40	0.12	2.30	0.08	2.20	0.10
800	2.60	0.12	3.00	0.10	2.30	0.10
1000	2.60	0.12	3.00	0.10	--	--

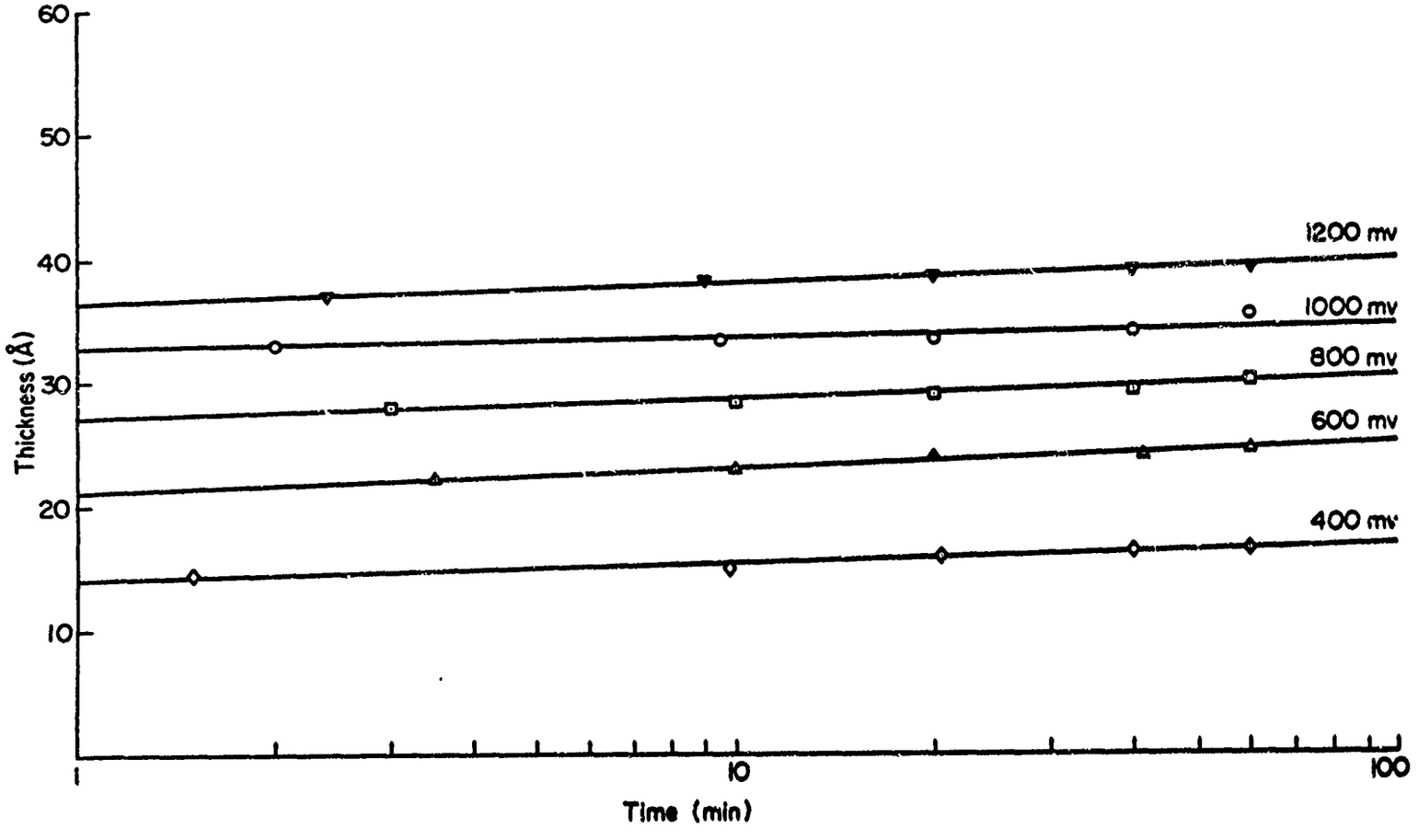

Fig. 91 - Growth of Passive Film on Fe-10Ni in Electrolyte of pH4

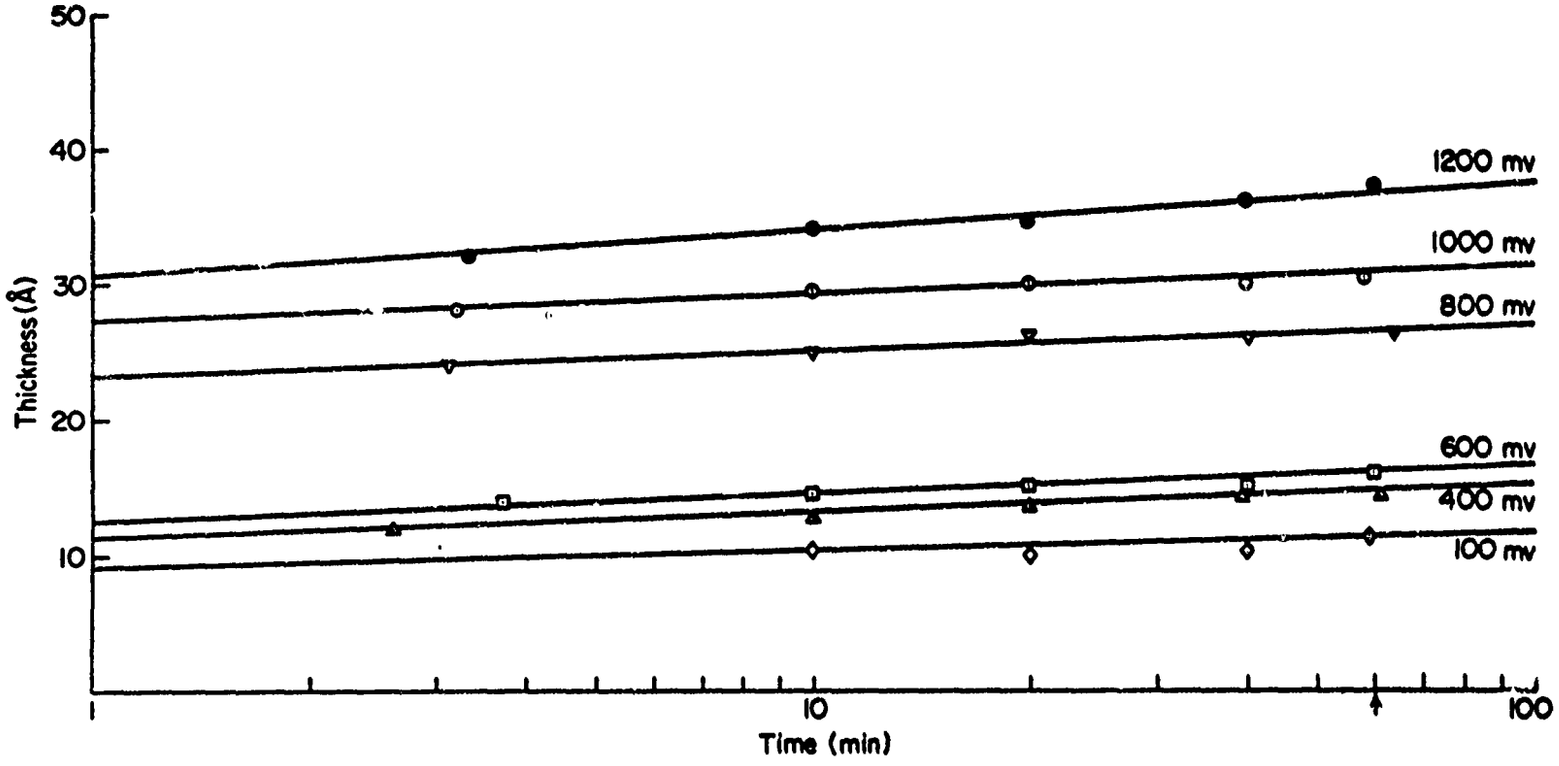

Fig. 92 - Growth of Passive Film on Fe-10Cr in Electrolyte of pH4

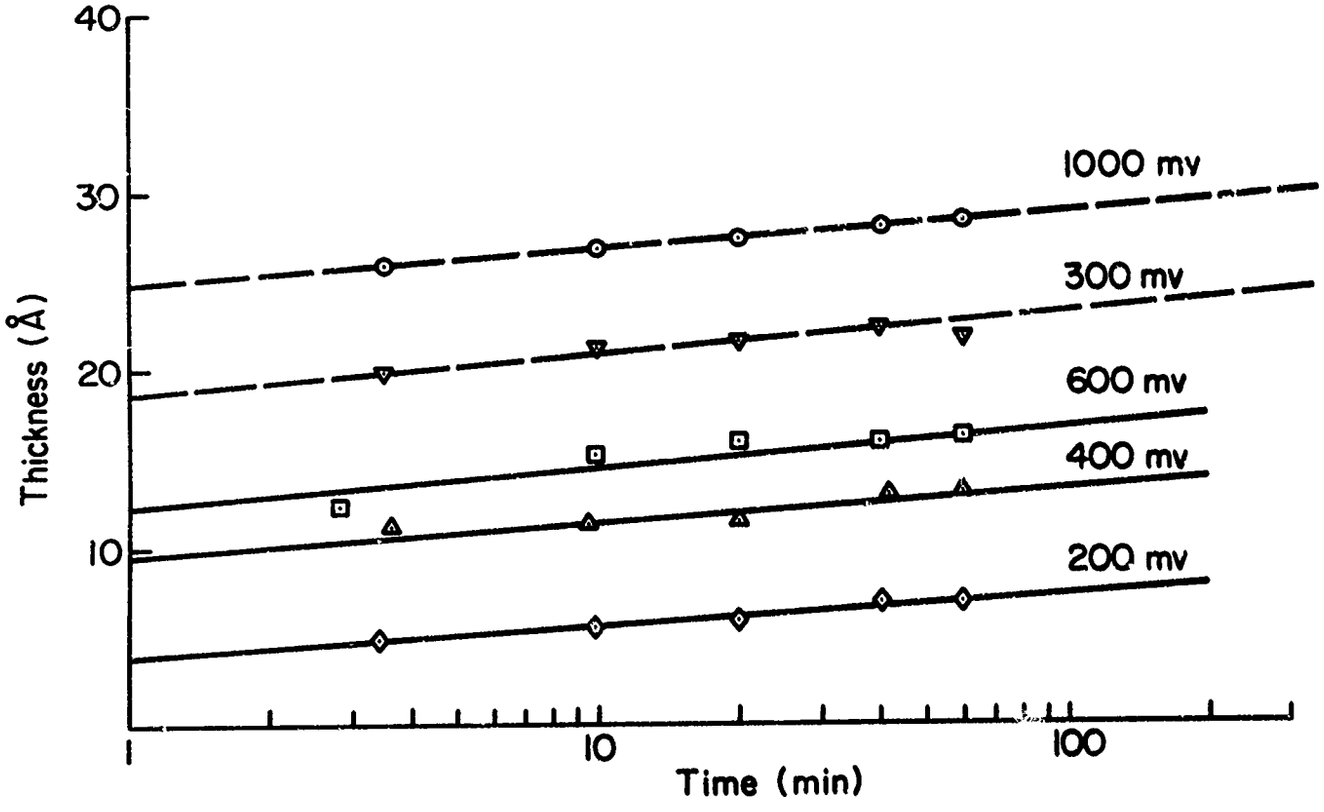

Fig. 93 - Growth of Passive Film on Fe-10Cr-10Ni in Electrolyte of pH 4

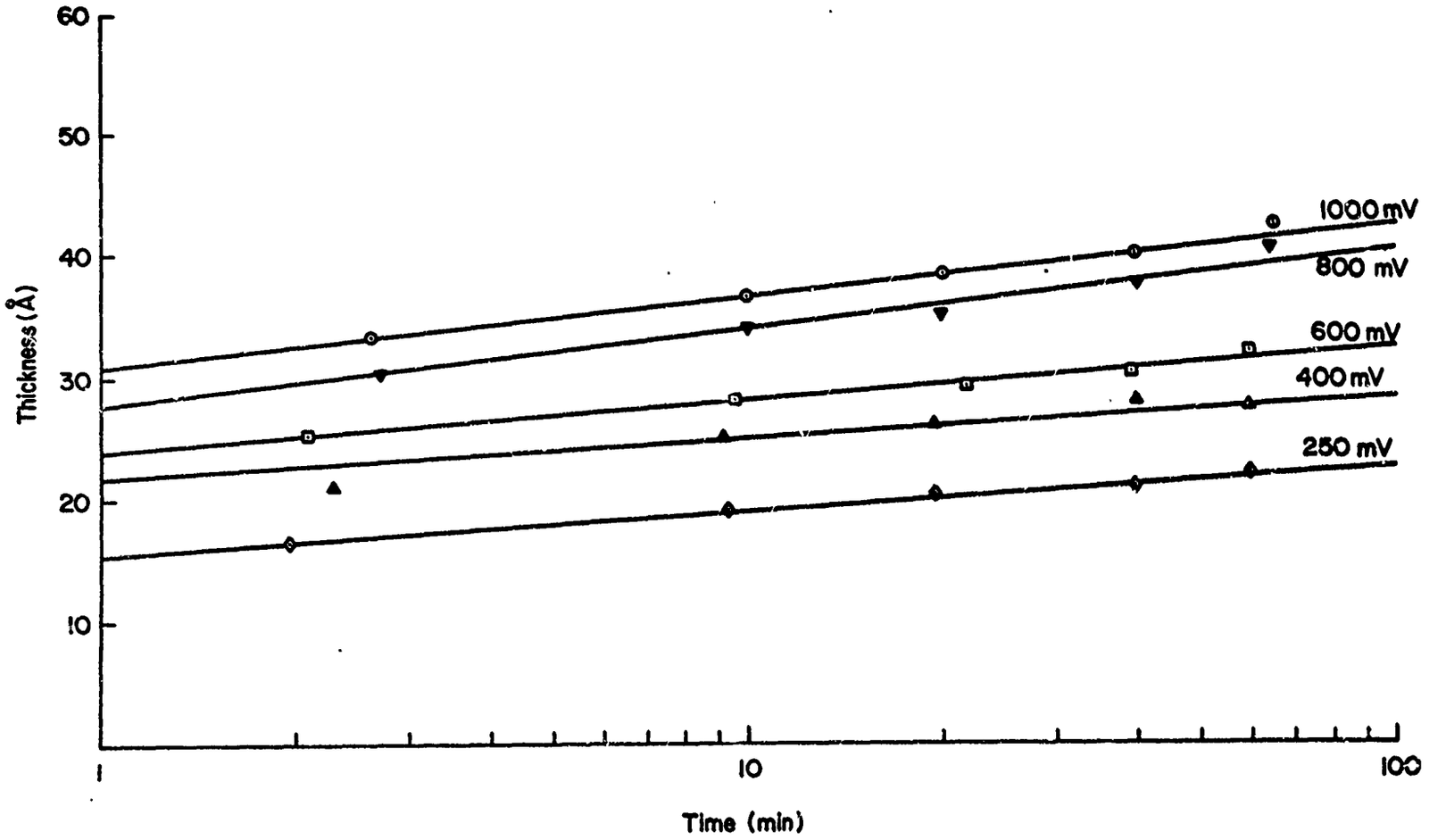

Fig. 94 - Growth of Passive Film on Fe-10Ni in Electrolyte of pH6

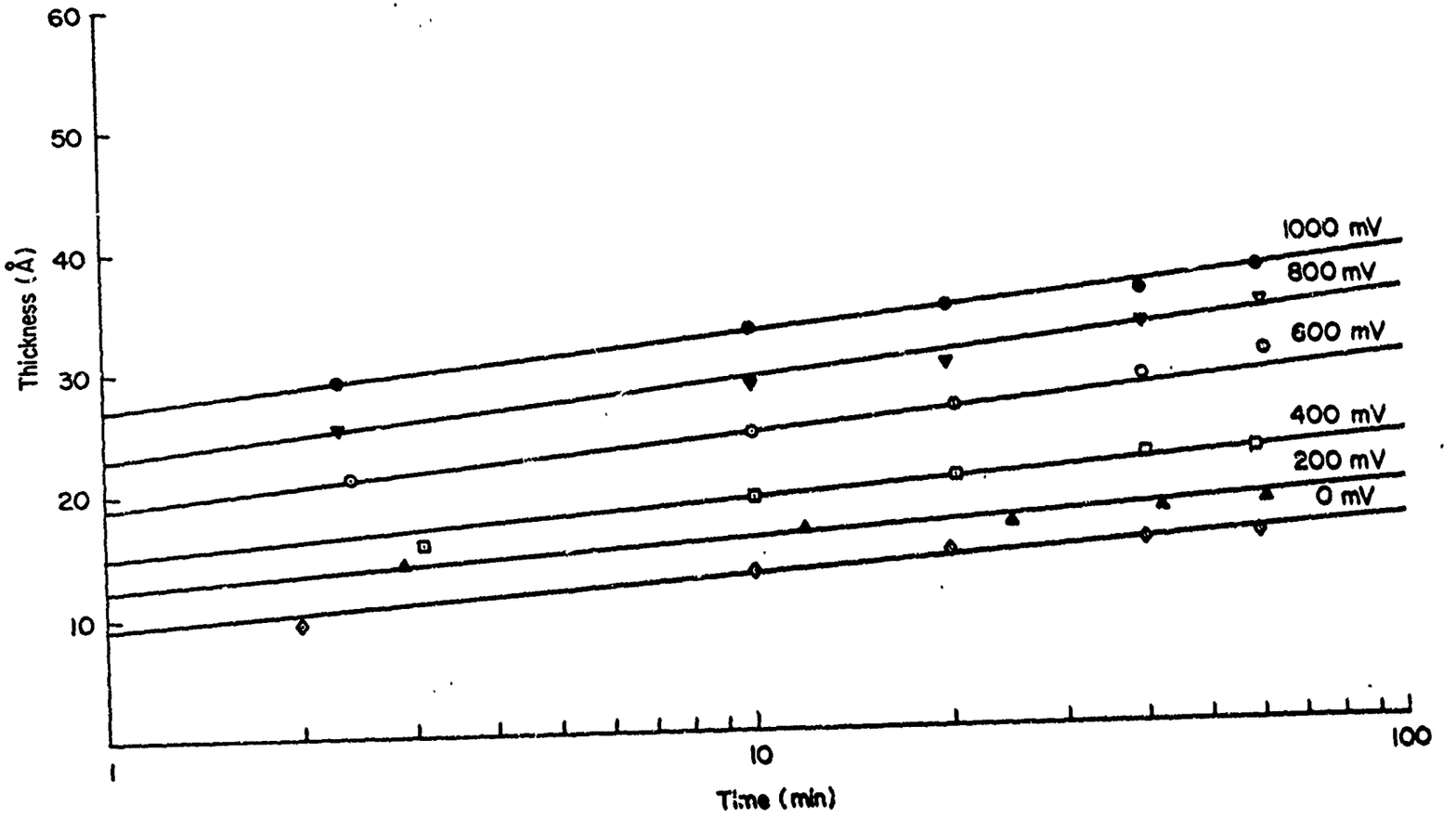

Fig. 95 - Growth of Passive Film on Fe-10Cr in Electrolyte of pH6

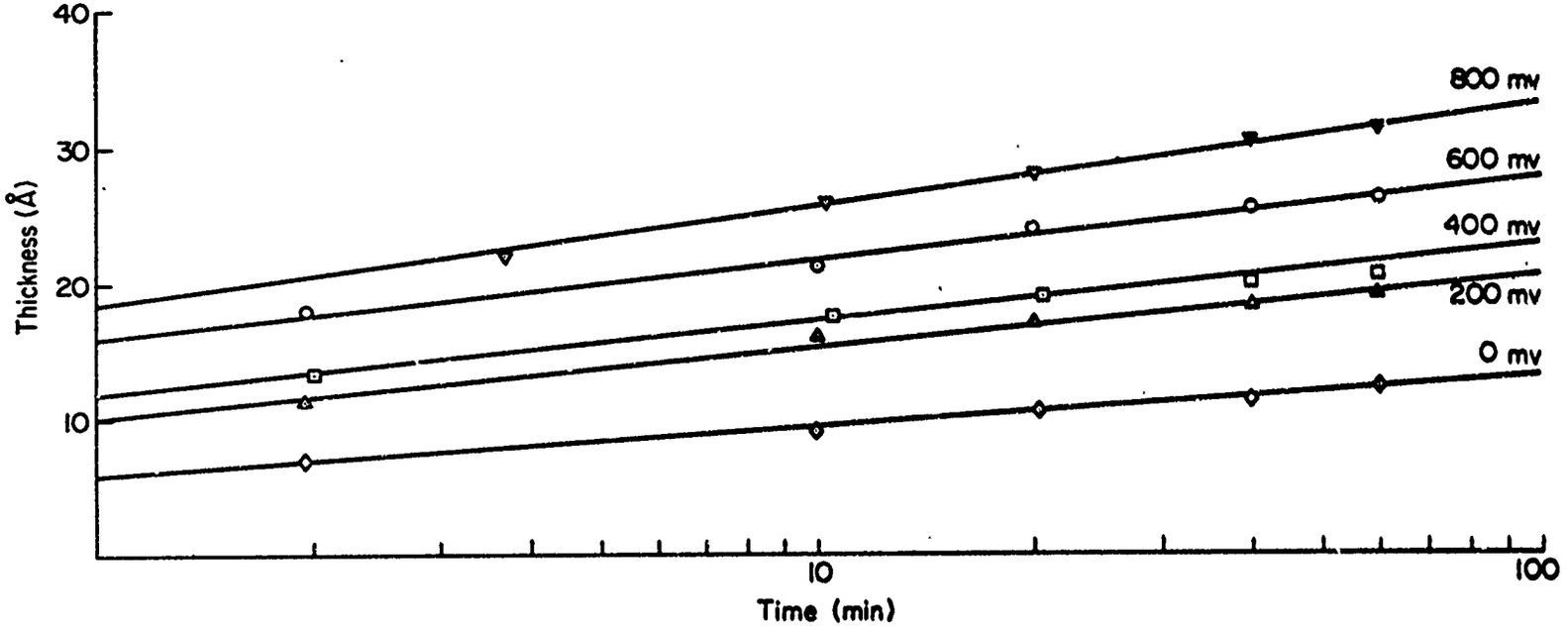

Fig. 96 - Growth of Passive Film on Fe-10Cr-10Ni in Electrolyte of pH6

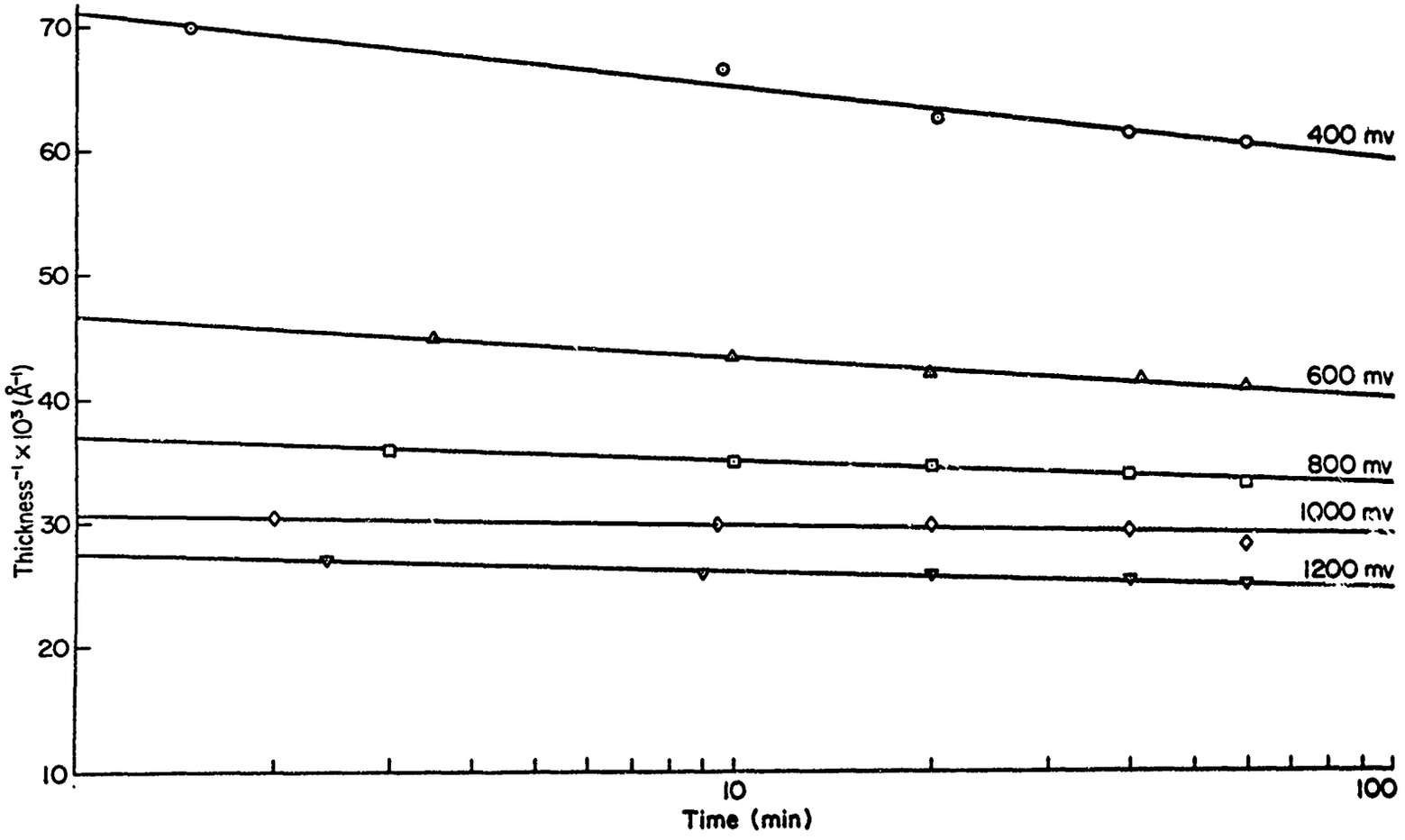

Fig. 97 - Reciprocal of Film Thickness vs. Log of Time for Fe-10Ni in Electrolyte of pH4

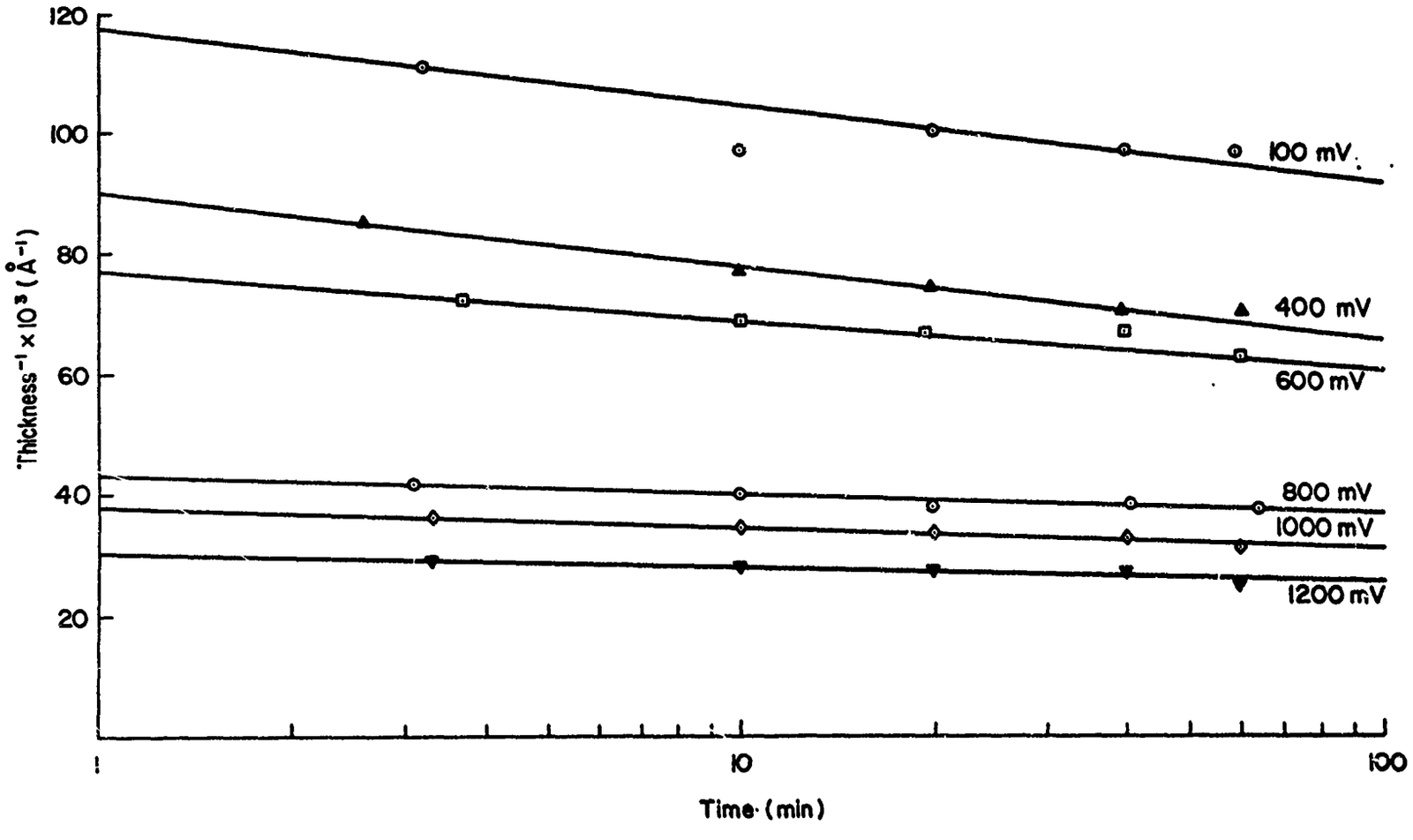

Fig. 98 - Reciprocal of Film Thickness vs. Log of Time for Fe-10Cr in Electrolyte of pH4

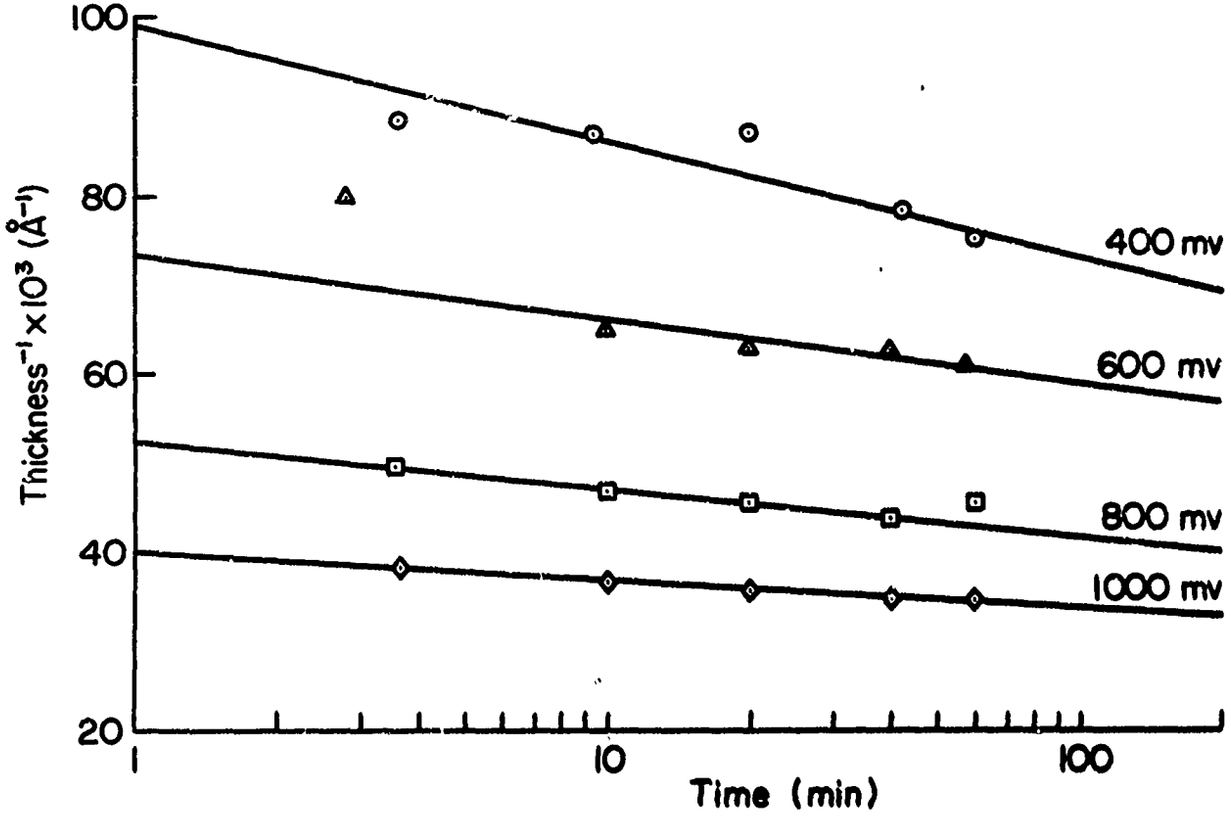

Fig. 99 - Reciprocal of Film Thickness vs. Log of Time for Fe-10Cr-10Ni in Electrolyte of pH4

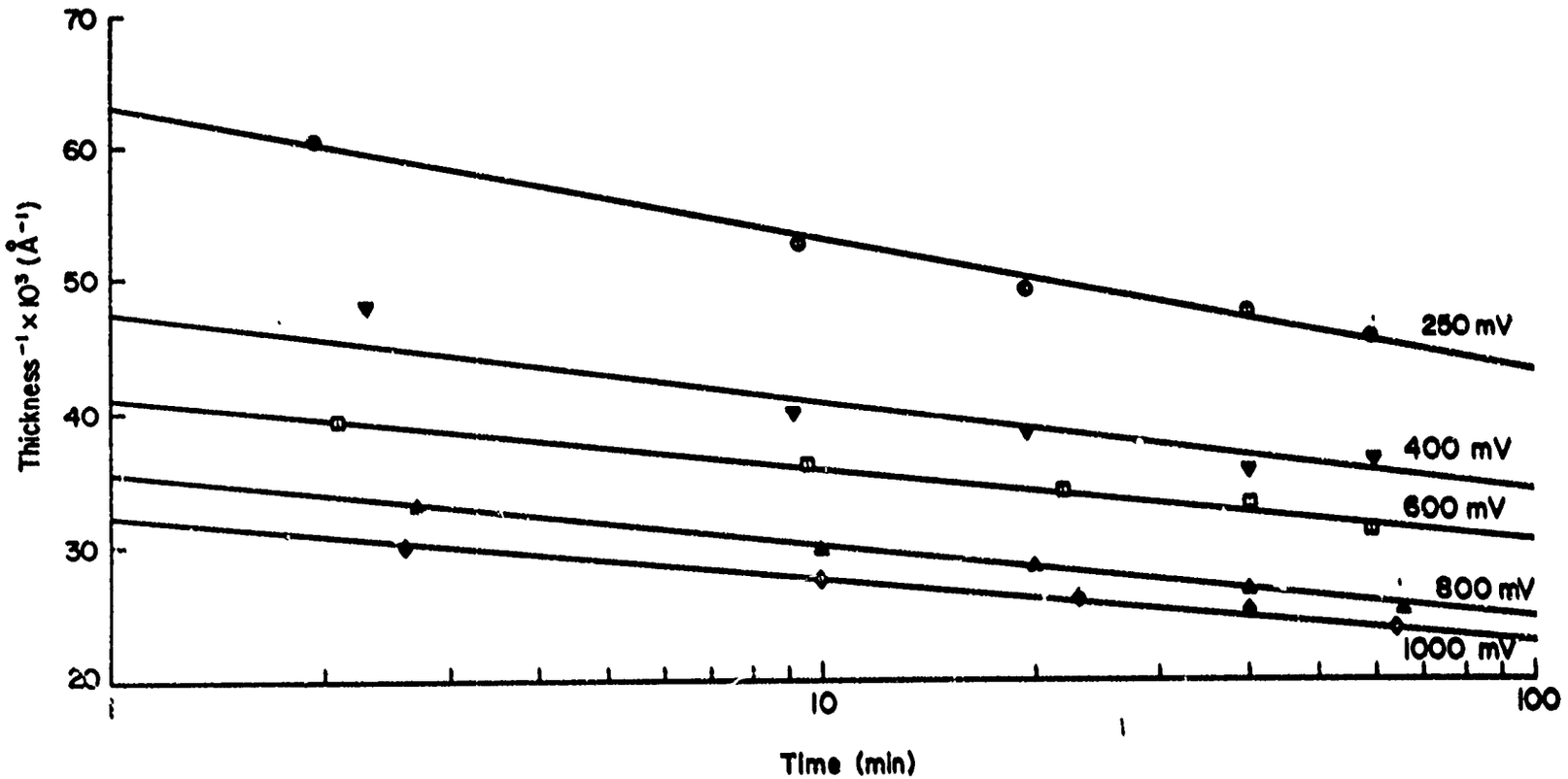

Fig. 100 - Reciprocal of Film Thickness vs. Log of Time for Fe-1.0Ni in Electrolyte of pH6

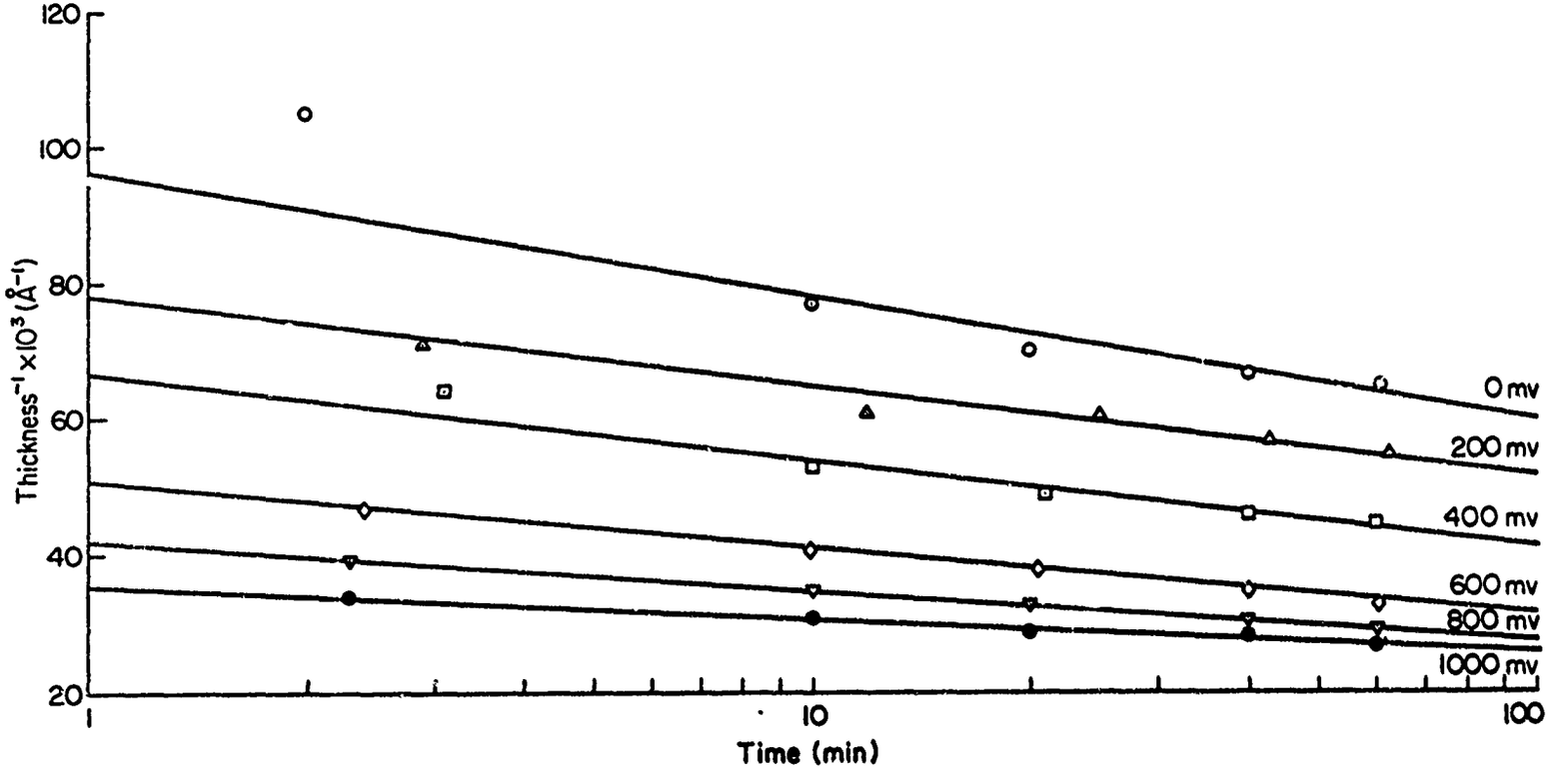

Fig. 101 - Reciprocal of Film Thickness vs. Log of Time for Fe-10Cr in Electrolyte of pH6

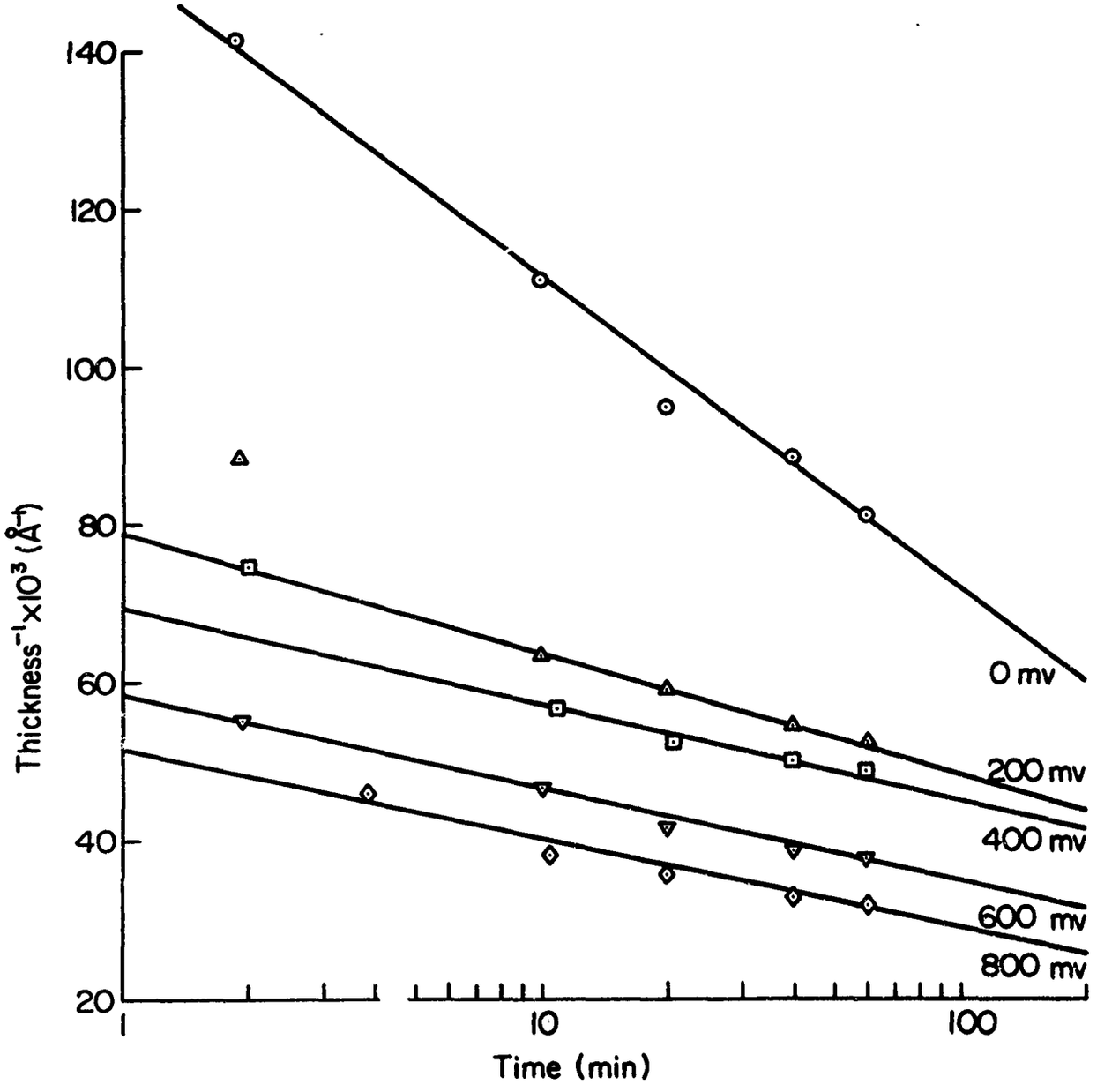

Fig. 102 - Reciprocal of Film Thickness vs. Log of Time for Fe-10Cr-Ni in Electrolyte of pH6

where n is the number of mobile ions per unit volume, ν is the frequency, qe is the charge on the mobile ion, η is the overvoltage, a* is the activation jump distance, and x is the film thickness. An approximate integration of the equation gives

$$\frac{1}{x} = \text{const} - \frac{1}{x_1} \ell n\, t \qquad (19)$$

where

$$\frac{1}{x_1} = \frac{kt}{qe\, a^* \eta}$$

From the expression for $1/x_1$, as derived from this theory, we can see that we would expect a plot of x_1 vs. η to yield a straight line. Figure 103 is such a plot for pH 6.

Since the dependence of x_1 on η as shown in Fig. 103, is reasonably linear and because an indirect logarithmic rate law is observed, we can consider that the mechanism of passive film growth on these alloys is similar to that for aluminum and tantalum; namely, field-assisted migration of cations through the film to react with oxygen or OH^- at the solution-oxide interface. The reasonableness of this concept can be seen if we first calculate a value for the jump distance, a*, using the slope from Fig. 103 and the expression for x_1 in Eq. (19). The values in this plot are based on the assumption that the field is across the entire film. The values of jump distance, a*, along with the height of the activation barrier, W, for Fe-10Ni, Fe-10Cr, and Fe-10Cr-10Ni are given in Table X. In the calculation of jump distance, a*, it was assumed that the mobile ion has a charge of 3. These values are very reasonable.

Table X - The Value of Jump Distance, a*, for Iron-Base Alloys, Studied in pH 6

Element	Slope (Å/V x 10^2)	Jump Distance (Å)	Activation Barrier, W (eV)
Fe-10Ni	2.63	2.3	1.30
Fe-10Cr	2.55	2.2	1.27
Fe-10Cr-10Ni	2.53	2.2	1.30

The variation of film thickness at a given time with applied potentials is shown in Figs. 104 and 105 for pH 4 and 6, respectively. The film thickness is almost linearly proportional to the applied potential for all materials. A comparison of film thicknesses is given in Table XI for solutions of different pH. The variation of film thickness at a given potential with the pH of the solutions is shown in Fig. 106. The film thicknesses of passive films formed on these alloys increase linearly as the pH of the electrolyte increases.

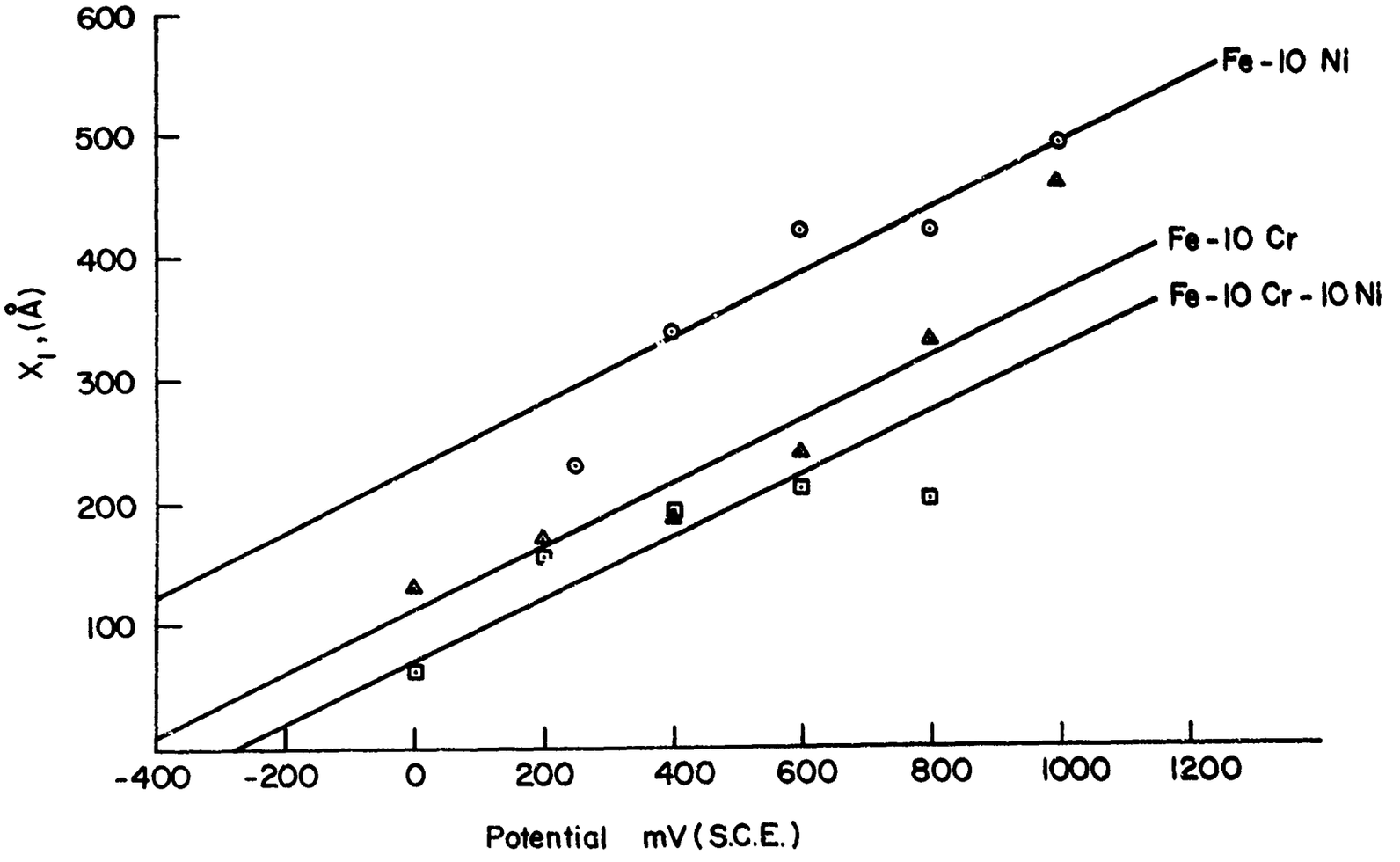

Fig. 103 - x_1, The Rate Constant vs. Passivation Potential for Electrolyte of pH 6

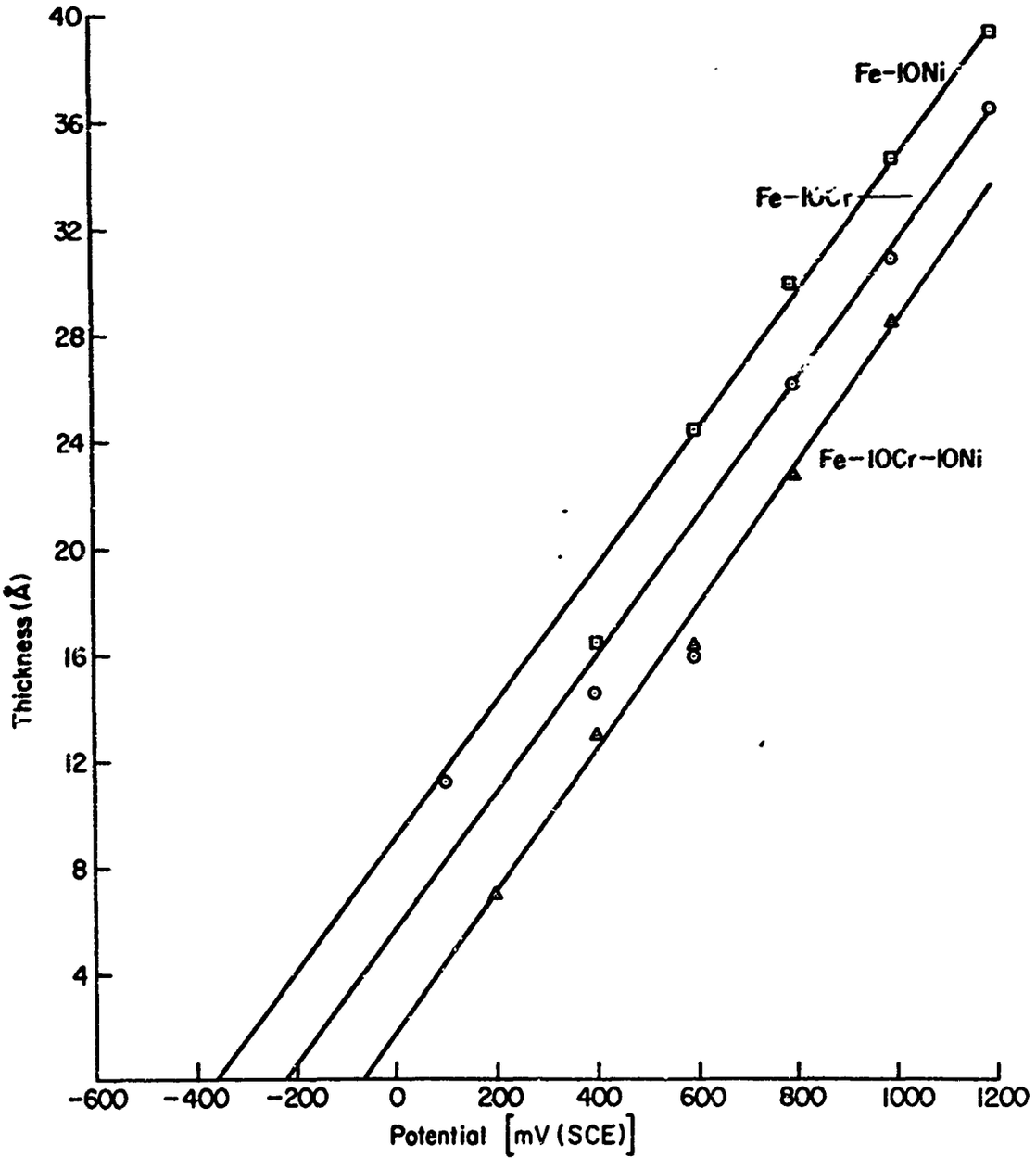

Fig. 104 - Film Thickness vs. Passivation Potential for One Hour of Passivation in Electrolyte of pH 4

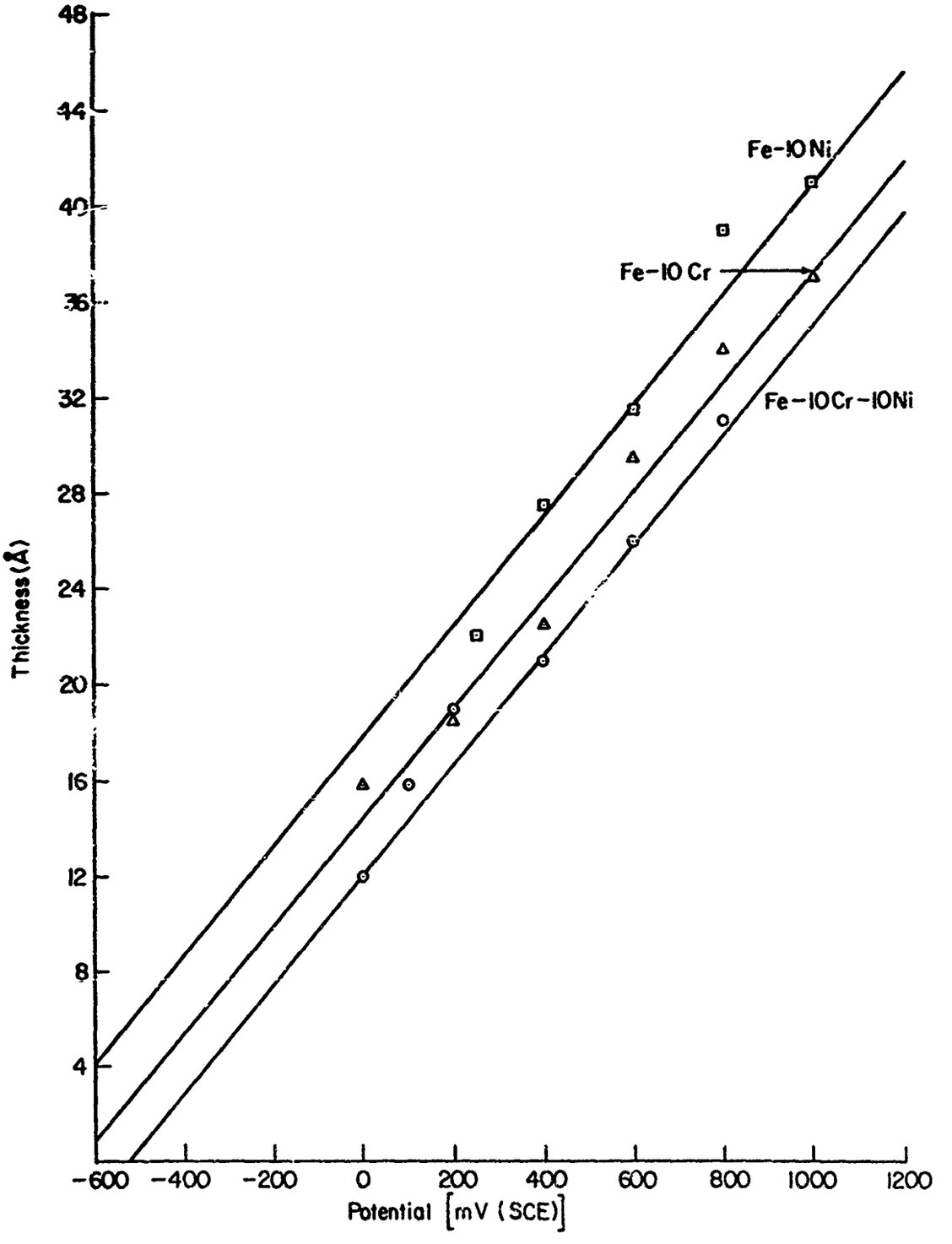

Fig. 105 - Film Thickness vs. Passivation Potentials for One Hour of Passivation in Electrolyte of pH 6

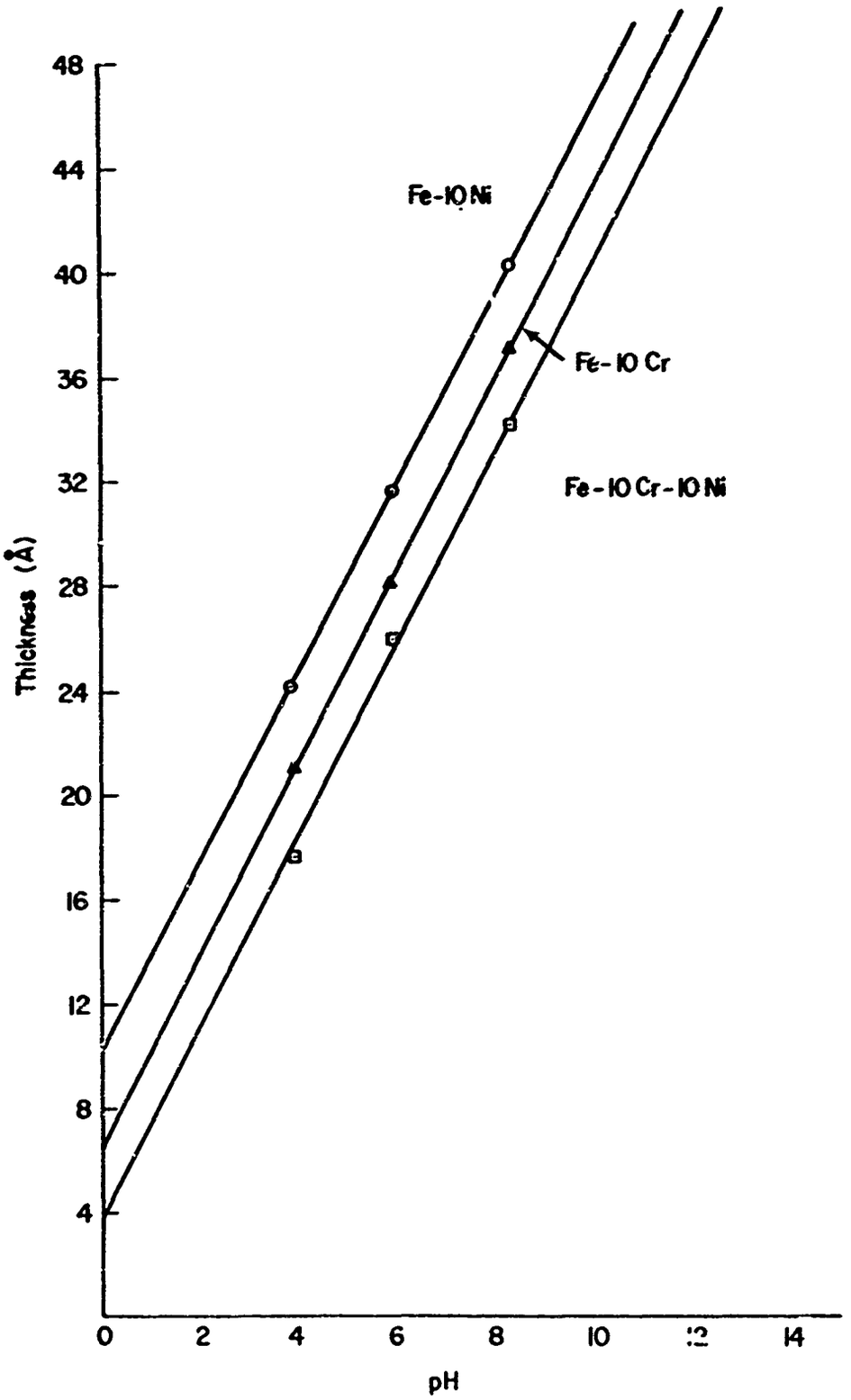

Fig. 106 - Film Thickness vs. pH of Electrolyte

Table XI - Comparison of the Thickness of Passive Films Formed on Fe-10Ni, Fe-10Cr, and Fe-10Cr-10Ni Alloys in Solutions of Different pH

Potential mV(SCE) / pH	Fe-10Ni			Fe-10Cr			Fe-10Cr-10Ni		
	Film Thickness (Å)								
	4	6	8.4	4	6	8.4	4	6	8.4
200	14.2*	22.5*	28.2	10.8	19.0	25.4	7.0	16.7	22.3
400	19.2	27.1	34.3	16.0	23.6	31.3	12.4	21.3	28.2
600	24.3	31.7	40.4	21.0	28.2	37.2	17.6	26.0	34.2
800	29.4	36.3	46.5	26.2	32.8	43.1	22.8	30.4	40.1
1000	34.4	41.0		31.2	37.3		28.2	35.0*	
1200	39.4								

*Extrapolated values

Future attempts will be made to study growth kinetics of passive films on these alloys in solutions of higher pH, say 10 and 12. A complete analysis of the effect of alloying elements, pH of the solution, and passivation potentials will be done.

G. STUDY OF ACOUSTIC EMISSIONS IN AISI 4335 STEEL
(G. E. Kerns)

1. Aims of Current Research

The purposes of this investigation are (1) to determine the effects of environmental variables and mechanical properties on the kinetics of stress corrosion cracking in high-strength steels, (2) to determine whether acoustic emissions from stress corrosion cracks are a function of such environmental or metallurgical variables, and (3) to ascertain whether measurable parameters of the acoustic signal can give information as to the mechanism of stress corrosion cracking in these materials.

2. Background of Acoustic Techniques

Prior investigations[50-53] have shown that acoustic emissions are observed during plastic deformation or stress corrosion cracking of many metals and alloys. These emissions are detected by piezoelectric devices (crystals, accelerometers, ceramics). However, experimental

results to date have given no information as to the amplitude or frequency content of the actual signal. Effects such as reflection (and mode conversion), material attenuation, and the piezoelectric properties of the detector must be evaluated in order to obtain information regarding the initial signal. Attenuation will depend on the geometry of the wave (planar, spherical), as well as other wave properties. Therefore, knowledge as to reflection phenomena and detector response must first be obtained in order to know the properties of the acoustic signal leaving a crack.

Two avenues of approach are available to determine these effects: (1) to experimentally determine the response characteristics of the piezoelectric detector and to determine what reflections have occurred before the signal reaches the piezoelectric device, or (2) to alter the physical dimensions of transmitting medium, as well as the response characteristics of the transducer such that reflections and transducer resonance are minimal.

3. Acoustic Emission Program

a. Investigation of the Response Characteristics of Endevco 2272 Accelerometer

(1) Test Procedure

The first investigation was that of determining how the Endevco accelerometer used in past studies (Tech. Report AFML-70-2) responds to stress waves of various frequencies while mechanically loaded by coupling to steel. Using an elliptical PZT-4 ceramic disc ($\frac{1}{2}$"x1"x0.049") as a driving transducer, stress waves of various frequencies were transmitted to the accelerometer directly, and through two thicknesses of AISI 4335 steel, as shown in Fig. 107. Dow Corning ignition sealing compound DC-4 was used as the couplant. The stress wave was generated by a sinusoidal voltage (4.0 V peak-to-peak) applied across the driving transducer. This voltage was held constant, and the output of the accelerometer (after amplification and filtering) was monitored as a function of oscillator frequency. The sine wave was generated by a Hewlett-Packard 200 CD test oscillator. The value of 4.0 V for the voltage across the driving ceramic was chosen because it produced measureable accelerometer outputs at all frequencies up to the radial mode resonance frequency of the driving element (164 kHz).

(2) Results and Discussion

The accelerometer response curves and the electrical circuit are shown in Figs. 108-110. The presence of a radial mode resonance in the driving transducer at 164 kHz produced an explainable response peak for the accelerometer at that frequency. The response curves of the accelerometer show that the use of an accelerometer to

DIRECT COUPLING

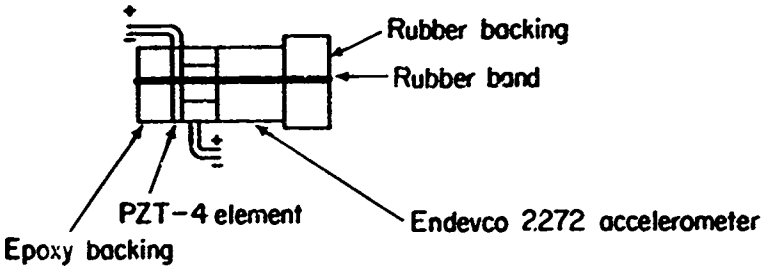

COUPLING THROUGH 1/2" DIMENSION OF STEEL SECTION*

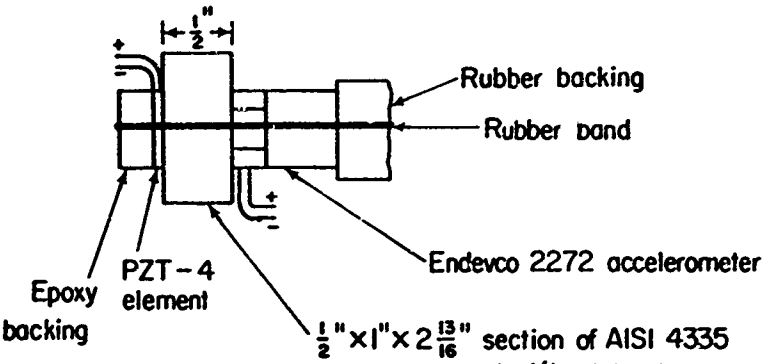

COUPLING THROUGH 1" DIMENSION OF STEEL SECTION*

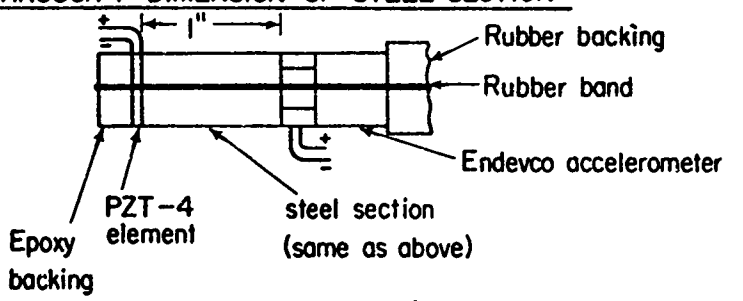

*In both cases transducer and accelerometer were located midway along the length of the steel section

Fig. 107 - Methods of Coupling PZT-4 Disc to Endevco Accelerometer

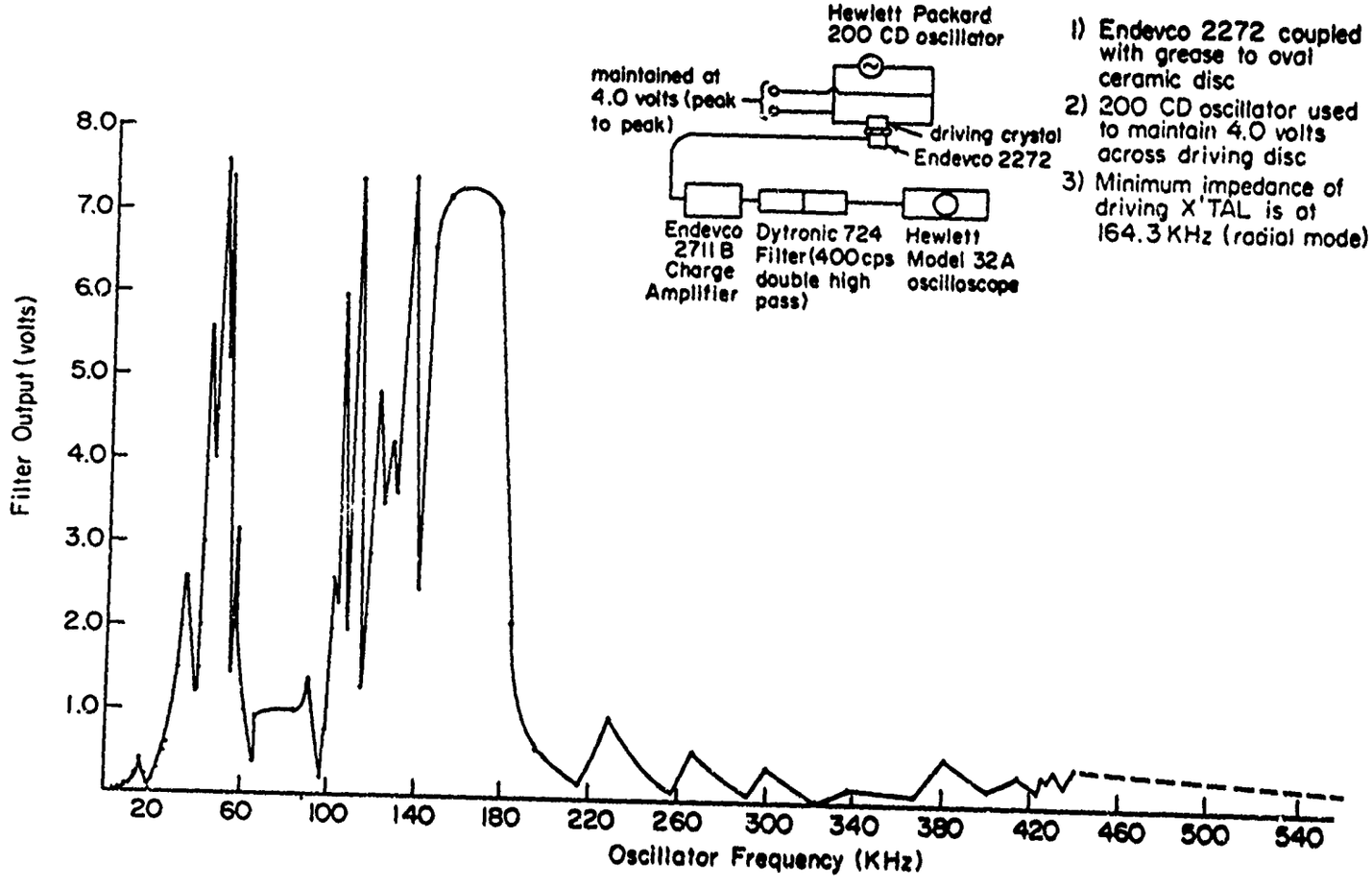

Fig. 108 - Response Curve of Endevco 2272 Accelerometer When Coupled Directly to PZT-4 Crystal

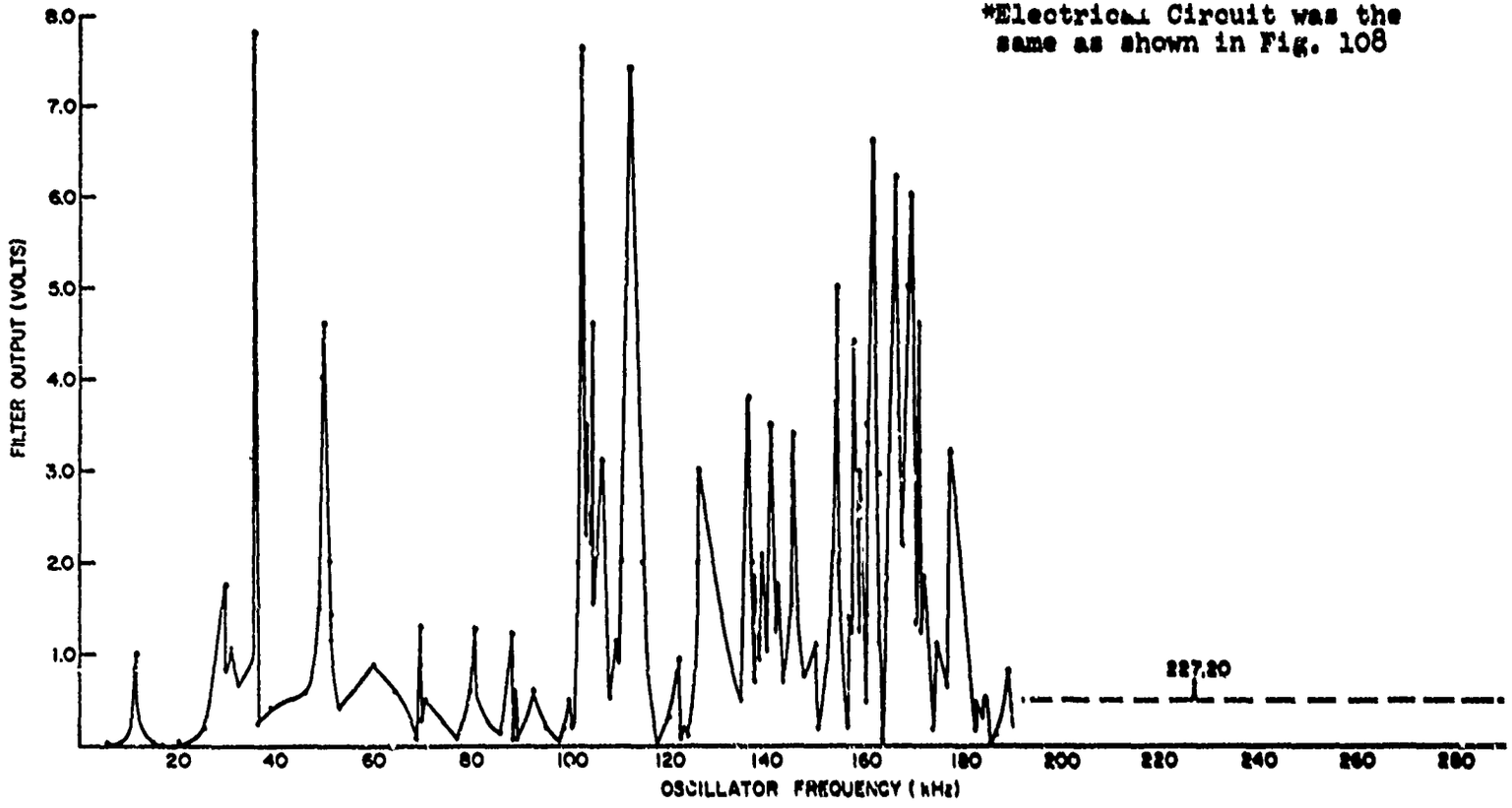

Fig. 109 - Response Curve of Endevco 2272 Accelerometer When Coupled to PZT-4 Crystal through $\frac{1}{2}$" Dimension of Steel Section*

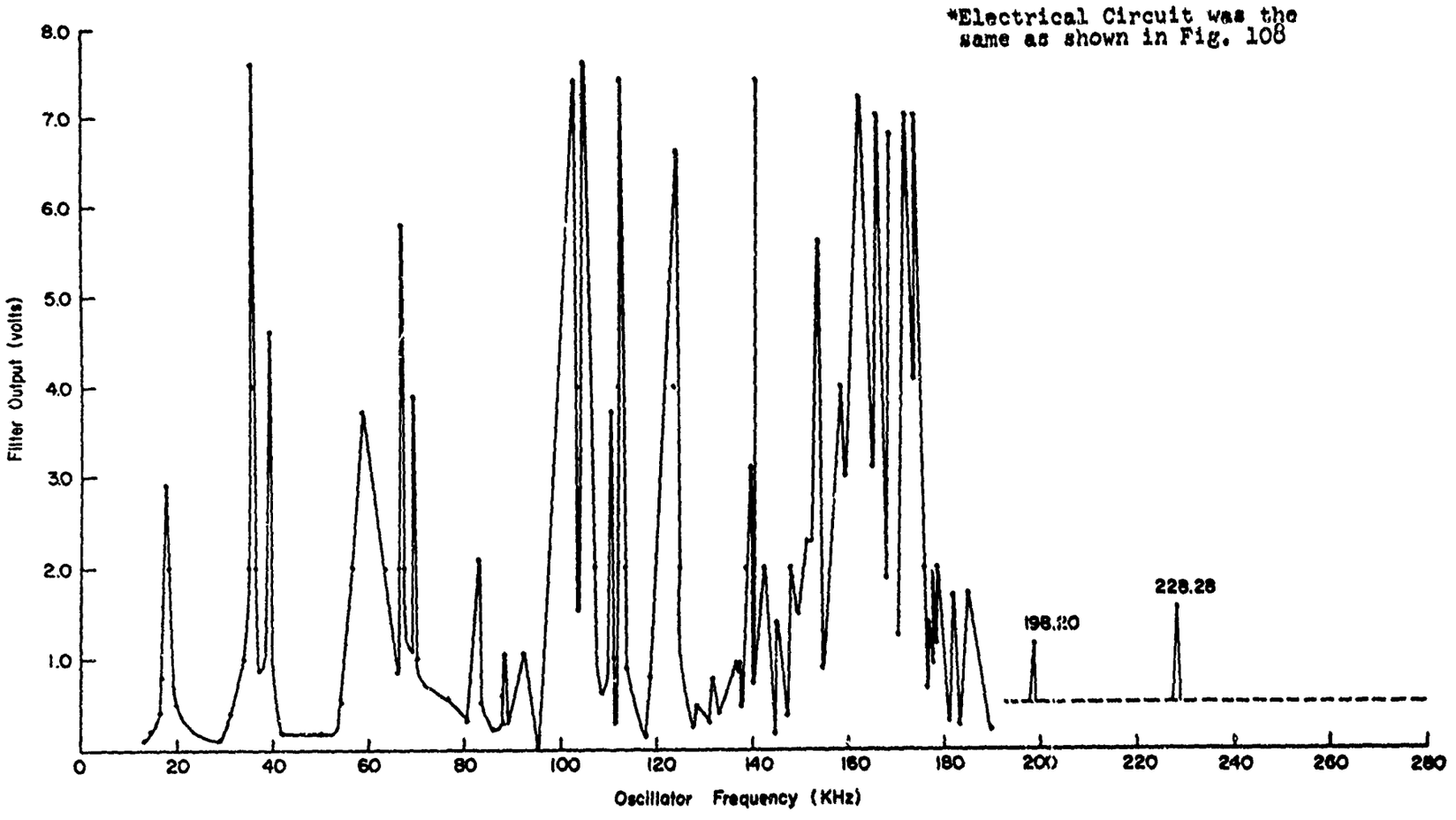

Fig. 110 - Response Curve of Endevco 2272 Accelerometer When Coupled to PZT-4 Crystal through 1" Dimension of Steel Section*

detect frequency components in a stress wave above that of its own resonance frequency (37 kHz) is impractical, even in the case of a simple specimen geometry and a periodic, continuous stress wave. The response of the accelerometer appears to be a function of source-to-detector distance, and is undoubtedly affected by mechanical oscillation of the specimen. In Fig. 110, for example, the response peaks at approximately 100 kHz may be explained by standing waves in the 1-inch dimension of the steel section. Taking the velocity of a longitudinal wave in Armco iron as 23.5×10^4 inch/s,[4] and calculating the frequency for standing waves in the 1-inch dimension, it is seen that mechanical resonance of the specimen can occur at 117.5 kHz. All of the response peaks, however, cannot be explained by simple harmonic modes of vibration of the steel section. Therefore, the response of an accelerometer is quite complex when mechanically loaded and excited by frequencies above its resonance frequency.

b. Experimentation Using a 16-MHz Branson Transducer

(1) Test Procedure

In order to avoid transducer resonance, a Branson Z-103-B transducer (16 MHz resonance frequency) was used to detect acoustic emissions from stress corrosion cracks growing in various environments. The specimens were of the single cantilever beam type used in prior studies (Tech. Reps. AFML-69-16, 70-2). The material was AISI 4335 steel, heat-treated as follows: 1500°F/1 hr, O.Q. + 400°F/1 hr, A.C. The cantilever loading assembly was the same as that used in the prior work cited above.

A sinusoidal voltage was applied across the transducer using a Hewlett-Packard 651 B test oscillator. The frequency was varied to a maximum (test oscillator limit) of 10 MHz. The voltage across the transducer was monitored, and no resonance occurred below 10 MHz. The transducer was mounted on the test specimens as shown in Fig. 111. Seven tests were performed by allowing a fatigue crack to grow in gaseous and aqueous environments, while the acoustic signals were recorded photographically. Random photographs were taken during each test. The applied stress intensity factors and environments are given in Table XII. The electrical system is shown in Fig. 111. The gas-purifying system and aqueous corrosion apparatus were the same as described in Technical Report AFML-69-16.

(2) Results and Discussion

Figures 112-118 show five random photographs of the transducer output for each test. The results show considerable variation in pulse shape for each environment. Also the presence of periodic signals (Figs. 112,113) appear to indicate reflection phenomena with frequency components well below the natural resonance frequency of the

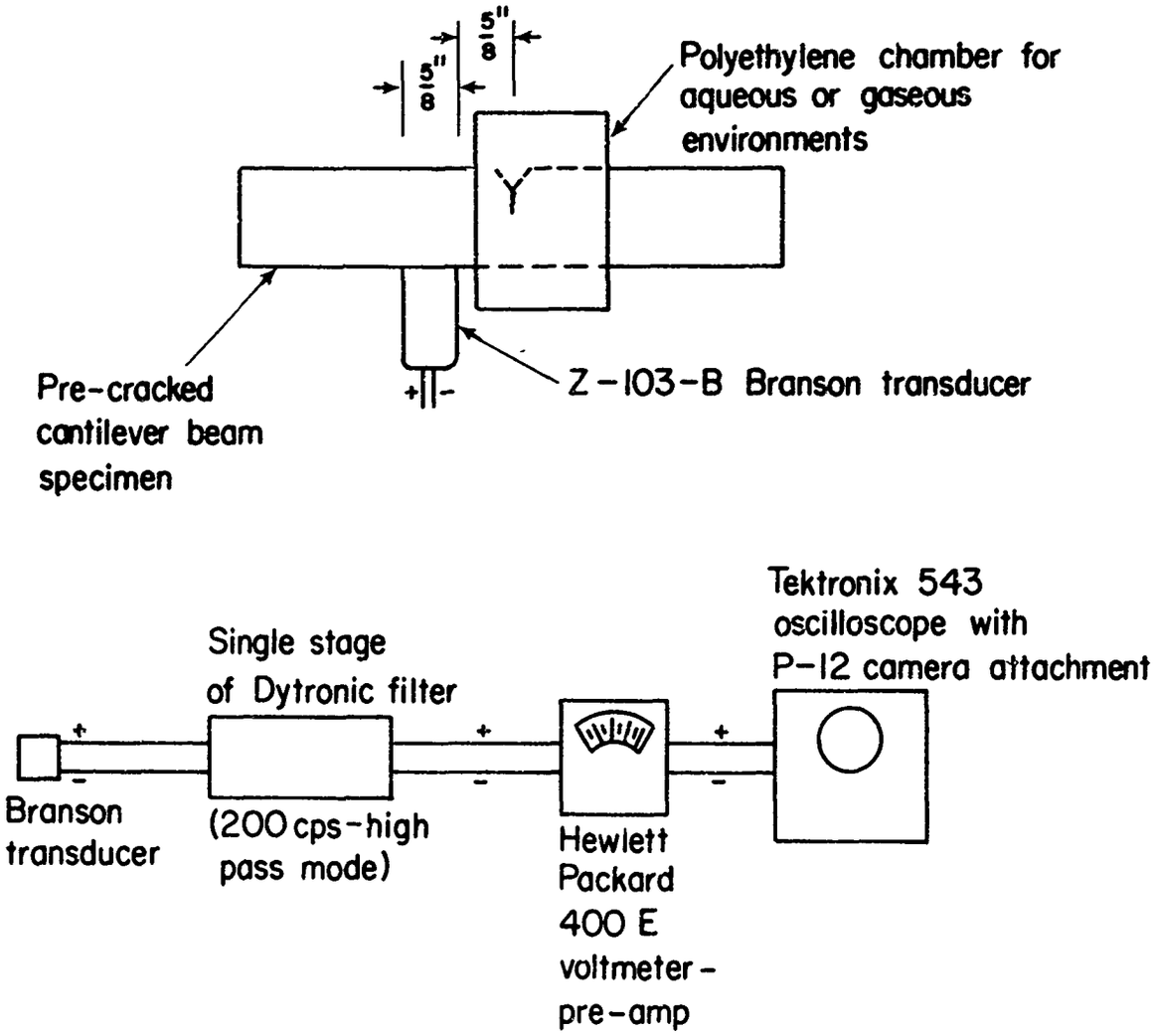

Fig. 111 - Test Apparatus for Experiments with Branson Transducer

Table XII - Test Conditions for Cantilever Beam Specimens

Specimen	Initial Stress Intensity Factor (ksi-in.$^{1/2}$)	Environment*	Applied Potential**
CDG-78	38.04	23.1% H_2	--
CDG-79	40.30	23.1% H_2	--
CDG-80	42.82	23.1% H_2	--
CDG-81	38.56	100% H_2	--
CDG-82	41.39	1N HCl	-1.0 V
CDG-83	46.23	1N HCl	+1.0 V
CDG-84	49.42	3½% NaCl adj. to pH = 13 with NaOH	+1.5 V

* Total flow rate of gaseous mixtures and pure H_2 was 6.5 cc/minute

** Potential controlled by Magna Research potentiostat Model 4700M, and all potentials are w.r.t. SCE

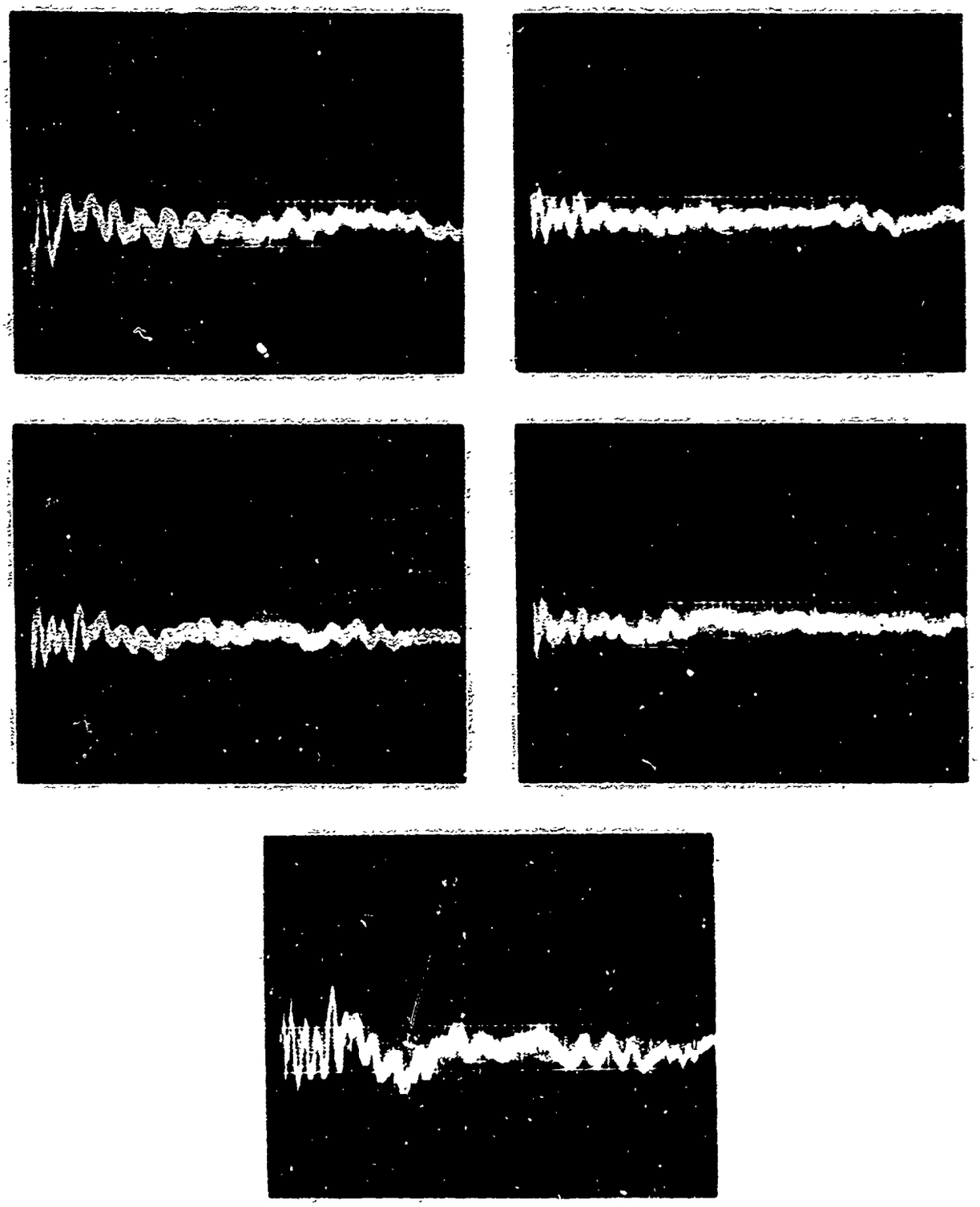

Fig. 112 - Photographs of Acoustic Emissions in 23.1% H_2 (Spec. CDG-78); horizontal scale - 500 μsec/cm
vertical scale - 5 mV/cm

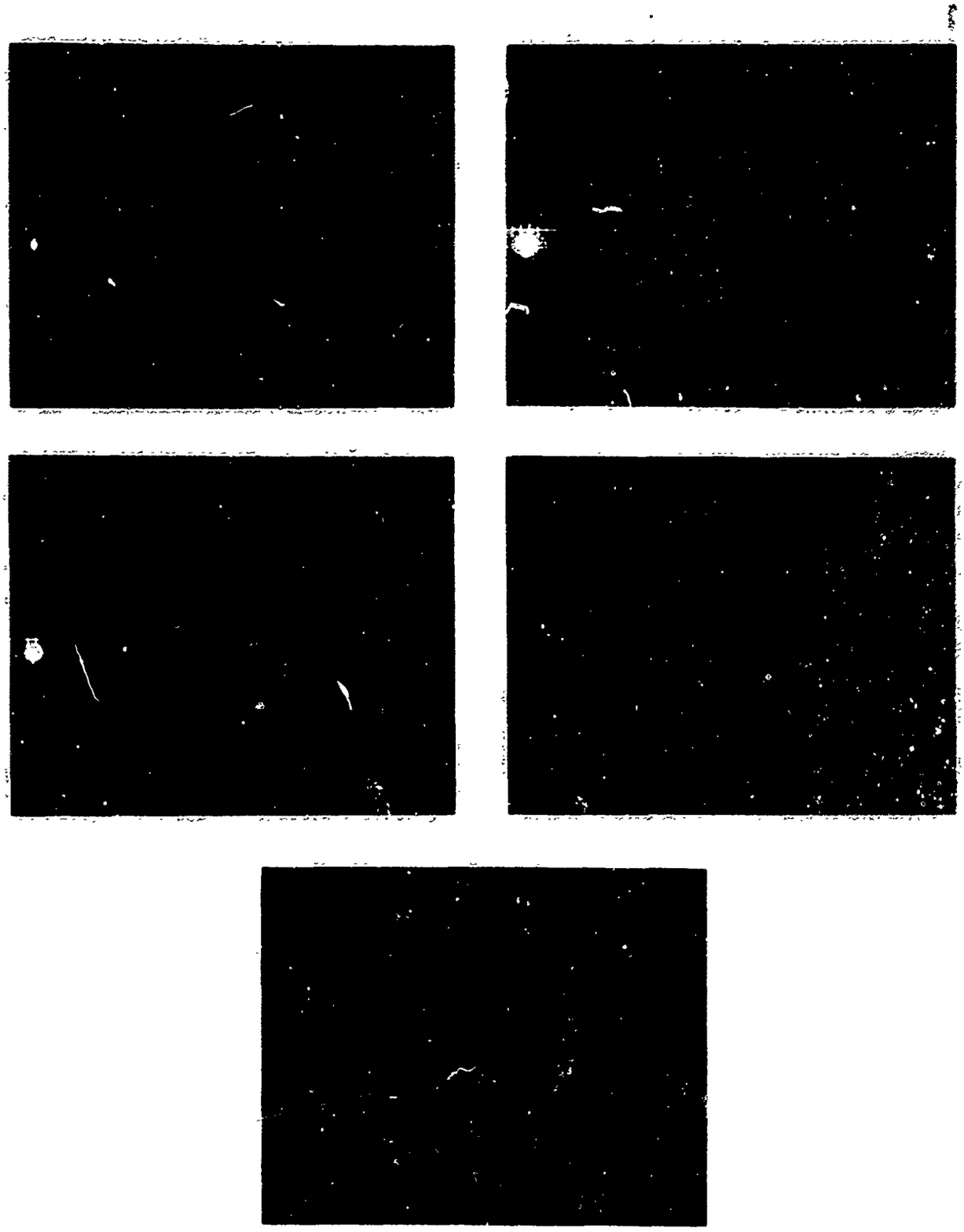

Fig. 113 - Photographs of Acoustic Emissions in 23.1% H_2 (Spec. CDG-79); horizontal scale - 1 μsec/cm
vertical scale - 10 mV/cm

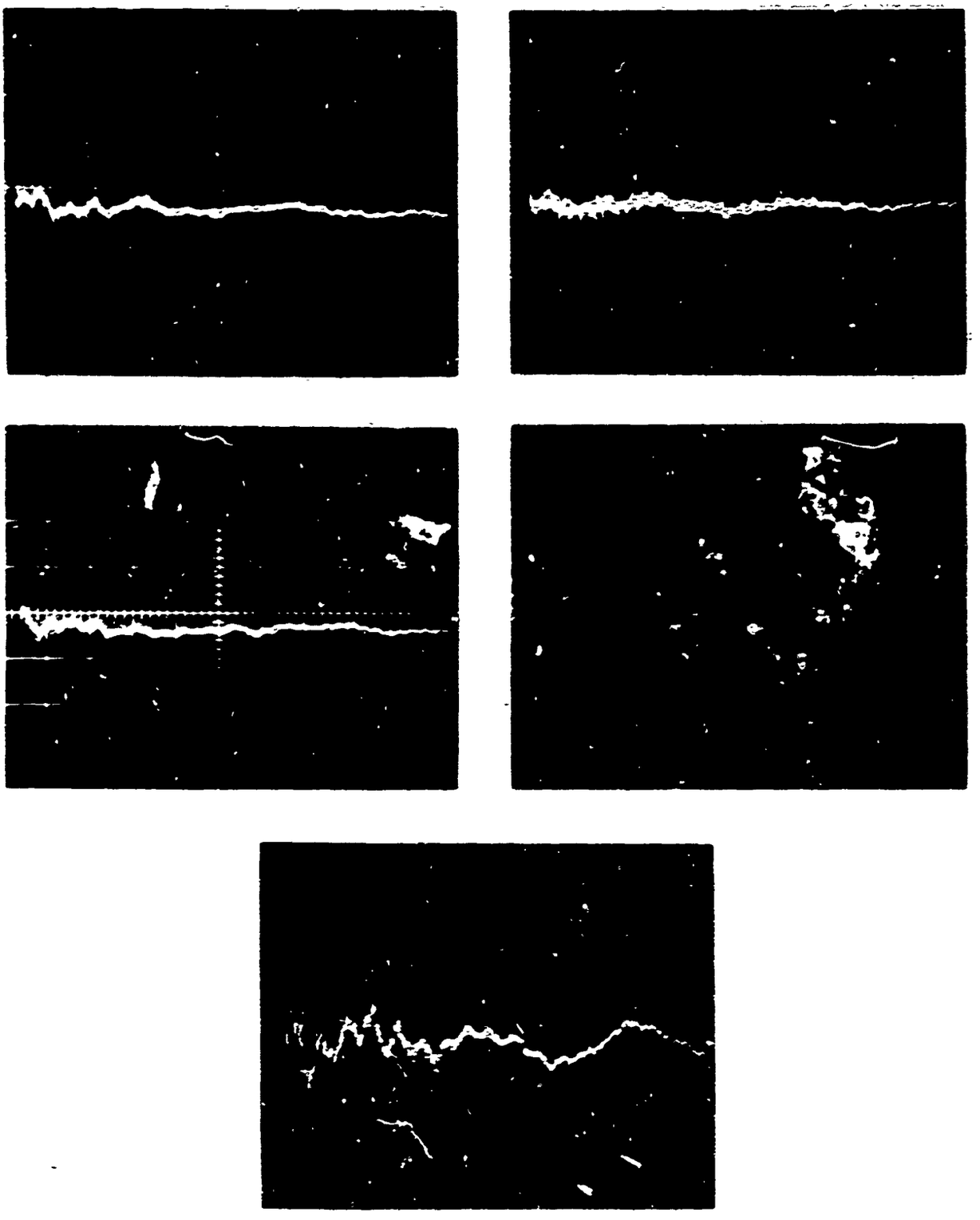

Fig. 114 - Photographs of Acoustic Emissions in 23.1% H_2 (Spec. CDG-80); horizontal scale - 50 μsec/cm
vertical scale - 10 mV/cm

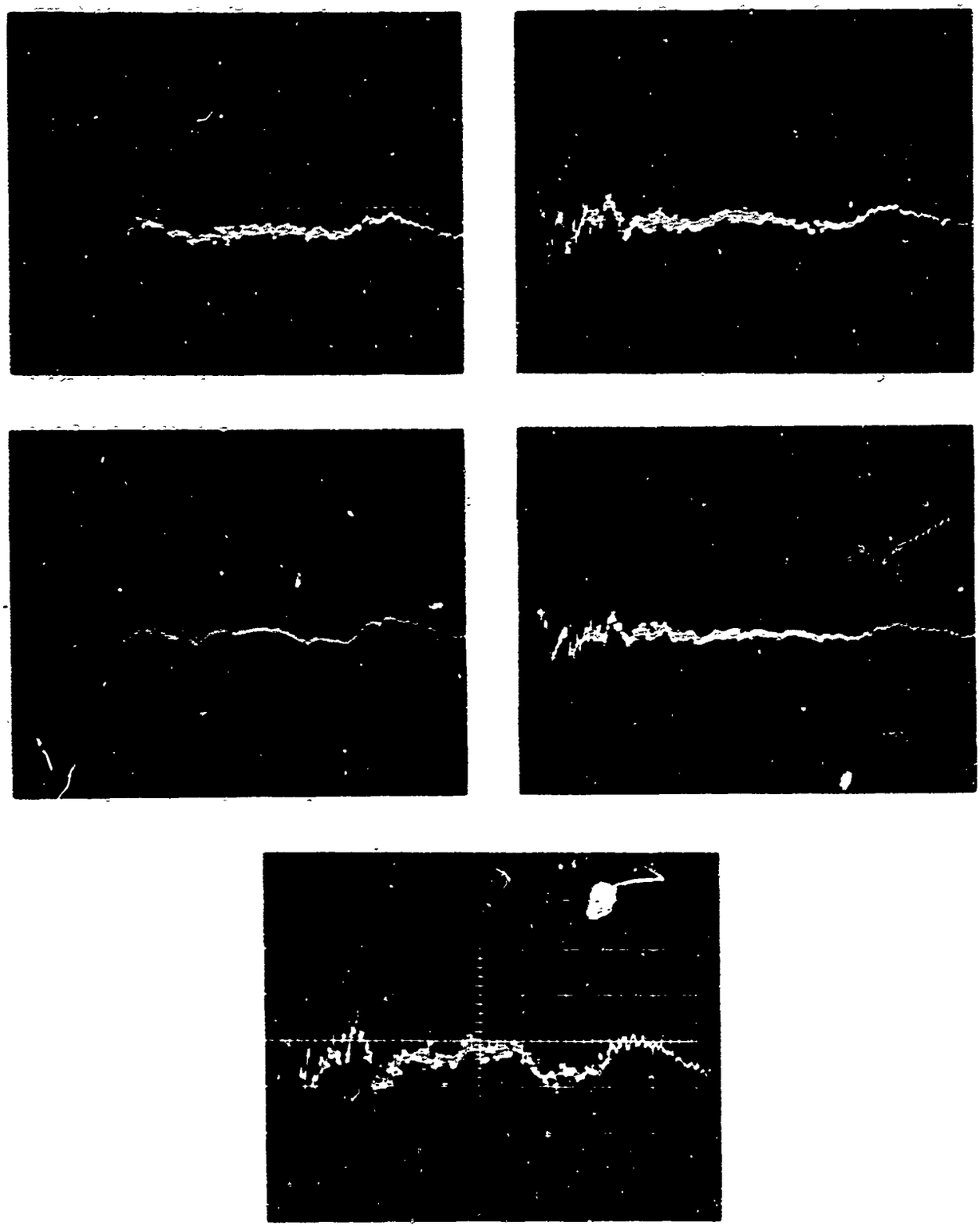

Fig. 115 - Photographs of Acoustic Emissions in Pure H_2 (Spec. CDG-81); horizontal scale - 50 μsec/cm
vertical scale - 10 mV/cm

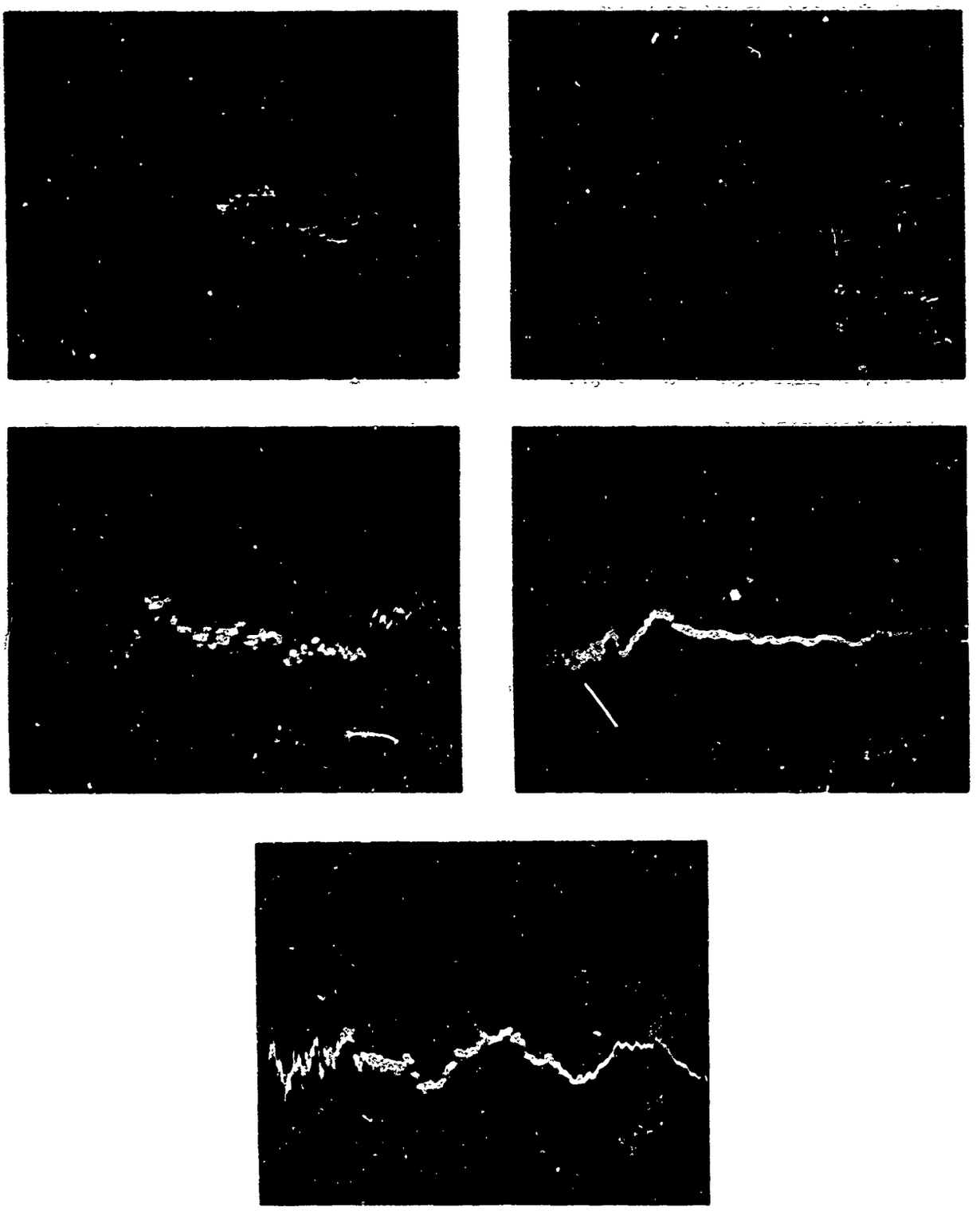

Fig. 116 - Photographs of Acoustic Emissions in 1N HCl at -1500 mV WRT (SCE) (Spec. CDG-82); horizontal scale - 50 μsec/cm
vertical scale - 10 mV/cm

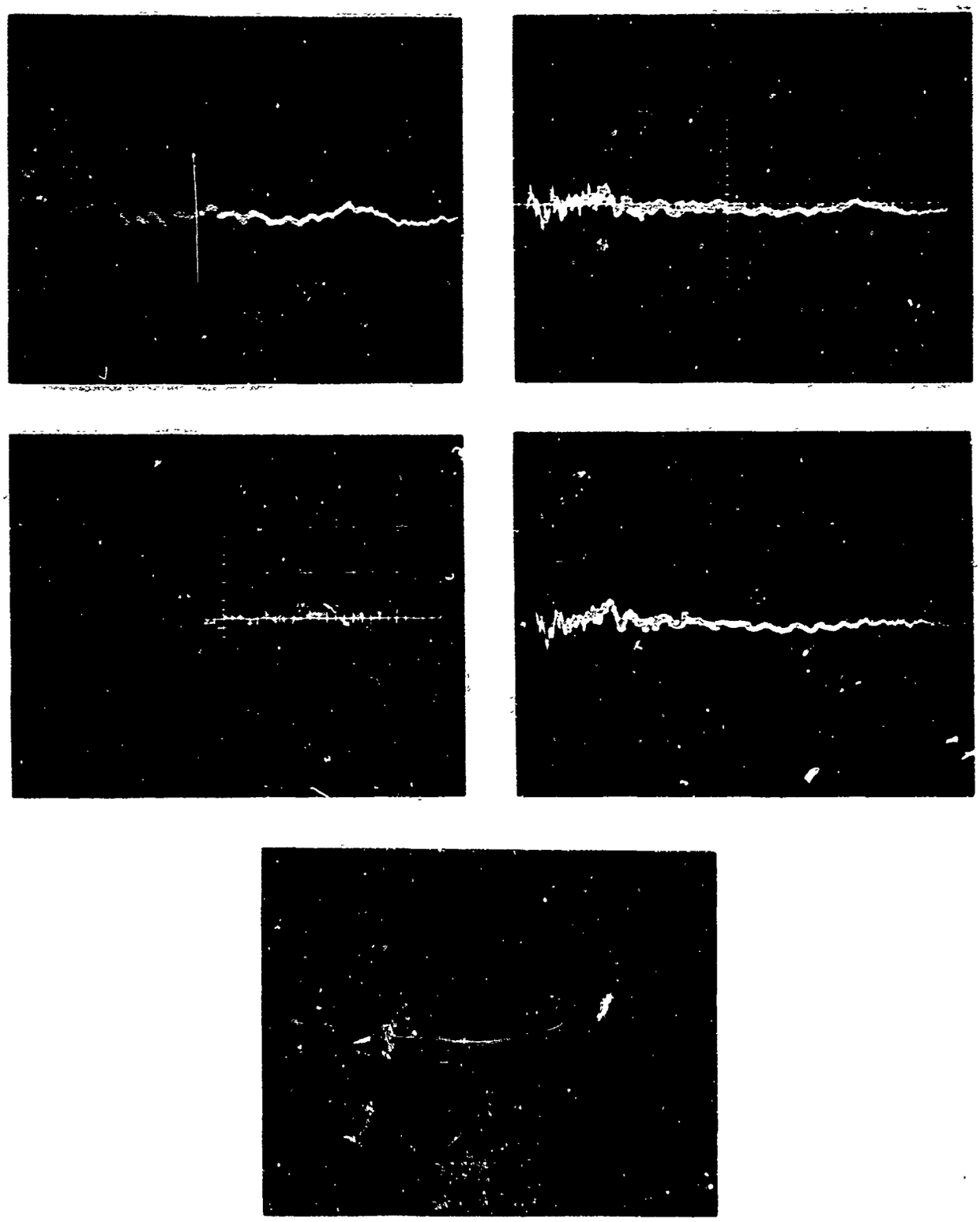

Fig. 117 - Photographs of Acoustic Emissions in 1N HCl at +1200 mV WRT (SCE)(Spec. CDG-83); horizontal scale - 50 μsec/cm
vertical scale - 10 mV/cm

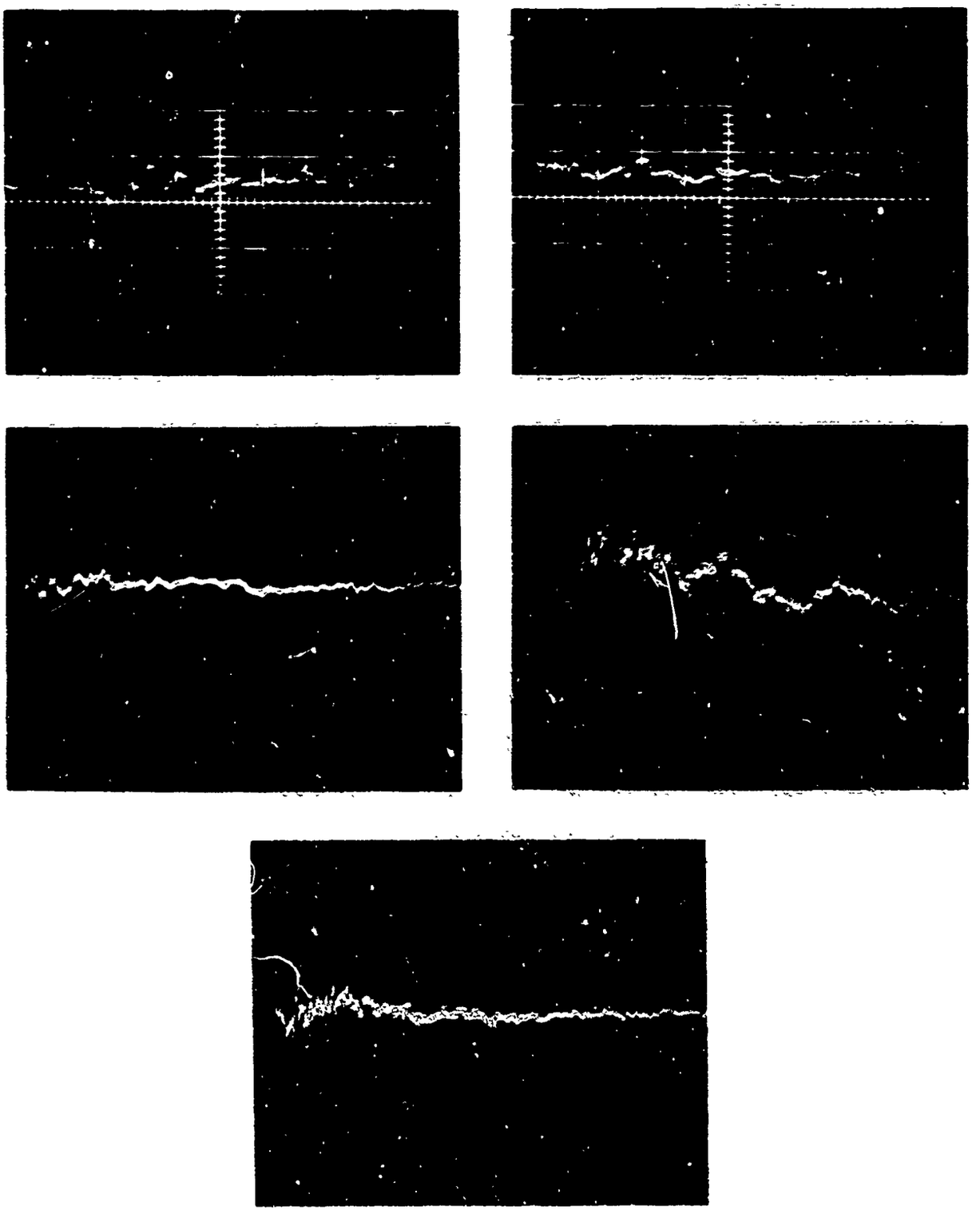

Fig. 118 - Photographs of Acoustic Emissions in $3\frac{1}{2}$% NaCl (adjusted to pH = 13.0 with NaOH) at +1500 mV WRT (SCE) (Spec. CDG-84);
horizontal scale - 50 μsec/cm
vertical scale - 10 mV/cm

transducer. On a comparative basis, there appears to be little effect of environment on signal shape using this experimental technique.

c. Experimentation Using PZT-4 Ceramic Element and Sections of Steel on Sides of Specimens

(1) The effect of reflections in the transmitting medium can be determined by (a) providing an acoustic medium adjacent to the specimen such that portions of the wave which would normally reflect from free surfaces are attenuated, preventing their superposition on the wave portion which travels directly to the detector; or (2) to provide a medium (which is acoustically matched to the specimen material) into which the wave may pass and undergo reflection at a much later time.

Condition (b) is easily met by coupling sections of 4335 steel to the sides of the test specimen, as shown in Fig. 119. If the prefatigue crack length is large, and the piezoelectric detector is placed below the crack, the source-to-detector distance can be made quite small. As shown in Fig. 120, if the detecting element is 0.235-inch from the crack and we assume a longitudinal wave of velocity 23.5×10^4 inch/s generated at the mid-thickness of the specimen, the time to reach the detector is 1 μs. The minimum distance for the wave to travel if it reflected from the free surface of the specimen (with steel sections on the sides) is 1.5 inch. The time required for this portion of the wave to reflect and then strike the detector is at least 6 μs. The shortest time would be 5.3 μs (source is at specimen-side plate interface). Therefore, by examining only the first 5 μs of the signal, the effect of superimposed reflections should be minimal.

Two tests were performed using the technique described above. The prefatigue crack was extended to within 0.25 inch of the detecting element. To detect the emissions, a portion of the PZT-4 disc (described in this report) having a maximum dimension of 0.50 inch was used. The electronic system was the same as that used with the Branson transducer. In the first test the PZT-4 ceramic was backed by a rubber stopper. In the second test a 1/2 inch cube of PZT-4 (with the polarization direction parallel to the plane of the detecting disc) was used. The environment was 0.1N HCl applied to the crack tip from a beaker. This procedure was used so as (1) to allow access to the transducer, and (2) to prevent uncoupling of the transducer from the specimen while inserting the specimen into an environment chamber.

A second series of tests was performed, with two detecting elements (PZT-4) and a Tektronix Type 555 dual beam oscilloscope. Signals from the crystals were photographed by allowing one of the crystal output signals to trigger the oscilloscope sweep. The cracks were propagated in a dry H_2 (pure) environment. Both detecting crystals were backed by PZT-4. The oscilloscope and pre-amplifiers were adjusted to give the same gain for both crystals.

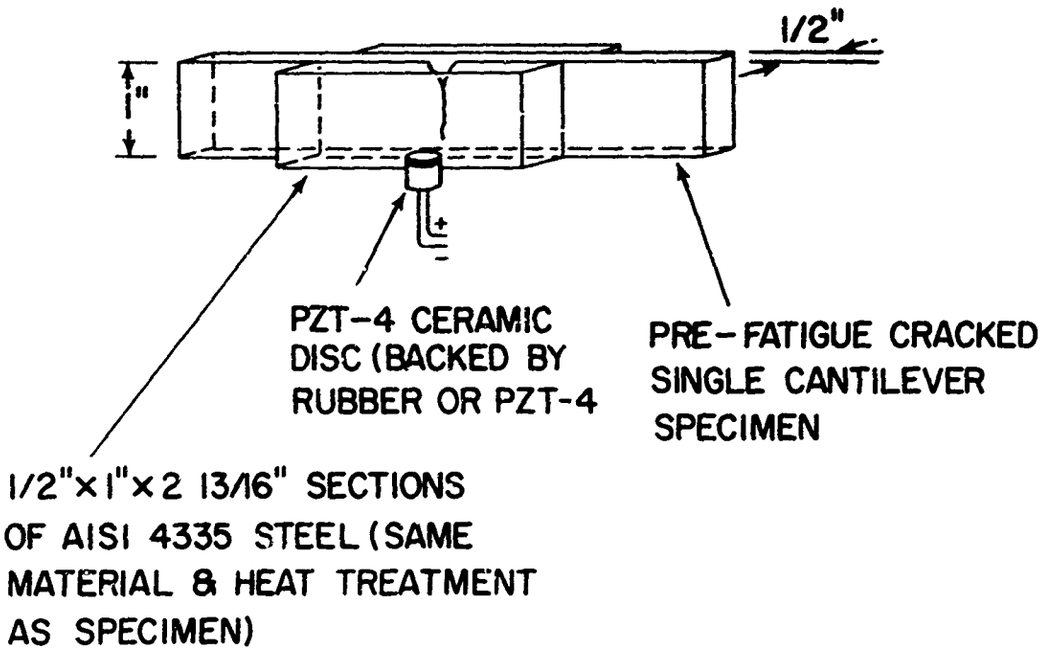

Fig. 119 - Test Apparatus for Experiments with PZT-4 Ceramic Disc

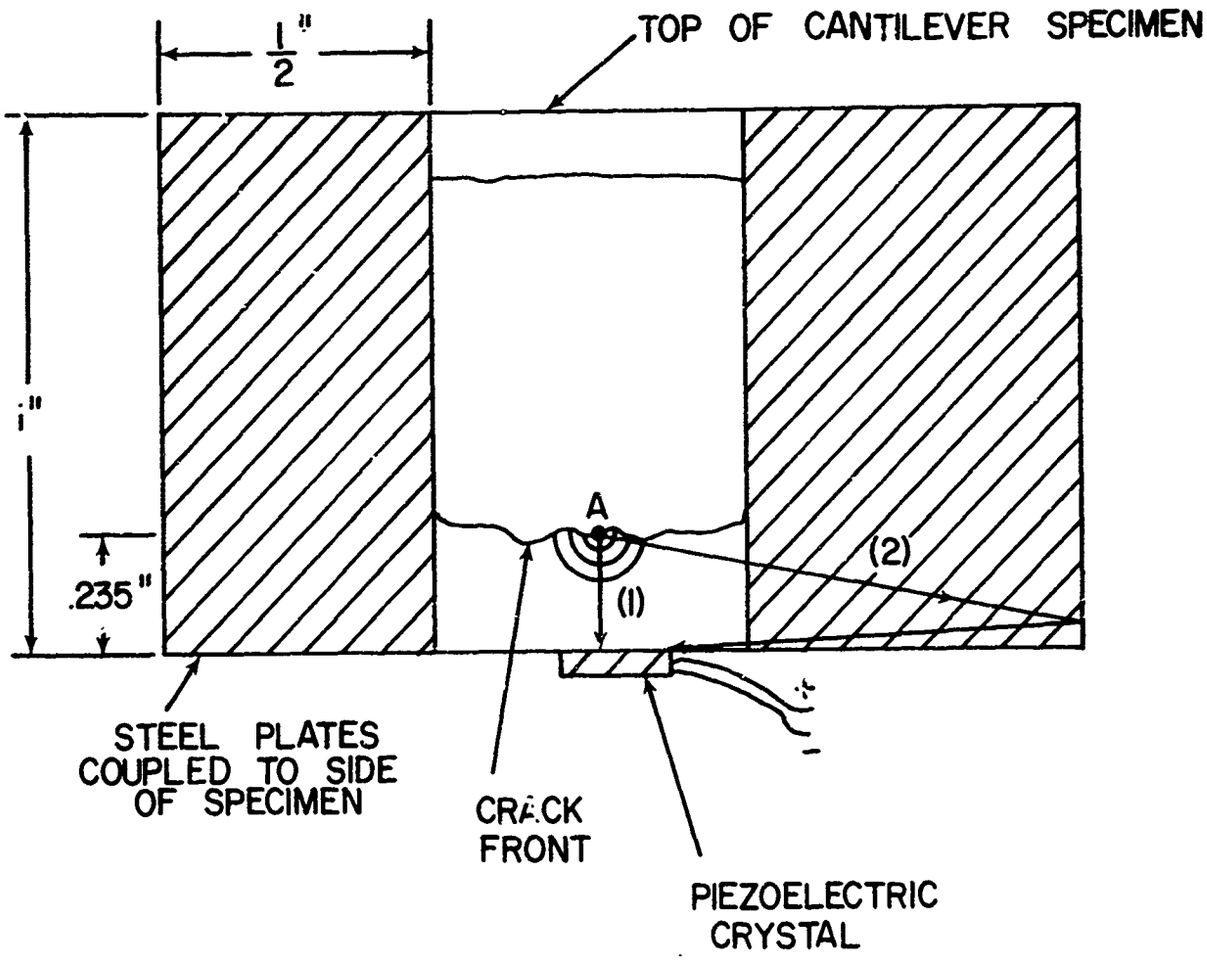

Path (1) - Direct Wave Strikes Crystal in 1 μs
Path (2) - Reflected Portion of Wave Strikes Crystal in 5.3 μs (or longer)
Point A - Wave Source

Fig. 120 - Cross-Sectional View of Cantilever Specimen Showing Wave Paths to Crystal

(2) Results and Discussion

Figure 121 shows five randomly photographed signals for the case where the single PZT-4 disc was backed by a rubber stopper. The photographs show two resonance modes of the detecting disc to be present. These frequencies (2.0 to 2.5 MHz and 250 kHz) are in fair agreement with the predicted[55] values for a 0.050 inch disc, 0.350 inch diameter (1.5 MHz and 250 kHz). The disc was irregularly shaped to avoid the lower frequency radial mode. Its average width was approximately 0.350 inch, however, indicating that the radial resonance mode still occurred. The backing of the detecting disc by the PZT-4 cube in the second test gave a medium of the same acoustic impedance as the detecting crystal. This removed the free surface condition for reflection and satisfied the conditions for minimum acoustic impedance mismatch described by Mason.[56] The results are shown by the five photographs in Fig. 122. No apparent resonance effects were present.

Figure 123 shows five random photographs obtained when two piezoelectric discs were used. The oscilloscope sweep was triggered by the upper beam signal. The applied initial stress intensity factor was 45.80 ksi-in.$^{1/2}$.

By further experimentation it was found that pulses of microsecond duration, such as those in Figs. 121, 122, and 123, could be produced by electrical light switches in the laboratory. Also ultra-high frequency signals (several megahertz), as seen in Fig. 123, were found to be noise signals from the Hewlett-Packard voltmeter pre-amplifiers. In many cases, however, signals such as in Fig. 121c and in Figs. 123a and b, show crystal resonance. It is, therefore, very possible that the acoustic signal is of microsecond duration, since it is unlikely that power line noise (switches, etc.) could excite mechanical resonance of the transducer. In general, the pulse shapes observed during cracking were varied and similar to that shown in Fig. 121c. The electrical noise signals observed were rather similar in that they were either of very short duration, with no obvious periodicity, or of very high frequency content (well above any natural first harmonic frequency of the crystal).

d. Conclusions

The experimental results to date have shown that:

(1) The removal of conditions for reflection in the transducer and in the transmitting medium greatly alters the signal produced by a piezoelectric detector when stress waves are produced.

(2) The elimination of reflection phenomena by altering detector and specimen geometry provides a simpler approach to stress wave analysis than the attempt to determine the distortion of the wave due to reflections.

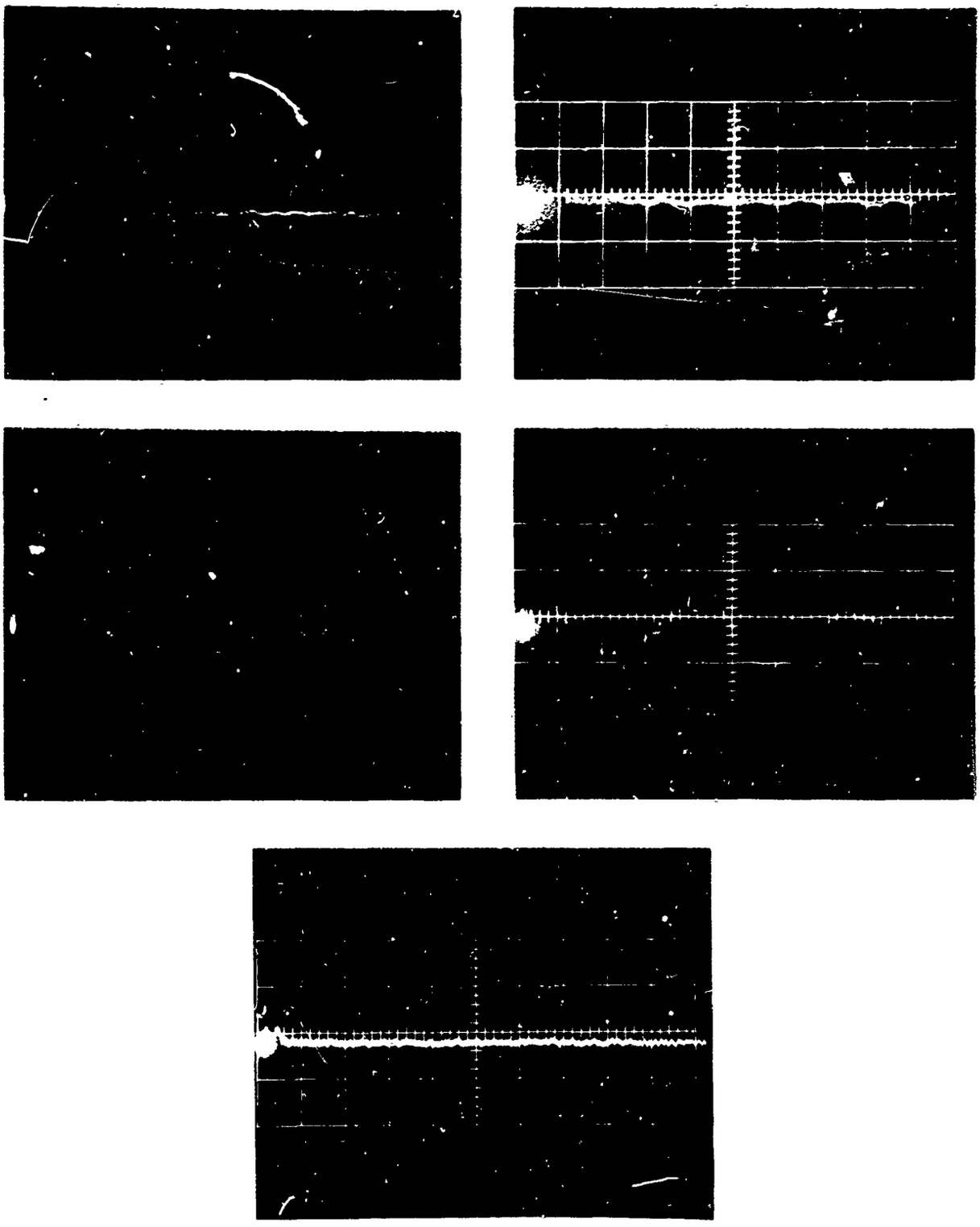

Fig. 121 - Photographs of Acoustic Emissions in 0.1N HCl (Spec. CDG-85); horizontal scale - 1 μs/cm (photos 1-4)
5 μs/cm (photo 5)
vertical scale - 4 mV/cm

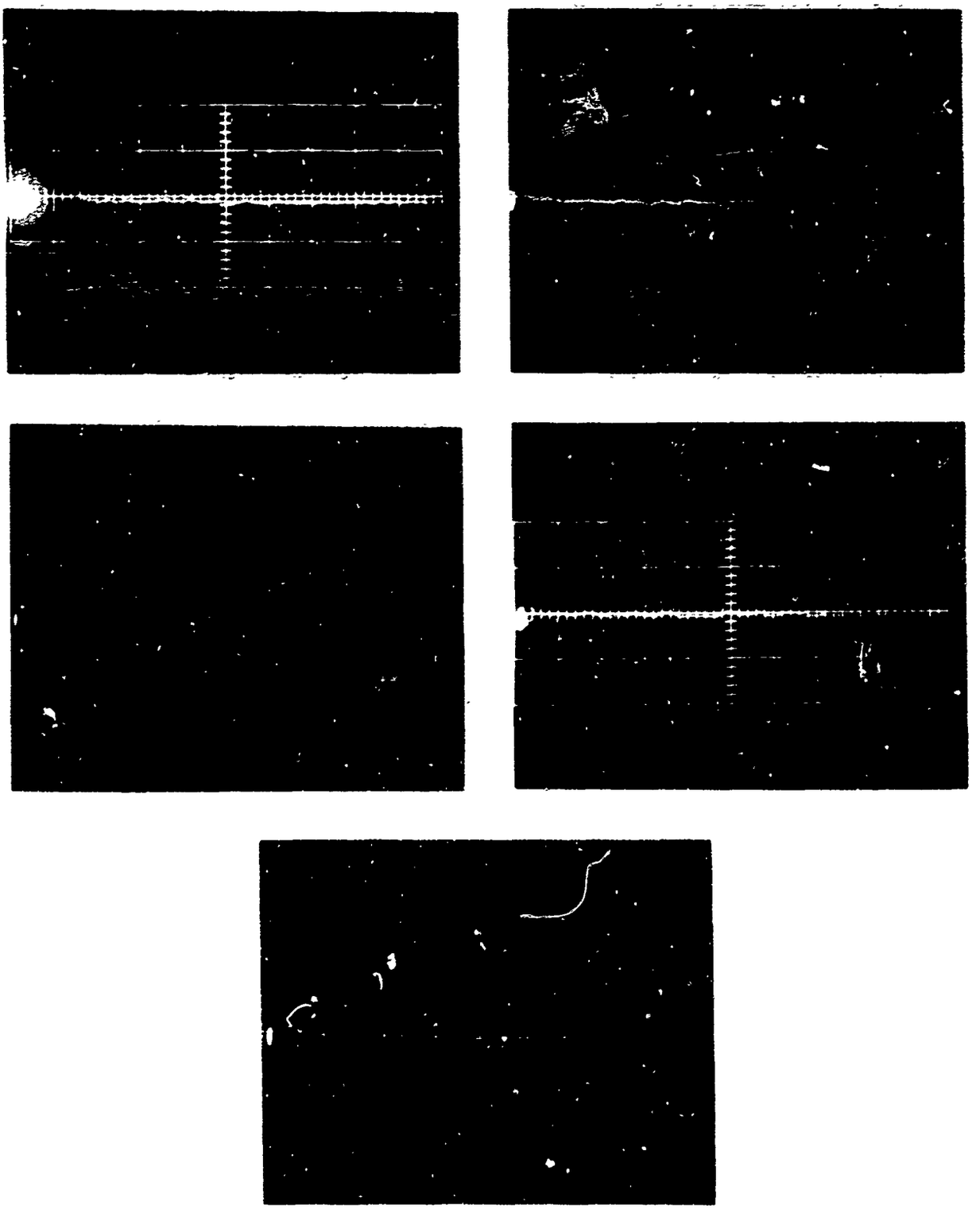

Fig. 122 - Photographs of Acoustic Emissions in 0.1N HCl (Spec. CDG-86); horizontal scale - 1 μs/cm
vertical scale - 5 mV/cm

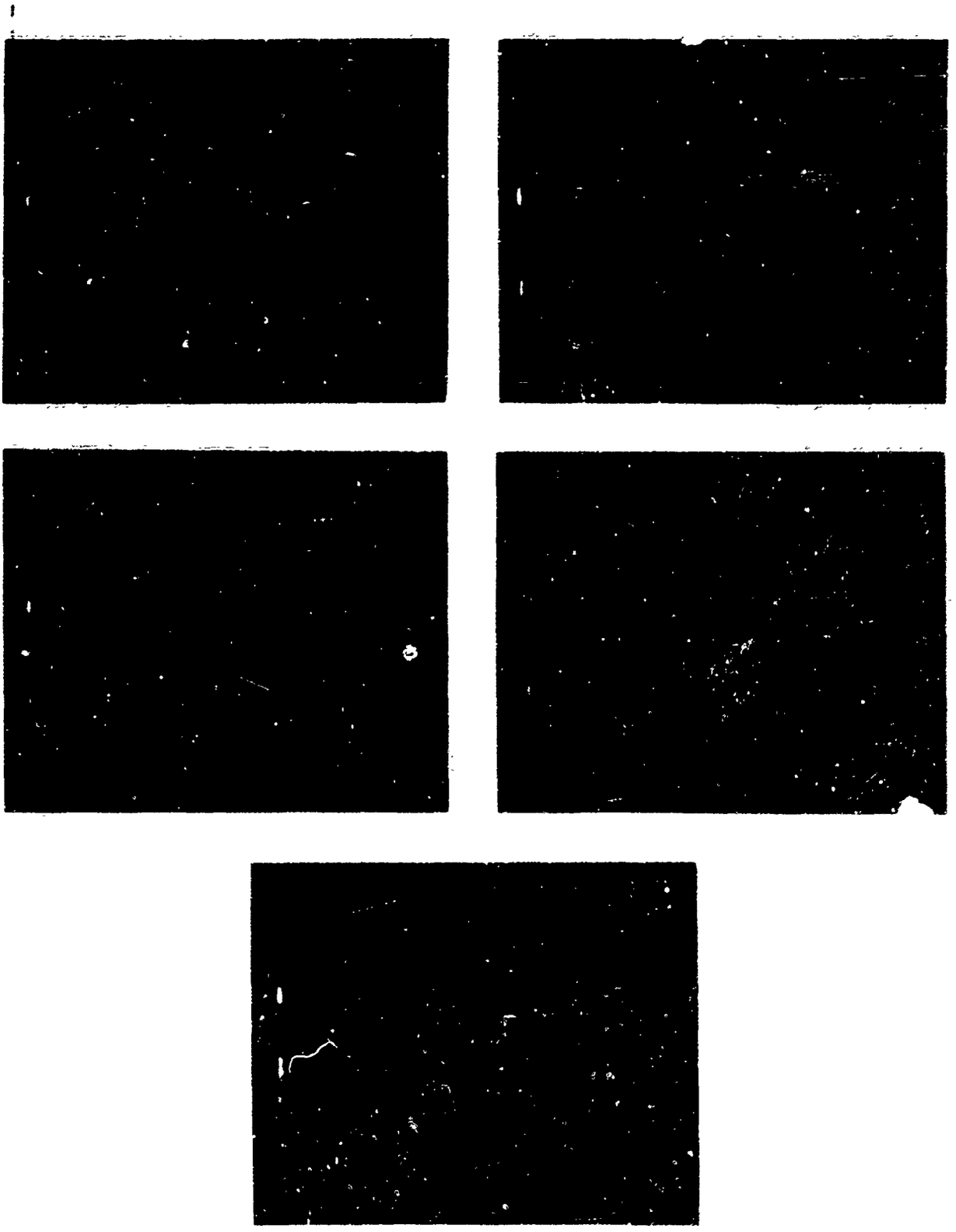

Fig. 123 - Photographs of Acoustic Emissions in Pure H_2 (Spec. CDG-88); horizontal scale - 1 μs/cm

H. DELAYED FAILURE OF HIGH STRENGTH STEELS
(D. Langstaff, G. Meyrick, and J. P. Hirth)

1. Introduction

The in situ charging apparatus for qualitative time-to-failure studies which had been designed, constructed, and tested with favorable results at the time of the last report has been modified to optimize test conditions. These modifications resulted in the minimization of stray currents in the circuit, the minimization of spurious ions in the electrolyte, the capability to grip the wire at large loads without specimen failure induced at the grips, the maintaining of galvanostatic conditions in the circuit, and the use of instrumentation having at least ±1% accuracy in the test circuitry. The selected specimen preparation method was investigated to confirm that it resulted in no deterioration of the specimen. It was then adopted as a standard procedure.

For in situ cathodic charging the test results yielded the characteristic load vs. time or static fatigue curve associated with hydrogen-induced, delayed failure. An apparent inverse relationship between charging current and the square root of the time to failure was obtained. A qualitative anodic polarization curve was run to assess the feasibility of obtaining additional polarization curves as material parameters.

2. Experimental

The test cell is now constructed completely of nonmetallic components to eliminate corrosion and the possibility of spurious cations entering solution from the apparatus. Because of its chemical stability in a wide range of environments, a mesh platinum anode has been obtained to replace the stainless steel one. A high anode to cathode area ratio is maintained to achieve a more uniform current density over the specimen. Initially, a conventional galvanostatic set-up consisting of a resistance several orders of magnitude greater than that of the cell resistance in series with the cell was used with a filtered dc power supply. However, a solid state constant current source relying on feedback control to maintain galvanostatic conditions has been assembled and has replaced the conventional control. In preliminary testing, the solid state device (designed by Mr. Joseph Dryer) provides constant current even with rapid changes in supply voltage and in simulated cell resistance.

During testing, subsequent to specimen preparation but without in situ charging, using the cam-type grips at higher loads (e.g., 90%-95% of the maximum load), difficulties with specimen fracture in the grips became evident. Suitable adaptors were made so that pin vises could be substituted for the cam-type grips in the apparatus; there have been no further problems. The pin-vise arrangement has the advantage that the wire is subjected to a minimal torque on loading, an improvement over the cam-type grips.

3. Results

The results of the investigation of the effect of specimen preparation with regard to embrittlement or specimen deterioration (Fig. 124) indicate that the selected method is acceptable and will be used as a standard procedure. Additional evidence as to the susceptibility of the 0.0202-inch diameter, 400 ksi UTS, AISI 4140 wire to delayed failure came to light when several specimens fractured after a time when subjected to in situ cathodic charging while bearing no load or only that load required to straighten the wire and hold it in place. Another observation for the above material when under a constant load of 26.10 lb was that the squre root of the time to failure was inversely proportional to the charging current (Fig. 125). This relation will be checked again with better instrumentation and experimental control.

A plot of load vs. time to failure characteristic of hydrogen-induced delayed failure was obtained for Malin's No. 6 Music Wire (Fig. 126) as well as for the 4140 wire. Malin's Music Wire has high strength, is easily handled, and is responsive to the variables being considered in this investigation; e.g., load and cathodic current density. The music wire is being used in preliminary tests to firmly establish test procedures before proceeding with the limited supply of Hy-Tuff and AISI 4140. The time-to-fail curves exhibit the normal behavior; i.e., decreased current density yielding displacement of the curve to longer times.

A Luggin probe-salt bridge assembly was constructed so that the cathodic half-cell potential could be monitored with respect to a standard cell of calomel saturated with potassium chloride. An anodic polarization curve of the AISI 4140 wire was determined to evaluate the feasibility of determining polarization curves as qualitative material parameters of the substances under investigation (Fig. 127).

4. Future Work

Polarization curves will be determined for substances under investigation to be used as qualitative material parameters. Time-to-failure as a function of load for the various strength levels, sizes, and materials at hand will be determined under various charging conditions.

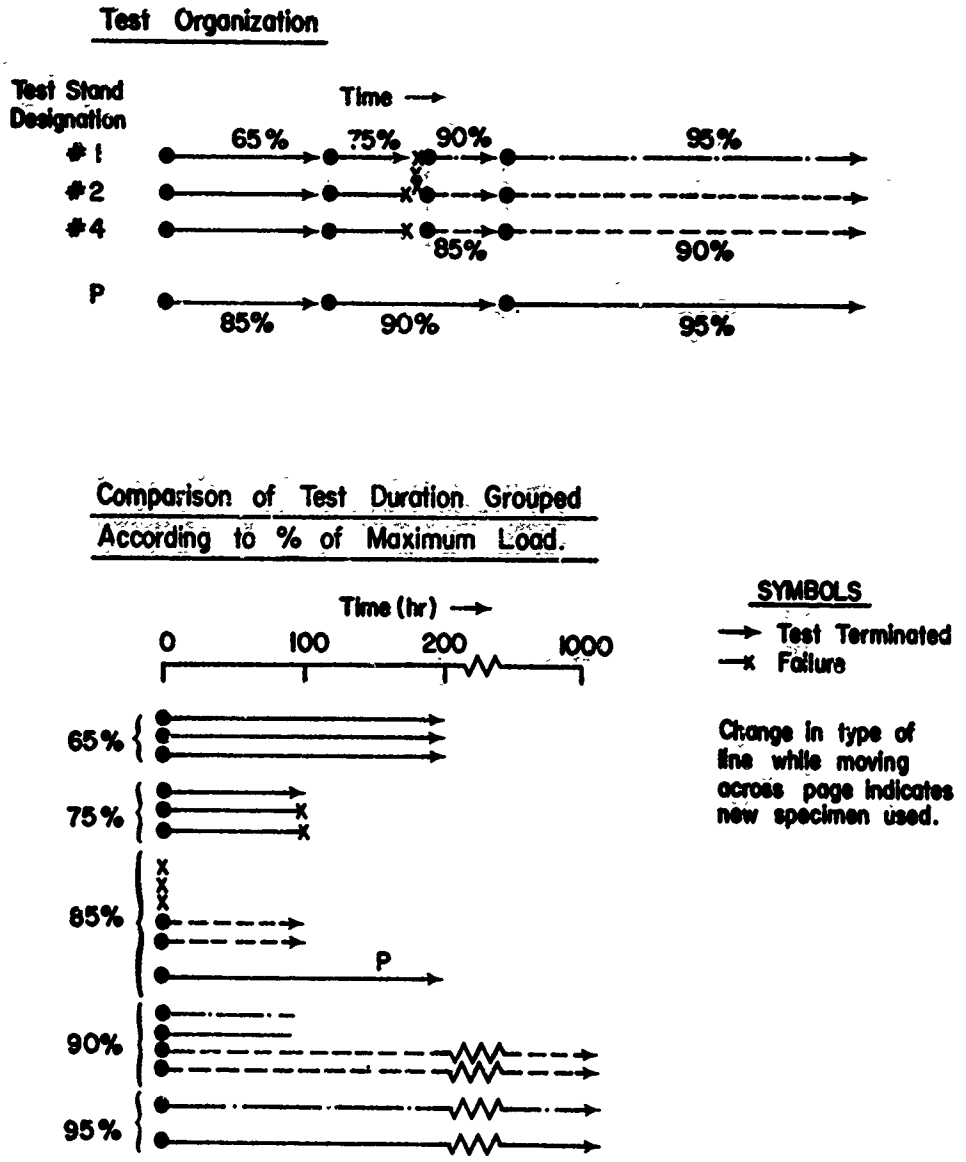

Fig. 124 - Results of the Effect of Wire Preparation on Its Subsequent Strength

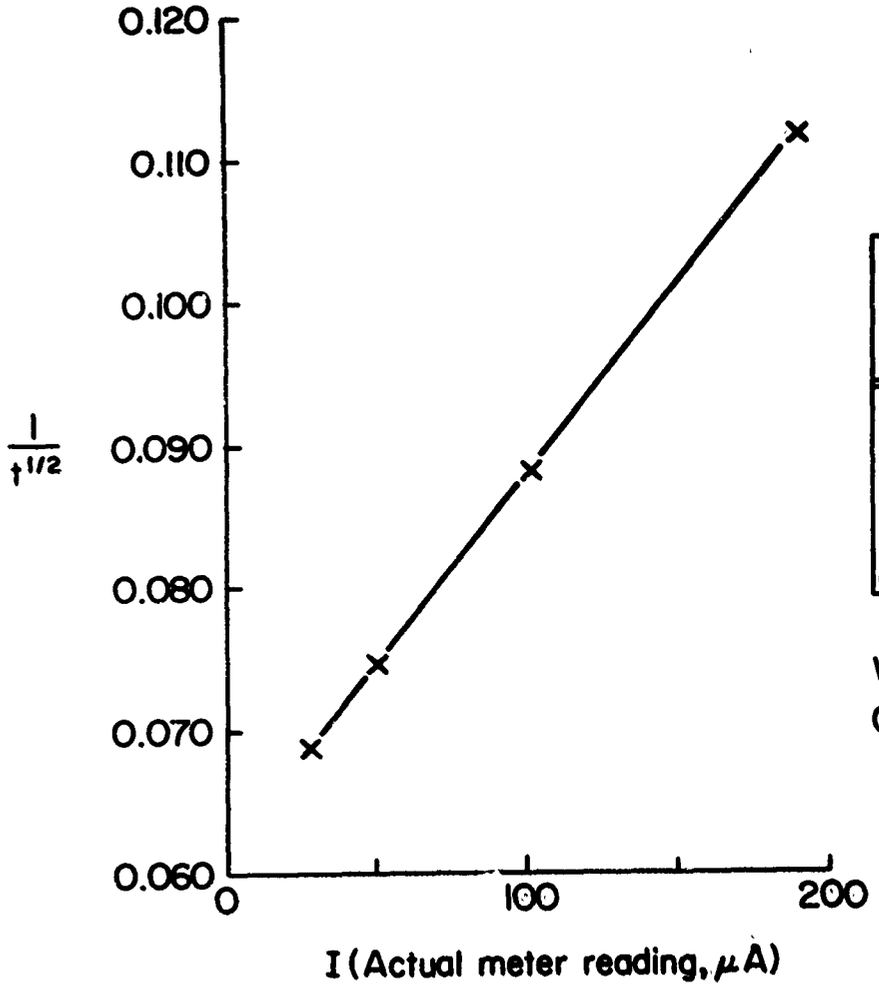

Current Reading of Shunted Microammeter (μA)	Time to Failure (sec)	$\frac{1}{t^{-1/2}}$
190	80.0	0.1118
102	127.8	0.0885
51	179.8	0.0746
28	211.4	0.0689

Wire diameter: 0.016 inch
Gauge length: 3.0 inches

Fig. 125 - Relation of Time-to-Failure to Cathodic Charging Current for Malin's No. 6 Music Wire under a Constant 26.10 lb Load in 1N N_2SO_4 Solution Poisoned with Thiourea (1g/l) at 38°F

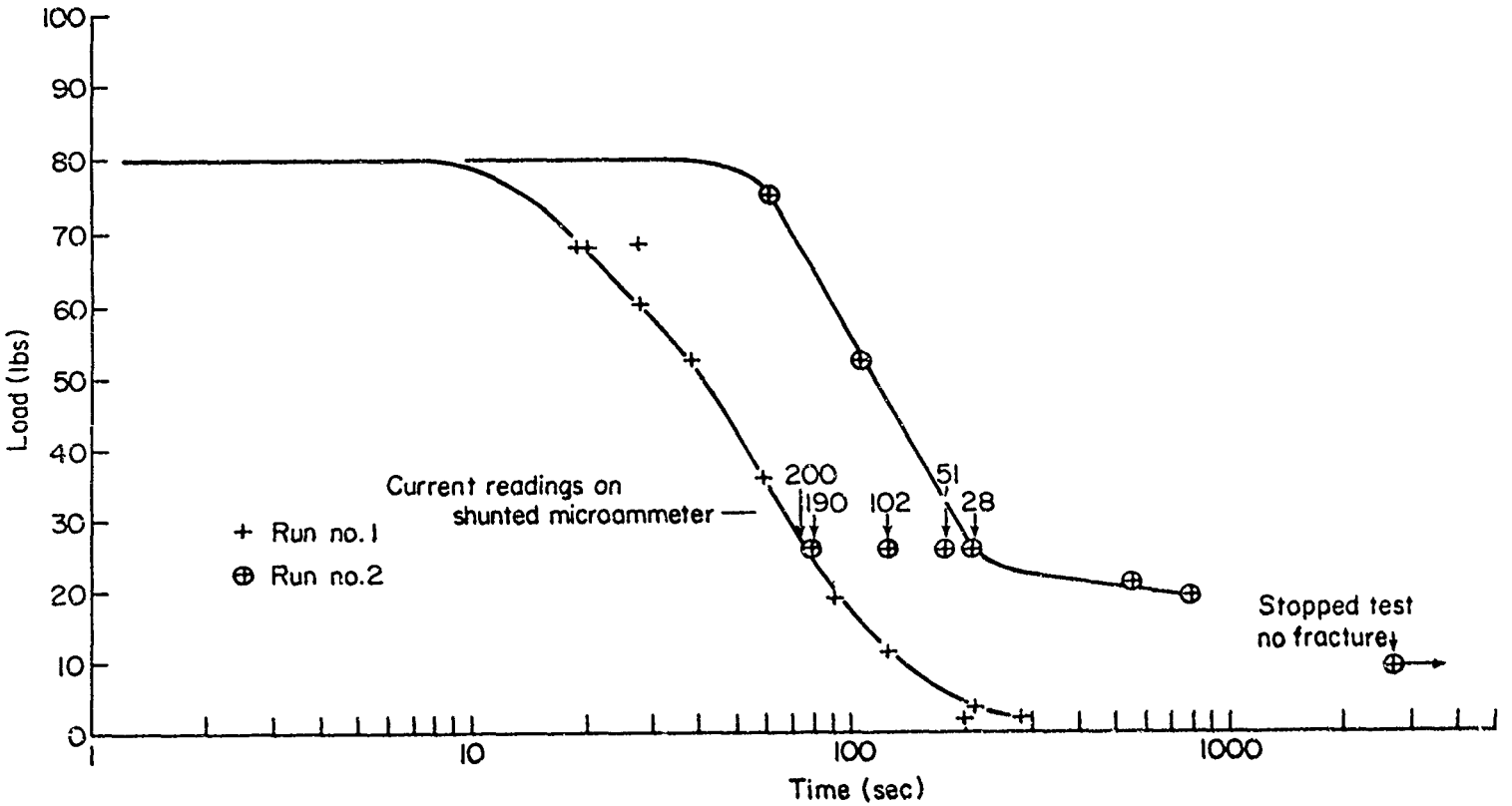

Fig. 126 - Displacement of Static Fatigue Curve by Varying Cathodic Charging Current
Material: 3-Inch length of Malin's No. 6 Music Wire
Electrolyte: 1N H_2SO_4 + thiourea (1g/ℓ).

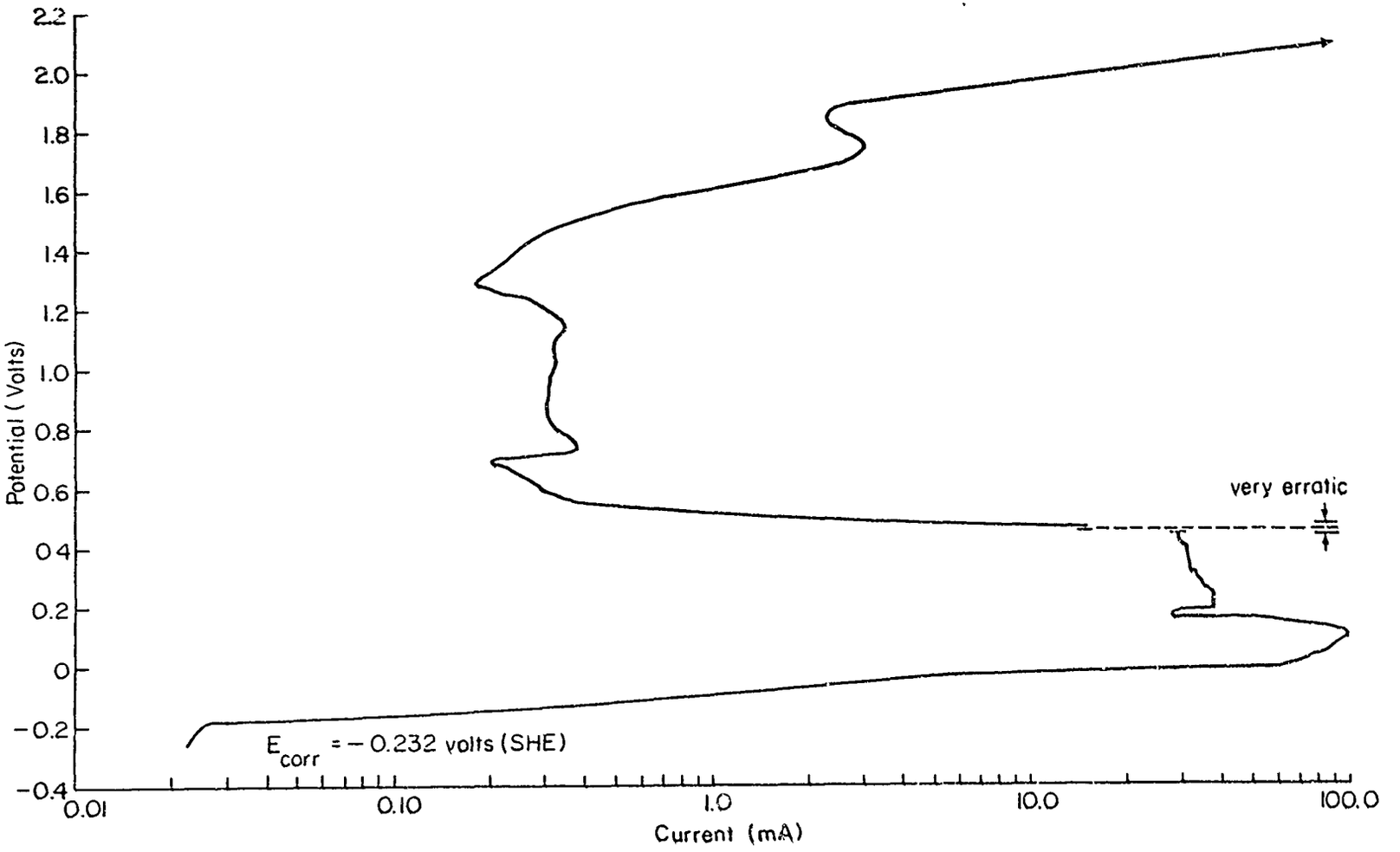

Fig. 127 - Potentiostatic Anodic Polarization Curve of 90% Cold-Worked 4140 Steel Wire in 1N H_2SO_4 + Thiourea (1g/ℓ) at 38°F
Wire Diameter: 0.0202 inch
Gauge Length: 2.0 inch

SECTION IV

COORDINATION AND BRIEFING
(Met. E., - OSU Staff)

Seminars and lectures presented by the staff at the Air Force Materials Laboratory follow:

Date	Subject	Staff Member
November 25, 1969	Cracking of Thin Films on Rigid Substrates	Turner Alfrey, Jr.
January 20, 1970	Nuclear Magnetic Resonance in Liquid Metals	D. A. Rigney
February 4, 1970	Advances in Steel Making	G. R. St. Pierre
April 13, 1970	Stress Corrosion of High Strength Steels	R. W. Staehle
May 5, 1970	Stress Corrosion of Titanium Alloys	F. H. Beck

During the 1970-1971 academic year a series of AFML lectures at OSU is planned. These lectures will be presented on technical and administrative subjects.

The first lecture was presented by B. Cohen on 1 December 1970. This was a two-hour lecture on the subject of failure causes and analysis in aircraft.

SECTION V

MISCELLANEOUS

Dr. C. M. Chen continues his research at AFML under this program. No degrees were granted during this period but at least one masters and two Ph.D. degrees are expected during the next period.

REFERENCES

1. N. J. Petch, J. Iron and Steel Institute, 173, p. 25, (1953).

2. J. D. Eshelby, F. C. Frank, and F. R. N. Nabarro, Phil. Mag., 42, p. 351 (1951).

3. A. N. Stroh, Proc. Roy. Soc., 223, pp. 404-14, (1954).

4. W. R. Robertson and A. S. Tetelman, Strengthening Mechanisms in Solids, ASM, 1960.

5. F. G. Haney, W. F. Wearmouth, G. Goldberg, F. F. Ernsberger and W. T. Brehm, "Investigation of Stress Corrosion Cracking of Titanium Alloys," Mellon Institute Progress Report No. 3, NGR-39-008-014, (November, 1967).

6. E. G. Coleman, D. Weinstein and W. Rostoker, "On a Surface Energy Mechanism for Stress-Corrosion Cracking," Acta Met., Vol. 9, p. 491, (1961)).

7. A. J. Sedriks, J. A. S. Green and P. W. Slattery, "Stress Corrosion Cracking Behavior of Ti and Ti-Al Alloys in Methanol-Iodine Solutions," Corrosion, Vol. 24, p. 172, (1968).

8. D. T. Powell and J. C. Scully, "Stress Corrosion Cracking of Alpha Titanium Alloys at Room Temperature," Corrosion, Vol. 24, p. 151, (1968)).

9. W. L. Baenwell, J. F. Myers and F. K. Sauer, "Effect of Grain Size on Stress Corrosion of Type 302 Austenitic Stainless Steel," Corrosion, Vol. 22, p. 261, (1966).

10. G. Sanderson, D. T. Powell and J. C. Scully, "Metallographic Studies of Stress-Corrosion Cracking of Titanium Alloys in Aqueous Chloride Solutions," Proceedings of the International Conference on Fundamental Aspects of Stress Corrosion Cracking, The Ohio State University, (September 1967).

11. Discussion, "Chemical and Environmental Behavior," The Science, Technology and Application of Titanium, edited by Jaffee and Promisel, published by Pergamon Press, p. 324.

12. N. D. Tomashow, F. N. Altovskiy and V. B. Vladimirow, Reference 10.

13. A. J. Sedriks, P. W. Slattery and J. A. S. Green, "Failure of Alpha Titanium in Methanol-Hydrochloric Acid-Water Solutions," Trans. A.S.M., Vol. 61, p. 625 (1968).

14. A. J. Sedriks and J. A. S. Green, "Stress Corrosion Cracking of Titanium in Organic Liquids," RIAS Technical Report 69-11, August, 1969.

15. I. R. Lane and J. L. Carvalho, "Applications of Related Phenomena in Titanium Alloys," ASTM STP 432, American Society for Testing and Materials, Philadelphia, Pa., p. 147 (1967).

16. R. J. Green and J. R. Myers, "Effect of Grain Size on Incubation and Propagation of Stress Corrosion Cracks in Type 302 Steel," Corrosion, Vol. 24, p. 137 (1968).

17. R. E. Johnson, "NASA Experiences with Ti-6Al-4V in Methanol," DMIC Memorandum 228, Battelle Memorial Institute, p. 2 (March, 1967).

18. J. C. Williams, "Some Observations on the Stress-Corrosion Cracking of Three Commercial Titanium Alloys," Trans. A.S.M., Vol. 60, p. 646 (1967).

19. J. C. Scully, "Kinetic Features of Stress-Corrosion Cracking," Corrosion Science, Vol. 7, p. 197 (1967).

20. M. J. Bladderum and J. C. Williams, "Metallurgical Aspects of the Stress Corrosion Cracking of Titanium Alloys," Proceedings of the Conference on Fundamental Aspects of SCC, The Ohio State University, NACE, Houston, Texas ((1967)), p. 620.

21. G. Sanderson and J. C. Scully, "Hydride Formation in Commercial Titanium Alloys," Corrosion Science, Vol. 6, p. 541 ((1966)).

22. T. R. Beck, M. J. Bladderum, and M. O. Speidel, Quarterly Progress Report No. III, NASS 7-489, ((March, 1969)).

23. T. R. Beck, "Electrochemical Mechanism in the Stress Corrosion Cracking of Titanium Alloys," The Science, Technology and Application of Titanium, edited by Jaffee and Promisel, published by Pergamon Press, p. 239 ((1970)).

24. R. L. Wenk, "Stress Corrosion Cracking of Ti-8Al-1Mo-1V in Methanol-NaCl-Water Solutions," M. S. Thesis, The Ohio State University, ((1967)).

25. H. Herrigel, "Titanium U-Bends in Organic Liquids and the Effect of Inhibitions," DMIC Memorandum No. 228, Battelle Memorial Institute, Columbus, Ohio ((March 6, 1967.

26. J. Mitchell and D. Smith, Aquametry, Interscience Publishers, Inc., New York ((1948)).

27. H. Tamd and J. Bjerrum, Berichte der Chemische Gesellschaft 64, 210 ((1931)).

28. L. R. Smith, J. W. Highhower, and C. G. Harkins, Corrosion 26, 3777 ((1970)).

29. Mars G. Fontana, "Corrosion Cracking of Metallic Materials," Technical Report AFML-69-16, ((February, 1969)).

30. Mars G. Fontana, "Corrosion Cracking of Metallic Materials," Technical Report AFML-70-2, January, 1970)).

31. B. F. Brown, C. T. Fujii, E. P. Dahlberg, "Methods for Studying the Solution Chemistry within Stress Corrosion Cracks," J. Electrochem. Soc. 116, p. 218 ((1969)).

32. J. A. Smith, M. H. Peterson and B. F. Brown, "Electrochemical Conditions at the Tip of an Advancing Stress Corrosion Crack in AISI 4340 Steel," to be published in NACE Corrosion.

33. G. R. Irwin, "Critical Energy Rate Analysis of Fracture Strength," Welding Research Supplement 33, p. 1935-1985 ((1954)).

34. W. A. Van der Sluys, Babcock and Wilcox Co., Alliance Research Center, Alliance, Ohio, private communication, December 1, 1969.

35. W. A. Van der Sluys, "Mechanism of Environment Induced Subcritical Flaw Growth in AISI 4340 Steel," Engineering Fracture Mechanics 1, p. 1147, 1969)).

36. E. A. Steigerwald, W. D. Benjamin, "Environmentally Induced Delayed Failures in Martensitic High Strength Steels," Report AFML-TR-68-80, TRW Inc., Contract AF 33((615))-3651, ((April, 1968)).

37. A. J. Stavros, H. W. Paxton, "Stress Corrosion Cracking Behavior of an 18% Ni Maraging Steel," Metallurgical Trans. 1, p. 3049, ((1970)).

38. M. Smialowski, and Z. Szlarska-Smialowski, Bull Acad. Pol. Sci. 2, 73 ((1954)).

39. J. M. West, Electrodeposition and Corrosion Processes, D. Van Nostrand ((1965)).

40. T. P. Radhakrishnan and L. L. Shreir, Electrochem. Acta 11, 1067, ((1966)).

41. J. F. Newman and L. L. Shreir, Corrosion Science 9, 631 (1969).

42. K. Farrell, Corrosion 26, 105 (1970).

43. A McNabb and D. K. Foster, TAIME 227, 618 (1963).

44. R. A. Oriani, Acta Met. 18, 147 (1970).

45. M. A. Genshaw and J. McBreen, Proceedings of Conference, Fundamental Aspects of Stress Corrosion Cracking (Ohio State University) p. 51 (September, 1967).

46. E. Hornbogen and R. C. Glenn, TAIME 218, 1064 (1960).

47. Report AFML-70-2, p. 154, "Corrosion Cracking of Metallic Materials."

48. M. Nagayama and N. Cohen, J. Electrochem. Soc. 109, 781 (1962).

49. N. Cabrera and N. F. Mott, Rep. Prog. Phys. 12, 163 (1949).

50. H. Dunegan and D. Harris, "Acoustic Emission - A New Nondestructive Testing Tool," Ultrasonics, Vol. 7, No. 3, (1969).

51. R. M. Fisher and J. S. Lally, "Microplasticity Detected by an Acoustic Technique," Canadian Journal of Physics 45, 1147 (1967).

52. W. W. Gerberich and C. E. Hartbower, "Some Observations on Stress Wave Emission as a Measure of Crack Growth," Int. Journ. of Fract. Mech., 3, No. 3, 185-192 (September, 1967).

53. W. W. Gerberich and C. E. Hartbower, "Monitoring Crack Growth of Hydrogen Embrittlement and Stress Corrosion Cracking by Acoustic Emission," Proc. Conf. on Fundamental Aspects of Stress Corrosion Cracking (Ohio State University), pp. 420-438 (September, 1967).

54. W. P. Mason, Physical Acoustics and the Properties of Solids, D. VanNostrand, Inc., Princeton, New Jersey, p. 17 (1958).

55. Clevite Corp., Modern Piezoelectric Ceramics, Publ. No. PD-9247.

56. Reference, 54, p. 27.